UNIVERSITY OF CALIFORNIA SAN DIEGO

Design and synthesis of phosphors to improve efficiency for solid state lighting application

A dissertation submitted in partial satisfaction of the

requirements for the degree of Doctor of Philosophy

in

Materials Science and Engineering

by

Jungmin Ha

Committee in charge:

Joanna McKittrick, Chair
Ekaterina Evdokimenko
Javier Garay
Olivia A. Graeve
Shyue Ping Ong
Andrea Tao

2019

The Dissertation of Jungmin Ha is approved, and is acceptable in quality and form for publication on microfilm and electronically:

_____

_____

_____

_____

_____

_____

Chair

University of California San Diego

2019

DEDICATION

To my family

TABLE OF CONTENTS

LIST OF FIGURES

LIST OF TABLES

GLOSSARY

CCT	Correlated color temperature
CIE	Commission Internationale de l‘Eclairage
CRI	Color rendering index
QE or Φ	Quantum efficiency
HID	High density discharge lamp
LCD	Liquid crystal display
LED	Light emitting diode
lm	Luminous flux
lm/W	Luminous efficacy (lumen/watt)
nUV	Near ultraviolet (380-410 nm)
pcLED	Phosphor onverted light emitting diode
PL	Photoluminescence
RE	Rare earth element
RGB	Red, green, and blue color
RT	Room temperature
SEM	Scanning electron microscopy
SSL	Solid state lighting
UV	Ultraviolet
XRD	X-ray diffraction

ACKNOWLEDGEMENTS

I would like to thank my advisor Prof. Joanna McKittrick for her guidance, support, and encouragement my doctoral studies. I could not complete my doctoral work without her support. I would also like to thank my dissertation committee members, Prof. Olivia A. Graeve, Prof. Shyue Ping Ong, Prof. Javier Garay, Prof. Andrea Tao, and Dr. Ekaterina Evdokimenko for their time, interest, and valuable comments. I would like to thank my labmates, Frances Su, Wei Huang, Jae-young Jung, Mike Frank, Steven Naleway, Issac Cabrera, Sean Garner, Keisuke Matsushita for their help and discussion. I would like to thank also my undergrads, Chenhui Zhou and Natalie Lam for their help. I would like to say thanks to my frineds, Jayoung Kim, Hyunchul Chung, Hyunwoong Kim for their moral and emotional support to complete my doctoral work. Most of all, I would like to express my thanks to my framily, Yongsu Ha, Jeomsuk Shin, Minju Ha for their unconditional love and support. My life and doctoral studies would have not been ever started without their devotion.

Chapter 2, in full, is a reprinted of the materials as it appears in "An integrated first principles and experimental investigation of the relationship between structural rigidity and quantum efficiency in phosphors for solid state lighting" Journal of Luminescence, vol 179, pp 297-305, 2016. This work was coauthored by Z. Wang, E. Novitskaya, G. A. Hirata, O. A. Graeve. J. McKittrick and S. P. Ong are the corresponding authors. The dissertation author is the first author of this work.

Chapter 3, in full, is a reprinted of the materials as it appears in "A facile method to improve the quantum efficiency of submicron particles sized phosphors using a flux for solid lighting application", *Ceramics,* 1, 5, 2018. This work was coauthored by E. Novitskaya, G. A. Hirata, C.

Zhou, R. E. Ridley, O. A. Graeve. J. McKittrick is the corresponding author. The dissertation author is the first author of this work.

Chapter 4, in full, is a reprinted of the materials as it appears in "Mining Unexplored Chemistries for Phosphors for High-Color-Quality White-Light-Emitting Diodes", *Joule*, 2, 1-13, 2018. This work was coauthored by Z. Wang, Y. H. Kim, J. McKittrick, S. P. Ong, W. B. Im are the corresponding authors. The dissertation author is the first author of this work.

Chapter 5, in full, has been accepted for publication of the material as it appears in "Color tunable single-phase Eu^{2+} and Ce^{3+} co-activated Sr_2LiAlO_4 phosphors", Journal of Materials Chemistry C 2019. This work was coauthored by Y. H. Kim, E. Novitskaya, Z. Wang, M. Sanchez, O. A. Graeve, W. B. Im, S. P. Ong. J. McKittrick is the corresponding author. The dissertation author is the first author of this work.

Chapter 6, in full, has been submitted for publication of the material as it may appear in "Synthesis of Mn^{4+} activated Na_2SiF_6 red-emitting phosphors using an ionic liquid", Journal of Luminescence 2019. This work was coauthored by E. Novitskaya, L. Lam, M. Sanchez, Y. H. Kim, Z. Li, W. B. Im, O. A. Graeve. J. McKittrick is the corresponding author. The dissertation author is the first author of this work.

The financial support of this work by the United States National Science Foundation, Ceramics Program Grant DMR-1411192.

VITA

2019 Ph.D. Materials Science and Engineering

University of California San Diego, La Jolla, CA

Dissertation: Design and synthesis of phosphors to improve efficiency for solid state lighting application

Advisor: Professor Joanna McKittrick

2012 M.S. Fuel Cells and Hydrogen Technology

Hanyang University, Seoul, Korea (ROK)

2010 B.S. Chemical Engineering

Hanyang University, Seoul, Korea (ROK)

PUBLICATIONS

S.-H. Lee, J. I. Choi, Y. J. Kim, J. K. Han, **J. Ha**, E. Novitskaya, J. B. Talbot, J. McKittrick, "Comparison of luminescent properties of Y_2O_3:Eu^{3+} and $LaPO_4$:Ce^{3+}, Tb^{3+} phosphors prepared by various synthetic methods", *Materials Characterization*, 103, 162-169, 2015. DOI: 10.1016/j.matchar.2015.03.027

J. Ha*, Z. Wang*, E. Novitskaya, G. A. Hirata, O. A. Graeve, S. P. Ong, J. McKittrick, "An integrated first principles and experimental investigation of the relationship between structural rigidity and quantum efficiency in phosphors for solid state lighting", *Journal of Luminescence*, 179, 297–305, 2016. DOI: 10.1016/j.jlumin.2016.07.006 *Contributed Equally

Z. Wang*, **J. Ha*,** Y. H. Kim*, W. B. Im, J. McKittrick, S. P. Ong, "Mining Unexplored Chemistries for phosphors for high-color-quality white-light-emitting diodes", *Joule*, 2, 1-13, 2018. DOI: 10.1016/j.joule.2018.01.015 *Contributed Equally

J. Ha, E. Novitskaya, G. A. Hirata, C. Zhou, R. E. Ridley, O. A. Graeve, J. McKittrick, "A facile method to improve quantum efficiency of submicron particles sized phosphors using a flux for solid lighting application", *Ceramics*, 1, 5, 2018. DOI:10.3390/1010005

J. Jung, S. E. Naleway, Y. N. Maker, K. Y. Kang, J. Lee, **J. Ha**, S. S. Hur, S. Chien, J. McKittrick, "3D printing templating of extrinsic freeze-casting for macro-microporous biomaterials", *ACS Biomaterials Science & Engineering*, 2019, 5 (5), 2122-2133

J. Ha, Y. H. Kim, E. Novitskaya, M. Sanchez, O. A. Graeve, W. B. Im, S. P. Ong, Joanna

McKittrick, "Color tunable single-phase Eu^{2+} and Ce^{3+} co-activated Sr_2LiAlO_4 phosphors", submitted to *Journal of Materials Chemistry C.*

J. Ha, E. Novitskaya, N. Lam, M. Sanchez, O. A. Grave, J. McKittrick, **"**Synthesis of Mn^{4+} activated Na_2SiF_6 red-emitting phosphor using an ionic liquid", in preparation.

CONFERENCE PRESENTATIONS

J. Ha, Z. Wang, S. Lee, E. Novitskaya, O. A. Graeve, S. P. Ong, J. McKittrick, "Development of Phosphors for Solid-State Lighting", UCSD Jacob School of Engineering Research Expo 2015, San Diego, April 16, 2015

J. Ha, Z. Wang, E. Noviskaya, G. A. Hirata, O. A. Graeve, S. P. Ong, J. McKittrick, "Discovery of near-UV excited phosphors: a combined experimental and computational study", Phosphor Safari 2015, Niigata, Japan, July 27-30, 2015.

J. Ha, Z. Wang, E. Novitskaya, G. A. Hirata, O. A. Graeve, S. P. Ong, "Phosphor design and development for solid state lighting", International Materials Research Congress, Cancún, México, August 20, 2015.

J. Ha, E. Novitskaya, G. A. Hirata, O. A. Graeve, J. McKittrick, "A method to improve quantum efficiency of nanosized phosphors for near-UV-LEDs", UCSD Jacob School of Engineering Research Expo, 2016, San Diego, April 14, 2016.

J. Ha, E. Novitskaya, G. A. Hirata, O. A. Graeve, J. McKittrick, "Improvement of quantum efficiency of the nanosized phosphors using a flux", Electrochemical Society spring meeting, San Diego, May 2016.

J. Ha, E. Novitskaya, G. A. Hirata, O. A. Graeve, J. McKittrick, "A method to improve quantum efficiency of luminescent ceramics during an annealing process for solid state lighting", Ceramics in Solid state study at Gorden Research Conference, South Hadley, MA, USA, July 31 – August 5, 2016.

J. Ha, E. Novitskaya, G. A. Hirata, O. A. Graeve, J. McKittrick, "A method to improve quantum efficiency of nanosized phosphors for near UV-LEDs", International Materials Research Congress, Cancun, Mexico, August 18, 2016.

J. Ha, Z. Wang, E. Novitskaya, G. A. Hirata, O. A. Graeve, S. P. Ong, J. McKittrick, "Discovery of near-UV excited phosphors: a combined experimental and computational study", International Materials Research Congress, Cancun, Mexico, August 17, 2016.

J. Ha, "Synthesis and luminescent properties of phosphors for near UV-emitting applications" Center for Nanoscience and Nanotechnology, Ensenada, Mexico, August 9 2017, **invited talk*

J. Ha, E. Novitskaya, G. A. Hirata, O. A. Graeve, J. McKittrick, "A method to improve quantum efficiency of nano-sized phosphors for near UV-LEDs", 6th UCSD-Korea University Joint Materials Science and Engineering Workshop, La Jolla, CA, August 11 2017

ABSTRACT OF DISSERTATION

Design and synthesis of phosphors to improve efficiency for solid state lighting application

by

Jungmin Ha

Doctor of Philosophy in Materials Science and Engineering

University of California San Diego, 2019

Professor Joanna McKittrick, Chair

White-emitting light sources based on light-emitting diodes (white-emitting LEDs) are considered to be the next generation in lighting. A common approach to create a white-emitting LED is to combine a blue-emitting InGaN LED with a yellow-emitting phosphor, but it has a low color rendering index (CRI) value due to the rack of red emission. An alternative approach is to combine a near UV-LED (nUV-LED) with blue-, green-, and red-emitting phosphors. However, the development of phosphors for the white-emitting LEDs is still challenging due to the numerous

factors that influence on the luminescent properties. In this research, five approaches have been investigated to design and synthesize phosphors for solid state lighting:

First, the Debye temperature (Θ) was used as a descriptor for phosphors with high quantum efficiency (Φ) (> 80%). Compositions with Θ > 500K were considered. $CaMgSi_2O_6:Eu^{2+}$ and $Ca_7Mg(SiO_4)_4:Eu^{2+}$ were synthesized through a co-precipitation and a sol-gel reactions, respectively, due to the high Θ. However, a correlation between high Θ and high Φ was not found.

Second, a flux (NH_4F, NH_4Cl, or H_3BO_3) was introduced during co-precipitation synthesis of $CaMgSi_2O_6:Eu^{2+}$ to increase the Φ. The flux affected both the crystallite size and the Φ of the submicron sized phosphors. It was found that the Φ increased 3X compared to no flux.

Third, newly identified phosphors, green-emitting $Sr_2LiAlO_4:Eu^{2+}$ and blue-emitting $Sr_2LiAlO_4:Ce^{3+}$ were discovered by data mining unexplored chemistries for potentially high Φ. The new, $Sr_2LiAlO_4:Eu^{2+}$ and $Sr_2LiAlO_4:Ce^{3+}$ were successfully predicted and synthesized.

Fourth, color tunable single phase phosphors were developed using the Eu^{2+} and Ce^{3+} co-activated Sr_2LiAlO_4 for improvement of Φ. The Φ increased by 40% with Eu^{2+} and Ce^{3+} co-activation compared to the singly activated phosphors.

Fifth, the synthesis of Na_2SiF_6 was demonstrated through a green synthetic method without toxic HF that is typically used for fluorides synthesis. The red-emitting phosphor, $Na_2SiF_6:Mn^{4+}$ was prepared in a low concentration HF solution using the synthesized Na_2SiF_6 as a host.

This study provides strategies to design and synthesize phosphors with improved quantum efficiency and thermal stability for white-emitting near-UV LEDs for potential applications in solid state lighting.

CHAPTER 1: INTRODUCTION AND BACKGROUND

1.1 Introduction

There is a national need to develop more efficient light sources to replace those currently used in everyday life. Twenty-two percent of the total US electrical energy is used for lighting, and $50 billion per year spent on lighting with 130 million tons of carbon emitted into the atmosphere from fossil fuel plant [1-3]. Therefore, there is an urgent need for new research on how to improve the efficiency of lighting sources from the point of view of energy consumption and the environmental issues.

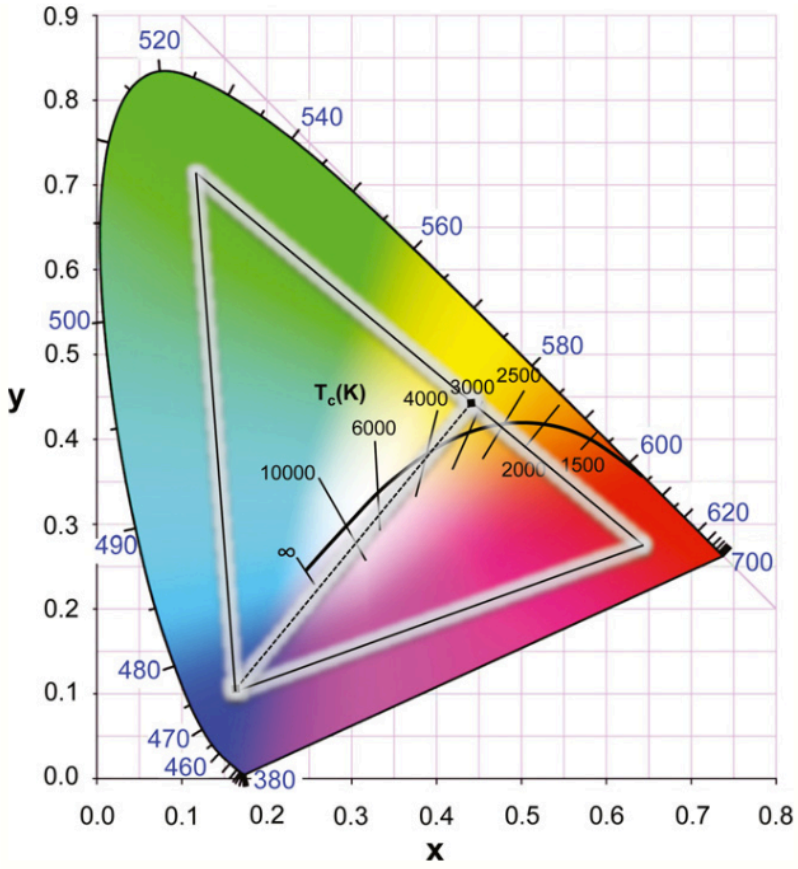

Figure 1.1 Commission Internationale de I'Eclairage (CIE) chromaticity diagram, where all colors the eye can distinguish are presented. Each color has specific x, y coordinates [4].

White lighting is crucial for general luminescent applications, is achieved by mixing blue and yellow emissions or red-, green, and blue emissions, shown in the Commission Internationale de I'Eclairage (CIE) chromaticity diagram (Figure 1.1) [5], where all colors the eye can distinguish are presented in x, y coordinates. The dashed straight line in the CIE chromaticity diagram provides white emission by mixing yellow and blue emissions. Another approach to produce a white light is mixing of red, green, and blue emissions, presented in the triangle in the CIE diagram. All colors inside the triangle can be achieved depending on the quantity of each color.

White light has a correlated color temperature (CCT) that refers to the color characteristics based on a reference (black body). A lamp with a CCT value < 3200 K is considered as warm white and that with a CCT value > 3200 K is considered as cool white.

Table 1.1 Luminous efficacy, correlated color temperature (CCT), color rendering index (CRI), lifetime, and cost for various light sources [6].

	Incandescent	Compact fluorescent	Linear fluorescent	Commercial white-emitting LEDs
Luminous efficacy (lm/W)	15	60	110	70-170
Correlated color temperature (CCT) (K)	2760	2700	4100	2600-8300
Color rendering index (CRI)	100	82	85	70-92
Life time (khr)	1	12	25	25-75
Cost ($/klm)	0.6	2	4	30

Traditional lighting sources are the incandescent and the fluorescent and incandescent lighting is installed for 85 % of residential and 32 % of commercial lighting, and fluorescent lighting is served in balance [7]. Table 1.1 compares the luminous efficacy, correlated color

temperature (CCT), color rendering index (CRI), lifetime, and cost for various light sources. The luminous efficacy is the ratio of the total luminous flux radiated by any source to the total radiant flux from that souce, commonly expressed in lumens per watt, where luminous flux is energy per unit time. The CRI is the measurement of the ability to reproduce the colors of various objects in comparison to sunlight. The sun is defined as having a CRI of 100. The incandescent lamp has an excellent CCT, a high CRI value and low cost, but lowest luminous efficacy and short life time. The fluorescent lamp shows much higher luminous efficacy, longer life time, and a reasonable CRI. However, it requires mercury (3 – 5 mg), causing a disposal problem. The most recent lighting development is white-emitting light sources based on light-emitting diodes (white-emitting LEDs) that conbine a LED in the blue (450 nm) or ultraviolet (380 – 400 nm) with luminescent materials known as phosphors. White-emitting LEDs have superior luminous efficacy, and CRI values can be adjusted by phosphors blending. The life time of LEDs is also much longer than other lighting sources. Therefore, white-emitting LEDs are desired to achieve high efficacy, good CRI and CCT, and long life time for the next generation lighting. Figure 1.2 shows the spectral energy distribution for the sun, a fluorescent lamp, an incandescent lamp, and white emitting LED to comare with noon sunlight [8]. When only considering the wavelength range of 400 nm to 700 nm in the visible light (the two gray dashed lines), the spectral energy distribution of the incandescent is most silimar to that of noon sunlight, causing that the CRI value of the incandescent bulb is 100. The spectral energies of the compact fluorescence and the white-emitting LED are distributed from 400 nm to 700 nm, but have the lower intensities than that of incandescent. Thus, the CRI values of the compact fluorescence and the white-emitting LED are lower than that of the incandescent, but are reasonable due to the widespread emission from 400 – 700 nm.

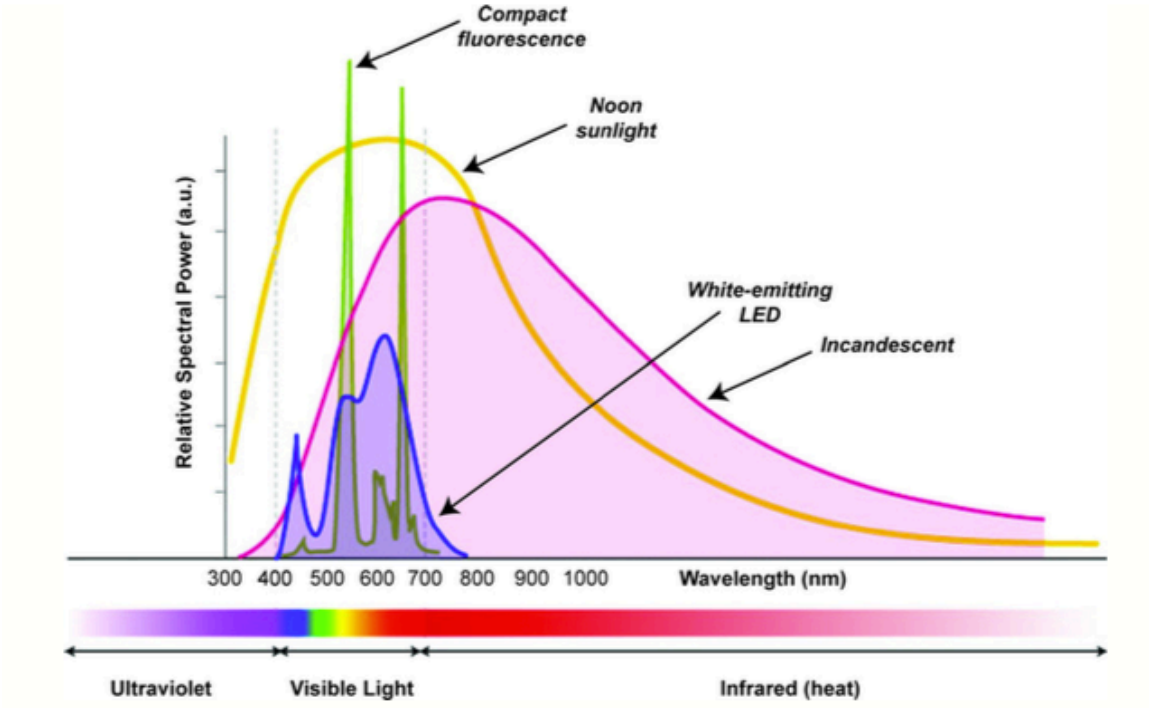

Figure 1.2 Spectral energy distribution for different light-emitting sources [8].

Figure 1.3 shows the two approaches to create white-emitting LEDs. The most common approach is to combine a blue-emitting (450 nm) InGaN LED with a broad-band yellow-emitting phosphor (Figure 1.3a), where a phosphor is defined as a substance that emits radiation under an external energy source. However, this approach has several drawbacks: Low CRI value due to the lack of red emission (Figure 1.3b); color variation with input power due to current drop problem at the driving current density (20 A/cm^2), as shown in Figure 1.4, where the external quantum efficiency is defined as the ratio of the emitted light by the phosphor to the emitted light by the excitation light source [9-11].

An alternative method to produce white light is mixing of red-, green-, and blue-emitting phosphors on a UV LED chip shown in Figure 1.3c [12-14]. This approach can achieve a high CRI

value by optimization of phosphor blending (Figure 1.3d) and having a higher extraction efficiency due to a smaller current drop at driving currents (Figure 1.4) [11].

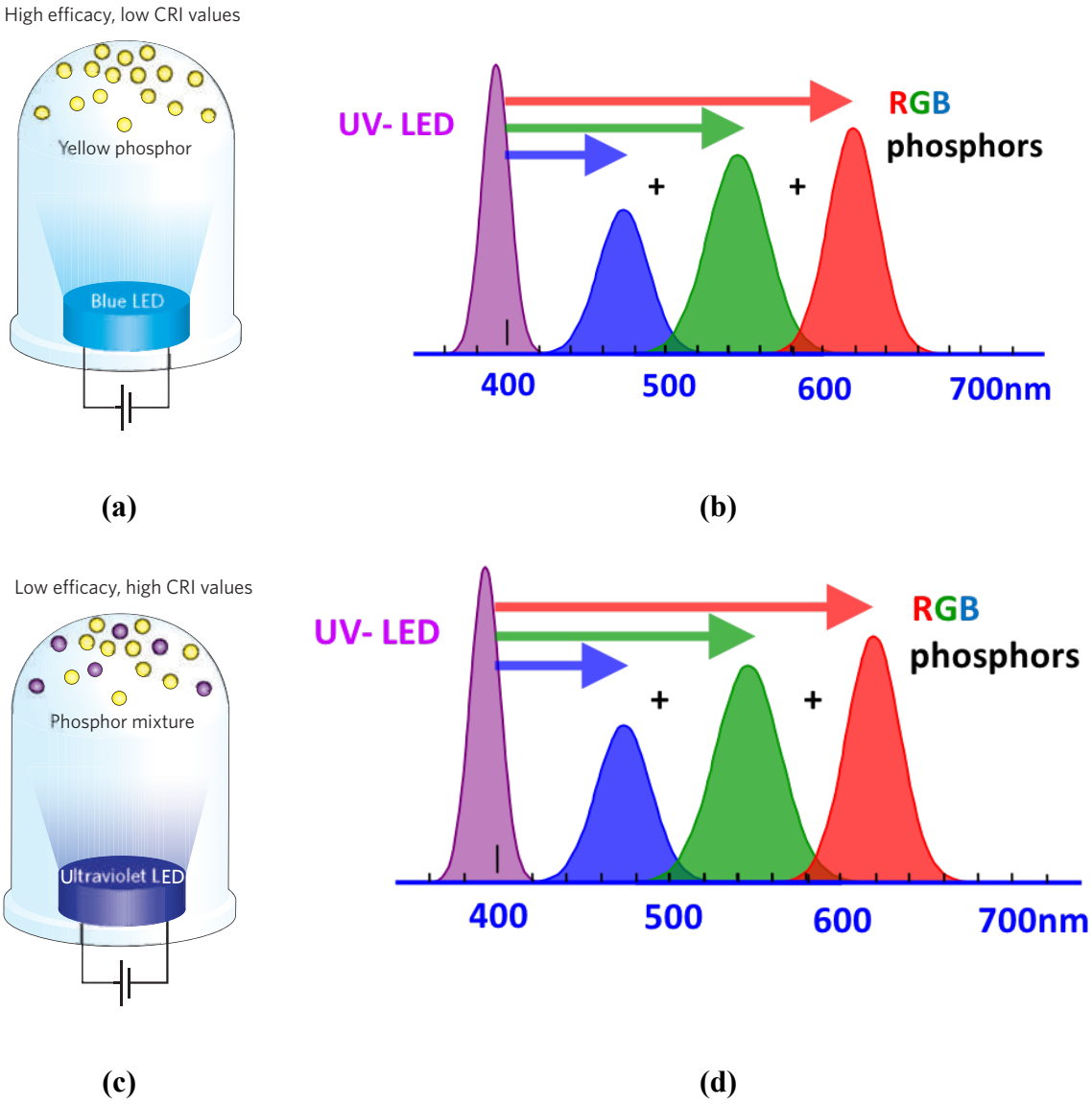

Figure 1.3 Fabrication white-emitting LEDs by mixing (a) blue LED chip and yellow phosphors, $Y_3Al_5O_{12}:Ce^{3+}$ with (b) spectra and (c) red-, green-, blue-emitting phosphors on the UV-LED chip with (d) spectra [15].

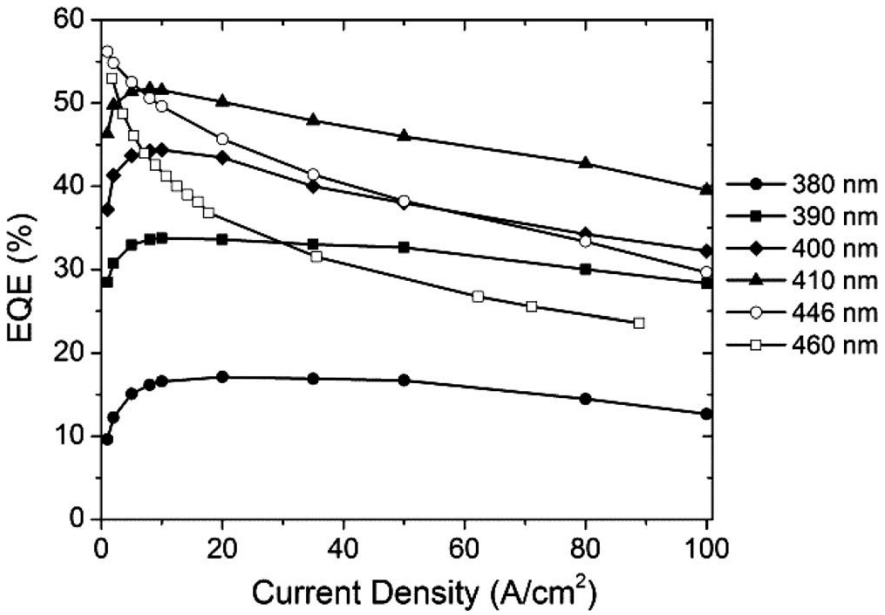

Figure 1.4 The external quantum efficiency plot as a function of current density plot for four different nUV LED chips (solid symbol) and twoof blue LED chip (void symbol)[11].

The white-emitting LEDs using red, green, blue phosphors are also called as the phosphor converted LEDs (pc-LEDs). To improve the efficiency of pc-LEDs, the factors that are related to efficiency, should be considered. The efficiency of pc-LEDs is expressed by:

$$\eta_{\text{pc-LEDs}} = \eta_{\text{LED}} \times \eta_{\text{phosphor}} \times \eta_{\text{package}} \times \eta_{\text{s}} \quad (1)$$

where $\eta_{\text{pc-LEDs}}$ is the final phosphor converted LED efficiency, η_{LED} is LED efficiency, η_{phosphor} is phosphor quantum efficiency (Φ), η_{package} is the package efficiency (extraction efficiency), and η_{s} is Stokes conversion efficiency. All of these should be maximized to create high efficiency pc-LEDs. However, the development of high efficient phosphors is challenging due to the multiple factors including the synthetic processes and post-annealing treatment that influence the luminescent properties.

The goal of this study is to develop thermally stable, high Φ phosphors that can be excited by near-UV (380 – 410 nm) in order to obtain efficient solid state lighting. The dissertation is organized as follows: Chapter 2 explores a descriptor to predict Φ of phosphors and investigated

blue-emitting $CaMgSi_2O_6:Eu^{2+}$ and green-emitting $Ca_7Mg(SiO_4)_4:Eu^{2+}$ to validate the descriptor. Chapter 3 provides a method to improve Φ during the synthesis processes using a flux with $CaMgSi_2O_6:Eu^{2+}$. The discovery of the novel potential high Φ phosphors is introduced in Chapter 4. Chapter 5 shows a design of a co-activated color tunable single-phase phosphor to improve Φ of phosphor; Eu^{2+} and Ce^{3+} co-activated Sr_2LiAlO_4 was examined. Development of a synthetic method for a red-emitting phosphor is discussed in Chapter 6. Chapters 2-6 are manuscripts that have been published, in press or submitted. Conclusions and suggestions for future work are provided in Chapter 7.

1.2 Background

1.2.1 Solid-state lighting

The white-emitting LEDs are typically encased in an epoxy resin and consist of the LED chip, phosphors, and the reflector cup. Figure 1.5 illustrates the placement and arrangement of phosphors in the reflector cup [16]. A uniform phosphor distribution is shown in Figure 1.5a, which represents the current commercial design. This distribution method limits $\eta_{package}$ because of the close proximity of the phosphors to the LED. The phosphor emission redirects a significant amount of light back towards the low reflectivity LED, where the light is reabsorbed. This issue can be resolved by using the remote phosphors distribution, where the phosphors are arranged in a layer on a transparent substrate and placed above the LED chip (Figure 1.5b). The remote phosphors distribution reduces the reabsorption of back-scattered visible radiation from the LED.

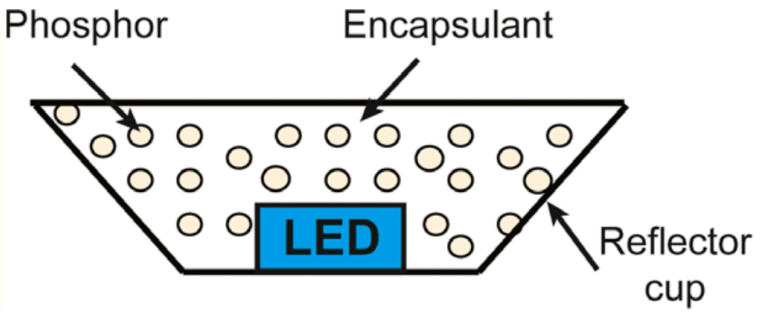

(a)

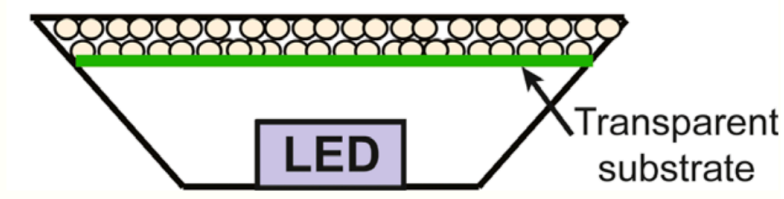

(b)

Figure 1.5 (a) Uniform phosphors distribution, (b) remote phosphor distribution where the phosphor particles are arranged as a layer on a transparent substrate located above the LED [16].

1.2.2 Correlated color temperature and color rendering index

There are two terms to describe color quality of white light: The correlated color temperature (CCT) and the color rendering index (CRI). Figure 1.6a shows that the CCT values of warm (< 3200 K)and cool white (> 4000 K)) and the CCT value of daylight [17] in the CIE diagram. Figure 1.6b and 1.6c are examples of the lamps with cool and warm white, respectively. Figure 1.7 shows the difference of the color qualities between objects under the light with a low CRI and a high CRI [18]. The color of an object under the light with a high CRI value looks similar to the real object.

(a) **(b)** **(c)**

Figure 1.6 (a) The CCT value of warm and cool white (from 2500 to 1000 K) and the CCT value of daylight (pointed) in the CIE diagram [17]. Photographs of (b) cool white LED and (c) warm white LED [19].

Figure 1.7 Objects under the light with low CRI and high CRI values [19].

1.2.3 Light emission from phosphors

There are different types of luminescence that depends on the excitation source [20]: Photoluminescence (PL), cathodoluminescence, electroluminescence, bioluminescence, chemiluminescence. Photoluminescence (PL) is the light emission when excited by photons. Cathodoluminescence is the light emission resulting from electron bombardment. Electroluminescence is the light emission produced by an electric field (~10^6 V/cm), e.g. LEDs. Bioluminescence is the light emission resulting from the biochemical reaction in the living organism. Chemiluminescence is the light emission from an exothermic chemical reaction. Photoluminescence (PL) is only presented in this dissertation.

A phosphor is a substance which emits electromagnetic radiation under an external energy source. It typically consists of an inert host lattice, usually wide band gap materials (e.g. oxides, nitrides, and sulfides) and a small amount of dopant ion (an activator), or a functional group as the luminescent center. The notation is given as host:activator. The process of light emission is shown in Figure 1.8. When the phosphor absorbs external energy, electrons are excited from the ground state to the excited state. The excited electrons move to the relaxed state by releasing the nonradiative radiation and then release to the ground state by emitting photons.

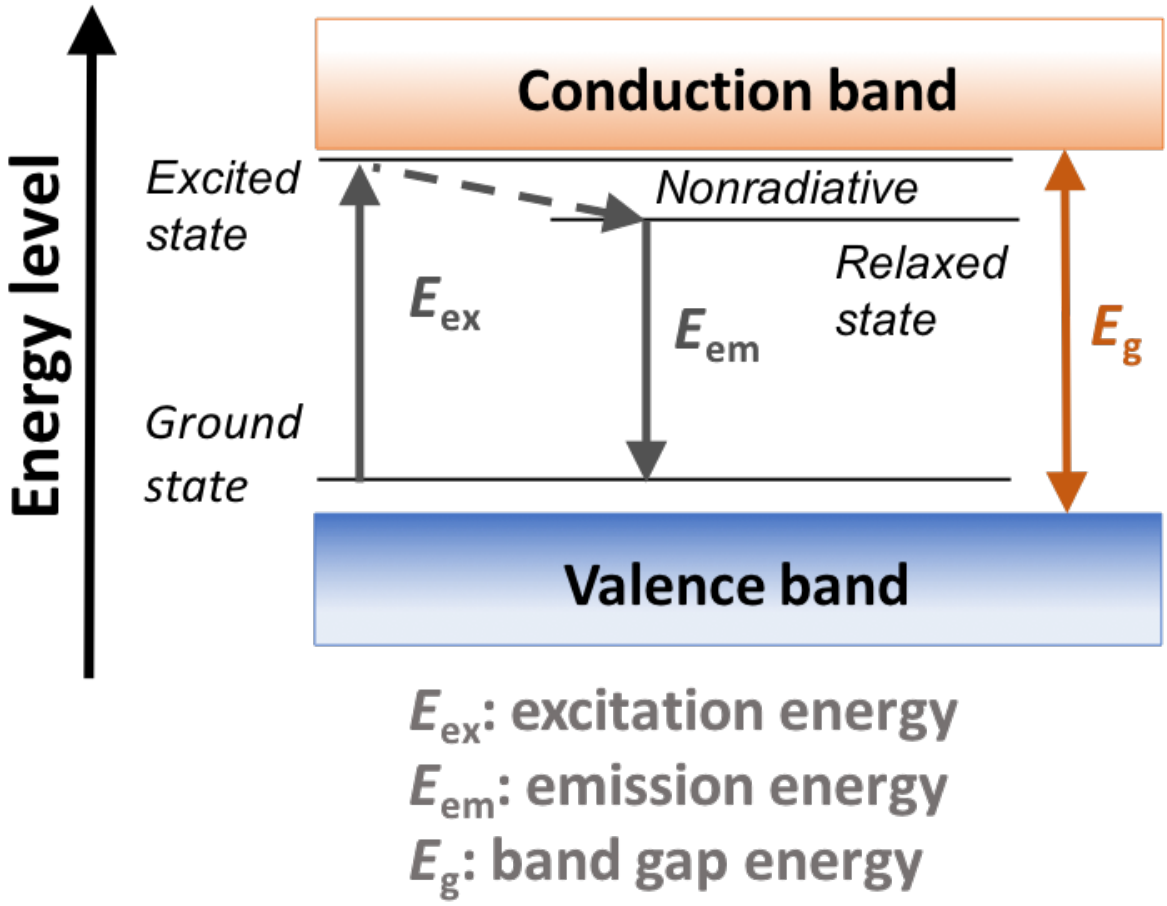

Figure 1.8 The process to emit light of phosphors when applied to the external energy, UV light.

The optical transition in a localized luminescent center can be explained by the configuration coordinate model (Figure 1.9) [21]. The curves illustrate the energy of ground and excited state of luminescent center as a function of the interatomic distance between the activator and surrounding ions. The total energy is the sum of the electron energy and ion energy. The luminescent ion and its nearest neighbor ion are only considered for the configuration coordinate diagram. The luminescent center is excited through the energy absorption from A→B. Nonradiative reaction occurs from B→C and the emission releases from C→D with the nonradiation relaxation from D→0. Thermal activation can occur from C→E with the nonradiative relaxation from E→0, which explains the thermal quenching that refers to a decrease in emission intensity when temperature increases.

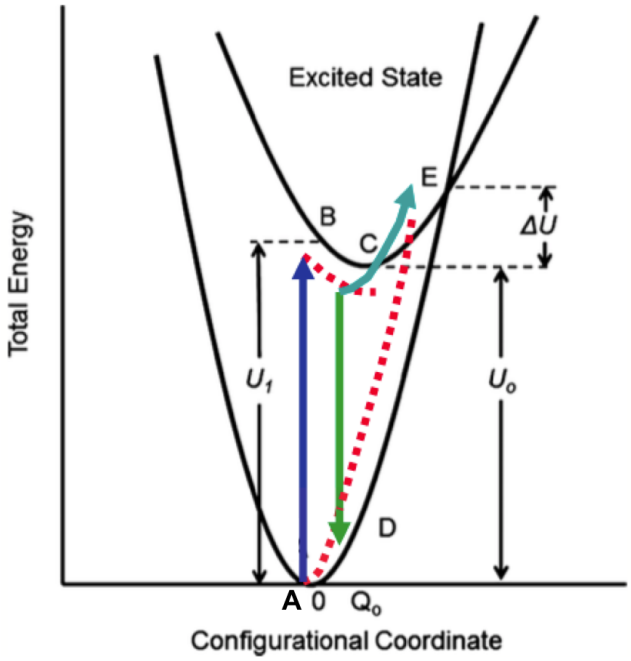

Figure 1.9 The configuration coordinate diagram. The curves illustrate the energy of ground and excited state of luminescent center. The *x* axis is the interatomic distance between the activator and surrounding anions [21]. U_1 is the absorption energy. U_0 is the energy of the zero phonon line. ΔU is the energy barrier of thermal quenching.

Phosphors can be identified by activators and activators can be classified according to the optical absorption electronic transition [21]:

1. $4f^n \rightarrow 4f^n$, $5f^n \rightarrow 5f^n$ (rare-earth and actinide ions)

2. $4f^n \rightarrow 4f^{n-1}5d$ (most rare-earth ions)

3. $3d^n \rightarrow 3d^n$, $4d^n \rightarrow 4d^n$ (transition metal ions)

4. Charge transfer between an anion p-electon and an empty cation orbital (e.g., VO_4^{3-}, WO_4^{2-}, and MoO_4^{2-}).

The rare-earth ions are characterized by a partially filled 4*f* shell. In the case of 4*f*-4*f* transition, electrons transfer between different energy levels of the 4*d* orbital in lanthanide ions in the 3+ state (Ln^{3+}), which is forbidden by the parity selection rule that states the electronic transitions between energy levels with same parity cannot occur [22], where parity relates to the symmetry of electron wave function. However, in reality, the 4*f*-4*f* transition occurs because the parity rule is relaxed due to the electron vibration coupling [23]. The optical transitions are not strongly affected by the host lattice because the electrons of $5s^2$ and $5p^6$ shield the electrons in the *4f* shell of Ln^{3+}. Therefore, each Ln^{3+} has a unique set of energy levels (Figure 1.10), that is not related to the host lattice, and has narrow *f-f* absorption/emission spectra. The identification of Ln^{3+} transitions was reported by Dieke in 1960s [24]. The transitions are identified based on the energy levels of Ln^{3+} in the Figure 1.11.

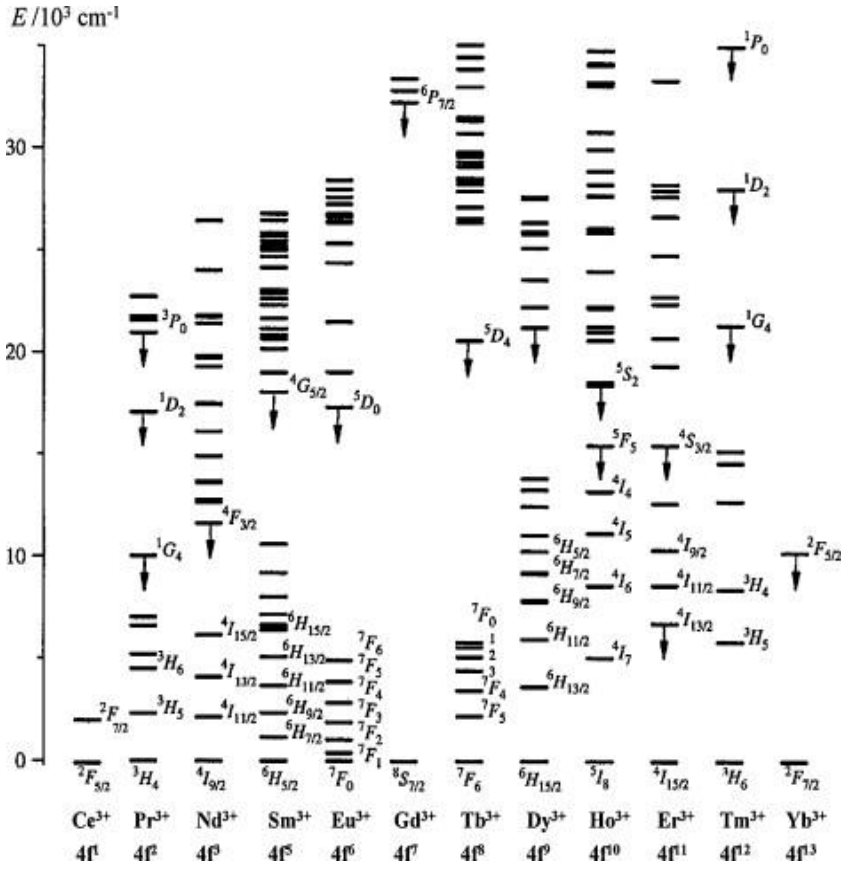

Figure 1.10 Energy levels of free trivalent lanthanid ions [24].

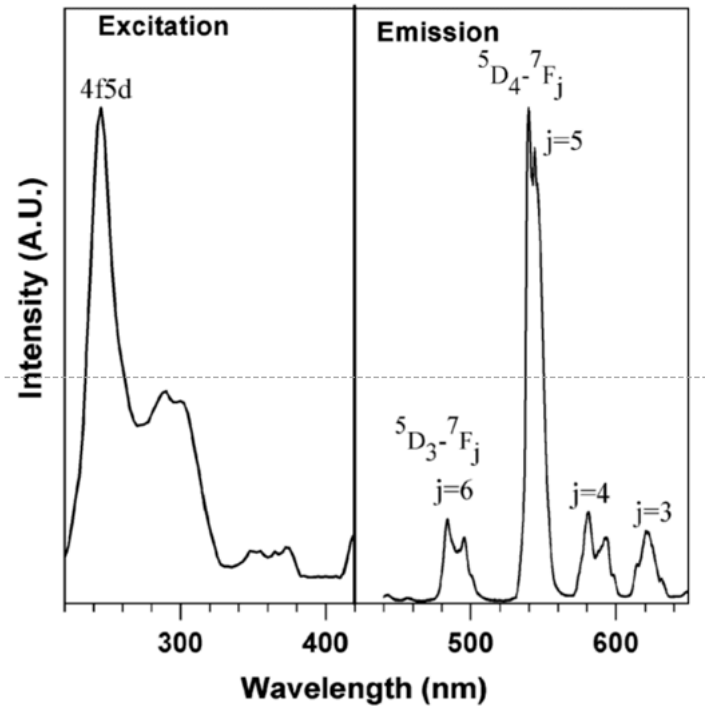

Figure 1.11 Excitation (measured at 545 nm) and emission (at 254 nm excitation) spectra of Y_2SiO_5:Tb^{3+} [25].

Figure 1.11 shows an example of Ln^{3+} activated phosphor, Y_2SiO_5:Tb^{3+} [25]. The absorption arises from from $^7F_6 \rightarrow 4f^7 5d$ transition, showing the absorption peak centered at 254 nm. Small absorption also occurs between 280 nm and 400 nm from the $4f_8$-$4f_8$ transition [26]. The primary emission is from $^5D_4$-^7F_j, showing a narrow emission peak centered at 545 nm. The small peaks from $^5D_3$-^7F_j (j = 3, 4, 6) are also observed. This illustrates the narrow band absorption and emission peaks that are characteristics of Ln^{3+} ions.

Most rare-earth ions are excited from a state in the $4f^n$ configuration to an excited state in the $4f^{n-1}5d$ configuration. Unlike the $4f^n$ transitions that are strictly forbidden, the 4*f*-to-5*d* transitions are dipole allowed. Since the 5*d* states are overlapped with the orbitals of the host material, the 4*f*-to-5*d* transitions are stongly dependent on the host. Therefore, the the spectral ranges of $4f^n \rightarrow 4f^{n-1}5d$ transitions are varied from the deep UV to far-infrared region with broad

excitation and emission bands, depending on the host. Due to the capability to emit all colors, these activators are widely used in phosphors.

The crystal field is defined as the electron field at the site of an ion influenced by the surrounding ions [27]. The crystal field affects the 5*d* state of activators, causing the color adjustability of phosphors. The schematics of an effect of the crystal field on the 5*d* energy level of Ce^{3+} and the *4f-5d* energy level of Eu^{2+} are shown in Figure 1.12 [20, 28], where the emission color is varied from blue, green, to red, due to the crystal field effect from the host lattice. One electron in 4*f*-shell is in the electronic configuration of Ce^{3+}, which absorbs and emits through 4*f*-to-5*d* transition. For Eu^{2+}, the excited state level of $4f^7$ configuration is higher than that from the $4f^6 5d^1$ configurion in energy. Thus, Eu^{2+} absorbs and emits in the similar manner with Ce^{3+}. However, for other ions of the $4f^n \rightarrow 4f^{n-1}5d$ transition, the energy levels of the excited states, arising from $4f^n$ configuration, are located in the energy gap between the ground state of $4f^n$ configuration and the lowest energy level of $4f^{n-1}5d^1$ configuration, which causes that the electrons are not normally relaxed to the ground state through 5*d*-to-4*f* transition, but through the energy levels related to the multiplet states of $4f^n$ configuration. These electrons will exhibit either the line peaks related to the transition of $4f^n$ states or a mixture of transitions associated with the $4f^{n-1}5d^1$ and $4f^n$ configurations. Therefore, only Ce^{3+} and Eu^{2+} have transitions at visible wavelength when absorbing near-UV for the use in phophors for solid state lighting.

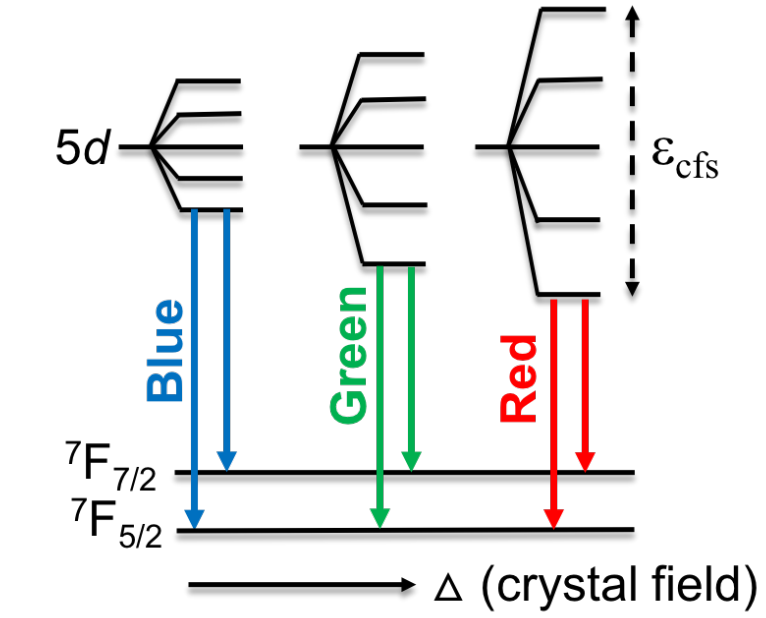

(a)

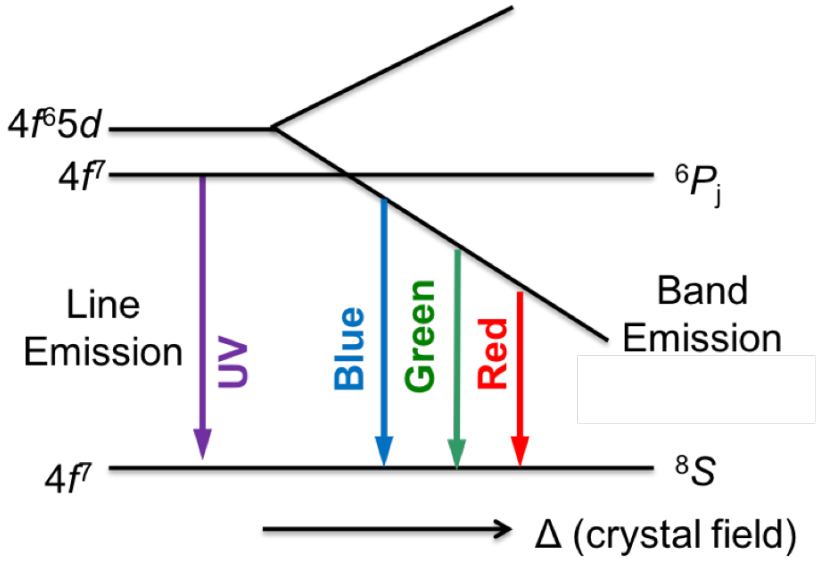

(b)

Figure 1.12 The schematics of effect of crystal field on (a) the 5*d* energy level of Ce^{3+} and (b)4*f*-5*d* energy level in Eu^{2+}. ε_{cfs} is the crystal field splitting.

Table 1.2 summarizes the luminescence properties of Eu^{2+} or Ce^{3+} activated phosphors for near-UV LEDs. The phosphate, halo-phosphate, halo-silicate, silicate, and nitride are available for blue (emission wavelength, λ_{em} ~ 400 to 490 nm) and green-yellow (λ_{em} ~ 490 to 580 nm), for Eu^{2+} or Ce^{3+} activated phosphors. There are a relatively few orange-red emitting phosphors (λ_{em} ~ 580 to 650 nm) reported based on Eu^{2+} or Ce^{3+} activators. The most pomissing host material for the red-emitting phosphors is a nitride. Energy transfer from Eu^{2+} to Mn^{2+} is another approach for red-emitting phosphors. The absorption of Mn^{2+} is weak due to the forbidden *d-d* transition, but can be increased with an addition of Eu^{2+} due to the enrgy transfer from Eu^{2+} to Mn^{2+}. The spectral overlap between the emission band of Eu^{2+} and the excitation band of Mn^{2+} should be significant for efficient transfer between Eu^{2+} to Mn^{2+}. The Φ of phosphors are varied depending on host materials

Table 1.2 Luminescent properties of phosphors for near UV-LEDs application. λ_{ex} and λ_{em} are the excitation and emission wavelength. Φ is the quantum efficiency.

Group	Activator	Composition	λ_{ex} (nm)	λ_{em} (nm)	Φ at 400 nm	Ref.
Phosphate	Eu^{2+}	$LiCaPO_4$	400	475	88	[29]
	Eu^{2+}	$LiSrPO_4$	350	450	35	[30]
	Eu^{2+}	$SrMg_2(PO_4)_4$	375	420	-	[31]
	Eu^{2+}-Mn^{2+}	$Ca_3Mg_3(PO_4)_4$	300	625	-	[32]
Halo-phosphate and silicate	Ce^{3+}	$(Sr,Ba)_3AlO_4F$	400	502	61	[33]
	Eu^{2+}	$Ca_8Mg(SiO_4)_4Cl_2$	365	510	90	[34]
	Eu^{2+}	$Ca_5(SiO_4)_2Cl_2$	375	585	60	[35]
Silicate	Eu^{2+}	Ba_2SiO_4	360	510	94	[36]
	Eu^{2+}	$Ba_2MgSi_2O_7$	380	505	92	[37]
	Eu^{2+}	$Ca_2MgSi_2O_7$	395	541	15	[38]
	Eu^{2+}	$Ca_3MgSi_2O_8$	375	475	42	[39]
	Eu^{2+}	Sr_3SiO_5	400	580	96	[40]
Nitride	Eu^{2+}	$BaSi_3Al_3O_4N_5$	300	470	56	[41]
	Ce^{3+}	$LaSi_3N_5$	355	465	34	[42]
	Ce^{3+}	$LaAl(Si_5Al)(N_9O)$	350	470	35	[43]
	Eu^{2+}	$SrLiAl_3N_4$:Eu^{2+}	440	654	76	[44]

For transition metal ions, the *d* orbitals of transition metal ions are unfilled and the electron configuration is $3d^n$ ($1 < n < 10$). The 3*d* electron is in the outer shell, which is sensitive to the crystal environment. The transition metals, Cr^{3+} and Mn^{4+} prefer an octahedral coordination [45, 46] and Mn^{2+} prefers both the tetrahedral and octahedral coordinations [47]. The crystal field causes the five degenerated *d* orbitals ($d_{x^2-y^2}, d_{xy}, d_{z^2}, d_{xz}$ *and* d_{yz}), illustrated in Figure 1.13, to split into the doubly degenerate e_g and triple degenerate t_{2g} (Figure 1.14). The distance between e_g and t_{2g} is denoted as 10Dq that is a parameter to characterize the field strength. The Tanabe – Sugano (T-S) digram (Figure 1.15) shows the relationship between the energy levels of metal ions (E/B), and crystal field strength (Dq/B) of the d^2 – d^8 congifuations in the crystal, where B is the Racah parameter to describe the effects of electron-electron repulsion within the metal complex. T-S diagram provides the identification of each emission peak to energy levels of transition metal ions.

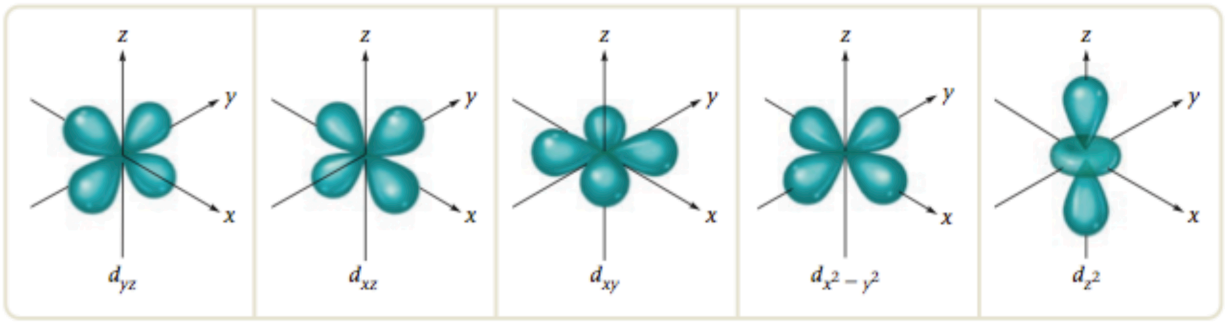

Figure 1.13 Schematic representation of the five 3*d* orbitals [48].

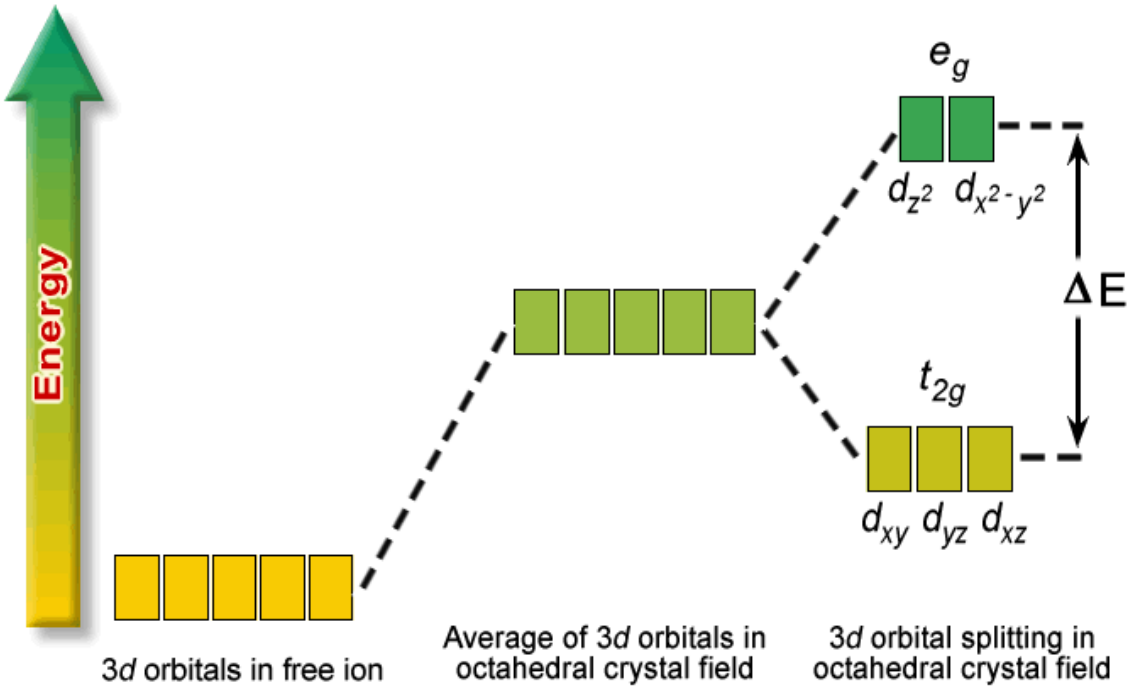

Figure 1.14 Energy splitting of the five d orbitals for octahedral crystal field and the orbits of the free ion [49].

.

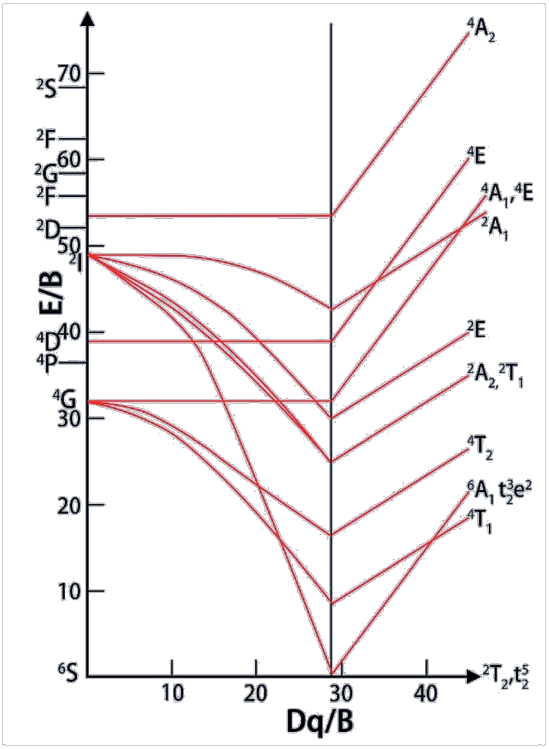

Figure 1.15 Tanabe – Sugano diagram for the d^5 electron configuration [50].

Mn^{2+} prefers both tetrahedral and octahedral coordinations, where the spin forbidden *d-d* transition ($^4T_1 \rightarrow {}^6A_1$) occurs. The octahedrally coordinated Mn^{2+} usually exhibits an orange to red emission, whereas Mn^{2+} in the tetrahedral coordination shows a green emission. The emissions from both octahedral and tetrahedral coordinations are attributed to the $^4T_1 \rightarrow {}^6A_1$ transition of the Mn^{2+}, meaning that the spin forbidden *d-d* transition ($^4T_1 \rightarrow {}^6A_1$) of Mn^{2+} emits from green to red emission depending on the coordination [47].

Mn^{4+} activated phosphors are promissing red-emitting phosphors. They have a strong crystal field and emission spectra that arise from the $^2E_g \rightarrow {}^4A_{2g}$ transition (sharp peaks) [51]. The measured two broad bands as excitation are from the $^4A_{2g} \rightarrow {}^4T_{1g}$ and $^4A_{2g} \rightarrow {}^4T_{2g}$ spin-allowed transitions [52]. The $^2E_g \rightarrow {}^4A_{2g}$ transition has a variation of energy levels because the energy of the ^2E_g state in the d^3 electronic configuration does not depend on the crystal field (Figure 1.16). Table 1.3 provides the composition of Mn^{4+} activated phosphors with the excitation (λ_{ex}) and emission (λ_{em}) wavelength.

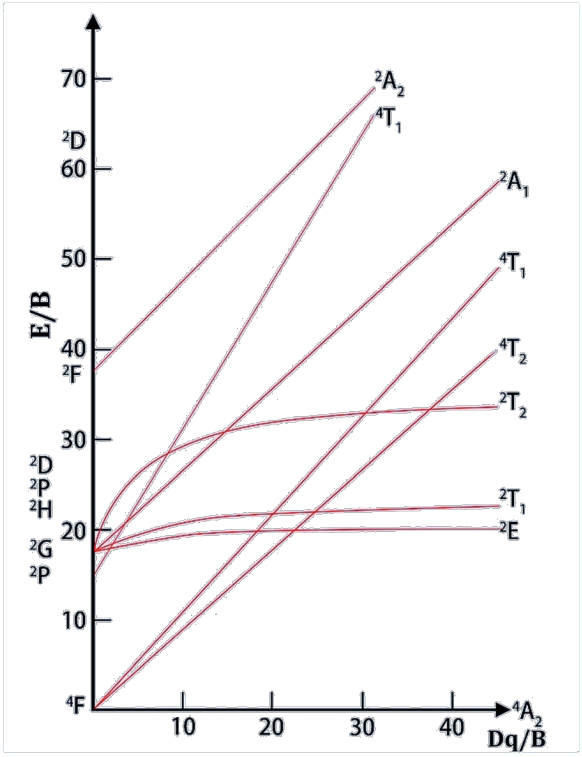

Figure 1.16 Tanabe – Sugano diagram for the d^3 electron configuration in an octahedral crystal field.

Table 1.3 Mn^{4+} activated red-emitting phosphors. λ_{ex} and λ_{em} are the excitation and emission wavelength.

Chemical composition	λ_{ex} (nm)	λ_{em} (nm)	Ref.
$BaTiF_6:Mn^{4+}$	365, 468	634	[53]
$Na_2SiF_6:Mn^{4+}$	360, 460	600 – 650	[54]
$Na_3GaF_6:Mn^{4+}$	460	630	[55]
$Sr_2MgAl_{22}O_{36}:Mn^{4+}$	312	658	[56]
$CaAl_{12}O_{19}:Mn^{4+}$	325, 457	600 – 700	[57]
$Li_2MgGeO_4:Mn^{4+}$	323	671	[58]

For the complex functional groups (e.g. WO_4^{2-}, Mo_4^{2-}), AMO_4 (A = alkaline earth, M = Mo, W) are self activated due to the presence of MO_4 groups; they absorb energy in the far UV

from the charge transfer band, corresponding to electrons excited from oxygen 2*p* states to tungsten 5*d* states within the MO_4 group. However, the excitation wavelength is too low (~ 300 nm) that is not ideal for use in near-UV LEDs [59].

1.2.4 Requirements for ideal phosphors in solid-state lighting

There are severe requirements for phosphors in solid state lighting as listed below [4]:

1. High photoluminescent (PL) quantum efficiency (Φ)
2. Low thermal quenching
3. Low reflectance at the excitation wavelength
4. Excellent chemical and thermal stability
5. Low light scattering

Quantum efficiency (Φ) is the ratio of the emitted light to the absorbed light. The ideal Φ is for solid state lighting is 90 – 95%. Thermal quenching should be low (< 10% Φ loss at 150°C) when considering device operating condition and good color control over a range of operating power. Low reflectance at the excitation wavelength is important for phosphors to strogly absorb the LED light. Excellent chemical and thermal stability is needed that phosphors do not react with moisture or degrade with temperature up to 150°C that arises from the heat generation during LED operation. The light scatterring from the particles causes emission loss. Micron-sized particles produce light scatterring, reducing the efficienty of the near-UV LED package.

1.2.5 Empirical studies.

The main issue for phosphors is to identify the activators and host that can be used for near-UV LED. An empirical relationship between the excitation energy and emission energy was proposed by Dorenbos [60, 61]. The excitation energy, E_a(Re,A) required to excite a *4f* electron to the lowest *5d* level split by a crystal field, depends on the free ion energy, E_F(Re), and crystal field

depression in host A that is the redshift due to the interaction between the crystal field and activator, *D(A)*:

$$E_a(\text{Re, A}) = E_F(\text{Re}) - D(\text{A}) \quad (2)$$

This equation shows that the excitation energy depends on both the rare-earth ion and the host lattice A. The emission energy, E_e(Re, A), also shows a similar relationship:

$$E_e(\text{Re, A}) = E_F(\text{Re}) - D(\text{A}) - S(\text{A}) \quad (3)$$

where S(A) is the Stokes shift in host A and is independent of the rare-earth ions. These equations have been validated both empirically and by calculations for rare-earth ions in solids within ±500 cm^{-1} as an error [62, 63]. The values of E_F(Re) are available for most rare-earth ions [64]; a list of D(A) is provided by Dorenbos for rare-earth ions. Since the $E_F(Ce^{3+})$ is 49340 cm^{-1}, E_a(Re, A) can be expressed by:

$$E_a(Ce^{3+}, \text{A}) = 49340\ cm^{-1} - D(\text{A}) \quad (4)$$

The range of excitation wavelength for near-UV is 380-400 nm, so that hosts with the range of D(A) from 23025 to 24340 cm^{-1} are necessary for near-UV LEDs. The D(A) values can be obtained in iodies, oxides, oxy-halides, sulfides and oxy-nitrides; examples are shown in Table 1.4 [65, 66].

Table 1.4 A list of D(A) values of hosts for Ce^{3+}. *D(A)* that is the crystal field depression in host.

Host	D(A) (cm^{-1})	Host	D(A) (cm^{-1})	Host	D(A) (cm^{-1})	Host	D(A) (cm^{-1})
$Cs_3Gd_2O_9$	23830	$Mg_3F_3BO_3$	24716	LuOCl	24716	LaOI	23748
$NaYGeO_4$	23284	LiYGeO4	24477	Gd_2SiO_5	23298	Y_2SiO_5	23093
$SrLaAlO_4$	24332	$Y_4Al_2O_9$	22974	$Y_3AlGa_4O_{12}$	24480	$GdTaO_4$	24038
SrY_2O_4	24529	$Ce_3(SiS_4)_2Cl$	23567	$Ce_3(SiS_4)_2F$	23366	$BaSi_2S_5$	24462
$BaAl_2S_4$	23366	$BaGa_2S_4$	23230	$SrAl_2S_4$	24151	$CaAl_2S_4$	24088

The 4*f*-to-5*d* trasition energies of other trivalent rare-earth ions are higher than that of Ce^{3+} as shown in Figure 1.17 [60, 61]. Therefore, larger value of D(A) of hosts is required to be excited

at 380-400 nm for nUV LED lighting. It is very unlikely that a host with high D(A) value can be found for trivalent rare-earth ions except for Ce^{3+} to be excited directly at 380-400 nm.

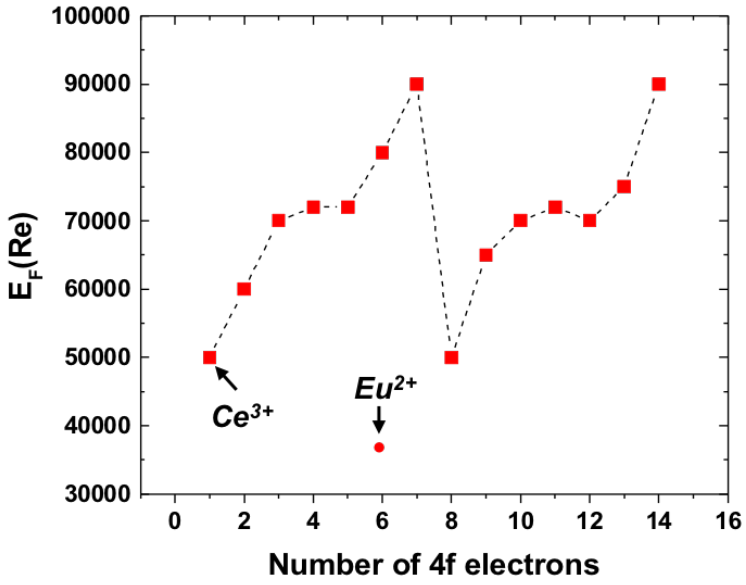

Figure 1.17 Free ion values of elements that have 4*f* orbital [60, 61]

For Eu^{2+}, excitation energy is given by [61]:

$$E_a(Eu^{2+}, A) = 34000\ cm^{-1} - D(A) \quad (3)$$

Therefore, the range from 7685 cm^{-1} to 9000 cm^{-1} for D(A) for hosts is required for Eu^{2+} to be excited at 380-400 nm range. The range from 2700 cm^{-1} to 8300 cm^{-1} for S(A) is necessary for the emission ranging from 450 nm to 600 nm. Although the study by Dorensbos shows the relationship between excitation and emission energy, it did not provide the enough insights into quantum efficiency, thermal and chemical stability, particles size effects, and best synthesis methods.

1.2.6 Particle size effects

An intergration of phosphors in an LED package requires small particle sized phosphors with a narrow size distribution. When the radii of particles are smaller than ~400 nm that is the excitation wavelength for nUV LED, the light scattering is negligible. This can be explained by the scattering cross-section of a particle [67]:

$$C_{scatter} = \frac{8}{3}(\pi a^2)\left(\frac{2\pi a}{\lambda}\right)^4 \left|\frac{m^2-1}{m^2+2}\right| \quad (4)$$

where λ is the wavelength of radiation, a is the radii of particles, and m is the refractive index of particles. When $a < \lambda$, C_{scatter} approaches zero, meaning that scattering of a particle is neglibigle, and Φ of phosphor is maintained on the LED package. In the remote phosphors configuration, the packing density of the micron-sized and nano-sized phosphors are illustrated in Figure 1.18. The micron-sized phosphors decrease the paking density on the LED package, which is attributed to the voids between the particles, as shown in Figure 1.18. It increases the thickness of phosphors layer to cover the substrate above the LED and consumes a relatively large amount of phosphors powders. In contrast to the micron-sized phosphors, nano-sized phosphors powders have high packing density in the remote configuration as shown in Figure 1.18. It enables to use a relatively small amount of phosphors on the LED package. A disadvantange of nano-sized phosphors is its poor Φ comparing to micron-sized phosphors. A high concentration of surface atoms and defects on the surfaces from high surface to volume ratio are the main reasons for the poor Φ of nano-sized phosphors. In addition, the increase in charge-carrier trapping centers on the surface defects decreases the Φ of nano-sized phosphors [68].

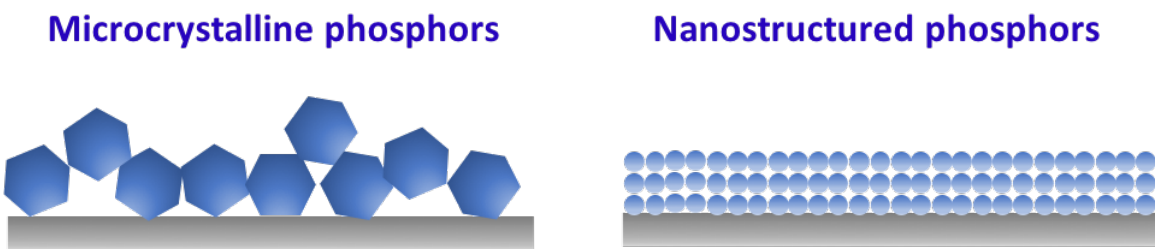

Figure 1.18 The scheme of the phosphors powder on the subtract for near-UV LEDs: microcrystalline and nanostructured phosphors.

1.2.7 Synthetic method

Different synthetic methods to produce inorganic phosphors have been reported for decades. The solid state reaction is the traditional method, but it results in micron-sized powders. On the other hand, solution based synthetic methods include co-precipitation, sol-gel reaction, combustion, and hydrothermal reactions are usually yield submicron-sized powders. The selection of a synthetic method depends on the desired outcome. For example, if simple, low cost, and large volume of phosphors are desired, the solid state reaction is suitable. Table 1.5 provides the summary of the syntheric methods and possible outcomes with regards to particles size/distribution, morphology control, purity, cost, and simplicity of the process. The different synthetic methods are also outlined below.

1.2.7.1 Solid state reaction

The solid state reaction is the conventional method to synthesize phosphors. This method produces micron-sized powders with higher quantum efficiency than small sized phosphors particles [69-71], and it is suitable for mass production. Oxides, (oxy)fluorides, (oxy)chlorides and (oxy)nitride are prepared by solid state reaction. Metal oxides or metal carbonates are typical precursors and they are mixed by ball-milling in a media (acetone). This method requires high

annealing temperature with a long reaction time to eliminate intermediate phases. Also, impurities can be produced due to the unreacted precursors [72] which reduces the luminescent properties.

1.2.7.2 Co-precipitation

Co-precipitation is a simple synthetic method to prepare submicron sized oxide phosphors [73-75]. Precursors are usually metal nitrates, acetates, or chlorides, which are dissolved in a solvent (water or alcohol). After the precursors are dissolved completely, precipitating agents are added in the solution that forms fine, solid particles in the solution. The precursors need to be dissolved in the solvent, while the precipitates should not be soluble, meaning the selection of solvent is crucial. After the product is obtained, a post-annealing step is usually required, 800ºC – 1200 ºC. The final particles have a narrow size distributions, are sub-micron sized and uniformly shaped [72, 76].

1.2.7.3 Sol-gel reaction

The sol-gel reaction results in oxides with high purity due to the presence of a chelating agent that enables precursors to be mixed homogeneously during the synthetic process [75, 77]. Metal nitrates are the typical precursors and they are dissolved in water followed by the addition of the chelating agent (e.g. citric acid). Ethylene glycol and polyethylene glycol are added in the solution to produce crosslinking with the citric acid. The resulting precipitate is fired between 800ºC – 1200ºC to produce the final product. The resultant product usually has a high purity with particles in sub-micron range with a narrow size distribution [75, 77].

1.2.7.4 Combustion

The combustion reaction is a simple and fast method to synthesize oxide powders [71]. This method involves igniting an aqueous solution containing dissolved metal nitrate precursors at ~500 ºC with an organic fuel (e.g. urea, carbohydrazide, or gycine). A highly exothermic and

oxidative reaction usually accompanied with a flame and the product is obtained after the solvent is evaporated. The reaction is complete in 5 – 10 min. Post-annealing treatment between 800ºC – 1200ºC is required to to remove organic residues which increases luminescent properties of the resultant material. The phosphors particles synthesized by the combustion reaction are homogeneous morphology and have low impurities [72, 76].

1.2.7.5 Hydrothermal reaction

The hydrothermal reaction is a method that applies pressure during the reaction, therefore a sealed autoclave is required for this method[78]. Metal nitrates precursors are dissolved in a solvent (water or organic solvent) and a precipitating agent is added. Next, the precipitates are put in the autoclave. The autoclave is placed in the oven at 150 ºC, and pressure is applied from the ensuing vapor. The resultant product is calcinated between 800ºC – 1200ºC to increase the luminescent properties. The size of phosphor particles is sub-micron with a narrow size distribution. The shape of particles is controllable but the reaction time is long [72, 76].

Table 1.5 Summary of the synthetic methods to produce phosphors [72, 76].

Synthesis method	**Solid-state reaction**	**Co-precipitation**	**Sol-gel reaction**	**Hydrothermal reaction**	**Combustion**
Particle size	> 5μm	10 nm – 2 μm	10 – 1 μm	10 nm – 1 μm	500 nm – 2 μm
Particle size distribution	Narrow - Broad	Narrow	Narrow	Narrow	Medium
Morphological control	Poor – Good	Good	Very Good	Good	Poor
Purity	Poor – Good	Good	Medium	Medium – good	Medium – good
Cost	Low	Medium	Medium	Medium-high	Low – medium
Synthesis time	Short – long	Medium	Medium	Very long	Short
Suitable phosphors	All compounds	All compounds except nitrides	Oxides and fluorides	All compounds	All compounds except nitrides
Advantages	Simplicity	Control of particle size, homogeneous morphology	Control of particle size, homogeneous morphology	Control of morphology	Short reaction time, homogenous morphology
Disadvantages	Enlarged crystals, agglomerates	Oxidative character of solvents	Carbon contamination	Long reaction time	Emission of harmful gases

CHAPTER 2: AN INTEGRATED FIRST PRINCIPLES AND EXPERIMENTAL INVESTIGATION OF THE RELATIONSHIP BETWEEN STRUCTURAL RIGIDITY AND QUANTUM EFFICIENCY IN PHOSPHORS FOR SOLID STATE LIGHTING

2.1 Abstract

In this paper, we outline an integrated approach for exploring novel near-UV excited phosphors. To test the hypothesis of whether high host structural rigidity results in phosphors with high quantum efficiency (Φ), we calculated the Debye temperatures (Θ) for 27 host materials using density functional theory calculations. We identified Eu^{2+}-activated $Ca_7Mg(SiO_4)_4$ and $CaMg(SiO_3)_2$ as having a relatively high Θ = 601 K and 665 K, respectively, and predicted excitation energies of 3.18 eV (337 nm) and 3.29 eV (377 nm), respectively, both of which are in good agreement with the results of photoluminescence spectroscopy. However, the measured Φ for these two phosphors was < 30%, which indicates that Θ alone is not a sufficient condition for a high Φ. This work demonstrates the potential of combined first-principles calculations and experiments in the discovery and design of novel near-UV excited phosphors.

2.2 Introduction

White-light sources based on light-emitting diodes (w-LEDs) have attracted intense interest for next generation solid-state lighting technologies due to their longer lifetime, superior efficiency, and low operating temperatures compared with traditional incandescent bulb and fluorescent lamp technologies [79-81]. The common approach to create white-emitting LEDs is to combine a blue-emitting (450 nm) InGaN LED with a yellow-emitting phosphor [9, 82]. The drawbacks of this method are a non-uniform light output and a low color rendering index (CRI) value. An alternative, more attractive approach is to combine a near UV-LED (nUV-LED, 370-410 nm) with blue, green, and red phosphors to produce high-efficiency w-LEDs. A high CRI value can be achieved by optimization of phosphor blends and, ultimately, a higher extraction

efficiency can be obtained due to a smaller current drop at high driving currents, compared to the blue-emitting LEDs [12-14].

Traditional trial-and-error approaches in the discovery of new blue-, green- and red-emitting phosphors for nUV-LED phosphors are time consuming and costly. Recently, new methodologies, such as mineral-inspired prototype evolution [83, 84] and single-particle-diagnosis [85] have been proposed for the discovery of new phosphors. Although these methods have achieved significant progress for developing new phosphors, in essence, they still focus on the exploration case-by-case.

An alternative approach is to use easily computable or measurable descriptors as a means to screen for various desired properties for phosphors, such as an appropriate excitation wavelength (370-410 nm), a high quantum efficiency (> 80%), good thermal quenching behavior (< 20% decrease in emission intensity from room temperature to 150˚C), and chemical stability (e.g. moisture stability). For example, the narrow-band descriptor combined with band gap and phase stability was recently proposed to discover promising narrow-band red-emitting phosphors for high-power LEDs in a high throughput approach [86]. Based on the analysis of over 1000 rare-earth activated compositions, Dorenbos [60, 61] proposed that the excitation energy, E_a(Re, A) can be predicted from the following empirical relationship:

$$E_a(\text{Re, A}) = E_F(\text{Re}) - D(\text{A}) \quad (1)$$

where E_F(Re) and D(A) are the rare earth (Re) free ion energy and crystal field depression in host A, respectively. However, D(A) is difficult to calculate. It is usually tabulated and strongly related to the crystal structure of the host, therefore it is not easy to use Eqn. (1) for new host materials without knowledge of D(A).

More recently, the *ab initio* calculated Debye temperature (Θ) of host materials was proposed to have a positive relationship with the experimental photoluminescence (PL) quantum efficiency (Φ). For Ce^{3+}-activated phosphors, a $\Theta \geq 500$ K was suggested for $\Phi \geq 80\%$ [87]. For example, the calculated Θ for $Y_3Al_5O_{12}:Ce^{3+}$ ($YAG:Ce^{3+}$) is 726 K with Φ measured to be 90% [87]. These preliminary results suggest that host materials with a high Θ may yield high Φ with an appropriate host band gap. However, there have been relatively few efforts utilizing a combined first-principles and experimental approach for the discovery of new phosphors.

In this work, 27 host materials were selected based on the criterion that Ce^{3+}- or Eu^{2+}-doping results in an absorption wavelength in the near-UV light range (370-410 nm). These host materials were found from potential phosphor compositions in the literature [11, 60, 61, 88, 89]. The Θ of these 27 hosts were calculated using density functional theory (DFT) calculations. Two potential candidates, $Ca_7Mg(SiO_4)_4:Eu^{2+}$ and $CaMg(SiO_3)^2:Eu^{2+}$ having higher Θ were identified, and their excitation energies were calculated. Then, powders were synthesized. The $(Ca_{0.96}Eu_{0.04})_7Mg(SiO_4)_4$ phosphor was prepared by the sol-gel/Pechini method and the $Ca_{0.94}Eu_{0.06}Mg(SiO_3)_2$ phosphor was prepared by the co-precipitation method. Subsequently, the PL properties were analyzed to compare to the first-principles predictions.

2.3 Methods

2.3.1 *Computational methods*

All first-principles calculations were performed using the projector augmented wave (PAW) method as implemented in the Vienna *ab initio* simulation package (VASP) [90, 91]. The Perdew–Berke–Ernzerhoff (PBE) [92] exchange-correlation functional was used. More specific calculation parameters can be found in references [93, 94].

The Debye temperature, Θ, was calculated using the quasi-harmonic model given by [87]

$$\Theta = \frac{\hbar}{k_B}(6\pi^2 V^{\frac{1}{2}} n) f(\nu) \sqrt{\frac{B}{M}} \quad (2)$$

where V, n, $f(\nu)$, B and M are the unit cell volume, the number of atoms in the unit cell, a scaling function in terms of Poisson's ratio ν, the bulk modulus and the molar mass, respectively; ħ and k_B refer to the Plank constant and the Boltzmann constant, respectively. The elastic moduli were calculated by employing the Voigt-Reuss-Hill (VRH) approximation based on the computed elastic tensor [95]. Previous research indicated that an effective Hubbard U of 2.5 eV can reproduce the experimental E(VBM-4f) for Eu^{2+}-activated oxides, [96] and the band width of the Eu^{2+} 4f bands are not very sensitive to the U value used [86]. We here adopted U = 2.5 eV for the evaluation of orbital-projected density of states (DOS) with the PBE functional. The band structures of hosts were calculated using the modified Becke-Johnson localized-density functional (MBJLDA), which has been shown to yield more accurate band gap values for insulators compared to the standard generalized gradient approximation (GGA), but at a much lower computational cost compared to hybrid density functionals [97].

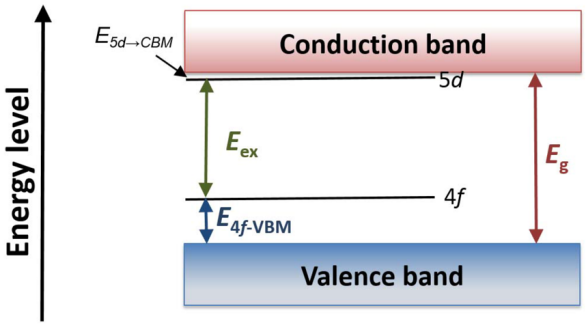

Figure 2.1 Schematic diagram of 4f→5d transition in Ce^{3+} or Eu^{2+} activated phosphors. Eg, Eex and E4f-VBM denote the band gap of host material, excitation energy, and 4f-VBM energy gap, respectively.

According to experimental findings on the absolute location of lanthanide (Ce^{3+} and Eu^{2+}) energy levels, the 4*f* and 5*d* energy levels generally lie in the band gap, with the 5*d* level closer to the conduction band minimum [98, 99]. This PL mechanism ($4f^{n-1}5d^1 \rightarrow 4f^n$ transition) for Ce^{3+} and Eu^{2+} activated phosphors is described in Figure 2.1 [98, 99]. The excitation energy (E_{ex}) is proposed from the following equation:

$$E_{ex} \approx E_g(\text{host, band gap}) - E(\text{VBM-}4f). \quad (3)$$

where E_g (host, band gap) is the band gap of the host material and E(VBM-4*f*) is the energy gap between the valence band maximum (VBM) and 4*f* level. It is noted that there are some errors in the estimate of the excitation energy on the order of ~1 eV due to the neglect of the gap between the ground state Eu5d level and the CBM. Dorenbos [100] found that the excited Eu 5d level is generally located within about 1.0 eV below the conduction band minimum (CBM). Also, the Stokes shift usually lies in the range of 0.64 eV ~ 1.22 eV. Nevertheless, the relative trend is reasonable. The Fermi energy in Eu^{2+}-activated systems refers to the highest occupied 4f orbital and is set to zero in the DOS plot.

2.3.2 Synthesis of phosphors

2.3.2.1 Reagents

All chemicals were used without further purification and included tetraethyl orthosilicate (TEOS, 99.9%, Sigma Aldrich), nitric acid (69.3%, Fisher Scientific), Eu_2O_3 (99.99%, Alfa Aesar), $Mg(NO_3)_2 \cdot 6H_2O$ (98.3%, Fisher Scientific), $Ca(NO_3)_2 \cdot 4H_2O$ (99.0%, Macron Fine Chemicals), citric acid ($C_6H_8O_7 \cdot H_2O$, Macron Fine Chemicals), ethylene glycol (C_2H_6OH, Fisher Scientific), polyethylene glycol (PEG, $C_2H_4O \cdot nH_2O$, molecular weight = 20,000 g/mole, Sigma Aldrich), and ammonium hydroxide (28~30%, BDH Aristar Plus).

2.3.2.2 Preparation of $(Ca_{0.96}Eu_{0.04})_7Mg(SiO_4)_4$

The sol-gel/Pechini process was used to synthesize $(Ca_{0.96}Eu_{0.04})_7Mg(SiO_4)_4$ powders. The 4 at.% Eu^{2+} concentration was chosen because it has been reported to have the highest PL emission intensity [88]. First, tetraethyl orthosilicate (2.23 mL) was added to ethanol (20 mL) with several drops of nitric acid and stirred for 30 min. Next, Eu_2O_3 was added in a dilute nitric acid solution to form a solution of aqueous $Eu(NO_3)_3$. $Mg(NO_3)_2•6H_2O$, and $Ca(NO_3)_2•4H_2O$ were dissolved in deionized water. After these solutions became transparent, silica sol and the $Eu(NO_3)_3$ solution were poured to the $Mg(NO_3)_2$ and $Ca(NO_3)_2$ solution with stirring. Next, citric acid (4.2 g) and ethylene glycol (2.23 mL) were added to the mixed solution (metal:citric acid:ethylene glycol = 1:1:2), which acts as a chelating agent for the metal ions. Polyethylene glycol (2.5 g) was introduced in the mixture, which was used as a crosslinking agent. After stirring the solution for 30 minutes to ensure uniformity, precipitation occurred by adding drops of ammonium hydroxide until the pH reached 4. After completing the preparation, the mixture was continuously stirred at 80˚C overnight to form a gel. The white colored product was preheated to remove organic materials at 350˚C for 1 hour, and then annealed at 1100˚C or 1350˚C for 3 h, or 1400˚C for 10 h in air. All samples were finally calcined at 1100˚C for 4 h under a slight reducing condition (mixture of 5% H_2 and 95% N_2).

2.3.2.3 Preparation of $Ca_{0.94}Eu_{0.06}Mg(SiO_3)_2$

$Ca_{1-x}Eu_xMgSi_2O_6$ powders were synthesized by a co-precipitation technique that was modified from a previous reported method [101]. TEOS (2.23 mL) was added into ethanol (20 mL) with HNO_3 (5 mL) and stirred for 30 minutes to hydrolyze TEOS. The desired amount of Eu_2O_3 (x = 0.02, 0.06, 0.1, and 0.2) was introduced in a dilute nitric acid solution to form a solution of aqueous $Eu(NO_3)_3$. $Mg(NO_3)_2•6H_2O$ and $Ca(NO_3)_2•4H_2O$ were dissolved in 30 mL of deionized

water. After the europium solution and the magnesium and calcium solution became transparent, the silica sol and europium solution were poured into the magnesium and calcium solution and the mixture was stirred for 1 hour. Ammonium hydroxide was added dropwise into the solution until the pH was 10 to create a white precipitate. The precipitate solution was stirred for 8 h at room temperature. Next, the precipitate was centrifuged and washed with deionized water three times. The products obtained by centrifugation were dried at 100˚C for 12 hours. Then a post-annealing step was performed at 1100˚C for 2 h under air and then at 1100˚C for 4 h under 5% H_2 / 95% N_2 to change Eu^{3+} to Eu^{2+}.

2.3.2.4 Characterization

The crystallite phases and crystallite sizes of the annealed powders were determined by X-ray diffraction (XRD, Bruker D2 Phaser) using CuKα radiation and a step size of 0.014° over the 2θ range of 20 to 80 degrees. The analysis was performed using the Diffrac.Eva plus program. Lattice parameters and crystallite sizes were calculated using the approach of Rietveld refinement by the TOPAS 4.2 software (Bruker), which averages the lattice constants associated with each XRD peak across the entire spectrum. The size and morphology of the particles were analyzed by a field emission scanning electron microscope (FESEM, XL30, Philips) at 10 keV. Samples were coated with iridium at 85 μA for 10 s before FESEM imaging. Absolute quantum efficiency (Φ) measurements were performed using an integrating sphere system, with sodium salicylate (Φ = 44%) as a reference standard. Photoluminescence emission and excitation spectra were acquired with a fluorescence spectrophotometer (Hitachi F-7000) using λ= 350 nm excitation wavelength (pulse = 0.025 sec). This excitation wavelength was chosen as it produced the highest PL emission intensity. The thermal quenching analysis (25˚C ~ 150 ˚C) was performed using a custom designed device that consist of a heater, thermocouple, and the spectrophotometer.

2.4 Results And Discussion

2.4.1 Screening of rigid structures and predicting the excitation energy

High structural rigidity confines accessible phonon modes that result in non-radiative recombination. As mentioned previously, Θ was recently proposed as a descriptor of structural rigidity [87]. The higher Θ, the fewer lattice vibration modes can be accessed and thus the more rigid is a crystal structure. The calculated Θ of the 27 host candidates are summarized in Table 2.1. Six host candidates (in bold) have Θ > 500 K, implying a strong rigidity of the crystal structure and correspondingly, a possible high Φ.

Among these six candidates, only the three silicate host materials Mg_2SiO_4, $Ca_7Mg(SiO_4)_4$, and $CaMg(SiO_3)_2$, were considered further because of their high chemical stability, good thermal quenching properties [102], and facile synthesis methodologies. Since, in Mg_2SiO_4 the radius of Mg^{2+} (< 0.07 nm) is too small to be replaced by Eu^{2+} (~0.130 nm), $Ca_7Mg(SiO_4)_4:Eu^{2+}$ and $CaMg(SiO_3)_2:Eu^{2+}$ were selected further. In this case, Eu^{2+} can replace Ca^{2+} in the crystal structure due to similar ionic radii (0.118 nm and 0.123 nm for 9-coordinated and 10-coordinatd Ca^{2+}, respectively; 0.130 nm and 0.135 nm for 9-coordinated and 10-coordinated Eu^{2+}, respectively) [103].

Table 2.1 Calculated Debye temperature (Θ) of 27 identified host for Ce^{3+} or Eu^{2+} activation. The compositions in bold have Θ > 500K. The excitation energy (Eex) and emission energy (Eem) were selected from [9, 12, 25, 27, 28, 41, 42].

Host material	E_{ex}**(nm)**	E_{em}**(nm)**	**Θ (K)**
$Mg_2SiO_4:Ce^{3+}$	373	432	734
X1-$YSiO_2N:Ce^{3+}$	-	-	695
$CaMg(SiO_3)_2:Eu^{2+}$	365	450	665
$Mg_3F_3BO_3:Ce^{3+}$	399	474	615
X2-$YSiO_2N:Ce^{3+}$	370	405	606
$Ca_7Mg(SiO_4)_4:Eu^{2+}$	350	505-520	601
X2-$Y_2SiO_5:Ce^{3+}$	381	480	512
X1-$Y_2SiO_5:Ce^{3+}$	365	430	491
$SrY_2O_4:Ce^{3+}$	397	560	465
$La_2Be_2O_5:Ce^{3+}$	365	445	464
β-Sr_2SiO_4	310	~543	428
$LuBO_3$ (vaterite) :Ce^{3+}	365	388	423
$Ba_3Mg(SiO_4)_2:Eu^{2+}$	410	438	422
X2-$Lu_2SiO_5:Ce^{3+}$	376	462	416
X1-$Sr_2SiO_4:Eu^{2+}$	390	490	410
$NaF:Ce^{3+}$	390	472	387
$CaAl_2S_4:Ce^{3+}$	396	440	373
α-Sr_2SiO_4	310	573	360
$Sr_2SiCl_2O_3:Eu^{2+}$	410	490	349
$SrAl_2S_4:Ce^{3+}$	397	462	338
$BaAl_2S_4:Ce^{3+}$	384	444	331
$ThO_2:Ce^{3+}$	408	-	319
Ba_2SiO_4	360	512	307
$Ba_2YB_2O_{62}Cl:Ce^{3+}$	370	466	300
$Ba_2LuB_2O_6Cl:Ce^{3+}$	370	466	294
$La_3Si_2S_8I:Ce^{3+}$	370	446	262
$LaOI:Ce^{3+}$	385	435	161

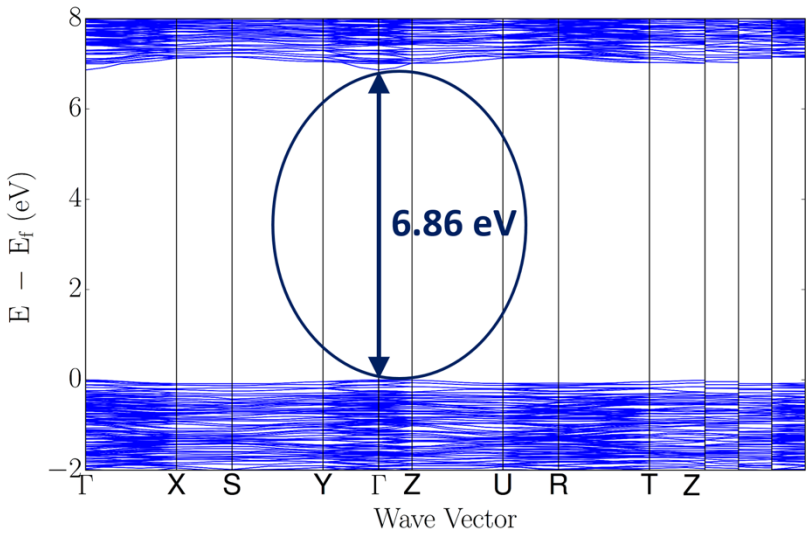

(a)

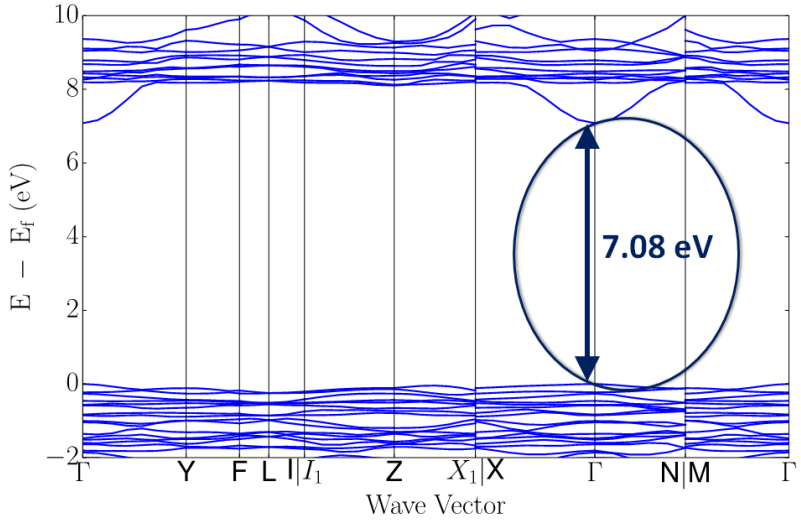

(b)

Figure 2.2 The band structure of the host material $Ca_7Mg(SiO_4)_4$ (a) and CaMgSi2O6 (b), where it has a direct Γ → Γ transition band gap of 6.86 eV and 7.08 eV, respectively.

Figures 2.2a and 2.2b show the calculated band structures of $Ca_7Mg(SiO_4)_4$ and $CaMg(SiO_3)_2$. Both hosts have direct ($\Gamma \rightarrow \Gamma$ transition) band gaps (E_g = 6.86 eV for $Ca_7Mg(SiO_4)_4$ and E_g = 7.08 eV for $CaMg(SiO_3)_2$). Figures 2.3a and 2.3b show the calculated orbital projected DOS. The energies between 4*f* (located at Fermi energy level of 0) and VBM for $Ca_7Mg(SiO_4)_4:Eu^{2+}$and $CaMg(SiO_3)_2:Eu^{2+}$ are 3.18 eV and 3.79 eV, respectively. The excitation energies can be estimated from Eqn. (3) by subtracting the calculated 4*f*-VBM gap (3.18 eV for $Ca_7Mg(SiO_4)_4:Eu^{2+}$ and 2.79 eV for $CaMg(SiO_3)_2:Eu^{2+}$) from E_g, which gives E_{ex} = 3.68 eV (337 nm) for $Ca_7Mg(SiO_4)_4:Eu^{2+}$ and 3.29 eV (377 nm) for $CaMg(SiO_3)_2:Eu^{2+}$.

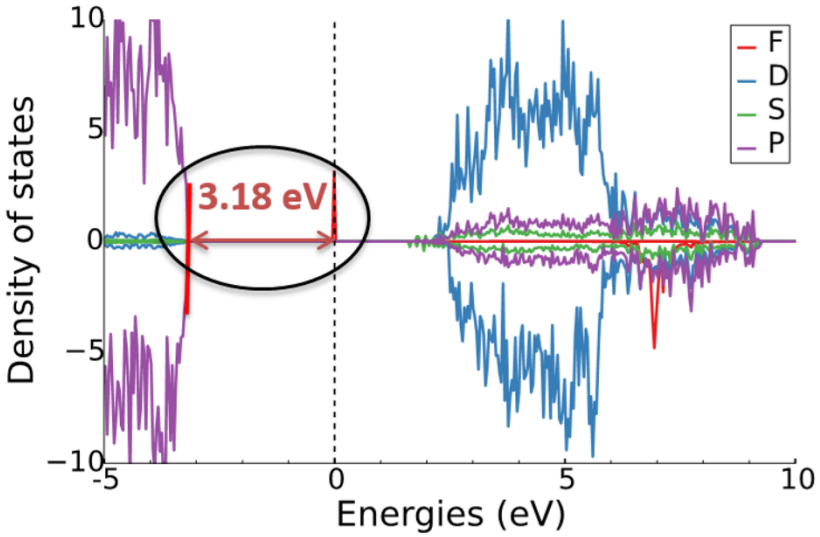

(a)

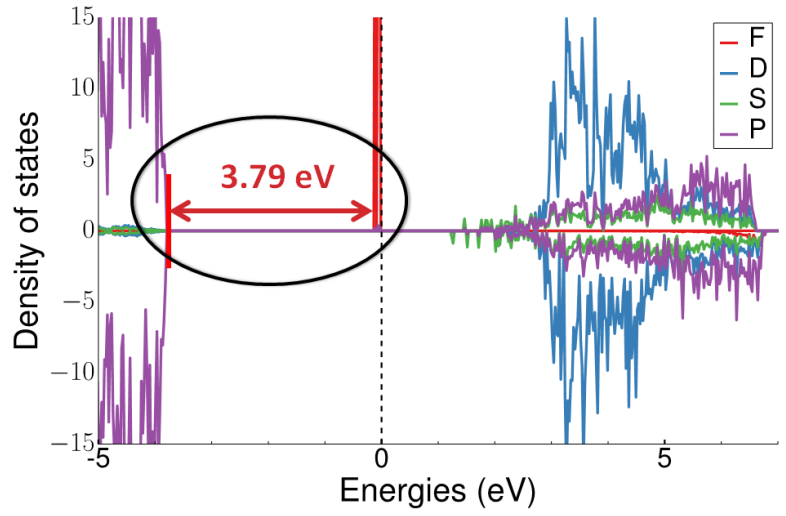

(b)

Figure 2.3 The orbital-projected density of state (DOS) of $Ca_7Mg(SiO_4)_4:Eu^{2+}$ (a), and $CaMgSi_2O_6:Eu^{2+}$ (b), where the 4f-VMB energy gap is 3.18 eV and 3.79 eV, respectively. The Fermi level is set to 0.

2.4.2 Crystal structure, X-ray diffraction, and scanning electron microscopy of the synthesized phosphors

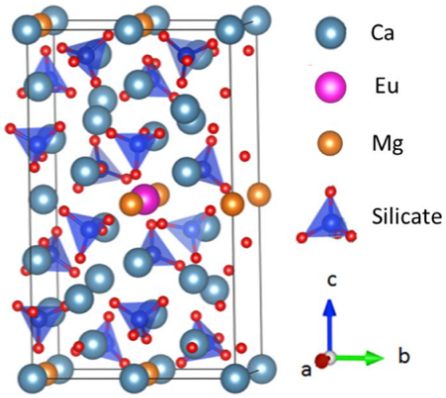

(a)

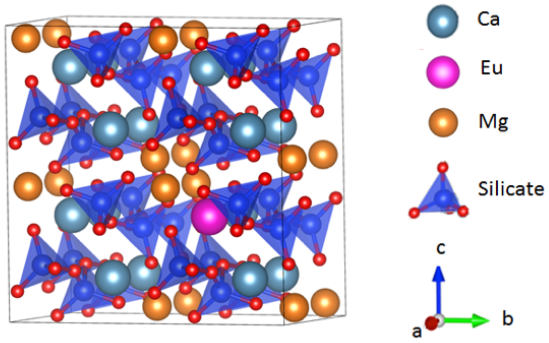

(b)

Figure 2.4 Unit cell representation of the crystal structure of (a) $Ca_7Mg(SiO_4)_4:Eu^{2+}$ (b) $CaMgSi_2O_6:Eu^{2+}$ drawn with VESTA [104]. $Ca_7Mg(SiO_4)_4$ has an orthorhombic structure with space group *Pnn2* with lattice constants a = 0.6742 nm, b = 1.0887 nm, c = 1.8339 nm. $Ca_7Mg(SiO_4)_4$ has a monoclinic structure with space group *C2/c* with lattice constants a = 0.9743 nm, b = 0.8879 nm, c = 0.5230 nm. Both sets of lattice parameters were calculated using TOPAS.

Figures 2.4a and 2.4b show the structures of $Ca_7Mg(SiO_4)_4:Eu^{2+}$ and $CaMg(SiO_3)_2:Eu^{2+}$ drawn by VESTA (Visualization for Electronic and STructural Analysis) [104]. In Figure 2.4a, $Ca_7Mg(SiO_4)_4$ (mineral bredigite) has an orthorhombic structure with a space group *Pnn2* where Ca^{2+} has three different crystallographic sites with coordination numbers 12, 10, and 9 [105]. As illustrated in Figure 2.4b, $CaMg(SiO_3)_2$ (mineral diopside) has a monoclinic structure with space group *C2/c*. The lattice parameters of $(Ca_{0.96}Eu_{0.04})_7Mg(SiO_4)_4$ and $Ca_{0.94}Eu_{0.06}Mg(SiO_3)_2$ were calculated using TOPAS and the computed lattice constants are a = 0.6742 nm, b = 1.0887 nm, c = 1.8339 nm for $(Ca_{0.96}Eu_{0.04})_7Mg(SiO_4)_4$ and a = 0.9743 nm, b = 0.8879 nm, c = 0.5230 nm for $Ca_{0.94}Eu_{0.06}Mg(SiO_3)_2$, which are consistent with previous reports for $Ca_7Mg(SiO_4)_4$ [105] and $CaMg(SiO_3)_2$ [106].

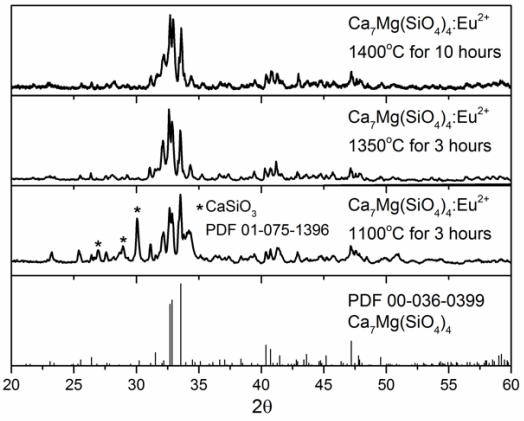

(a)

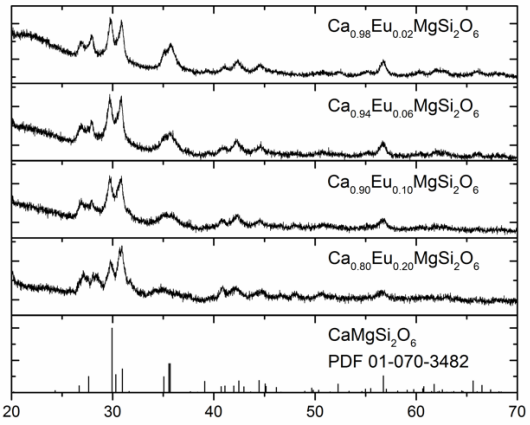

(b)

Figure 2.5 X-ray diffraction patterns: (a) $(Ca_{0.96}Eu_{0.04})_7Mg(SiO_4)_4$ prepared by the sol-gel/Pechini method with post-synthesis annealing conditions of 1100˚C or 1350˚C for 3 h or 1400˚C for 10 h. (b) $Ca_{1-x}Eu_xMgSi_2O_6$ (x = 0.02, 0.06, 0.1, and 0.2) prepared by the co-precipitation method with post-synthesis annealing condition of 1100˚C for 2 h.

XRD patterns of the $(Ca_{0.96}Eu_{0.04})_7Mg(SiO_4)_4$ powders for different calcination times and temperatures are shown in Figure 2.5a. The diffraction peaks were indexed by the standard data from PDF card 00-036-0399 ($Ca_7MgSi4O_4)_4$). A pattern for post-synthesis annealing at 1100˚C, shows impurity peaks around 2θ = 27, 29 and 30°, which correspond to $CaSiO_5$. However, these peaks disappear after annealing over 1350˚C. No other diffraction peaks, other than those

corresponding to $(Ca_{0.96}Eu_{0.04})_7Mg(SiO_4)_4$, are observed at both 1350˚C and 1400˚C. The crystallite sizes were determined by the TOPAS program and were ~54 nm, ~67 nm, and ~70 nm, for post-synthesis annealing at 1100˚C for 3 h, 1350˚C for 3 h, and 1400˚C for 10 h, respectively. These results are in a good agreement with previous studies demonstrating that crystallites grow with an increase of the post-synthesis annealing temperature and time [107, 108].

Figure 2.5b shows XRD patterns of the $Ca_{1-x}Eu_xMgSi_2O_6$ (x = 0.02, 0.06, 0.1, and 0.2) powders. It is observed that, when the activator concentrations are 0.02 and 0.06, the peaks in the XRD patterns are consistent with the standard PDF card 01-070-3482 ($CaMgSi_2O_6$), indicating the successful synthesis of a pure phase of $Ca_{1-x}Eu_xMgSi_2O_6$. The crystallite sizes from the TOPAS program were found to be ~16 nm, ~13 nm, ~17 nm, and ~10 nm for x = 0.02, 0.06, 0.1, and 0.2, respectively, indicating that crystallite sizes did not significantly change with x in the current range of activator concentrations due to similarity of ionic radii of Ca^{2+} and Eu^{2+}.

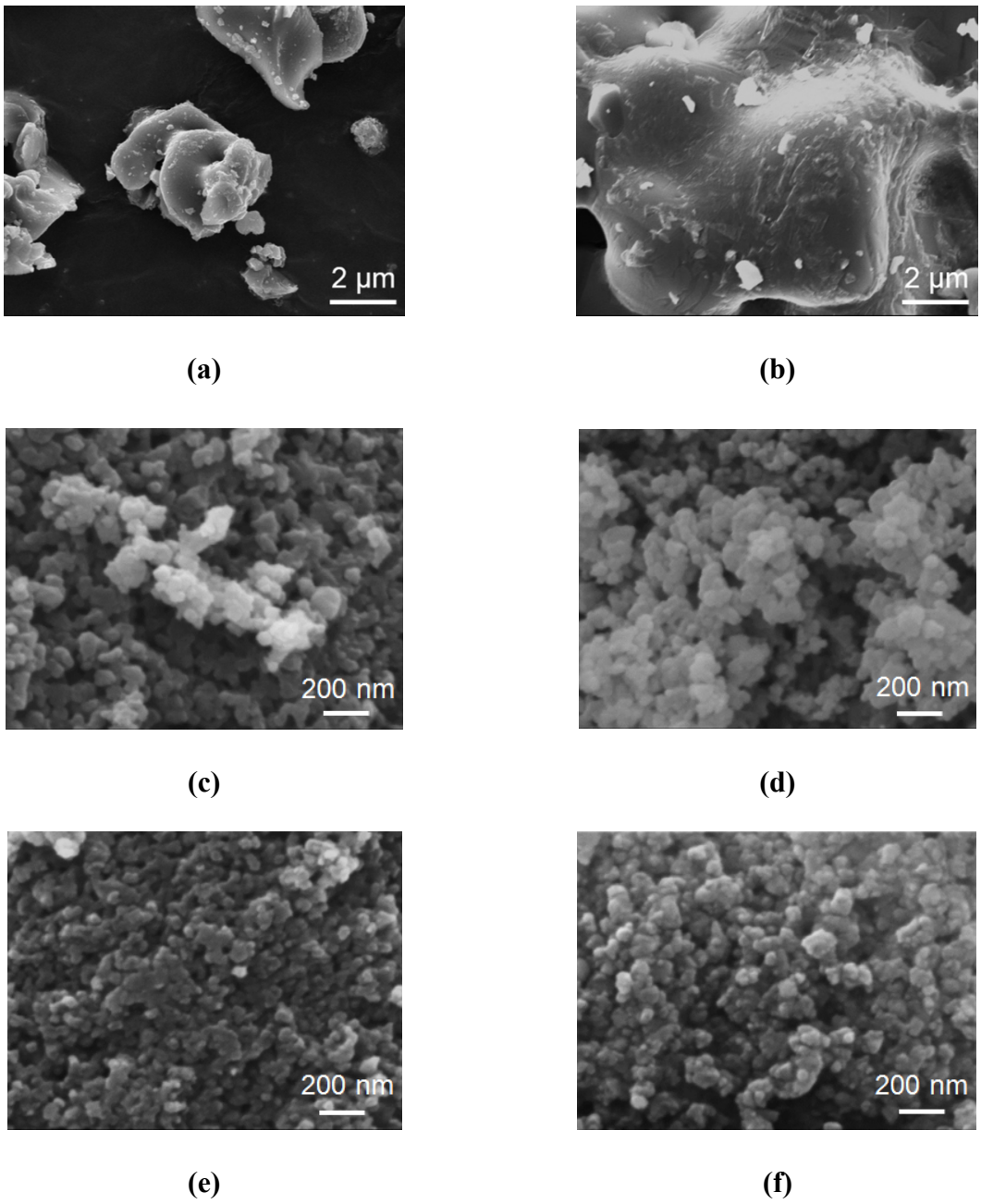

(a) **(b)**

(c) **(d)**

(e) **(f)**

Figure 2.6 Scanning electron micrographs of the powders. $Ca_{0.96}Eu_{0.04}Mg(SiO_4)_4$ after post-synthesis annealing at: **(a)** 1350˚C for 3 h and **(b)** 1400˚C for 10 h. $Ca_{1-x}Eu_xMgSi_2O_6$ with post-synthesis annealing condition of 1100˚C for 2 h: **(c)** $x = 0.02$ **(d)** $x = 0.06$, **(e)** $x = 0.10$ and **(f)** $x = 0.20$.

Figure 2.6a shows SEM images of the phosphors after post-synthesis annealing at 1350˚C for 3 h. The particles show agglomeration and form aggregates due to the high temperature during post-synthesis annealing. The morphology of the phosphors after post-synthesis annealing at 1400˚C for 10 h is shown in Figure 2.6b. The particles are more agglomerated than those in Figure 2.6a. Figure 2.6c-f show the SEM images of $Ca_{1-x}Eu_xMg(SiO_3)_2$ (x = 0.02, 0.06, 0.1, and 0.2). It should be noted that the morphology of $Ca_{1-x}Eu_xMg(SiO_3)_2$ is not altered when x increases.

2.4.3 Photoluminescence spectra, color calculator data and quantum efficiency of synthesized phosphors

Figure 2.7a shows the PL excitation (PLE, monitored at 511 nm) and PL emission (excitation wavelength, λ_{ex} = 350 nm) spectra for $(Ca_{0.06}Eu_{0.04})_7Mg(SiO_4)_4$. The PLE spectra show broadband absorption in the near UV region from 200 to 450 nm, with a maximum at ~350 nm, which arises from the allowed transition of Eu^{2+}. The experimental λ_{ex} (~350 nm) is very similar to the calculated λ_{ex} (337 nm), confirming the validity of our approach to discover new phosphor compositions. The PL emission spectrum consists of a broad band centered at 511 nm, which is attributed to the allowed $4f^65d^1 \rightarrow 4f^7$ transition of Eu^{2+}. The Φ of $(Ca_{0.96}Eu_{0.04})_7Mg(SiO_4)_4$ with the post-synthesis annealing conditions of 1100˚C for 3 h under air, 1350˚C for 3 h under air, and 1400˚C for 10 h under air, were ~19%, ~ 30%, and 11%, respectively. Generally, Φ is increased with increase of annealing temperature because of the increase of crystallite sizes [108]. In this work, although the crystallite sizes of the powders calcined at 1400˚C for 10 h is slightly larger than the powders calcined at 1100˚C for 3 h and 1350˚C for 3 h, the Φ

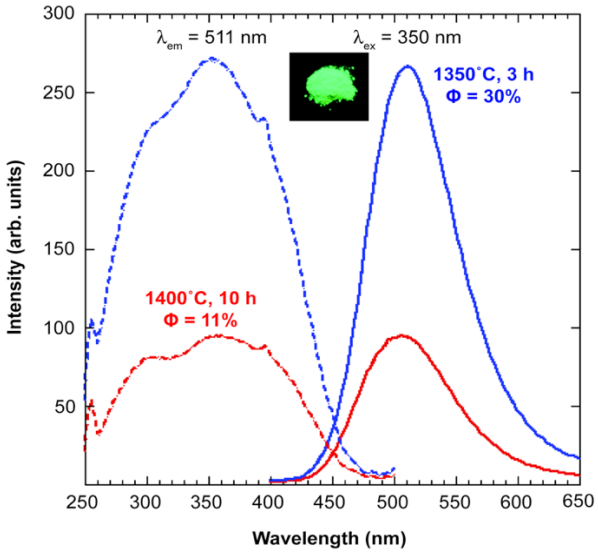

(a)

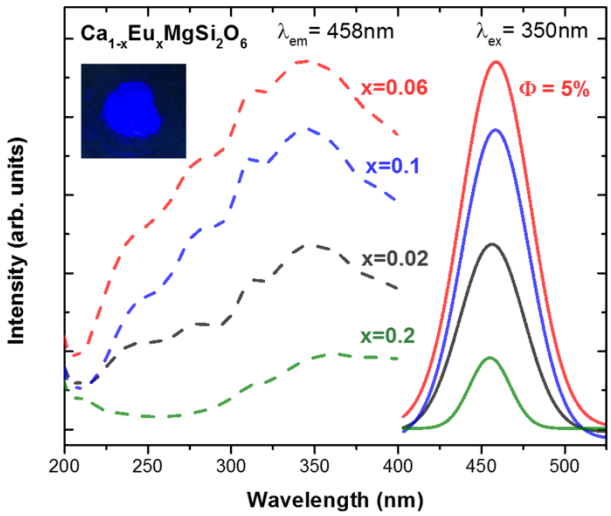

(b)

Figure 2.7 **(a)** Photoluminescence excitation (dashed line monitored at 511 nm) and emission (solid line, λ_{ex} = 350 nm) spectra of $(Ca_{0.96}Eu_{0.04})_7Mg(SiO_4)$. Blue lines = post-synthesis annealing at 1350˚C for 3 h and the red lines = post-synthesis annealing at 1400˚C for 10 h. Both powders were subsequently heated to 1100˚C for 4 h in a reducing atmosphere. **(b)** Photoluminescence excitation (dashed line monitored at 458 nm) and emission (solid line, λ_{ex} = 350 nm) spectra of $Ca_{1-x}Eu_xMgSi_2O_6$, x = 0.02, 0.06, 0.1, and 0.2. Post-synthesis annealing condition was 1100˚C for 2 h. The inset photographs are the phosphor powders excited with 365 nm. Φ = quantum efficiency.

be attributed to aggregation of the phosphors particles. As shown in Figure 2.6a and b, the powders calcined at 1400˚C form more aggregated structure compared to the powders calcined at 1350˚C. Hong *et al.* [109] and Lenggoro *et al.* [110] reported that highly aggregated phosphor powders showed a reduction in emission intensity, which is related to Φ. Aggregated powders can possibly have an influence on the reabsorption and light scattering, which results in a reduction of Φ [111]. Thus, non-aggregated powders play an important role for the obtainment of a high Φ.

Previously reported Φ for $(Ca_{1-x}Eu_{x.})_7Mg(SiO_4)_4$, 18% for $x = 0.04$ (λ_{ex} = 350 nm) [88] and ~23% for $x = 0.02$ (λ_{ex} = 400 nm) [89]), synthesized by solid state reaction at 1350˚C for 3 h in N_2/H_2 at 1100~1400˚C for 4 h in N_2/H_2, respectively, were similar to the present results. However, a high Φ (~64%) for $(Ca_{1-x}Eu_{x.})_7Mg(SiO_4)_4$ was previously found for an unusually low activator concentration, $x = 0.001$ (λ_{ex} = 365 nm) [112]. These powders were formed by a solid-state reaction at 1250˚C for 6 h in N_2/H_2. Since both the synthesis methodology and post-synthesis calcination, affect the crystallite sizes, the differences between values of Φ for the present work and for previous reports can be attributed to differences in synthesis method, post-processing temperature, and dopant concentration.

Figure 2.7b shows the PL excitation (PLE, monitored at 458 nm) and PL emission (excitation wavelength, E_{ex} = 350 nm) for $CaMg(SiO_3)_2:Eu^{2+}$. A broad excitation spectrum is observed from 200 nm to 400 nm, with a maximum at 350 nm, which is a result of the allowed transition of Eu^{2+}. This value is also close to our calculated excitation wavelength of 377 nm. The PL emission shows a spectrum maximum at 458 nm, which is attributed to the parity-allowed $4f^6 5d^1 \rightarrow 4f^7$ transition of Eu^{2+}. Solid lines in Figure 2.7b refer to the emission monitored at 350 nm for various concentrations of Eu^{2+} ($x = 0.02$, 0.06, 0.1, and 0.2) in $CaMg(SiO_3)_2$. The emission intensity increases until $x = 0.06$ and then decreases due to the concentration quenching effect. The

Φ was ~ 5% when $x = 0.06$ for $\lambda_{ex} = 350$ nm, which is the highest quantum efficiency among $x = 0.02, 0.06, 0.1$, and 0.2. This Φ is similar to the previously reported value for this material of ~9.1% [113].

Our results indicate that high structural rigidity, as quantified by high Θ, is not a sufficient condition for high Φ. Both silicates studied in this work have high Θ, but relatively low Φ. For compounds that have similar band gaps and chemistries, Θ indeed seems to be correlated with Φ. For example, the calculated Θ's of X1-Y_2SiO_5 (GGA band gap, 4.73 eV) and X2-Y_2SiO_5 (GGA band gap, 4.77 eV) are 491 K and 512 K (Table 2.1) and the Φ's are ~36% and ~45%, respectively, showing that as Θ increases, Φ also increases [114]. However, Φ is also strongly affected by the host band gap. Furthermore, it has been demonstrated that a host with low Θ yields high Φ when it is activated with Eu^{2+}. For instance, the computed Θ's for Ba_2SiO_4, α-Sr_2SiO_4 and β-Sr_2SiO_4 are 307 K, 360 K and 428 K, respectively, each of which is smaller than the suggested 500 K, whereas the experimentally measured Φ for Eu^{2+}-activated Ba_2SiO_4 and Sr_2SiO_4 are > 85% [77, 108]. These findings suggest that although calculated Θ may be a starting point, caution should be given to the reliability of Θ as a descriptor of Φ. Therefore, more efforts need to be devoted to explore more accurate descriptors to screen for phosphors with high Φ.

For $Ca_7Mg(SiO_4)_4:Eu^{2+}$, the color represented by the *x, y* color coordinates (0.25, 0.49) is located in the green region of the diagram on the Commission International de I'Eclairage (CIE) diagram. According to the National Television System Committee (NTSC) RGB colors, the values of good green-emitting phosphors are 0.21 and 0.71 [115]. The color coordinates previously reported (0.20, 0.47) were for powders produced by a solid state reaction with $x = 0.001$ and $\lambda_{ex} = 365$ nm [112]. The discrepancy in these coordinates with the present results can be explained by the difference in *x* and λ_{ex}. It was previously shown [112] that the coordinates were dependent on

both λ_{ex} and x (activator concentration), attributed to the three different Eu^{2+} sites. Emission wavelengths were found to be 455 nm ($Eu(1)^{2+}$), 504 nm ($Eu(2)^{2+}$), and 540 nm ($Eu(3)^{2+}$). Eu^{2+} will enter in the $Eu(1)^{2+}$ sites preferentially for small concentrations of Eu^{2+}, which will increase the emission intensity from the $Eu(1)^{2+}$ sites (455 nm). When the activator concentration increases, Eu^{2+} preferentially occupies $Eu(2)^{2+}$ and $Eu(3)^{2+}$ sites, which will decrease the emission from the $Eu(1)^{2+}$ sites. It should be noted that these three emission spectra overlap and display one broad emission peak from 450 nm to 600 nm. Thus, the width of emission spectra would change, depending on x and λ_{ex}. Despite the slight difference in values of the color coordinates in this work, the obtained values were in the green color range, indicating that $Ca_7Mg(SiO_4)_4:Eu^{2+}$ is a potential green-emitting phosphor for use in nUV LEDs.

The x, y color coordinates of $Ca_{0.94}Eu_{0.06}Mg(SiO_3)_2$ were 0.14 and 0.05, located in the blue region on the CIE diagram and the color coordinates of all samples (x ranging from 0.02 to 0.2) are similar. These values are similar to those defined by NTSC CIE for blue color (0.14, 0.08), indicating that $CaMg(SiO_3)_2:Eu^{2+}$ could be utilized as a blue-emitting phosphor for nUV LEDs.

2.4.4 Concentration quenching of $CaMg(SiO_3)_2:Eu^{2+}$

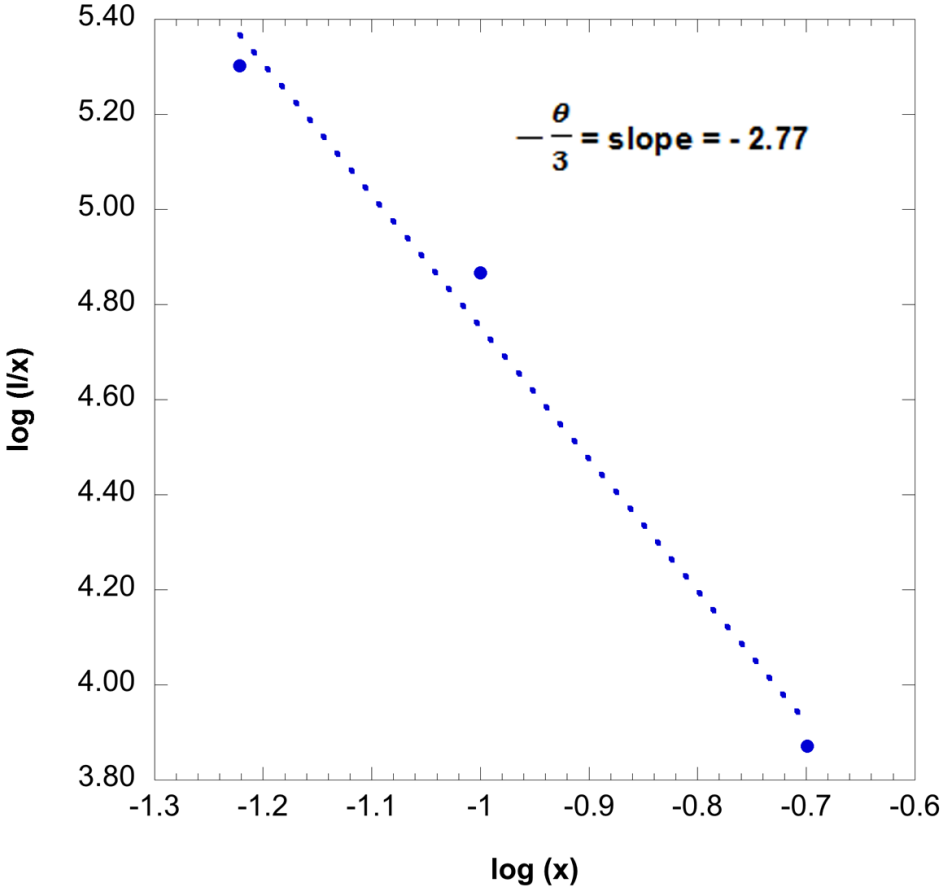

Figure 2.8 The relationship between the log(I/x) and log(x) of $Ca_{1-x}Eu_xMgSi_2O_6$. I = emission intensity, and x = concentration of Eu^{2+} (x = 0.06, 0.1, and 0.2).

The concentration quenching behavior was analyzed using the emission intensity change as a function of x. Blasse reported that the critical transfer distance (R_c) was defined as: [116]:

$$R_c = 2\left(\frac{3V}{4\pi x_c N}\right)^{1/3} \quad (4)$$

where x_c is the critical dopant concentration when the emission intensity shows the maximum value, V is the volume of the unit cell, and N is the number of cations in the unit

cell. R_c in $CaMg(SiO_3)_2$ was calculated to be ~1.5 nm by taking the values of V, x_c, and N as 0.438 nm^3, 0.06, and 4, respectively, from experimental and analytical evaluations. The interaction type was proposed by Dexter [117] when $x > x_c$ [118, 119]:

$$log\left(\frac{I}{x}\right) \propto -\frac{\theta}{3}\, log(x) \tag{5}$$

where I is the emission intensity and θ is a function of electric multipolar character.

There are three types of concentration quenching mechanisms that result from electrostatic multipolar interaction: dipole-dipole (*d-d*), dipole-quadrupole (*d-q*), and quadrupole-quadrupole (*q-q*) interactions, corresponding to θ = 6, 8, and 10, respectively. The type of interaction can be estimated by plotting (log (*I/x*) as a function of (log *x*). For $CaMg(SiO_3)_2:Eu^{2+}$ with x = 0.06, 0.1, and 0.2, the concentration quenching mechanism under 350 nm excitation was found to be *d-q* interaction (θ ~ 8), as shown in Figure 2.8. These findings are in contradiction with the previously reported (*d-d*) quenching mechanism for the same material for value of x_c = 0.01, with an excitation wavelength of 147 nm [120], possibly due to the difference in the excitation wavelength that could affect the emission intensity.

2.4.5 Thermal quenching process of $Ca_{0.96}Eu_{0.04})_7Mg(SiO_4)_4$ and $Ca_{0.94}Eu_{0.06}Mg(SiO_3)_2$

The thermal-quenching process of both phosphors was measured as the decrease of emission intensity as a function of temperature (from 25˚C to 150˚C). The data was then plotted using the following equation to describe thermal quenching of luminescence intensity *I(T)* with temperature *T* [100]:

$$I(T) = \frac{I_o}{1 + \frac{\Gamma_0}{\Gamma_\upsilon} exp\left(-\frac{\Delta E}{kT}\right)} \tag{6}$$

where I_0 is the initial intensity at 25˚C, ΔE is the energy barrier for thermal quenching, k is the Boltzmann's constant, Γ_0 is the attempt rate for thermal quenching at T = ∞, and Γ_υ is the radiative decay rate of the 5d state of Eu^{2+}. Here we adopted the Γ_0 and Γ_υ with values of 3×10^{13} Hz and 1.1×10^6 Hz, respectively, in line with estimations in the literature [100]. Figure 2.9a and b show the PL emission intensity as a function of temperature from 25˚C to 150˚C, demonstrating that there is a significant quenching of the luminescence over this temperature range. Figure 2.9c shows a plot of the relative intensity as a function of temperature for both phosphors. Γ_0/Γ_υ is 2.7×10^7. The values for average ΔE were obtained in each temperature. ΔE were 0. 56 ± 0.03 eV for $(Ca_{0.96}Eu_{0.04})_7Mg(SiO_4)_4$ and 0.52 ± 0.02 eV for $Ca_{0.94}Eu_{0.06}Mg(SiO_3)_2$. Note that there are many factors that influence the measured intensity than just thermal quenching alone (e.g. synthesis conditions, particle crystallinity). These factors will also affect the measured curve and subsequently the fitted thermal activation barrier. But we believe the relative trend for both cases is reasonable. These ΔE values were in good agreement with the range of calculated values of similar calcium compounds (0.2-0.6 eV) [100]. In general, the larger the thermal activation energy, the better Φ obtained for Eu^{2+}-activated phosphors. Although the predicted Θ for $(Ca_{0.96}Eu_{0.04})_7Mg(SiO_4)_4$ (601K) is smaller than $Ca_{0.94}Eu_{0.06}Mg(SiO_3)_2$ (665K), the Φ of $(Ca_{0.96}Eu_{0.04})_7Mg(SiO_4)_4$ (30%) is relative higher than $Ca_{0.94}Eu_{0.06}Mg(SiO_3)_2$ (5%), which can be attributed to its larger thermal activation energy.

A simplified relationship between the energy barrier and the quenching temperature $T_{0.5}$ (the temperature at which the emission intensity declined to 50% of the low temperature value) was developed by Dorenbos [29] from Eqn. (6):

$$\Delta E = \frac{T_{0.5}}{680}(eV) \tag{7}$$

From this equation, the obtained $T_{0.5}$ for $(Ca_{0.96}Eu_{0.04})_7Mg(SiO_4)_4$ and $Ca_{0.94}Eu_{0.06}Mg(SiO_3)_2$ are 381 K and 354 K, respectively. These low thermal quenching temperatures suggest that Φ's of $(Ca_{0.96}Eu_{0.04})_7Mg(SiO_4)_4$ and $Ca_{0.94}Eu_{0.06}Mg(SiO_3)_2$ can be severely degraded, even at room temperature.

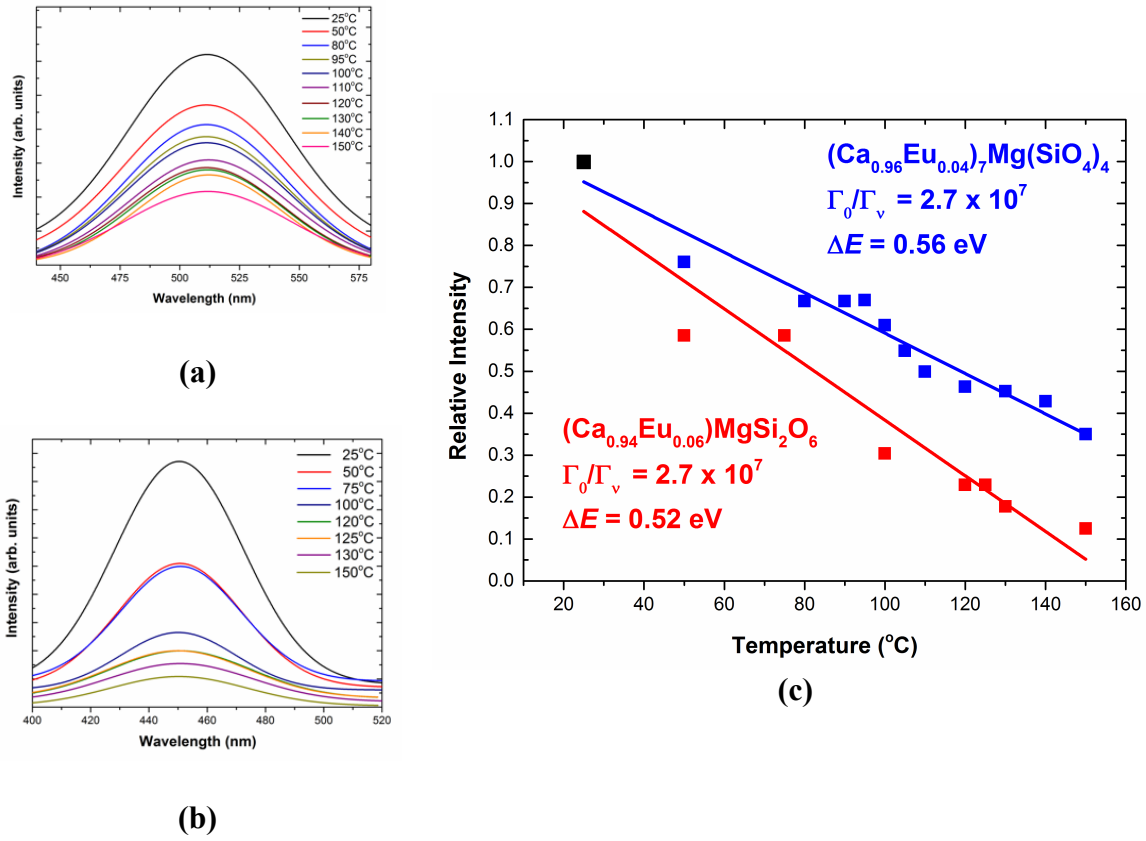

Figure 2.9 The emission intensity (I) of the photoluminescence spectra as a function of temperature for **(a)** $(Ca_{0.96}Eu_{0.04})_7Mg(SiO_4)_4$, **(b)** $Ca_{0.94}Eu_{0.06}Mg(SiO_3)_2$. **(c)** Plot of the relative intensity as a function of temperature from the data in (a) and (b). ΔE = activation energy and Γ_0 is the attempt rate for thermal quenching at T = ∞, and Γ_υ is the radiative decay rate of the 5d state of Eu^{2+}.

Other models of thermal quenching exist. For instance, the thermal ionization model [100] suggests that thermal quenching stability is related to the energy gap between the excited Eu 5d level and CBM. However, first principles determination of excited states is challenging, though a few recent works have explored this relationship using advanced techniques [121]. For high-

throughput screening, a more efficient approximation needs to be developed. For example, the band gap can sometimes be used as a proxy [86, 122]; the larger the band gap of the host, the more likely that there is a larger gap between the excited 5d level and the CBM (though the exact relationship depends on the magnitude of the Stokes shift). The investigation of these other first principles descriptors will be the subject of future work.

2.5 Conclusions

An integrated approach of exploring new phosphors for near-UV (nUV) excitation by combining experiments and calculations is outlined. The descriptors of Debye temperature (Θ) and excitation energy were combined to screen plausible phosphors that are predicted to have high quantum efficiency (Φ) and can be employed in near-UV emitting LEDs. From the calculation of 27 host materials, $Ca_7Mg(SiO_4)_4$ and $CaMg(SiO_3)_2$ were selected because predicted Θ for $Ca_7Mg(SiO_4)_4$ and $CaMg(SiO_3)_2$ were found to be 601 K and 665 K, respectively, which are expected to have high Φ (> 80%). The predicted and experimental excitation energies are similar. The measured values of Φ are lower than the expected values, based on high Θ. The main peak in the photoluminescence emission spectra under excitation of 350 nm is 511 nm for $(Ca_{0.96}Eu_{0.04})_7Mg(SiO_4)_4$, with chromaticity coordinates of (0.25, 0.49), and 458 nm for $Ca_{0.94}Eu_{0.06}Mg(SiO_3)_2$ with chromaticity coordinates of (0.14, 0.05). The concentration self-quenching mechanism for $CaMg(SiO_3)_2:Eu^{2+}$ under 350 nm is the *d-q* interaction. The thermal quenching temperatures ($T_{0.5}$) are 381 K and 354 K for $(Ca_{0.96}Eu_{0.04})_7Mg(SiO_4)_4$ and $Ca_{0.94}Eu_{0.06}Mg(SiO_3)_2$, respectively, indicating poor thermal stability. Despite having a high Θ, a low Φ is found for the two candidates. Conversely, other screened hosts (e.g. $Ba_2SiO_4:Eu^{2+}$) have low computed Θ, but are known to have a high Φ. Therefore, the use of high Θ as an indicator for high quantum efficiency should be treated with caution when screening host candidates. It is

desirable to develop more well-defined criteria for the screening of host candidates for high Φ phosphors. The approach developed in this work can be leveraged for the discovery of additional nUV excited phosphors.

Chapter 2, in full, is a reprinted of the materials as it appears in "An integrated first principles and experimental investigation of the relationship between structural rigidity and quantum efficiency in phosphors for solid state lighting" Journal of Luminescence, vol 179, pp 297-305, 2016. This work was coauthored by Z. Wang, E. Novitskaya, G. A. Hirata, O. A. Graeve. J. McKittrick and S. P. Ong are the corresponding authors. The dissertation author is the first author of this work.

CHAPTER 3: A FACILE METHOD USING A FLUX TO IMPROVE QUANTUM EFFICIENCY OF SUBMICRON PARTICLE SIZED PHOSPHORS FOR SOLID-STATE LIGHTING APPLICATIONS

3.1 Abstract

This work successfully verified that an addition of a flux (NH_4F, NH_4Cl, and H_3BO_3) during synthesis has an impact on the crystallite size and quantum efficiency of submicron-sized particles of $CaMgSi_2O_6:Eu^{2+}$ phosphors. The addition of NH_4F or NH_4Cl increased the crystallite size in the submicron-sized particles, yielding an increase in emission intensity and quantum efficiency. On the other hand, the use of the H_3BO_3 flux crystallized a secondary phase, SiO_2, and changed the lattice parameters, which degraded the luminescent properties. In addition, an excessive amount of NH_4Cl was examined and it resulted in nucleation of a secondary phase, $CaSiO_3$, which changed the lattice parameters with no improvement in luminescent properties. These results demonstrate that the addition of a flux can be a method to improve the quantum efficiency of submicron sized particles composed of nanocrystallites, however a judicious choice of the flux composition and amount has to be carefully considered

3.2 Introduction

Powder phosphors produced by the conventional solid-state reaction method have been widely researched for application in near UV-emitting LEDs (nUV-LEDs) [20, 123]. This method produces micron-sized powders that have higher quantum efficiencies than smaller sized powders [69, 70], whereas chemical synthesis methods produce sub-micron sized powders composed of nanocrystallites. Particle size and crystallite size should be differentiated to understand quantum efficiency of phosphors. A powder particle can be a single crystal or consist of crystallites, the crystallite size is typically measured by X-ray diffraction or transmission electron microscopy,

whereas the particle size is typically measured by dynamic light scattering or scanning electron microscopy. In the remote phosphor configuration, the phosphor particles are on a substrate that is suspended above a nUV-LEDs, as opposed to the conventional configuration where the phosphors are embedded in a polymer around a blue-emitting LED. In the remote configuration, the packing density of the large particles is low, which generates substantial light scattering [76]. To overcome this issue, phosphors with a small, narrow particle size distribution are required. If the particle radii are < ~400 nm, these particles will negligibly scatter visible and near UV radiation, because particle size is smaller than the wavelength the radiation. However, phosphor particles in the submicron-size regime with nano-sized crystallites have poor quantum efficiency compared to micrometer-sized, single crystal phosphor particles [123, 124].

One method that is used to improve the crystallinity and quantum efficiency of micrometer-sized particles is to use a flux [125-127]. A flux material is an inert high-temperature solvent used to accelerate crystallite growth. Generally, 0.5 wt.% ~ 10 wt.% of a flux is used [126, 128], forming a thin layer of molten material around crystals during the annealing process and facilitating a high diffusivity path through the flux [128]. Crystals grow in the molten salt solvents, thus normally called flux growth. The process is a well-known method for crystal growth in materials [20, 129, 130]. A flux is typically used in preparing phosphor powders through a solid-state reaction method, producing regular-shaped particles and enlarged crystallites, which cause the emission intensity to be enhanced [125-127, 131-135]. However, this process is rarely researched for nanocrystalline, submicrometer-sized phosphors prepared by wet chemical processes [136-139]. Table 3.1 shows the effect of various flux compositions on phosphor properties for application in nUV-LED lighting [125-127, 131-139]. In each case, the phosphor properties (e.g., quantum efficiency, particle size and surface smoothness) were enhanced with the addition of a flux. In fact, after

adding a flux, aluminates and oxides showed enlarged particles and smooth particle surfaces [125, 126, 133, 136], silicates and oxy-nitrides have larger crystallite sizes and regular particle morphology [132, 134, 137, 138]. Most importantly, these phosphors all have enhanced emission intensity or quantum efficiencies with the addition of a flux.

A flux is typically mixed with reactants [125, 126, 132-134, 137] or as-synthesized product [138] before an annealing step; thus, is present as the molten phase during the post-synthesis annealing process. Since the flux material should be evaporated after annealing to avoid formation of impurities or second phases in the final product, the melting and boiling temperature should be considered in relationship to the annealing conditions (temperature, atmosphere), when selecting a flux material. The criteria for selecting a flux are: (1) a low melting temperature, so that it is a liquid during the annealing process [127]; (2) a boiling temperature lower than the annealing temperature, so that the flux can be evaporated to avoid impurity or a second phase formation [131]. Fluxes having higher boiling temperature than the annealing temperature had been used in most of the previous literature (Table 3.1); and (3) the difference in ionic radii of the flux and the phosphor elements must be more than 30% to avoid doping of the flux elements in the phosphors [140]. Chiang *et al*. [125] reported a formation of a second phase of $BaAl_2O_4$ in $Y_{2.95}Ce_{0.05}Al_5O_{12}$ with a BaF flux. This suggests that some fluxes can remain after the reaction, producing by-products.

Table 3.1 Reported results of the addition of flux on phosphor preparation. T_m = melting temperature, T_b = boiling temperature, Φ = quantum efficiency.

Flux / T_m / T_b (˚C)	**Phosphor composition**	**Synthesis method**	**Annealing temperature (˚C)**	**Results**	**Ref.**
CaF_2 / 1418 /2533	$(Ca_{0.99}Ce_{0.01})_3Sc_2Si_3O_{12}$	Solid state reaction	1100-1450	Reduced impurities, decreased formation temperature, no reported crystallite size and Φ, emission intensity increased 2X, narrow particles distribution, removed flux by sublimation after reaction	[131]
BaF_2 / 1368 / 2260	$Y_{2.965}Ce_{0.035}Al_5O_{12}$	Spray pyrolysis	1300-1600	Enlarged, regular morphology, and non-aggregated particles, no reported crystallite size and Φ, emission intensity increased 1.4X	[136]
	$Y_{2.95}Ce_{0.05}Al_5O_{12}$	Solid state reaction	1000-1500	Able to reduce annealing temperature $BaAl_2O_4$, byproduct from BaF_2 Spherical shape and smooth surface Φ (external) increased 1.3X over commercial sample	[125]
	$Ba_{0.85}Eu_{0.15}Si_3Al_3O_4N_5$	Solid state reaction	1550	Enlarged crystallite size (no specific number) and particles size, narrow particles distribution, emission intensity increased slightly, no reported Φ	[132]
	$Ca_{0.99}Ce_{0.01}Sc_2O_4$	Solid state reaction	1550 and 1450	Φ (external) increased 1.1X, no reported crystallite size, enlarged and regular particles	[126]
LiF/ 845 / 1673	$Ba_{0.9}Eu_{0.1}Mg_{0.98}Mn_{0.02}Al_{10}O_{17}$	Molten salt synthesis	1100-1400	Particles size enlarged, Li^+ into the host lattice analyzed by lattice parameter, no report crystallite size from XRD, no reported Φ, emission intensity increased 2X	[133]

Table 3.1 Reported results of the addition of flux on phosphor preparation. T_m = melting temperature, T_b = boiling temperature, Φ = quantum efficiency (continued).

Flux / T_m / T_b (˚C)	**Phosphor composition**	**Synthesis method**	**Annealing temperature (˚C)**	**Results**	**Ref.**
NaF / 993 / 1695	$Lu_{2.925}Ce_{0.075}Al_{4.79}Si_{0.21}O_{11.79}N_{0.21}$	Solid state reaction	1500	Emission intensity increased 1.3X, regular morphology of particles, no report crystallite size and Φ	[134]
NaF / 993 /1695 LiF / 845/ 1675 H_3BO_3 / 171 / 300 NH_4F / 100 / decomposes	$Y_{1.55}Eu_{0.45}Ti_2O_7$	Solid state reaction	1350	Crystallite size enlarged (no specific number), emission intensity increased 11X (NaF), 9X (LiF), 5X (H_3BO_3), 2.5X (NH_4F), 39% of Φ (NaF), no reported Φ without flux, enlarged particles size	[127]
NH_4Cl / 338 / decomposes	$Ba_{1.488}Sr_{0.5}Eu_{0.012}SiO_4$	Spray pyrolysis	900-1400	Enlarged particles, enlarged crystallite size (no specific number), no reported Φ, emission intensity increased 1.3X, optimum annealing temperature decreased	[137]
K_2CO_3 / 891 / decomposes	$Ca_{0.68}Eu_{0.12}Mg_{0.2}SiO_3$	Co-precipitation	1200	Charge compensation, crystallite size increased 1.1X, Φ increased 2.5X, no phase composition change, no reported particles size	[138]
Li_2CO_3 / 734 / 1310	$(Sr_{0.92}Eu_{0.08})_8Al_{12}O_{24}S_2$	Solid state reaction	900	Improved purity, but still impurities remained. No report crystallite size and Φ	[135]
$SrCl_2$ / 874 / 1250	$Sr_{1.56}Eu_{0.04}Ba_{0.4}SiO_4$	Combustion	800-950	Crystallite size increased (no specific number), emission intensity increased 2.7X, no reported Φ, similar particles size	[139]

Dai *et al.* [127] discussed the effect of various fluxes (NH_4Cl, NH_4F, H_3BO_3, LiF, and NaF) on the emission intensity of $Y_{1.55}Eu(III)_{0.45}Ti_2O_7$ phosphors with an orange-red emission under near UV light for display devices such as high-resolution and field emission displays, as well as high-power white light-emitting diodes. It was found that uniform micrometer-sized (~4 μm) particles formed with NaF and LiF fluxes, and the maximum emission intensity was achieved with NaF flux, while a narrow size distribution of the particles was not achieved with NH_4Cl, NH_4F, or H_3BO_3 fluxes. Additionally, Zhang *et al.* [126] examined the influence of different concentrations of BaF_2 flux on the formation of $Ca_{0.99}Ce_{0.01}Sc_2O_4$ with green emission prepared by a solid state reaction. After introducing BaF_2, a higher particle growth rate, larger particle sizes, and more narrow particle size distribution were verified, which resulted in improved emission intensity. The emission intensity increased with the increase of the concentration of BaF_2 and the maximum emission intensity corresponded to 0.5 wt.% of BaF_2. The emission intensity decreased when the concentration of BaF_2 was higher than 0.5 wt.%, which was attributed to particle agglomeration. Wang *et al.* [138] examined the effect of Li_2CO_3 and K_2CO_3 fluxes on the formation of $Ca_{0.68}Mg_{0.2}Eu_{0.12}SiO_3$ prepared by a co-precipitation method. The crystallite size increased from ~93 nm to 99 nm (6% of Li_2CO_3) or to 100 nm (5% of K_2CO_3), and the quantum efficiencies were improved (from 12% to 27% with Li_2CO_3 flux and to 31% with K_2CO_3 flux).

In this work, blue-emitting $Ca_{0.94}Eu_{0.06}MgSi_2O_6$ powders were synthesized through a co-precipitation method [75, 101]. The powders were annealed with three different fluxes (NH_4F, NH_4Cl, or H_3BO_3). In our previous report [75], the $Ca_{0.94}Eu_{0.06}MgSi_2O_6$ powders formed submicrometer-sized particles having blue color with $x = 0.14$ and $y = 0.05$ on the CIE diagram, similar to those defined by the National Television System Committee color (0.14, 0.08), but the quantum efficiency was found to be low (Φ, ~ 5%). A low Φ is a drawback of nanocrystalline-

sized phosphors, therefore the main goal of this study was to improve the Φ using several different types of flux materials. NH_4F, NH_4Cl, and H_3BO_3 were selected as flux materials from the reported flux candidates [125-127, 131-138] due to their low melting and boiling temperatures (Table 3.2) as well as differences of >30% in ionic radii between ions of the flux components and the phosphor components.

Table 3.2 Melting and boiling temperature of the fluxes.

Flux	Melting point (°C)	Boiling point (°C)
NH_4F	100	Decomposition*
NH_4Cl	338	Decomposition**
H_3BO_3	171	300***

*NH_4F (s)→ NH_3 (g)+ HF(g) > 100°C
**NH_4Cl (s)→ NH_3 (g)+ HCl (g) > 338°C
***H_3BO_3 (s) → B_2O_3 (s)+ H_2O > 235°C

3.3 EXPERIMENTAL PROCEDURE

3.3.1 Reagents

All chemicals were used without further purification and included tetraethyl orthosilicate (TEOS, 99.9%, Sigma Aldrich), $Mg(NO_3)_2$•$6H_2O$ (98.3%, Fisher Scientific), $Ca(NO_3)_2$•$4H_2O$ (99.0%, Macron Fine Chemicals), Eu_2O_3 (99.99%, Alfa Aesar), nitric acid (69.3%, Fisher Scientific), citric acid ($C_6H_8O_7$•H_2O, ACS reagent grade, Macron Fine Chemicals), ethylene glycol (C_2H_6OH, certified, Fisher Scientific), polyethylene glycol (PEG, C_2H_4O•nH_2O, molecular weight = 20,000 g/mol, Sigma Aldrich), ammonium hydroxide (28~30%, BDH Aristar Plus), NH_4F (96%, Alfa Aesar), NH_4Cl (ACS reagent grade, Macron Fine Chemicals), and H_3BO_3 (99.5%, Sigma Aldrich).

3.3.2 *Preparation of $Ca_{0.94}Eu_{0.06}MgSi_2O_6$ with and without a flux*

The co-precipitation method was used to synthesize the powders by following previously reported procedures [75, 101]. The concentration of 6 at.% Eu^{2+} activator was chosen as it is

reported to have the highest photoluminescence (PL) emission intensity [75]. Tetraethyl orthosilicate (2.23 mL) was added to ethanol (20 mL) with several drops of nitric acid and deionized water while stirring for 30 minutes. Meanwhile, Eu_2O_3 (0.0015 mol) was dissolved in nitric acid (0.4 mL) solution to form aqueous $Eu(NO_3)_3$ solution. $Mg(NO_3)_2 \cdot 6H_2O$ (0.005 mol) and $Ca(NO_3)_2 \cdot 4H_2O$ (0.0047 mol) were dissolved in deionized water with stirring. After the two nitrate solutions became transparent, all three solutions (tetraethyl orthosilicate, $Eu(NO_3)_2$, and $Mg(NO_3)_2$ with $Ca(NO_3)_2$) were mixed together and then stirred for 1 hr. Subsequently, ammonium hydroxide was added dropwise into the solution to reach a pH of 10 and initiate precipitation. White precipitates were formed, and the suspension was stirred for 8 hours. Next, NH_4F, NH_4Cl, or H_3BO_3 was added to the solution at amounts of 2 wt.%, 6 wt.%, or 10 wt.% of $Ca_{0.94}Eu_{0.06}MgSi_2O_6$. The conversion of wt.% to mol.% for each flux is shown in Table 3.3. The solutions were then centrifuged and dried at 80°C for 12 hours. Finally, a post-synthesis annealing step was performed at 1100°C for 2 hours in air and then at 1100°C for 4 hours in a 5% H_2/95% N_2 atmosphere to transform Eu^{3+} to Eu^{2+}.

Table 3.3 Conversion of wt.% to mol.% for each flux in the solid phosphor powders.

Wt.% flux	**NH_4F (mol.%)**	**NH_4Cl (mol.%)**	**H_3BO_3 (mol.%)**
2	12	8	7
6	28	22	19
10	40	31	28

3.3.3 **Characterization**

The powders were analyzed by X-ray diffraction (XRD) on a D2 Phaser (Bruker, Karlsruhe, Germany) using CuKα radiation and a step size of 0.014° over a 2θ range of 20 to 80°. The crystallite sizes, lattice parameters, and ratio of the phases presented were calculated by Rietveld refinement using the TOPAS 4.2 software (Bruker). The sizes of the powders were

examined by dynamic light scattering (DLS) on a Nanotrac Wave II system (Microtrac Inc., York, PA, USA) [141-143]. Particles were distributed in an aqueous solution by sonication in a water bath for DLS experiments. A field emission scanning electron microscope (FESEM, XL30, Philips, Amsterdam, Netherlands) at 10 keV was used to image the powders to confirm sizes and determine morphology. Samples were coated with iridium at 85 μA for 10 s before imaging. Energy dispersive spectroscopic analysis (EDS) was performed with a scanning electron microscope (Apreo SEM, FEI, Hillsboro, OR, USA) to analyze the concentration of elements. Absolute quantum efficiency (Φ) measurements were performed using an integrating sphere system, with sodium salicylate (Φ = 44%) as a reference standard. PL emission and excitation spectra were acquired with a fluorescence spectrophotometer (Hitachi F-7000, Tokyo, Japan) using λ= 350 nm excitation wavelength (pulse = 0.025 sec). This excitation wavelength was selected as it produced the highest PL emission intensity for $Ca_{0.94}Eu_{0.06}MgSi_2O_6$ [75].

3.4 Results And Discussion

3.4.1 Crystal structure and lattice parameters

Figure 3.1 shows the crystal structure of $CaMgSi_2O_6$. Also known as diopside, it has a monoclinic crystal structure with space group C2/c. The lattice constants are a = 0.9743 nm, b = 0.8879 nm, c = 0.5230 nm, and β = 105.53° [75]. The coordination numbers for Ca^{2+}, Mg^{2+}, and Si^{4+} of 8, 6, and 4, respectively. The ionic radii of the ions are listed in Table 3.4. The radii differences between ions in $CaMgSi_2O_6$ and the flux are Mg^{2+}-B^{3+} = 90%, Si^{4+}-B^{3+} = 81%, O^{2-}-F^- = 5% (4-coordinated, 6-coordinated), O^{2-}-Cl^- = 26% (6- coordinated). The F^- from NH_4F and Cl^- from NH_4Cl are likely to be composed to HF (g) and HCl (g) during the annealing process (Table 3.2) although the radii difference is less than 30% between O^{2-} and F^- /or Cl^-. H^+ may occupy interstitial sites in the lattice because of its small size.

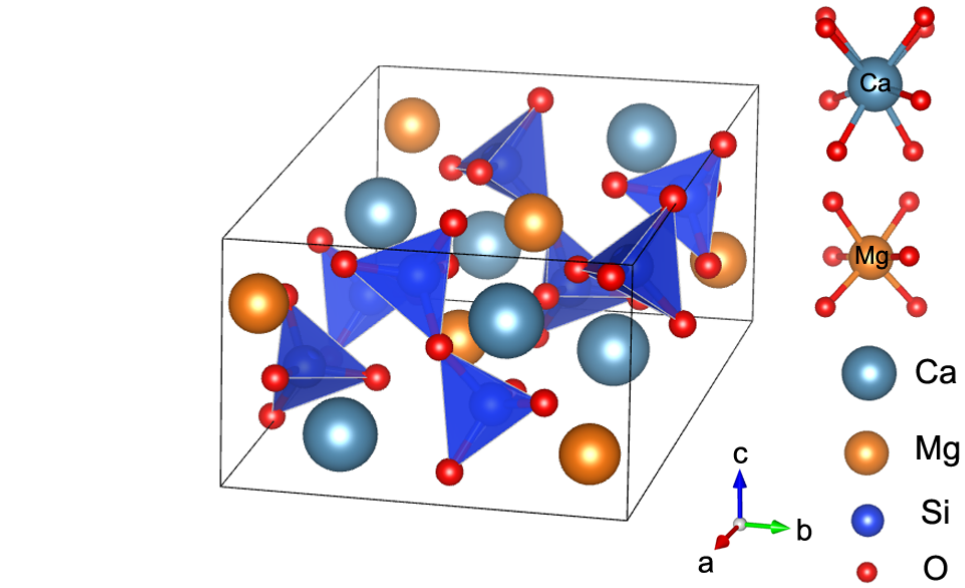

(a)

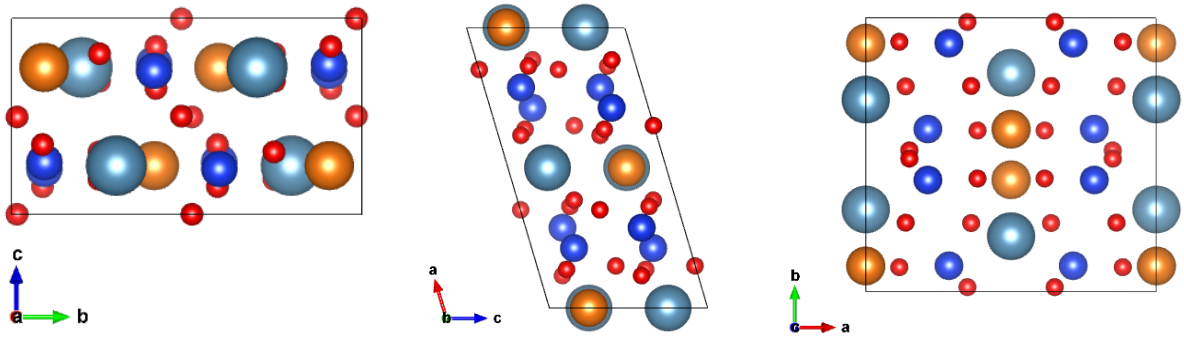

(b) (c) (d)

Figure 3.1 The crystal structure of $CaMgSi_2O_6$: **(a)** 3-D unit cell representation, **(b)** along the [100], **(c)** along the [010], and **(d)** along the [001] drawn by VESTA (Visualization for Electronic and Structural Analysis) [144].

Table 3.4 The ionic radii (nm) of ions of in $CaMgSi_2O_6$ and fluxes, NH_4F, NH_4Cl, H_3BO_3.

Ions	4-coordinated	6-coordinated	8-coordinated
Ca^{2+}	-	-	0.112
Mg^{2+}	-	0.072	-
Si^{4+}	0.026	-	-
O^{2-}	0.138	0.140	0.142
B^{3+}	0.011	0.027	-
F^{-}	0.131	0.133	-
Cl^{-}	-	0.181	-

XRD patterns of $Ca_{0.94}Eu_{0.06}MgSi_2O_6$ with and without NH_4F and NH_4Cl fluxes are shown in the Figure 3.2. The peak widths narrowed with an increase in the concentration of NH_4F (Figure 3.2a), indicating an increase in crystallite size. Several small peaks from $CaEu_4(SiO_4)_3O$ were recorded for 10 wt.% NH_4F. $CaEu_4(SiO_4)_3O$ was previously identified in $Ca_{0.94}Eu_{0.06}MgSi_2O_6$ under annealing temperature of 1247°C [145], which is a higher temperature than used in the present study, with no flux. As shown previously, a flux can decrease the temperature for the crystallization of phosphor materials [125, 131], so that excessive NH_4F may lead to the formation of $CaEu_4(SiO_4)_3O$ at the lower temperature by reducing the corresponding formation temperature. For the diffraction patterns from the powders prepared using NH_4Cl flux, shown in Figure 3.2b, the peak width also slightly narrowed with the increase of concentration of NH_4Cl. However, this narrowing is less pronounced in comparison with the NH_4F, indicating that the crystallite sizes with NH_4F flux were larger. The crystallite sizes for different concentrations of NH_4F and NH_4Cl fluxes are shown in Figure 3.2c. For the NH_4F flux, the crystallite size increased from roughly 13 nm with no flux to about 31 nm with 10 wt.% NH_4F. The maximum crystallite size for NH_4Cl flux

was about 19 nm with 2 wt.% NH_4Cl. Different diffusion rates of the reactants through a flux may explain why the material produced with NH_4F flux shows enlarged crystallite sizes compared to that made with NH_4Cl flux. Ions move through liquid flux during the annealing process with a diffusion coefficient expressed by $D = (1/f)\cdot kT$, where f is the frictional coefficient, k is the Boltzmann's constant, and T is the absolute temperature. The frictional coefficient can be expressed by $f = \pi\mu r$, where μ is viscosity and r is the radius of the ion. Therefore, a relationship $D \propto 1/r$ is found. F^- (0.119 nm) is smaller than Cl^- (0.167 nm), therefore NH_4F may act as a more effective flux compared to NH_4Cl from the point of view of enhanced diffusivity, assuming equivalent viscosities.

With the H_3BO_3 flux, SiO_2 impurities were detected, as shown in the XRD patterns in Figure 3.3a. Even though B^{3+} and Si^{4+} have quite different ionic radii (0.026 nm and 0.011 nm) [103], a substitution of B^{3+}on Si^{4+} sites on the tetrahedral site has been previously reported [146, 147] although there is a charge difference between B^{3+} and Si^{4+}. Marler et al. [146] reported synthetic tourmaline (olenite) to replace partial silicon ions with excessive boron ions; and the difference in charge between Si^{4+} and B^{3+} was compensated by protons leading to the unusually high water content. Xia et al. [147] studied $La_5(Si_{2-x}B_{1-x})(O_{13-x}N_x):Ce^{3+}$ by replacing partially B^{3+}-O^{2-} by the Si^{4+}-N^{3-}; and the charge difference from the replacement of B^{3+} by Si^{4+} was compensated by the substitution of O^{2-} by N^{3-}. In the current study, the charge difference from the partial replacement of Si^{4+} by B^{3+} could be compensated to produce oxygen vacancies due to no other ion replacements.

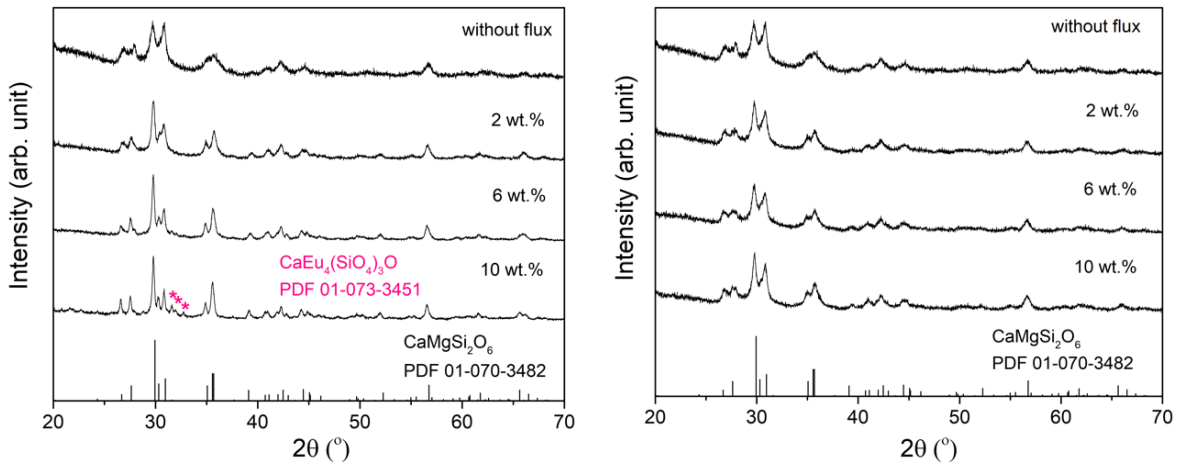

(a) **(b)**

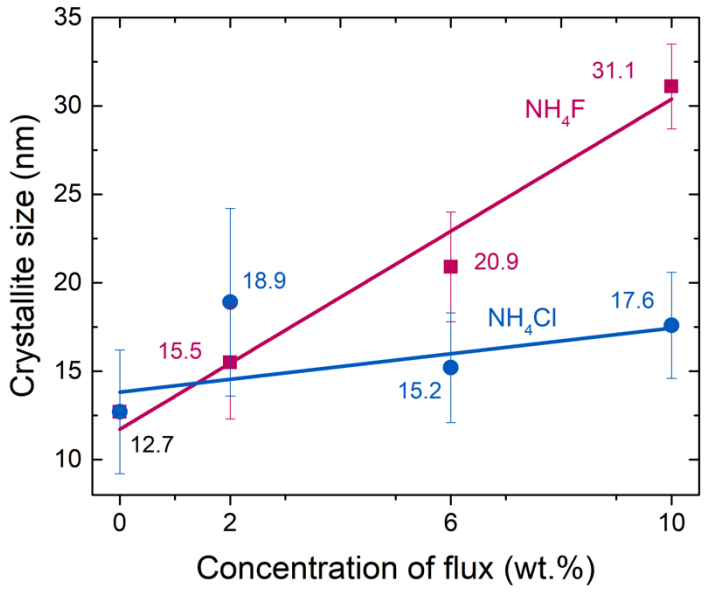

(c)

Figure 3.2 X-ray diffraction patterns of $Ca_{0.94}Eu_{0.06}MgSi_2O_6$ with a flux of **(a)** NH_4F and **(b)** NH_4Cl. **(c)** Calculated crystallite sizes of $Ca_{0.94}Eu_{0.06}MgSi_2O_6$ with NH_4F and NH_4Cl fluxes.

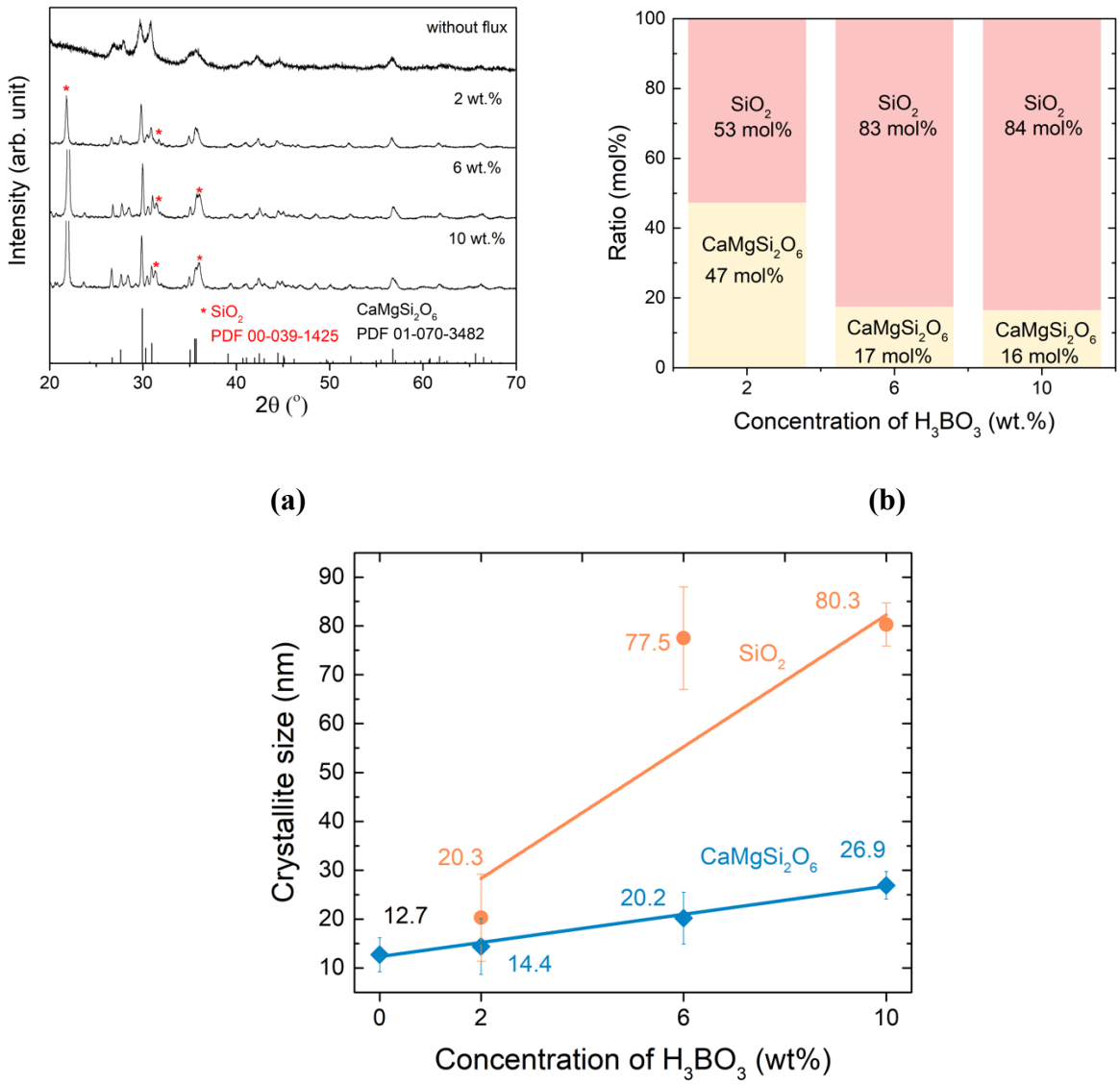

Figure 3.3 **(a)** X-ray diffraction patterns of $Ca_{0.94}Eu_{0.06}MgSi_2O_6$ with H_3BO_3 flux. **(b)** Calculated molar ratios of the phases present and **(c)** calculated crystallite sizes.

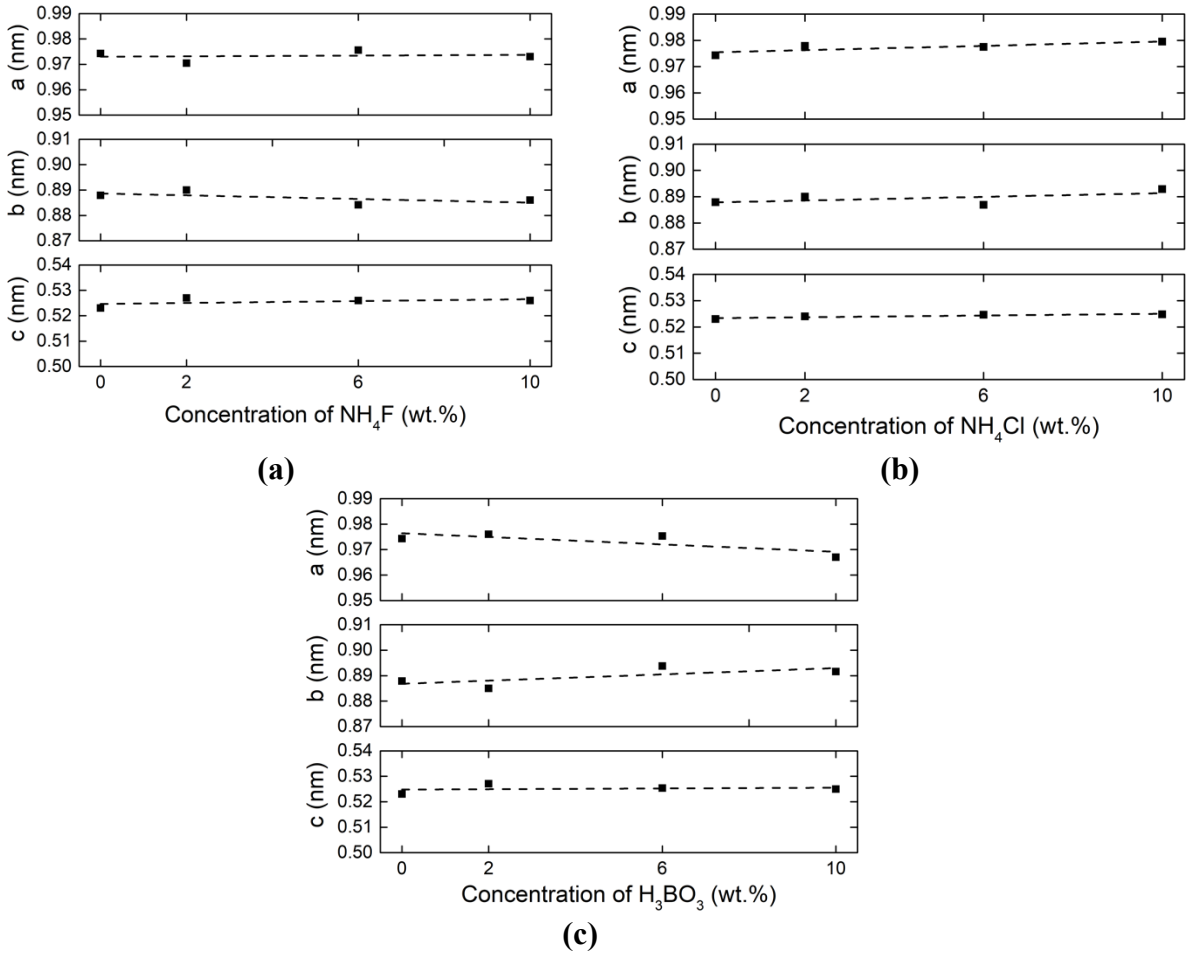

Figure 3.4 Calculated lattice parameters of $Ca_{0.94}Eu_{0.06}MgSi_2O_6$ from the X-ray diffraction results with a flux of **(a)** NH_4F, **(b)** NH_4Cl, and **(c)** H_3BO_3.

With an assumption that B ions partially replace the Si ions, the corresponding chemical reaction is:

$$CaMgSi_2O_6 + xH_3BO_3 \rightarrow CaMg(Si_{1-x/2}B_{x/2})_2O_6 + xSiO_2 + xH_2O + x/2H_2.$$

As the amount of H_3BO_3 increased (2-10 wt.%), the corresponding amount of SiO_2 increased (53-84 mol.%, Figure 3.3b). The crystallite size of the phosphor increased from ~13 nm to ~27 nm, while for SiO_2 it increased from 20 nm to 80 nm (Figure 3.3c).

The calculated lattice parameters of $Ca_{0.94}Eu_{0.06}MgSi_2O_6$ with and without each flux are shown in Figure 3.4. The lattice parameters of powders prepared with NH_4F and NH_4Cl (Figure

3.4a,b) were identical to the phosphors prepared without flux, indicating that these two fluxes did not affect the crystal structure of the resultant materials. In contrast, with H_3BO_3 flux, the *b* and *c* parameters did not show significant change, while *a* decreased from 0.9743 nm to 0.9670 nm. This is presumably due to the substitution of B^{3+} (0.011 nm) on Si^{4+} (0.036 nm) sites, causing the lattice parameter to decrease. Vegard's law [148], which is an empirical rule based on a linear relationship found between lattice parameters and the size of the constituent elements. The formation of ½O vacancies from the charge difference between Si^{4+} and B^{3+} can affect the lattice parameters. Therefore, the relationship between the initial lattice parameter and the one with B^{3+} is $a = a_0 - x(r_{Si} - r_B) - \frac{1}{2}xr_O$, where *a* is the lattice parameter (0.9670 nm) with 10 wt.% B^{3+} addition, a_o is the initial lattice parameter (0.9743 nm), x is the partial substitution of B on Si, r_{Si}, r_B, r_O are the radii of Si^{4+}, B^{3+}, and O^{2-}, respectively. The x value obtained is 0.09, which is smaller than the molar fraction of H_3BO_3 added (0.28 converted from 10 wt.% H_3BO_3). The excess B^{3+} was not be detected in the XRD patterns (detection limit of 3 ~ 5 wt.%). Therefore, due to the low boiling temperatures, it likely does not remain in the resultant powder. The change of lattice parameter *a,* while parameters *b* and *c* remain unchanged, can be explained by the ion arrangement. Along the [100] and [001] directions (see Figure 3.1b and 3.1d), there are two Si^{4+} along the *a*-axis, four along the *b*-axis, and three along *c*-axis. The fractions of one Si^{4+} along the *a*-, *b*-, and *c*-axes are 0.50, 0.25, and 0.33, respectively. The fraction of Si^{4+} along the *a*-axis is the largest, so that the replacement of Si^{4+} is affected more along this axis, resulting in a decrease of *a* with an addition of 10 wt.% H_3BO_3. Another possible reason for a change in lattice parameter of $Ca_{0.94}Eu_{0.06}MgSi_2O_6$ is H^+ dissolved in interstitial sites, but this would cause an increase of lattice parameters, which was not observed.

3.4.2 Scanning electron microscopy and dynamic lighting scattering analysis

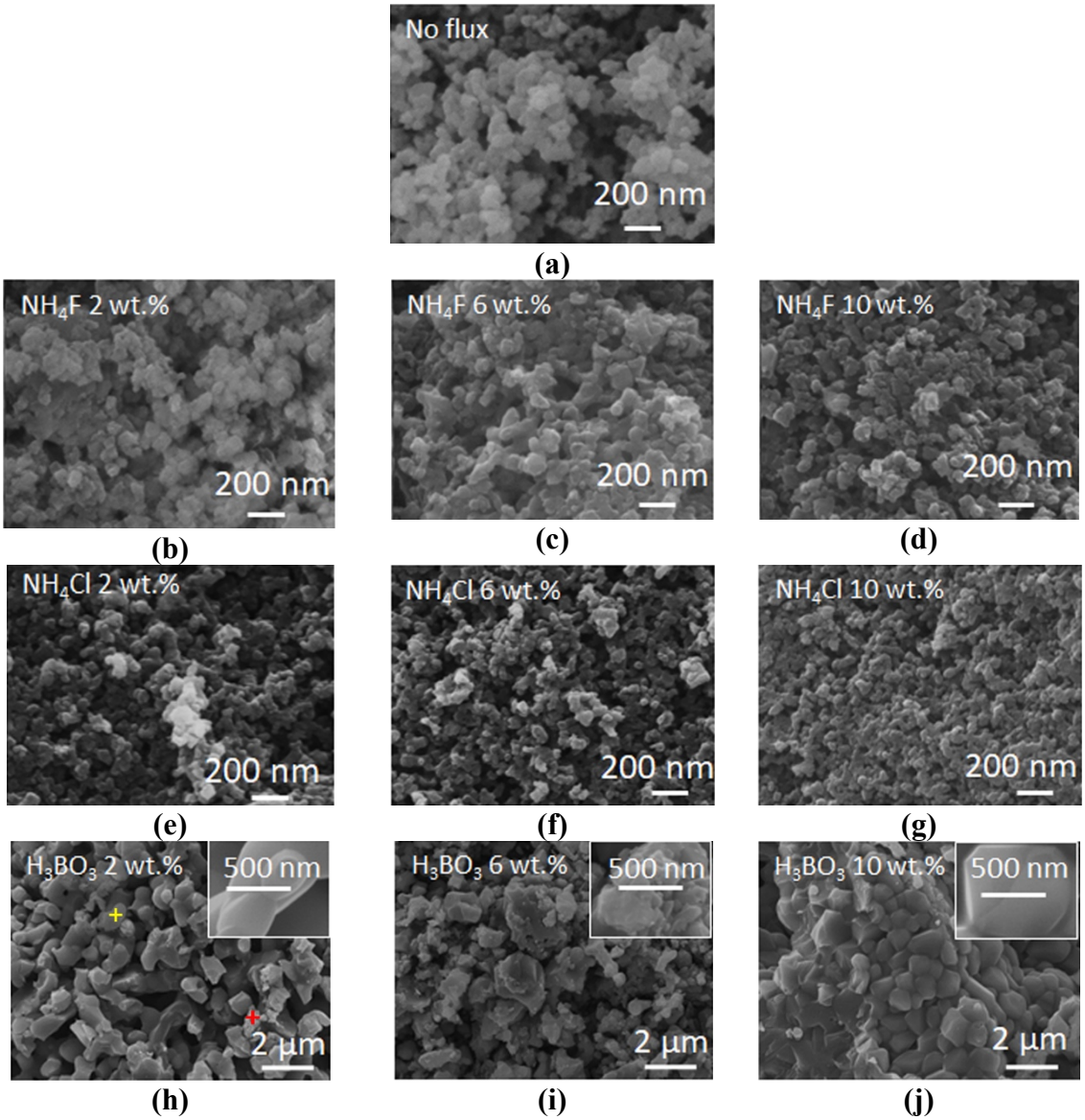

Figure 3.5 Scanning electron microscopy images of $Ca_{0.94}Eu_{0.06}MgSi_2O_6$. Without any flux **(a)** taken from [75].With NH_4F flux **(b)** 2 wt.%, **(c)** 6 wt.%, and **(d)** 10 wt.%. With NH_4Cl flux: **(e)** 2 wt.%, **(f)** 6 wt.%, and **(g)** 10 wt.%. With H_3BO_3 flux: **(h)** 2 wt.%, **(i)** 6 wt.%, **(j)** 10 wt.%.

SEM images of $Ca_{0.94}Eu_{0.06}MgSi_2O_6$ are shown in Figure 3.5a for no flux, Figure 3.5b-d for NH_4F flux addition, Figure 3.5e-g for NH_4Cl flux addition, and Figure 3.5h-j for H_3BO_3 flux addition. For NH_4F or NH_4Cl fluxes, the particle sizes and morphologies were similar to those without a flux. However, the particles with the H_3BO_3 flux were aggregated, and the particle sizes were irregular. From EDS analysis, the ratio of Ca:Mg:Si:O was 1:1:7:13 in the large particles (yellow

point in Figure 3.5h), where the amounts of Si and O are two to three times more than those of $CaMgSi_2O_6$ (Ca:Mg:Si:O = 1:1:2:6). In the small particles (red point in Figure 3.5h), the ratio of Ca:Mg:Si:O was 1:1:3:5 , which is closer to that of $CaMgSi_2O_6$. Although the results from EDS are considered more accurate for polished surfaces than the powders, the ratio of Ca, Mg, Si, O demonstrated differences between small and large particles. Also, given that the EDS analysis penetrates 1-2 μm below the surface [149], $CaMgSi_2O_6$ could be detected under the SiO_2 particles, which could be the reason why EDS analysis showed a small amount of Ca and Mg, when presumably large SiO_2 particles were analyzed. Therefore, large particles can be considered as SiO_2 and the aggregated, small particles as $CaMgSi_2O_6$.

From the DLS analysis (Figure 3.6) the average particle sizes were 83 nm for powders without flux. With the NH_4F flux, the average particles sizes were 80 nm (2 wt.%), 100 nm (6 wt.%), and 133 nm (10 wt.%), respectively For the NH_4Cl flux, the corresponding particle sizes were found to be 84 nm (2 wt.%), 82 nm (6 wt.%), and 118 nm (10 wt.%). Overall, this indicates that particles were still submicron sized with the addition of flux. However, some studies reported uniformly shaped and enlarged particles with up to 14 wt.% of flux addition [126, 132, 133, 137]. For the H_3BO_3 flux, the average particle sizes were 307 nm (2 wt.%), 318 nm (6 wt.%), and 375 nm (10 wt.%), which resulted from an increase in the amount of the SiO_2 particles.

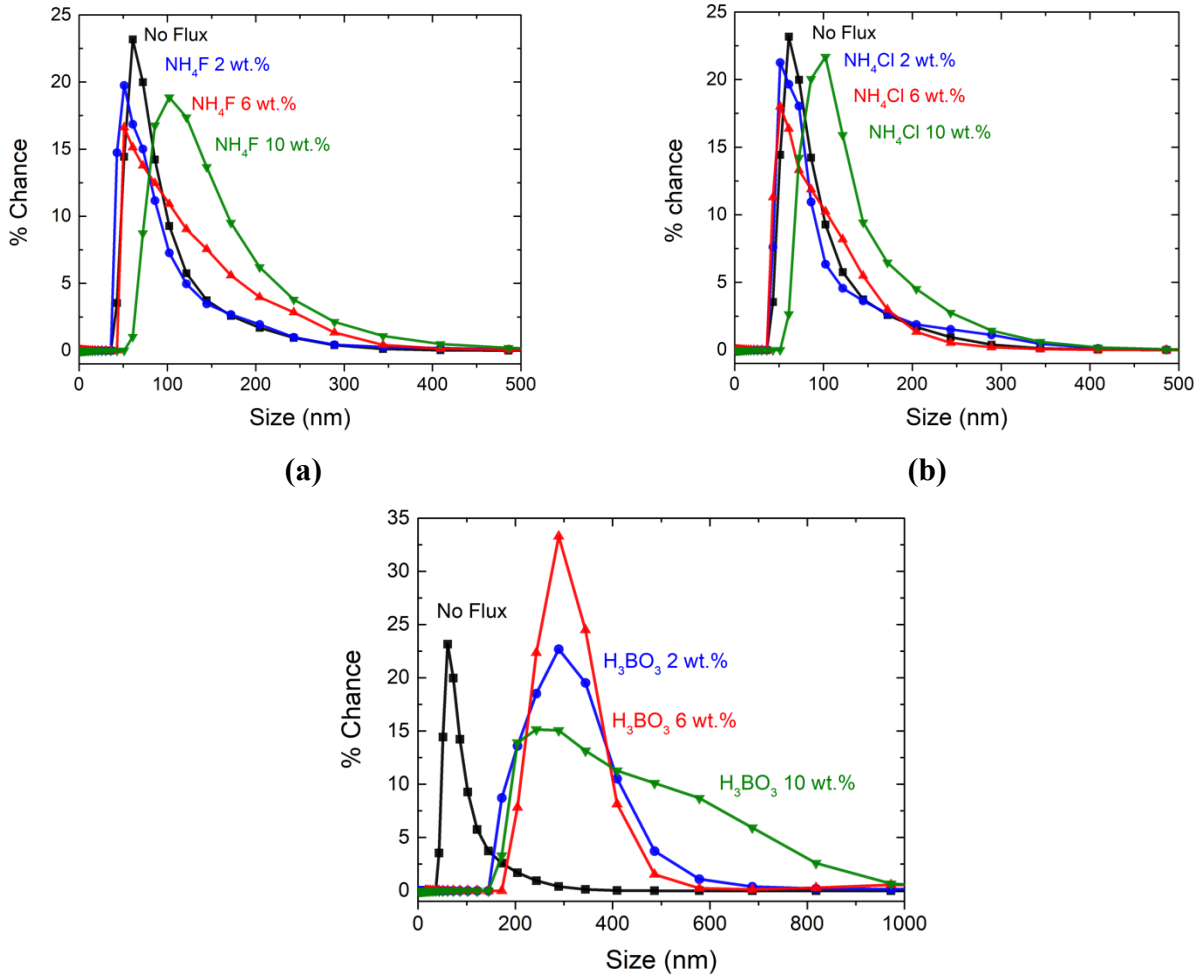

Figure 3.6 The distributions of particle sizes of $Ca_{0.94}Eu_{0.06}MgSi_2O_6$ with fluxes **(a)** NH_4F, **(b)** NH_4Cl and **(c)** H_3BO_3 analyzed by dynamic light scattering analysis.

3.4.3 Photoluminescence spectra and quantum efficiency

The PL excitation (PLE) was monitored at 458 nm, and the PL emission spectra were obtained under λ_{ex} = 350 nm as an excitation wavelength. Figure 3.7a-c shows the PLE spectra (dashed lines) with a broadband absorption in the near UV region from 200 nm to 400 nm, with a maximum at 350 nm, which is attributed to the allowed transition of Eu^{2+}.

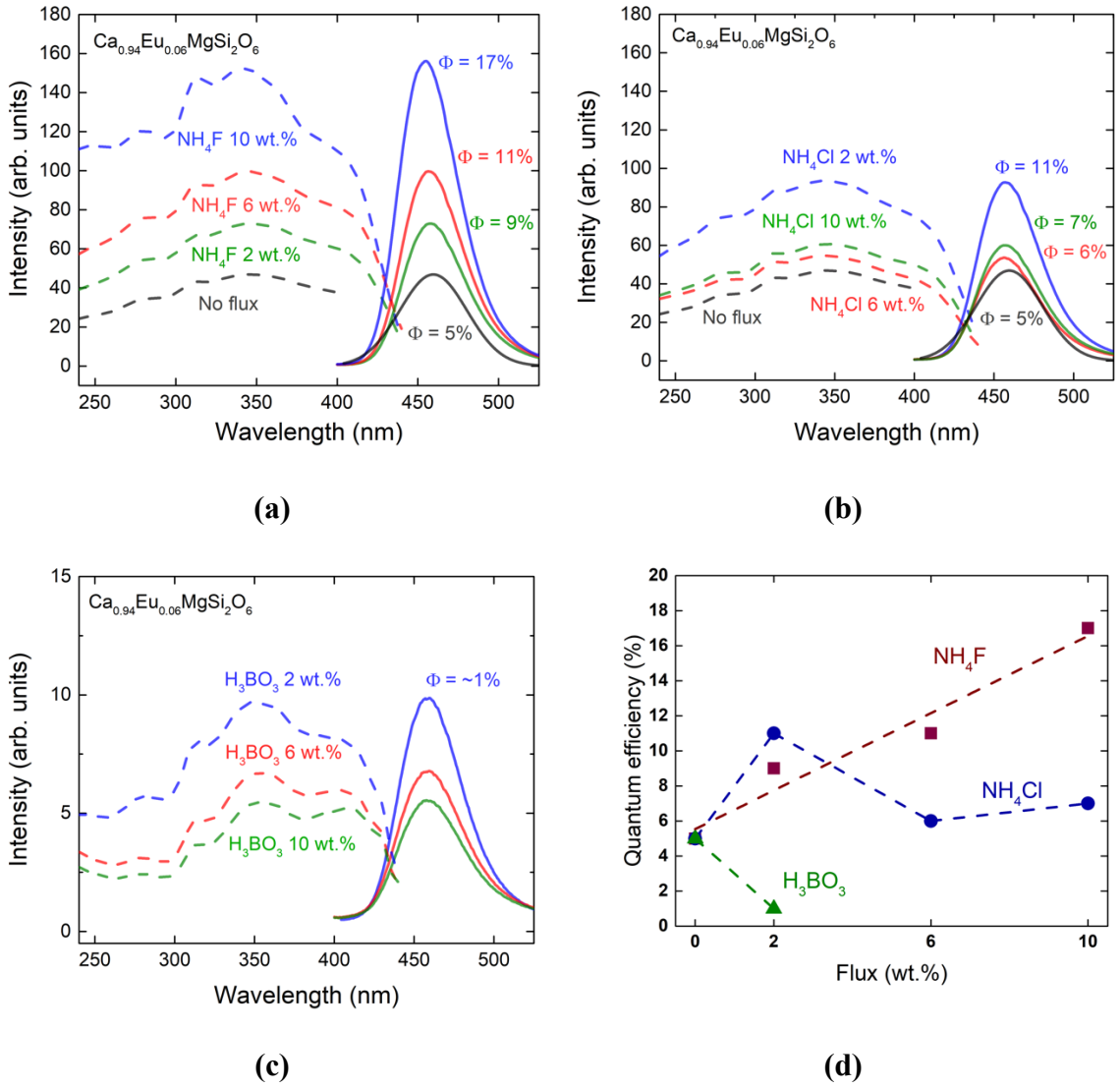

Figure 3.7 Photoluminescence excitation (dashed line monitored at 458 nm) and emission (solid line, λ_{ex} = 350 nm) spectra of $Ca_{0.94}Eu_{0.06}MgSi_2O_6$ with **(a)** NH_4F (no flux, 2 wt.%, 6 wt.%, and 10 wt.%), **(b)** NH_4Cl (no flux, 2 wt.%, 6 wt.%, and 10 wt.%), **(c)** H_3BO_3 (2 wt.%, 6 wt.%, and 10 wt.%). Φ□= quantum efficiency. **(d)** The relationship between quantum efficiency and the amount of flux.

The PL emission (solid lines) shows a spectrum with a maximum at 458 nm, which corresponds to the parity allowed $4f^6 5d^1 \rightarrow 4f^7$ transition of Eu^{2+}. In Figure 3.7a, the absorption and emission intensities together with the quantum efficiency (Φ) increased with the increase of the amount of NH_4F. A maximum Φ of 17% was found at 11 wt.% of NH_4F. For the NH_4Cl flux

(Figure 3.7b), the quantum efficiency increased from 5% to 11% when 2 wt.% of NH_4Cl was added. For the amounts of NH_4Cl >2 wt.%, Φ decreased. As shown in Figure 3.7c, Φ with H_3BO_3 was very low, ~1%, because of the significant amount of SiO_2 in the sample, as was confirmed by the XRD (Figure 3.3b). Figure 3.7d is a plot of Φ as a function of the amount of flux for all three fluxes used in the current study. A cumulative analysis of Figure 3.2c and Figure 3.7d demonstrates that the change in the crystallite sizes of the materials produced with NH_4F and NH_4Cl fluxes, directly relates to the change in their corresponding quantum efficiencies [150]. For 0-10 wt.% of NH_4F, the average crystallite size increased from 13 nm to 31 nm, and the corresponding quantum efficiencies improved from 5% to 17%. Similarly, for 0 wt.%, 2 wt.%, 6 wt.%, and 10 wt.%, of the NH_4Cl flux, the average crystallite sizes were 13 nm, 19 nm, 15 nm, 18 nm, respectively, and the corresponding quantum efficiencies showed the same trend. With 0-10 wt.% of H_3BO_3, the crystallite sizes of the phosphors are changed from ~13 nm to ~27 nm, but quantum efficiency was low due to the existence of the secondary phase, SiO_2.

3.4.4 Effect of high concentration of NH_4Cl

Increased amount of NH_4Cl was examined to determine if the high concentration of this particular flux resulted in the formation of second phase, a change in crystal structure, or further improvement of Φ while phosphors with NH_4F and H_3BO_3 already consist of secondary phases below 10 wt.% of the flux. Figure 3.8a shows the XRD patterns of $CaMgSi_2O_6$ produced with 14, 17, and 20 wt.% of NH_4Cl flux. There were no secondary

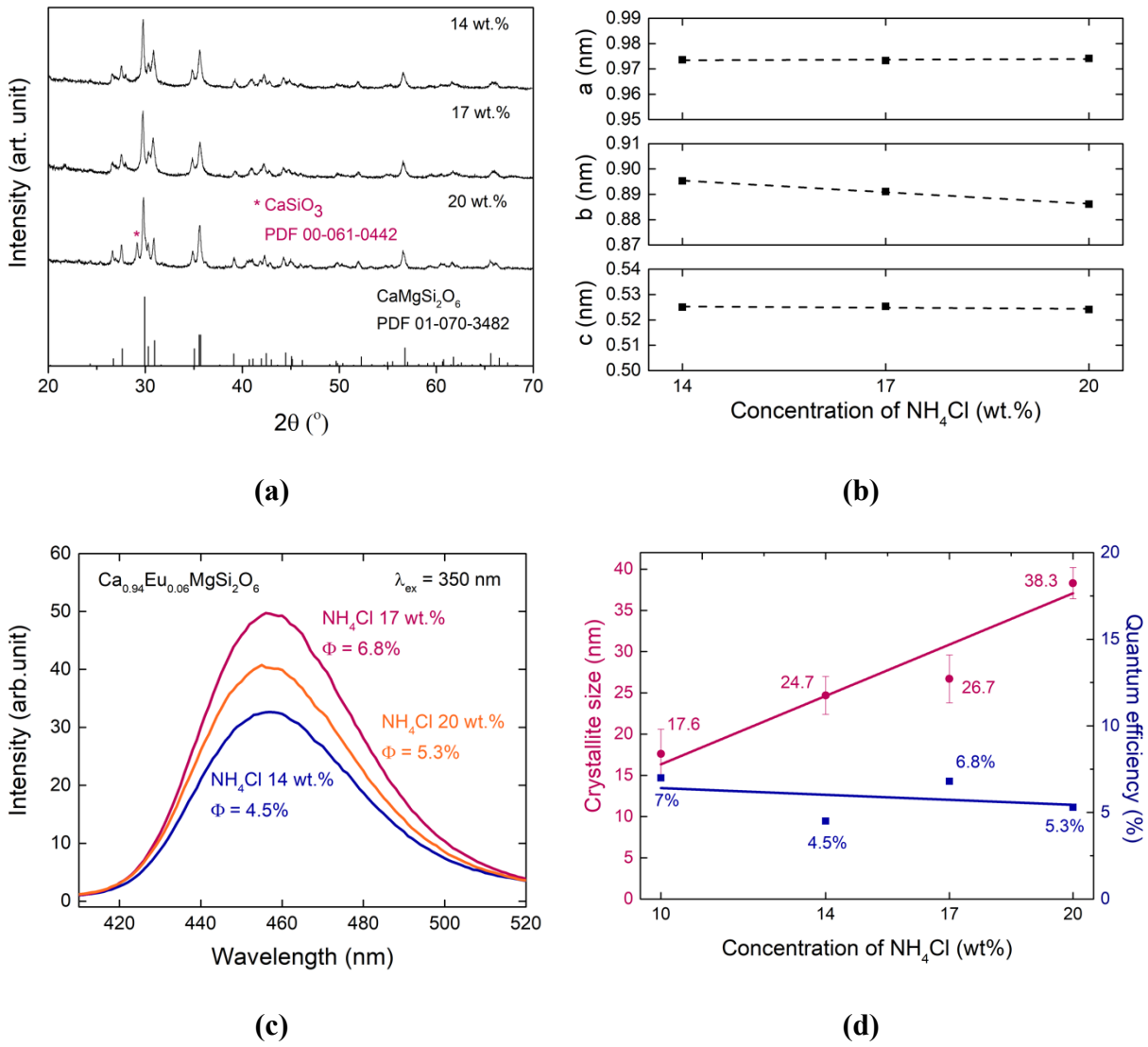

Figure 3.8 Effect of additional NH_4Cl flux (14 wt.%, 17 wt.%, and 20 wt.%) on $CaMgSi_2O_6:Eu^{2+}$. **(a)** X-ray diffraction patterns, **(b)** calculated lattice parameters of $CaMgSi_2O_6:Eu^{2+}$, **(c)** photoluminescence emission spectra (λ_{ex} = 350 nm) and quantum efficiencies **(d)** calculated crystallite sizes (pink color) and quantum efficiencies (blue color) from 0 to 20 wt.% NH_4Cl.

phases with 14 and 17 wt.%, but $CaSiO_3$ was detected for 20 wt.% of NH_4Cl. The lattice parameters *a* and *c* were not affected, but *b* decreased from 0.8867 nm (for 14 wt.%) to 0.8852 nm (for 20 wt.%) (Figure 3.8b). Given that the radii difference between Cl^- and O^{2-} is 26%, excessive Cl^- may substitute for O^{2-} and produce a charge imbalance. This could cause cation defects and/or the creation of secondary phases such as $CaSiO_3$. $MgSiO_3$ could also potentially be produced due

to the substitution O^{2-} by Cl^-, but it was not detected by XRD. Vegard's law can also be applied to the *b*–axis change, with an assumption that there are vacancy defects of ½ Ca^{2+}, ½ Mg^{2+} or ¼ Si^{4+} due to the charge difference between O^{2-} and Cl^-. To obtain the maximum difference between *b* and b_0, Ca^{2+} vacancies were assumed. The lattice parameter change is $b = b_0 - \frac{1}{2}xr_{Ca} - x(r_O - r_{Cl})$, where *b* is the lattice parameter (0.8852 nm) with 20 wt.% Cl^- additions, b_0 is the initial lattice parameter with no flux (0.8900 nm), *x* is the partial substitution of Cl^- on O^{2-}, and $r_{Ca}, r_{Si}, r_O, r_{Cl}$ are radii of Ca^{2+}, Si^{4+}, O^{2-}, and Cl^-, respectively. The obtained *x* value is 0.32, which is smaller than the molar fraction of Cl^- in $CaMgSi_2O_6$ (0.50, converted from 20 wt.% NH_4Cl). The remaining Cl^- is likely from the excessive addition of NH_4Cl. The crystal structure along the [001] (Figure 3.1d) and [010] (Figure 3.1c) directions shows one Ca^{2+} and one Mg^{2+} along the *a*- and *c*-axes and two Ca^{2+} and two Mg^{2+} along the *b*-axis, resulting in the fraction of Mg^{2+} and Ca^{2+} along the *b*-axis being twice higher than that along the *a*- and *c*-axes. Therefore, the *b*-axis was altered more than the *a*- and *c*-axes.

The PL emission spectra and Φs with additional NH_4Cl flux are shown in Figure 3.8c. The Φs were not significantly changed with an increase in the amount of NH_4Cl. A comparison between crystallite size and Φs on the amount of NH_4Cl flux is shown in Figure 3.8d. The maximum Φ corresponded to 2 wt.%; over 2 wt.% Φ initially decreased and eventually leveled off. However, the crystallite sizes increased with an increase in the concentration of the flux. This implies that the flux, although increasing the crystallite sizes, also changed lattice parameters resulting in no enhancement of Φ due to the inappropriate amount of flux addition.

3.5 Conclusions

The crystallite size and quantum efficiency of blue-emitting $Ca_{0.94}Eu_{0.06}MgSi_2O_6$ submicrometer-sized phosphors prepared by the co-precipitation method were altered with the

addition of a flux, NH_4F, NH_4Cl, or H_3BO_3. The particle sizes both with and without fluxes (NH_4F or NH_4Cl) were submicrometer-sized (~100 nm). A direct correlation between crystallite sizes of the materials produced with NH_4F or NH_4Cl fluxes and their corresponding quantum efficiencies was verified. For the NH_4F flux, the crystallite size increased from 13 nm (no flux) to 31 nm (10 wt.% flux). The corresponding quantum efficiencies improved from 5% (no flux) to 17% (10 wt.% flux), correlating with the increase in crystallite size. For the NH_4Cl flux, the crystallite sizes with 10 wt.% increased to 18 nm with 10 wt.% from 13 nm with no flux, with a corresponding increase in quantum efficiency from 5% to 11%. This demonstrates that NH_4Cl is not an effective flux, likely due to its lower liquid diffusion coefficient compared to NH_4F. Additionally, it was shown that further increasing the amount of the NH_4Cl flux (14-20 wt.%) only slightly improved the corresponding quantum efficiency. The H_3BO_3 flux produced a substantial amount of SiO_2 as a secondary phase, which negatively affected the quantum efficiency of the resultant material. From lattice parameter measurements, it is shown that the phosphor was contaminated with boron ions, and silicon was leached out of the lattice.

In summary, it is shown that the poor quantum efficiency of submicron-sized phosphors can be improved by using NH_4F flux for $CaMgSi_2O_6:Eu^{2+}$, but the flux composition and amount must be carefully assessed to evaluate the presence of secondary phases.

Chapter 3, in full, is a reprinted of the materials as it appears in "A facile method to improve quantum efficiency of submicron particles sized phosphors using a flux for solid lighting application", *Ceramics,* 1, 5, 2018. This work was coauthored by E. Novitskaya, G. A. Hirata, C. Zhou, R. E. Ridley, O. A. Graeve. J. McKittrick is the corresponding author. The dissertation author is the first author of this work.

CHAPTER 4: MINING UNEXPLORED CHEMISTRIES FOR PHOSPHORS FOR HIGH-COLOR-QUALITY WHITE-LIGHT-EMITTING DIODES

4.1 Abstract

There is a critical need for new earth-abundant phosphors to enable next-generation, highly efficient solid-state lighting. Here, we report the discovery of Sr_2LiAlO_4, the first known Sr-Li-Al-O quaternary crystal, via a carefully-targeted data-driven structure prediction and screening effort using density functional theory calculations. Sr_2LiAlO_4 is predicted and experimentally confirmed to be a thermodynamically and thermally stable phosphor host that can be excited with near-UV/blue sources. The Eu^{2+}- and Ce^{3+}-activated Sr_2LiAlO_4 phosphors exhibit broad emissions at λ_{max} ~ 512 nm (green-yellow) and λ_{max} ~ 434 nm (blue), respectively, with excellent thermal quenching resistance of > 88% intensity at 150°C. A prototype phosphor-converted white LED utilizing Sr_2LiAlO_4-based phosphors yields an excellent color rendering index exceeding 90. Sr_2LiAlO_4 therefore exhibits great potential for industrial applications in low-cost, high-color-quality WLEDs.

4.2 Introduction

Phosphor-converted white-light-emitting diodes (pc-WLEDs) are among the most promising solid-state lighting (SSL) technologies due to their high-energy efficiency and superior durability and reliability [44, 151]. For general illumination, we need a warm white light with excellent quantum efficiency, resistance to thermal quenching, and color quality, i.e., a low color-correlated temperature (CCT) < 3000 K and a high color rendering index (CRI) > 85 [152]. Typical commercial WLEDs based on blue-emitting (~450 nm) LED chips combined with a yellow-emitting phosphor ($Y_3Al_5O_{12}:Ce^{3+}$) have poor CRI < 80 and high CCT > 7000 K [153]. To improve the CRI and CCT, an alternative approach is to use near-ultraviolet (near-UV, 380-420 nm) or blue

LED chips with a mixture of red, green and blue phosphors. $Lu_3Al_5O_{12}:Ce^{3+}$ and $(Ba,Sr)_2SiO_4:Eu^{2+}$ are two well-known green emitters with good photoluminescence (PL) properties used for these phosphor mixtures [154]. Unfortunately, the former requires the rare-earth Lu in large quantities, while the latter suffers from severe thermal quenching. Meanwhile, most commercial red-emitters are Eu^{2+}-activated nitrides, such as $CaAlSiN_3:Eu^{2+}$ and $Sr_2Si_5N_8:Eu^{2+}$, which are synthesized under harsh conditions (high temperature and high pressure) [155, 156]. Yet another way to generate white light with high color quality is to leverage on a single-phase broad-band emitter that covers a wide range of the visible spectrum (400 ~ 700 nm). $Ba_{0.93}Eu_{0.07}Al_2O_4$ is an example of a recently discovered broad-band phosphor with good CRI > 80 and CCT < 4000 K [157], but its synthesis requires a high temperature of 1450°C and a low pressure of 667 Pa.

There is therefore an urgent need to discover novel earth-abundant phosphors with reasonably facile synthesis for pc-WLED applications. Hitherto, the discovery of phosphor materials has largely taken place through painstaking experiments, such as using exploratory crystal growth [44], combinatorial chemistry screening [158] and single particle-diagnosis [159], in an Edisonian fashion. In recent years, high-throughput density functional theory (DFT) calculations have emerged as a powerful complementary tool to experiments to accelerate materials discovery, with successes having been demonstrated in the many application areas [86, 160-162]. By enabling rapid evaluation across multiple application-specific properties, DFT calculations can be used to effectively screen thousands of materials to identify a small subset of candidates for subsequent synthesis and experimental evaluation. Nevertheless, there have been no successful demonstrations of *in silico* phosphor discovery to date, no doubt due in part to extensive experimental efforts in the field as well as the difficulty in predicting optical properties with DFT.

In this work, we report the discovery of a novel, earth-abundant phosphor host Sr_2LiAlO_4, which is also the *first known Sr-Li-Al-O quaternary compound* to the authors' knowledge. Sr_2LiAlO_4 was identified via a carefully-targeted data-driven structure prediction and DFT screening effort guided by statistical analysis of known phosphors in the Inorganic Crystal Structure Database (ICSD) [163]. We demonstrate that Sr_2LiAlO_4 is predicted by DFT calculations to be thermodynamically and dynamically stable and to have the necessary band gap, structural rigidity and near-UV excitation wavelength when activated with either Eu^{2+} or Ce^{3+}. High purity Sr_2LiAlO_4 was synthesized via industrially-scalable methods and characterized using X-ray diffraction and photoluminescence spectroscopy. The Eu^{2+}- and Ce^{3+}-activated Sr_2LiAlO_4 phosphors exhibit broad emissions of $\lambda_{max} \sim 512$ nm (green-yellow) and $\lambda_{max} \sim 434$ nm (blue), respectively, with excellent thermal quenching resistance of > 88% intensity at 150°C. A prototype pc-WLED utilizing $Sr_2LiAlO_4:Eu^{2+}$ yields an excellent CRI > 90.

4.3 Methods

4.3.1 Candidate structure generation

New crystal structure candidates for the target chemistries were generated by applying a retrained version of the ionic substitution algorithm developed by Hautier et al [161]. on the Inorganic Crystal Structure Database (ICSD) [163]. This algorithm codifies data-mined probabilities for substitution of one species by another. New candidates are generated by performing high-probability substitutions on a list of known crystal structures, in this case, all ordered crystal structures in the 2017 version of the ICSD.

4.3.2 Density functional theory (DFT) calculations

All DFT calculations were carried out using the Vienna *ab initio* simulation package (VASP) within the projector-augmented wave method [90, 164]. The generalized gradient

approximation Perdew-Burke-Ernzerhof (PBE) functional [92] was used for structural relaxations and energy calculations. The plane wave energy cutoff was 520 eV, and the Brillouin zone was integrated with a *k*-point grid at least of 100 per $Å^{-3}$ (reciprocal lattice volume). All host crystal structures were relaxed with parameters in line with Materials Project [94]. The Eu^{2+}/Ce^{3+}-activated phosphor structures were fully relaxed until the energies and forces were convered to 10^{-5} eV and 0.01 eV/ Å, respectively. All crystal structure manipulations and data analysis were carried out using the Python Materials Genomics package [165].

The phase stabilities of the predicted Sr-Li-Al-O compounds were estimated by calculating the energy above the linear combination of stable phases in the 0 K DFT phase diagram [166], also known as the energy above hull, E_{hull}. Previous studies have shown that ~60% of ICSD oxides have E_{hull} less than 30 meV/atom [167]; we therefore use this threshold as a reasonable cutoff for synthesizability. For phase diagram construction, the energies of all compounds other than those of direct interest in this work were obtained from the Materials Project [94] via the Materials Application Programming Interface [93]. Further, the dynamical stability of the identified Sr_2LiAlO_4 host was evaluated by computing the phonon spectrum using density functional perturbation theory as implemented in the Phonopy code [168] in conjunction with VASP [164] as the force calculator. More stringent energy and force criteria of 10^{-8} eV and 10^{-4} eV/Å, respectively, were used for these calculations.

Defect formation energies were calculated using the formalism presented by Wei et al. [169]:

$$E_f = E_{tot}^D - E_{tot}^B - \sum_i n_i \mu_i$$

where E_{tot}^D and E_{tot}^B are the total energies of the structure with and without the defect(s), respectively; μ_i is the atomic chemical potential of species *i*; n_i indicates the number of atoms of

species i being added ($n_i > 0$) or removed ($n_i < 0$) to form the defect. μ_i is estimated based on the chemical pontentials for each specie based on the relevant region of the 0 K DFT phase diagram.

The host band gaps were calculated using PBE for the initial rapid screening, and more detailed investigations of the electronic structure of Sr_2LiAlO_4 were carried out using the more computationally expensive and accurate screened hybrid Heyd−Scuseria−Ernzerhof (HSE) functional [170, 171] and single-shot *GW* method [172]. The Bether-Salpeter equation (BSE) [173] simulation was performed on top of G_0W_0 to calculate the absorption spectrum of Eu^{2+}/Ce^{3+}-activated Sr_2LiAlO_4 phosphors. A large supercell model (2×2×2, 128-atoms) was adopted to mimic the relatively low Eu^{2+}/Ce^{3+} concentrations in experiment, and to avoid interactions between periodic images of activators.

The Debye temperature, Θ_D, was evaluated using the quasi-harmonic model. The elastic tensor was calculated with more stringent electronic convergence criterion of 10^{-6} eV, and the elastic moduli were calculated using the Voigt−Reuss−Hill approximation [75, 86].

4.3.3 Local environment analysis.

The local environment of the Eu^{2+} activator was characterized using the average Eu-O bond length (l_{av}) and the distortion index (D) of the EuO_8 coordination polyhedron. As per previous works [86, 174], D is defined given by $D = \frac{1}{n}\sum_{i=1}^{n}\frac{|l_i - l_{av}|}{l_{av}}$, where l_i is the distance from the center atom to the ith coordinating atom, and n is the total number of Eu-O bonds (n = 8 in this case).

4.3.4 Synthesis

Solid state reaction synthesis was performed using SrO (Kojundo, 99.9%), Li_2CO_3 (Kojundo, 99.9%), α-Al_2O_3 (Kojundo, 99.9%), and Eu_2O_3 (Kojundo, 99.9%) or CeO_2 (Kojundo, 99.99%)**.** Stoichiometric amounts of the starting materials were ground in agate mortar, placed in alumina crucibles, and fired at 900°C for 4 h in a horizontal tube furnace using a 25% H_2/N_2 gas

mixture to obtain Sr_2LiAlO_4:$x$$Eu^{2+}$ and Sr_2LiAlO_4:$y$$Ce^{3+}$ ($0.0025 \leq x, y \leq 0.0500$). After heat treatment, the samples were cooled to room temperature and ground well with agate mortar into fine powders for further analysis. Excess Li source of up to 10 wt% was introduced to compensate for Li evaporation during synthesis.

Combustion reaction synthesis was performed using $Sr_2(NO_3)_2$ (99.99%, Sigma Aldrich), $LiNO_3$ (ReagentPlus, Sigma Aldrich), $Al(NO_3)_3$•$9H_2O$ (ACS reagent, J. T. Baker), $Eu(NO_3)_3$ from Eu_2O_3 (99.99%, Alfa Aesar) with nitric acid (69.3%, Fisher Scientific), and $Ce(NO_3)_3$ (99.99%, Alfa Aesar) as precursors, assisted by the exothermal reaction between urea (Certified ACS, Fisher Scientific) and ammonium hydroxide (Certified ACS, Fisher Scientific) at 600ºC. A post-annealing condition was 800ºC for five hours in a 5%H_2/95%N_2 atmosphere to transform Eu^{3+} to Eu^{2+} to obtain Sr_2LiAlO_4:$x$$Eu^{2+}$ and Sr_2LiAlO_4:$y$$Ce^{3+}$ ($0.001 \leq x, y \leq 0.040$). Excess Li source of up to 25 wt% was introduced to compensate for Li sublimation during synthesis.

4.3.5 Crystal structure characterization

The powders by combustion reaction were analyzed by X-ray diffraction (XRD, Bruker D2 Phaser, Karlsruhe, Germany) using CuKα radiation and a step size of 0.014° over a 2θ range of 20 to 80°. X-ray diffraction (XRD) data of powders by solid state reaction were obtain using CuKα radiation (Philips X'Pert). XRD data were collected over angles of $10° \leq 2\theta \leq 120°$ with a step size of 0.026°. Structural information of the synthesized samples was derived by refinement using the TOPAS software suite from the XRD result. The VESTA program [104] was used to draw the crystal structure.

4.3.6 Optical measurements

Photoluminescence of the solid-state-reaction synthesized samples was measured using a Hitachi F-4500 fluorescence spectrophotometer over a wavelength range of 200-700 nm. The

quantum yield was measured with 394 nm and 450 nm excitation using a xenon laser (Hamamatsu C9920-02) at the Korea Photonics Technology Institute (KOPTI), Gwangju, South Korea. The thermal quenching characteristics were measured in the temperature range of 25-200°C, connected to the Hitachi F-4500 fluorescence spectrophotometer with the integrated heater, temperature controller, and thermal sensor. Low-temperature PL spectra were obtained under excitation at 325 nm He-Cd laser connected to the cryostat system at the temperature of 10 K in the KOPTI, Gwangju, South Korea.

4.3.7 Fabrication of pc-WLED prototype

The white LED device prototype was fabricated by integrating the $Sr_2LiAlO_4:0.005Ce^{3+}$ and mixed $Sr_2LiAlO_4:0.005Ce^{3+}/Eu^{2+}$ phosphors on a InGaN near UV LED chip (λ_{max} = 400 nm) and the $Sr_2LiAlO_4:0.005Eu^{2+}$ phosphor on a InGaN blue LED chip (λ_{max} = 450 nm). The device was then encapsulated in a phosphor/silicon resin mixture, with the mixture placed directly on the headers of LED chip and cured at 150°C for 1 h. After the packaging was completed, the WLED device was measured in an integrating sphere under direct current forward bias condition.

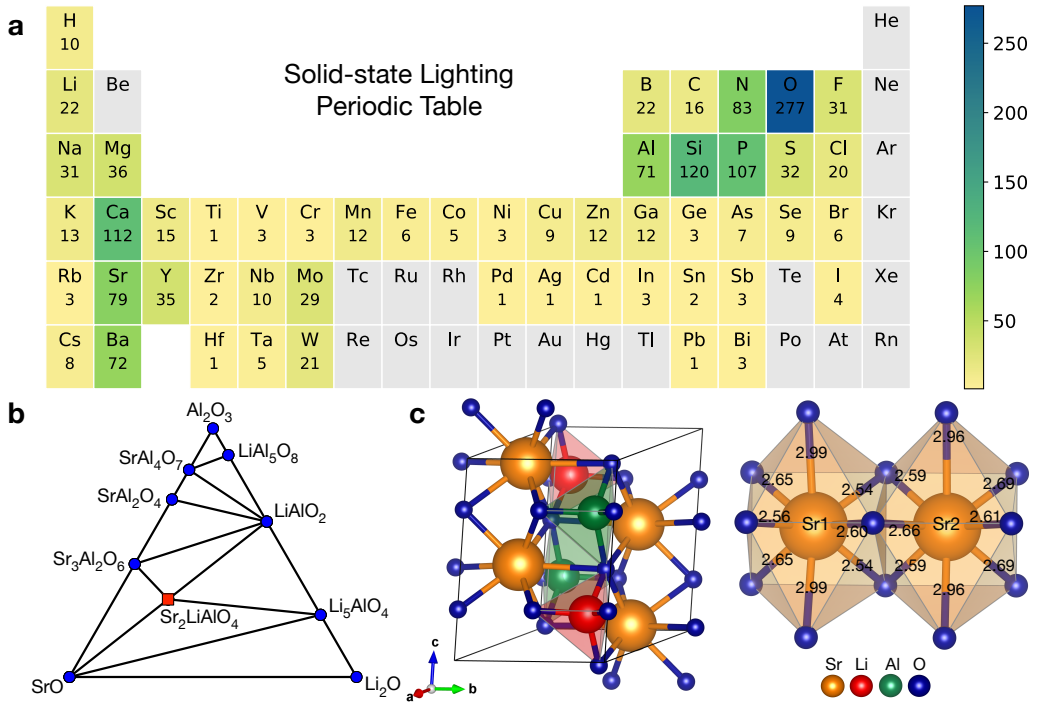

Figure 4.1 Data-driven discovery of Sr_2LiAlO_4. (a) Frequency at which each element appears in compounds having the word "phosphor" in the publication title in the 2017 version of ICSD. Only non-rare-earth elements are shown. Elements with frequency 0 are shaded in gray. (b) Calculated 0 K SrO-Li_2O-Al_2O_3 phase diagram. Blue circles: known stable phases in the Materials Project database; red square: new stable quaternary phase, Sr_2LiAlO_4. (c) Unit cell of the Sr_2LiAlO_4 ($P2_1/m$) crystal and the two symmetrically distinct Sr sites. Numbers indicate Sr-O bond lengths in angstroms.

4.4 Results And Discussions

4.4.1 Data-driven Discovery of New Phosphors

We began our search for novel phosphor hosts by constructing a "solid-state lighting" periodic table (Figure 4.1a) from a statistical analysis of all compounds in the 2017 version of the ICSD with the word "phosphor" in the publication title. The high frequency of elements N, S, F and Cl can be ascribed to the fact that (oxy)nitrides, (oxy)halides and sulfides are some of the most well-studied phosphor materials [76, 175, 176]. Nevertheless, oxides are overwhelmingly preferred in practical SSL applications due to their typically more facile synthesis and better chemical stability under ambient conditions; therefore, these other anion types will not be further

considered in this work. We may observe a preponderance of the alkaline-earth metals (Mg/Ca/Sr/Ba), alkali metals (Li/Na/K) and main group elements (Al/Si/P/B) among known phosphors. The presence of Ca and Sr is not surprising, given that the ionic radii of Ca^{2+} and Sr^{2+} are similar to those of the common Ce^{3+} and Eu^{2+} activators [151]. Na^{+} also presents a high frequency in phosphor hosts due to its similar size to Eu^{2+}. However, activation via aliovalent substitution of Na+ by Eu^{2+} would require the identification of the most stable charge-compensating defect and the use of large-supercell DFT calculations. Therefore, we have chosen to focus on systems containing Sr^{2+}/Ba^{2+}/Ca^{2+} in this work as these are isovalent with Eu^{2+}. Given that phosphates, silicates, aluminates and borates are among the most commonly studied oxides in SSL [76, 175, 176], we then proceeded to identify opportune chemistries for novel phosphor host discovery in the ternary M-X-O (M=Ba/Sr/Ca, X=P/Si/Al/B) and quaternary M-L-X-O (M=Ba/Sr/Ca, L=Li/Mg/Y, X=P/Si/Al/B) oxides.

We find that while ternary M-X-O oxides have been relatively well-explored, significant opportunities exist in quaternary M-L-X-O oxides. In particular, there are no reported compounds in the ICSD in seven chemistries – Ba/Sr/Ca-Li-Al-O, Sr-Li-P-O, Ba/Sr-Y-P-O, and Ba-Y-Al-O (Figure 4.2). A further search of the larger Pauling File database [177] turned up one known compound each in the Sr-Li-P-O, Ba/Sr-Y-P-O and Ba-Y-Al-O chemistries, and still no compounds in the Ba/Sr/Ca-Li-Al-O chemistries.

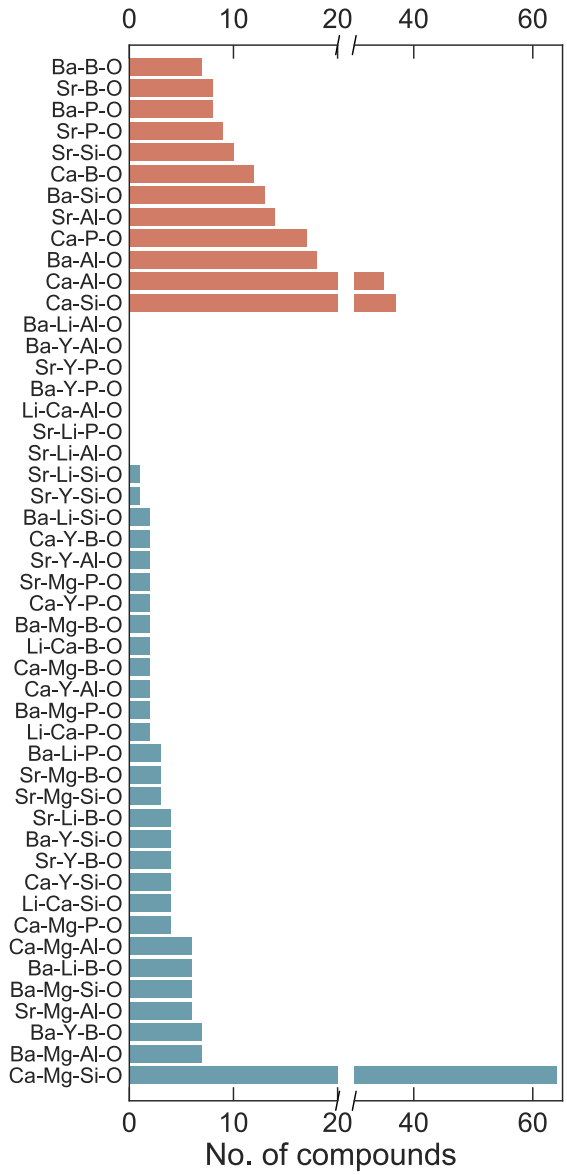

Figure 4.2 Number of known materials in the Inorganic Crystal Structure Database in the ternary M-X-O and quaternary M-L-X-O (M = Ba/Sr/Ca; L = Li/Mg/Y; X=P/Si/Al/B) chemical spaces.

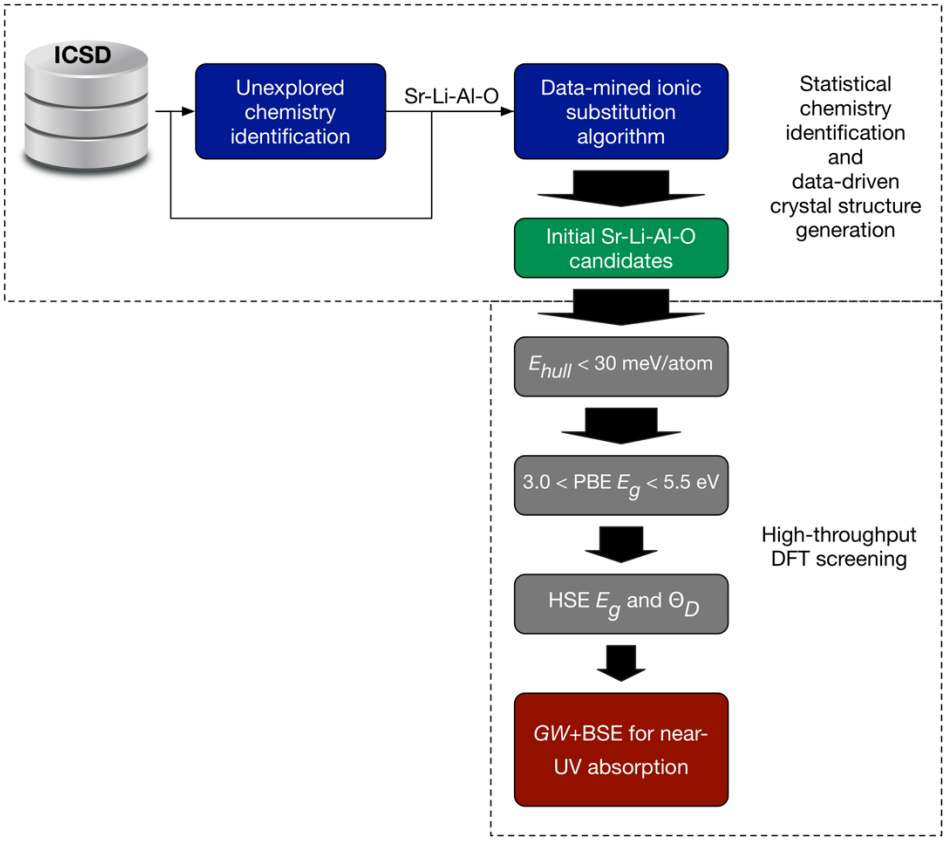

Figure 4.3 Computational high throughput screening workflow for identifying promising broad-band emitters. E_g is the host band gap calculated with both Perdew-Burke-Ernzerhof (PBE) functional and Heyd-Scuseria-Ernzerhof (HSE) functional. Θ_D is calculated Debye temperature. *GW*+BSE denotes the Bethe-Salpeter equation (BSE) calculation performed on top of G_0W_0.

We generated 918 new crystal structure candidates in these seven unexplored chemical systems by applying a data-mined ionic substitution algorithm [178] on the entire ICSD (see Methods). These candidates were then systematically evaluated via an efficiently-tiered series of DFT property calculations (Figure 4.3). The first criterion that any technological material must satisfy is synthesizability and stability. Thermodynamic stability is estimated by calculating the energy above the linear combination of stable phases in the 0 K DFT phase diagram, also known as E_{hull}. A typical threshold for synthesizability used in previous DFT screening works is an E_{hull} < 30~50 meV/atom [86, 167]. We find that the four known phosphors in the Sr-Li-P-O, Ba/Sr-Y-P-O and Ba-Y-Al-O chemistries reported in the Pauling database are indeed among the candidates

generated by the structure prediction algorithm, and all four compounds have a calculated E_{hull} < 35 meV/atom (Table 4.2). The successful prediction of these "unseen" known phosphors from the ICSD gives us confidence that viable candidates are identified via the combination of the data-mined ionic substitution algorithm and DFT calculations. Among the remaining Ba/Sr/Ca-Li-Al-O chemical systems with no known compounds, we will focus primarily on the Sr-Li-Al-O chemistry due the fact that Sr^{2+} has an ionic radius (1.26 Å) that is closest to Eu^{2+} (1.25Å), compared to Ba^{2+}(1.42Å) or Ca^{2+}(1.12Å) [151]. Also, Li and Al are inexpensive, earth-abundant elements that tend to form rigid bonds in crystals.

Table 4.1 Four known compounds in the Sr-Li-P-O, Ba/Sr-Y-P-O and Ba-Y-Al-O chemical spaces, their derivations, computed energy above ehull (E_{hull}) and the relevant phosphors. Know compounds are retrieved from Pauling File database.

Chemical space	**Compound**		***E*$_{hull}$ (meV/atom)**	**Phosphors**
	Known	Derivation		
Sr-Li-P-O	$SrLiPO_4$	$RbLiCrO_4$ (ICSD-72551)	27	$SrLiPO_4:Eu^{2+}$[1]
Ba-Y-P-O	$Ba_3Y(PO_4)_3$[a]	$YbK_3(SO_4)_3$ (ICSD-200547)	11	$Ba_3Y(PO_4)_3:Eu^{2+}$[2]
Sr-Y-P-O	$Sr_3Y(PO_4)_3$[a]	$YbCs_3(SO_4)_3$ (ICSD-200932)	34	$Sr_3Y(PO_4)_3:Eu^{2+},Mn^{2+}$[3]
Ba-Y-Al-O	$Ba_6Y_2Al_4O_{15}$	$Ba_6Y_2Fe_4O_{15}$ (ICSD-248954)	0	$Ba_6Y_2Fe_4O_{15}:Sn^{2+}$[4]

[a] The crystal structures of $M_3Y(PO_4)_3$ (M = Ba/Sr) are disordered in experiment, of which the lowest energy ordered structures are well reproduced in our calculations.

Figure 4.1b shows the calculated 0 K SrO-Li_2O-Al_2O_3 phase diagram. We find that one of the new candidates, Sr_2LiAlO_4, is predicted to be thermodynamically stable (E_{hull} = 0). The computed phonon spectrum (Figure 4.4) confirms it to be also dynamically stable. The crystal structure of Sr_2LiAlO_4 (spacegroup: $P2_1/m$) is shown in Figure 4.1c, and the structural parameters are provided in the Table 4.2. Sr_2LiAlO_4 is derived from Ba_2LiReN_4 (ICSD No. 411453) via a multi-species substitution of Ba^{2+} with Sr^{2+}, Re^{7+} with Al^{3+}, and N^{3-} with O^{2-}. This is clearly a non-trivial crystal prediction that cannot be obtained easily replicated using traditional chemical intuition.

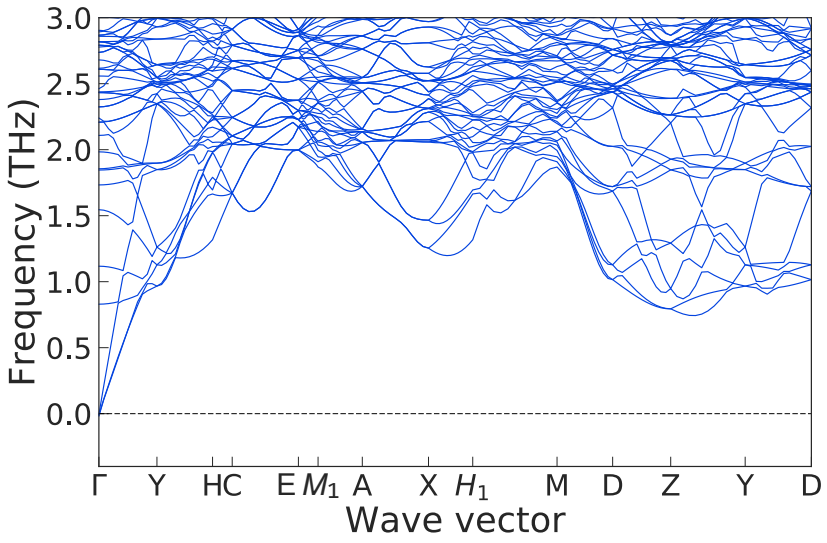

Figure 4.4 Calculated phonon spectrum for the predicted Sr_2LiAlO_4 ($P2_1/m$) crystal structure.

We evaluated the potential PL properties of the stable Sr_2LiAlO_4 host by calculating its electronic structure and Debye temperature (Θ_D). The calculated band gap E_g of Sr_2LiAlO_4 using the Perdew-Burke-Ernzerhof (PBE) functional [86] is 4.19 eV, which suggests that it would yield a green-yellow emission with Eu^{2+} activation based on the inverse relationship between experimental wavelength and the PBE E_g previously reported by the current authors [86]. In general, host materials that have a large photoionization barrier, defined as the energy gap between conduction band minimum (CBM) and excited 5*d* level, and are rigid tend to exhibit excellent thermal quenching resistance [100, 179]. The calculated bandgaps of Sr_2LiAlO_4 using the more accurate Heyd-Scuseria-Ernzerhof (HSE) [170, 171] functional and G_0W_0 [172] are 5.91 eV and 6.00 eV, respectively. This large bandgap suggests a strong likelihood of a large photoionization barrier. The calculated Θ_D of Sr_2LiAlO_4 is 466 K, indicating that it has rigid crystal structure [87].

There are two symmetrically distinct Sr crystallographic sites (labelled as Sr1 and Sr2 in Figure 4.1c) in Sr_2LiAlO_4, both of which are eight-fold coordinated with oxygen atoms. By performing an isovalent substitution a single Eu^{2+} into a 2 × 2 × 2 supercell of Sr_2LiAlO_4 (16

formula units), we determined using DFT calculations that the Eu^{2+} activator prefers the Sr1 site to the Sr2 site by about 35 meV. For Ce^{3+} activation, we comprehensively evaluated various charge-neutral defect configurations, taking into account typical experimental synthesis conditions such as excess Li from its volatility at elevated temperature. We find that the $2Ce_{Sr}^{\bullet}+Li_{Al}''$ defect combination (Kröger–Vink notation) has the lowest defect formation energy compared to $2Ce_{Sr}^{\bullet}+V_{Sr}''$ (0.22 eV/Ce^{3+} higher) and $Ce_{Sr}^{\bullet}+Li_{Sr}'$ (1.48 eV/Ce^{3+} higher). Hence, we conclude that the substitution of Ce^{3+} on Sr^{2+} is likely to be charged compensated by excess Li^{+} on the Al^{3+} tetrahedra, as opposed to vacancy formation or excess Li^{+} on the Sr^{2+} site. This is consistent with the fact that the small Li^{+} ion (ionic radius = 0.9 Å) is likely to prefer the AlO_4 tetrahedron rather than the much larger SrO_8 site. Henceforth, we will use the shorthand notation commonly used in the phosphor community, Sr_2LiAlO_4:$x$$Eu^{2+}$ and Sr_2LiAlO_4:$y$$Ce^{3+}$, to denote the activated structures with compositions $Sr_{2-x}Eu_xLiAlO_4$ and $Sr_{2-y}Ce_yLi_{1+y/2}Al_{1-y/2}O_4$, respectively. All subsequent DFT results on activated hosts, unless otherwise stated, were performed using the configuration with the lowest defect energy.

For efficient conversion, a phosphor should have absorption spectrum peaking at the maximum emission of LEDs chips. Given that the *excitonic* effect (electron-hole interaction) plays a crucial role in optical properties, the absorption spectra for Sr_2LiAlO_4:0.0625Eu^{2+} and Sr_2LiAlO_4:0.125Ce^{3+} were calculated using the Bethe-Salpeter equation (BSE) method [173] on top of G_0W_0. Figure 4.5 shows the calculated absorption spectra for Sr_2LiAlO_4:0.0625Eu^{2+} and Sr_2LiAlO_4:0.125Ce^{3+}. For both activated phosphors, the main absorption peaks are observed at 380-420 nm, which can be attributed to $4f^7 \rightarrow 4f^6 5d^1$ transition in Eu^{2+} or $4f^1 \rightarrow 4f^0 5d^1$ transition in Ce^{3+}. These findings suggest that both Eu^{2+}- and Ce^{3+}-activated Sr_2LiAlO_4 can be efficiently excited by near-UV LED chips.

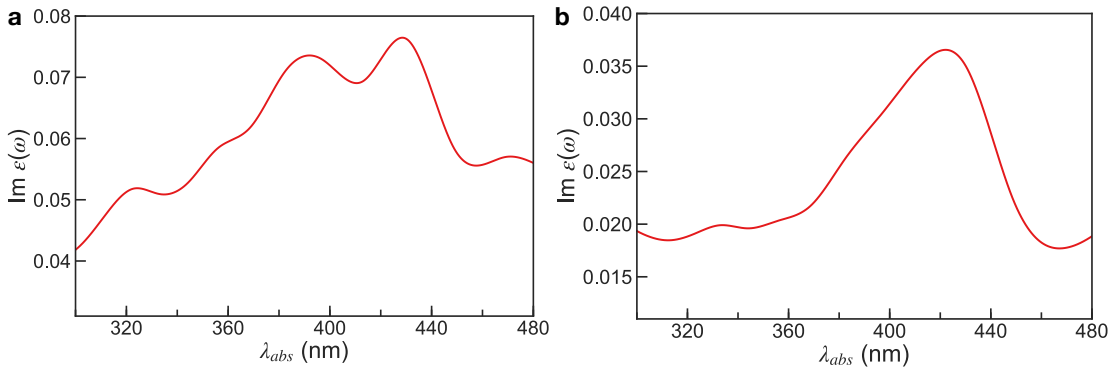

Figure 4.5 Computed absorption spectra for $Sr_2LiAlO_4:Eu^{2+}$ and $Sr_2LiAlO_4:Ce^{3+}$. (a) Absorption spectrum (characterized by absorption wavelength, λ_{abs}) for $Sr_2LiAlO_4:0.0625Eu^{2+}$ (with Eu^{2+} locating at the most stable site, Sr1) and (b) $Sr_2LiAlO_4:0.125Ce^{3+}$ (with the lowest energy $2Ce_{Sr}^{\bullet}+Li_{Al}''$ configuration) calculated using the Bethe-Salpeter equation method.

4.4.2 Synthesis and Photoluminescence Properties

The Sr_2LiAlO_4 host and the Eu^{2+}- and Ce^{3+}-activated phosphors were successfully produced using solid-state reaction as well as combustion synthesis. Here, we will discuss primarily the results from the samples synthesized via solid-state reaction, given that this is the preferred approach in commercial applications due to its low cost, availability of precursors, and potential for production on an industrial scale. In general, other than a higher purity (94% versus 86% for solid-state reaction), the measured structural parameters and PL properties of the combustion-synthesized samples are very similar. Figure 4.5 shows the simulated and measured XRD profiles of the host and activated phosphors, which are in excellent agreement and confirm the successful synthesis of the predicted Sr_2LiAlO_4 compound. The residual factors of Rietveld refinement analysis of the XRD profile (see Table S2) are R_{wp} = 9.11%, R_p = 6.69%, and goodness of fit (GOF) = 2.79. The refined structure parameters are also in excellent agreement with those from the DFT relaxed structure (see Table 4.2 and 4.3).

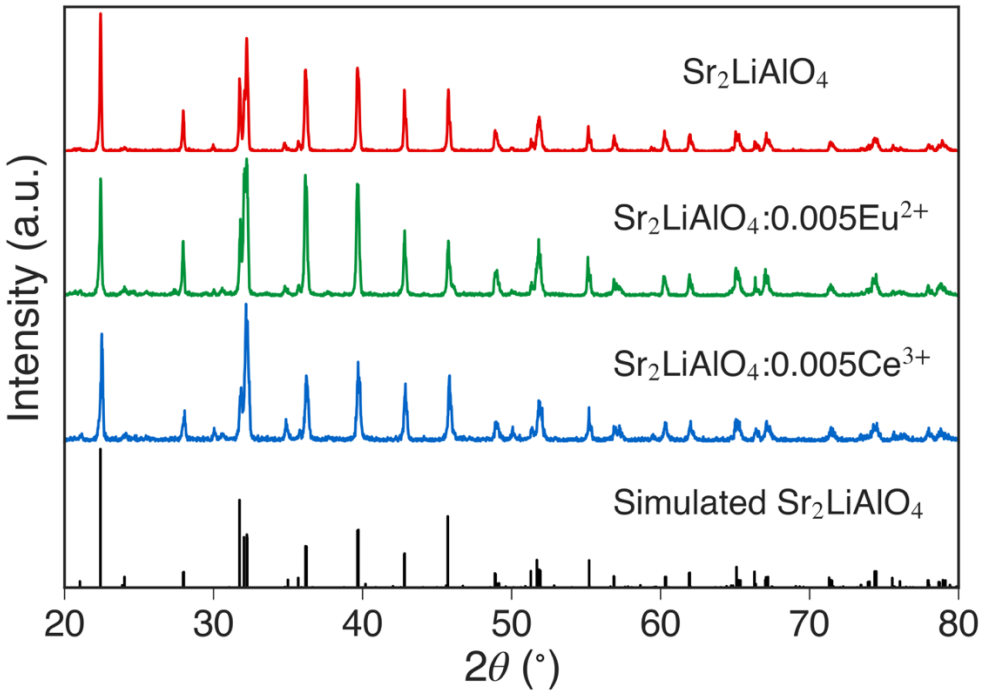

Figure 4.6 Simulated and measured X-ray diffraction patterns of Sr_2LiAlO_4, Sr_2LiAlO_4:0.005Eu^{2+} and Sr_2LiAlO_4:0.005Ce^{3+}.

Table 4.2 Calculated and experimental structural parameters of Sr_2LiAlO_4. The experimental values were obtained from XRD Rietveld refinement of the solid-state reaction samples.

Site	**Calculated**			**Experimental**			**Occupancy**	**Wyckoff Position**
	x	***y***	***z***	***x***	***y***	***z***		
Sr1	0.22801	0.25000	0.43191	0.23929 (67)	0.25000	0.43659 (60)	1	2e
Sr2	0.27038	0.25000	0.94227	0.24830 (66)	0.25000	0.93386 (60)	1	2e
Li3	0.30224	0.75000	0.69253	0.26130 (610)	0.75000	0.66930 (500)	1	2e
Al4	0.27851	0.75000	0.19918	0.13610 (480)	0.75000	0.40720 (470)	1	2e
O5	0.47754	0.50758	0.25164	0.50840 (320)	0.49180 (280)	0.25280 (260)	1	4f
O6	0.09917	0.75000	0.37670	0.27660 (250)	0.75000	0.19480 (260)	1	2e
O7	0.11359	0.75000	0.92812	0.11340 (350)	0.75000	0.89890 (270)	1	2e

Table 4.3 Calculated lattice parameters and Rietveld refinement parameters of X-ray diffraction profile of Sr_2LiAlO_4 synthesized with solid-state reaction. R_{exp}: expected residual factor; R_{wp}: weighted profile residual factor; R_p: profile residual factor; GOF: goodness of fit. Values in parentheses are the estimated standard deviations of the last significant figure.

Rietveld refinement parameters		**Calculated**
Symmetry	Monoclinic	Monoclinic
Space group	$P2_1/m$	$P2_1/m$
a/nm	0.581998(9)	0.58308
b/nm	0.563362(8)	0.56386
c/nm	0.665907(9)	0.66545
β/°	106.483(1)	106.70
Volume/nm^3	0.209362(6)	0.20956
R_{exp} (%)	3.26	-
R_{wp} (%)	9.11	-
R_p (%)	6.69	-
GOF	2.79	-

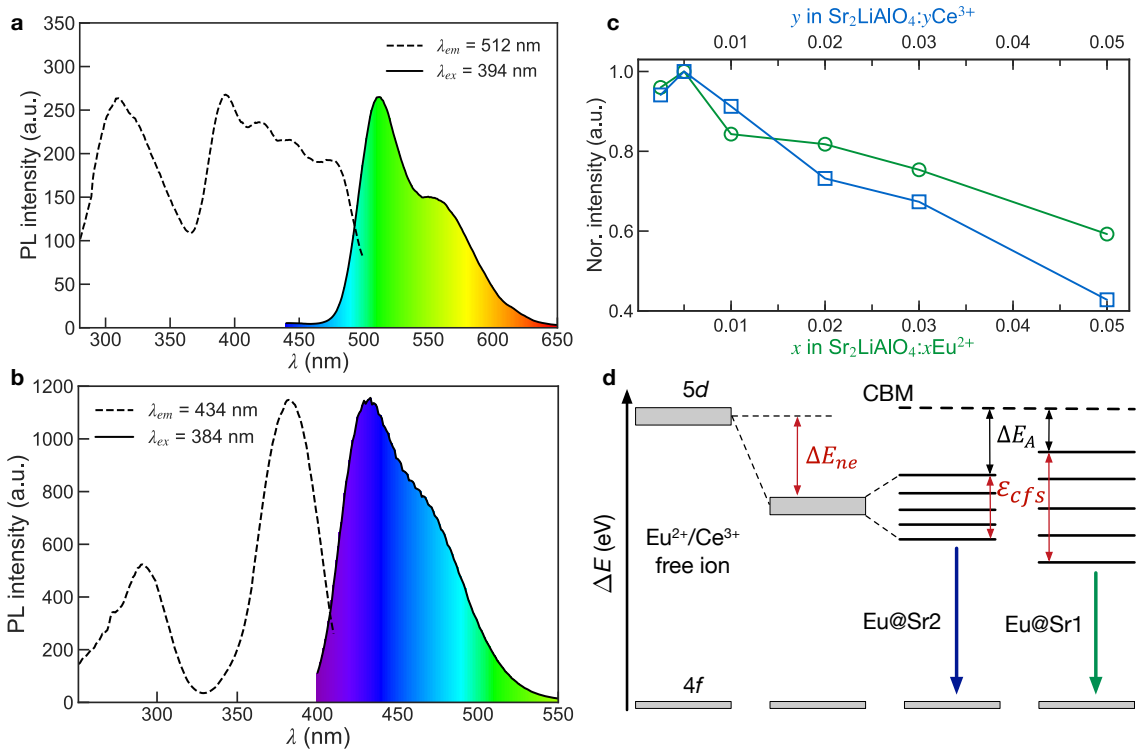

Figure 4.7 Photoluminescence properties of the Sr_2LiAlO_4:$x$$Eu^{2+}$ and Sr_2LiAlO_4:$y$$Ce^{3+}$ phosphors. Measured excitation and emission spectra of (a) Sr_2LiAlO_4:0.005Eu^{2+} and (b) Sr_2LiAlO_4:0.005Ce^{3+} phosphor. Colors are indicated under the emission spectra for easy reference. Normalized emission intensity of (c) Sr_2LiAlO_4:$x$$Eu^{2+}$ (under 394 nm excitation, green curve) with respect to the Eu^{2+} (x) concentration and Sr_2LiAlO_4:$y$$Ce^{3+}$ (under 384 nm excitation, blue curve) with respect to the Ce^{3+} (y) concentration. (d) Schematic energy level diagram for Eu^{2+}/Ce^{3+} ions in the Sr_2LiAlO_4 host crystal structure. ΔE_{ne} and ε_{cfs} denote the centroid shift due to the nephelauxetic effect and the crystal field splitting of Eu^{2+}/Ce^{3+} ions in the Sr_2LiAlO_4 host, respectively. ΔE_A is the photoionization barrier.

4.4.3 Photoluminescence Properties

The measured PL spectrum of the Sr_2LiAlO_4:0.005Eu^{2+} phosphor excited at 394 nm (Figure 4.7a) shows a green-yellow emission peaking at 512 nm with a shoulder peak of 559 nm. The emission spectrum is broad (FWHM = 73.6 nm) and asymmetric, indicating that Eu^{2+} ions occupy two distinct sites in the Sr_2LiAlO_4 host. The excitation spectrum monitored at 512 nm shows a broad band with two main peaks at 310 nm and 394 nm. The PL spectrum of the

Sr_2LiAlO_4:0.005Ce^{3+} phosphor measured at 384 nm excitation (Figure 4.7b) shows a broad blue emission with a main peak at 434 nm and a FWHM of 70.3 nm. The PL excitation recorded at 434 nm also presents two peaks – one major peak at 384 nm and one minor peak at 291 nm. The measured excitation spectra are consistent with the 4*f*-5*d* transitions of Eu^{2+}/Ce^{3+} ions, and the BSE-computed excitation wavelengths in Figure 4.5.

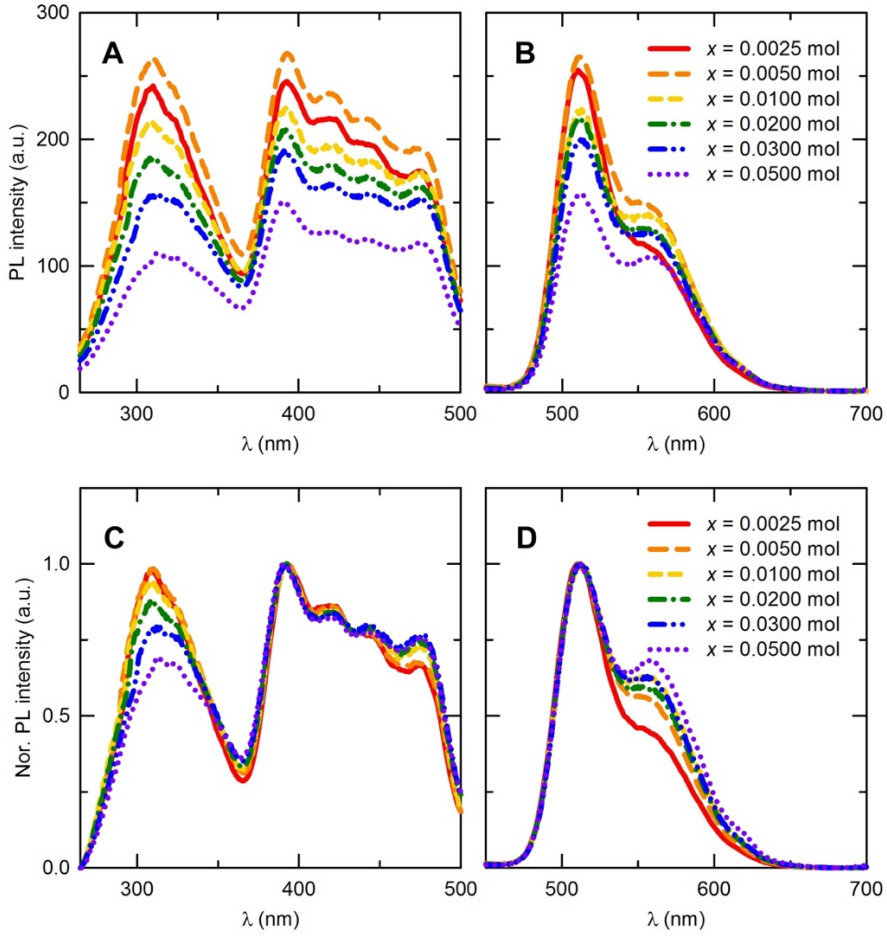

Figure 4.8 Photoluminescence excitation and emission spectra of Sr_2LiAlO_4:*x*Eu^{2+} phosphors. (A) Excitation and (B) emission spectra of Sr_2LiAlO_4:*x*Eu^{2+} phosphors and the normalized (C) excitation and (D) emission spectra of Sr_2LiAlO_4:*x*Eu^{2+} phosphors with respect to Eu^{2+}concentration.

A careful optimization of the PL properties of Sr_2LiAlO_4:*x*Eu^{2+} and Sr_2LiAlO_4:*y*Ce^{3+} was carried out with respect to activator concentration (*x, y*). As shown in Figure 4c, the emission

intensity slightly increases and then decreases with increasing activator concentration, with the maximum emission intensity occurring at x *or* $y = 0.005$ for both activators. The measured internal quantum efficiencies of the $Sr_2LiAlO_4:0.005Eu^{2+}$ and $Sr_2LiAlO_4:0.005Ce^{3+}$ phosphors are 25% (λ_{ex} = 394 nm) and 32% (λ_{ex} = 392 nm), respectively.

Figure 4.8 presents the unnormalized and normalized PL spectra of $Sr_2LiAlO_4:xEu^{2+}$ with respect to a series of Eu^{2+} concentrations ($0.0025 \leq x \leq 0.0500$) measured at room temperature. With increasing Eu^{2+} concentration, the relative intensity of short excitation wavelength (at 320 nm) gradually decreases, while the relative intensity of long wavelength (at 480 nm) slightly increases, as shown in Figure S4c. At the same time, a corresponding increase of emission intensity at 559 nm is also observed with increasing of Eu^{2+} concentration when normalized based on emission intensity at 512 nm, as shown in Figure 4.8d. We believe the lower energy emission (longer wavelength) peaks are associated with more Eu^{2+} occupying the energetically more favorable Sr1 site. The calculated average bond length (l_{av}) of EuO_8 polyhedron in the Sr1 site and Sr2 site are 0.269 nm and 0.272 nm, respectively, while the distortion indices (D) (see Methods for definitions) are 0.056 and 0.044, respectively. A shorter l_{av} and larger D is associated with a larger crystal field splitting (CFS) [174, 180]. The larger CFS of Eu^{2+} in the Sr1 site leads to a red shift in emission, as illustrated in Figure 4.7d. These conclusions are further supported by deconvolution of the PL emission spectra of $Sr_2LiAlO_4:0.005Eu^{2+}$ at 10 K and 298 K (Figure 4.9a and 4.9b), which shows a significant decrease in the long wavelength emission at room temperature. The lower thermal stability of the Eu in the Sr1 site is also a consequence of its larger CFS, which leads to a smaller barrier for photoionization (ΔE_A) [100]. To obtain further support for these conclusions, we calculated the HSE projected density of states (Figure 4.10) for a $Sr_2LiAlO_4:Eu^{2+}$ structure where Eu is introduced into both Sr1 and Sr2 simultanenously. We find

that Eu in the Sr1 site has a smaller gap (longer excitation wavelength) between the 4*f* and 5*d* states compared to Eu in the Sr2 site.

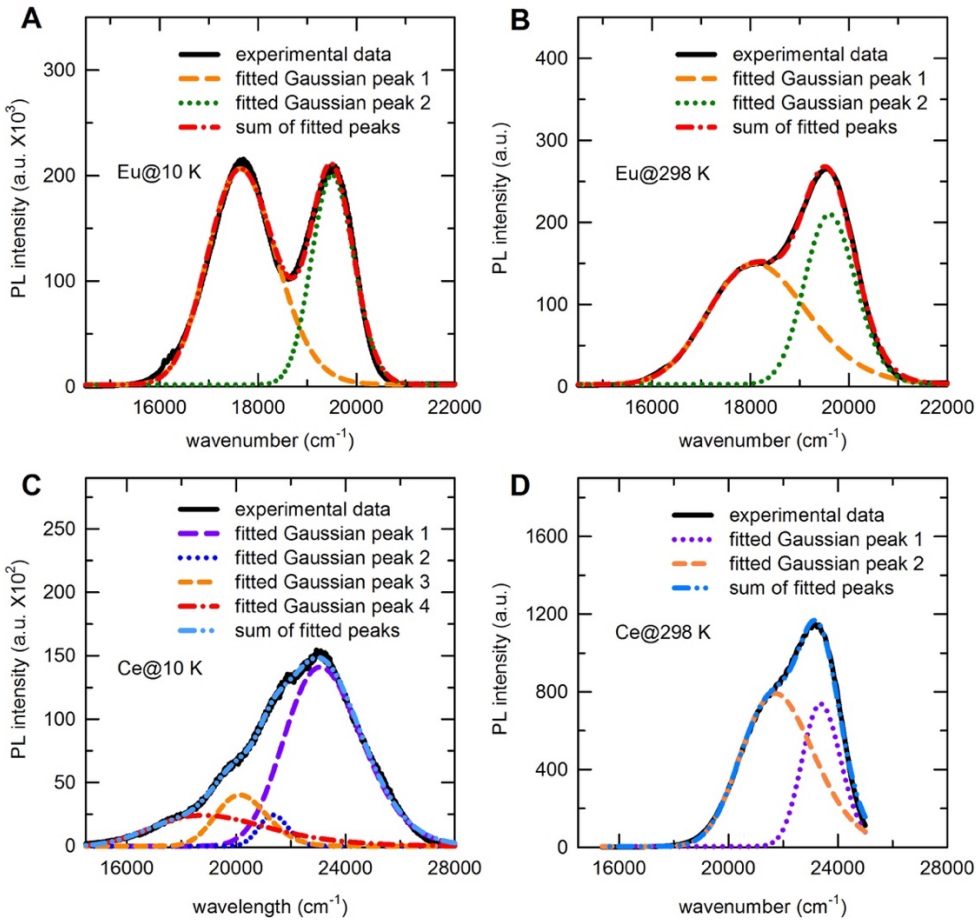

Figure 4.9 Deconvolution of emission spectra of Eu^{2+}/Ce^{3+}-activated Sr_2LiAlO_4 phosphors. Deconvoluted photoluminescence emission spectra (A-B) of Sr_2LiAlO_4:0.005Eu^{2+} at 10 K and 298 K, respectively and (C-D) of Sr_2LiAlO_4:0.005Ce^{3+} phosphors at 10 K and 298 K, respectively.

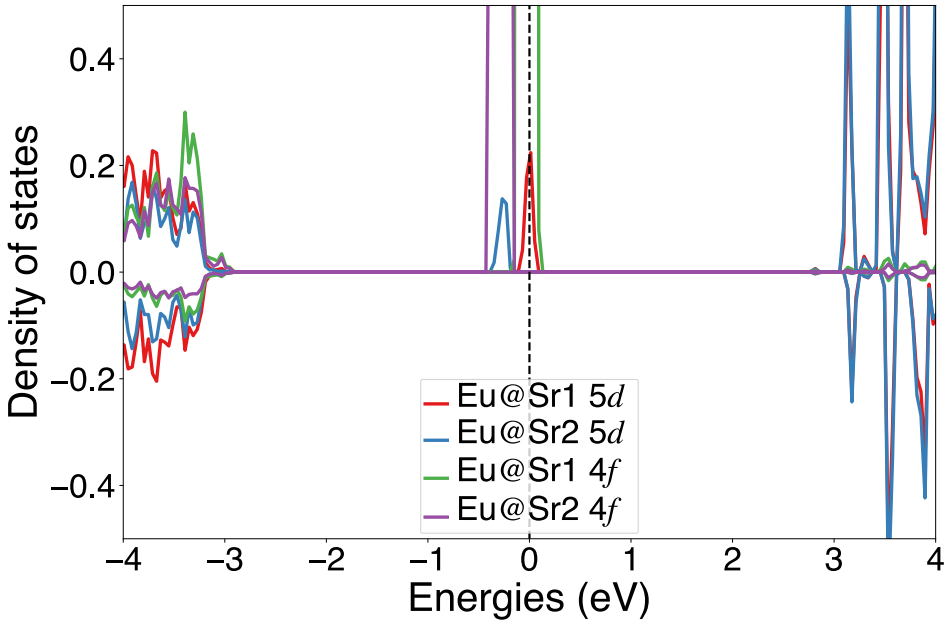

Figure 4.10 Projected density of states of Sr_2LiAlO_4:0.028Eu^{2+}. A 3 × 3 × 2 supercell of Sr_2LiAlO_4 (72 formula units) was constructed with two Eu atoms, one on the Sr1 site and the other on the Sr2 site.

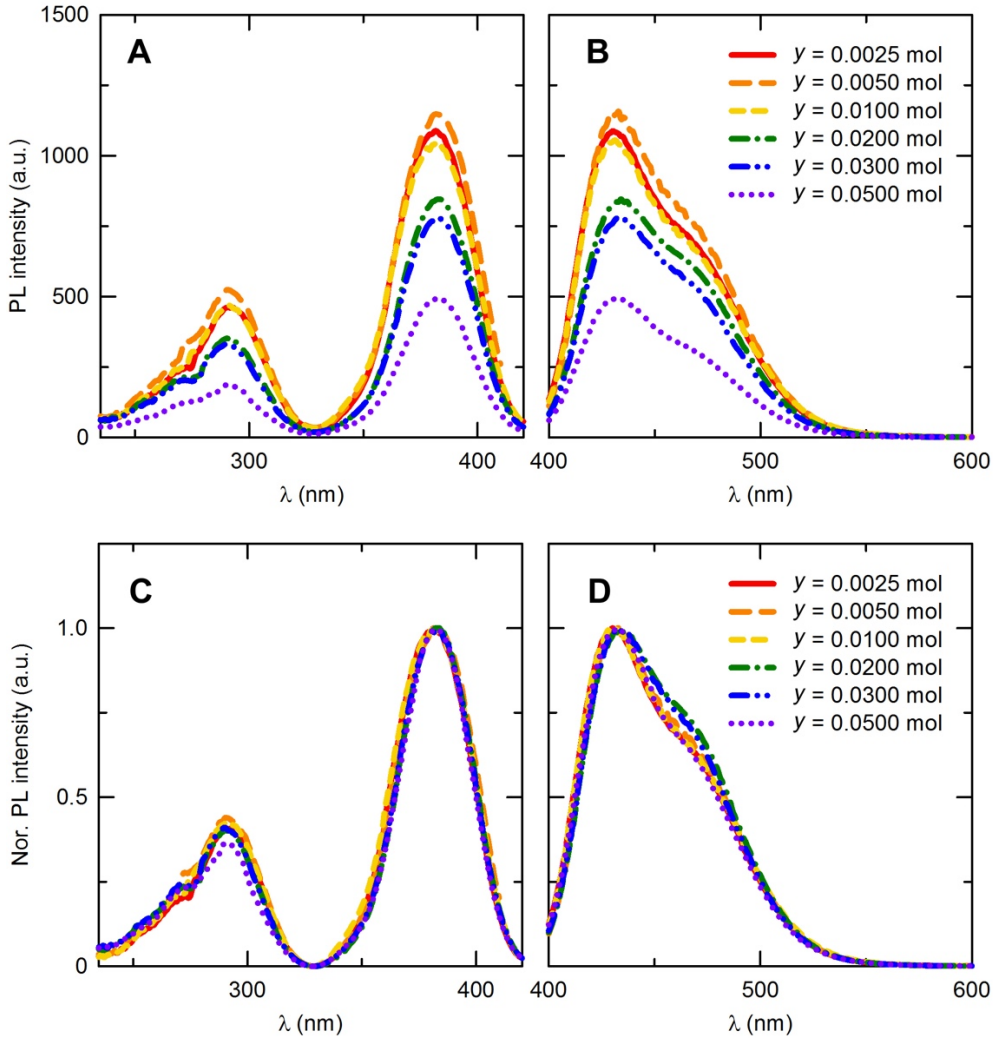

Figure 4.11 Photoluminescence excitation and emission spectra of Sr_2LiAlO_4:$y$$Ce^{3+}$ phosphors. (A) Excitation and (B) emission spectra and the normalized (C) excitation and (D) emission spectra of Sr_2LiAlO_4:$y$$Ce^{3+}$ phosphors with respect to Ce^{3+} concentration.

In contrast, there are no significant changes in the relative intensities of both the excitation and emission peaks at different wavelengths with increasing of Ce^{3+} concentration in Sr_2LiAlO_4:$y$$Ce^3$ (Figure 4.11). The emission spectra of Sr_2LiAlO_4:0.005Ce^{3+} can be deconvoluted into four Gaussian peaks at 10 K with position of 433 (peak 1: 23,095 cm^{-1}), 468 (peak 2: 21,368 cm^{-1}), 497 (peak 3: 20,121 cm^{-1}), and 532 nm (peak 4: 18,797 cm^{-1}), as shown in Figure 4.9c. The energy difference between peak 1 and peak 3 is about ~2,974 cm^{-1} (0.37 eV), and between peak 2

and peak 4 is about ~2,571 cm^{-1} (0.32 eV). These values correspond to the spin-orbit splitting energy of the lowest 4*f* level ($^2F_{5/2}$ and $^2F_{7/2}$) in Ce^{3+} [20]. However, at 298 K (Figure 4.9d), only two Gaussian peaks are observed at 427 nm (23,419 cm^{-1}) and 460 (21,739 cm^{-1}). These observations again suggest that the Sr1 site, associated with the long wavelength emission, is thermally unstable with no PL at room temperature.

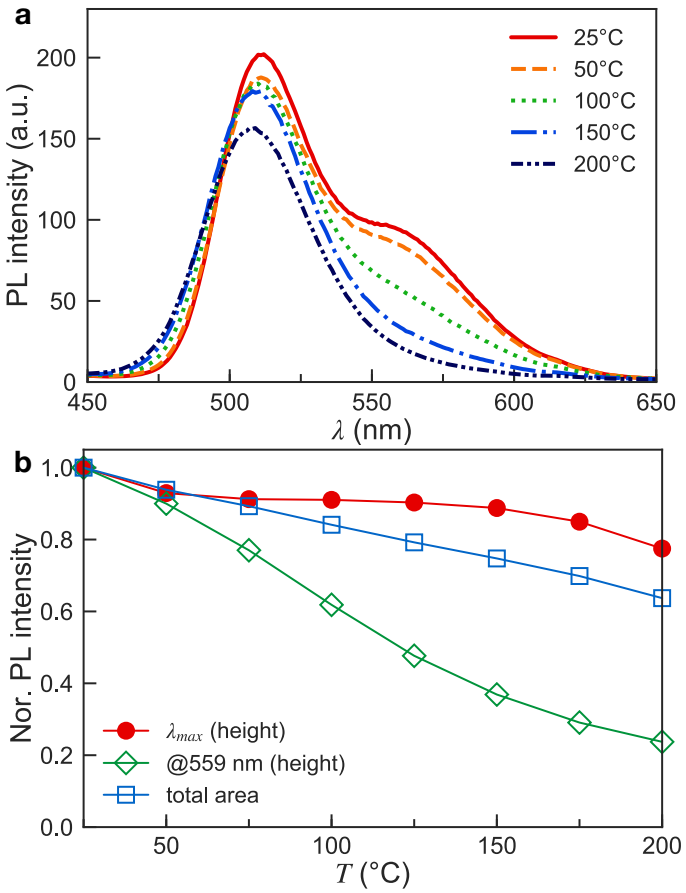

Figure 4.12 Thermal quenching and site dependent photoluminescence properties of Sr_2LiAlO_4:0.005Eu^{2+}. (a) Temperature-dependent emission spectra under 394 nm excitation in the temperature range of 25~200°C. (b) Normalized temperature-dependent emission intensity under the peak emission wavelength (λ_{max}), 559 nm and integrated emission intensity (total area) with a temperature interval of 25°C.

4.4.4 Thermal Stability

In practical applications, WLEDs typically operate at elevated temperatures (~150°C), and a key metric of phosphor performance is its resistance to thermal quenching. Figure 4.12 shows the measured temperature-dependent emission intensity for Sr_2LiAlO_4:0.005Eu^{2+}. At 150°C, the emission intensity of the main peak (λ_{em} = ~512 nm) is about 88% of that at room temperature. The emission intensity of secondary peak (λ_{em} = ~559 nm), which is associated with Eu^{2+} in the thermally less stable Sr1 site on the other hand, reduces significantly with increasing temperature. Overall, Sr_2LiAlO_4:0.005Eu^{2+} exhibits excellent resistance to thermal quenching. The Sr_2LiAlO_4:0.005Ce^{3+} phosphor is found to have a slightly better resistance to thermal quenching, retaining 91% of room-temperature peak emission intensity at 150°C (Figure 4.13).

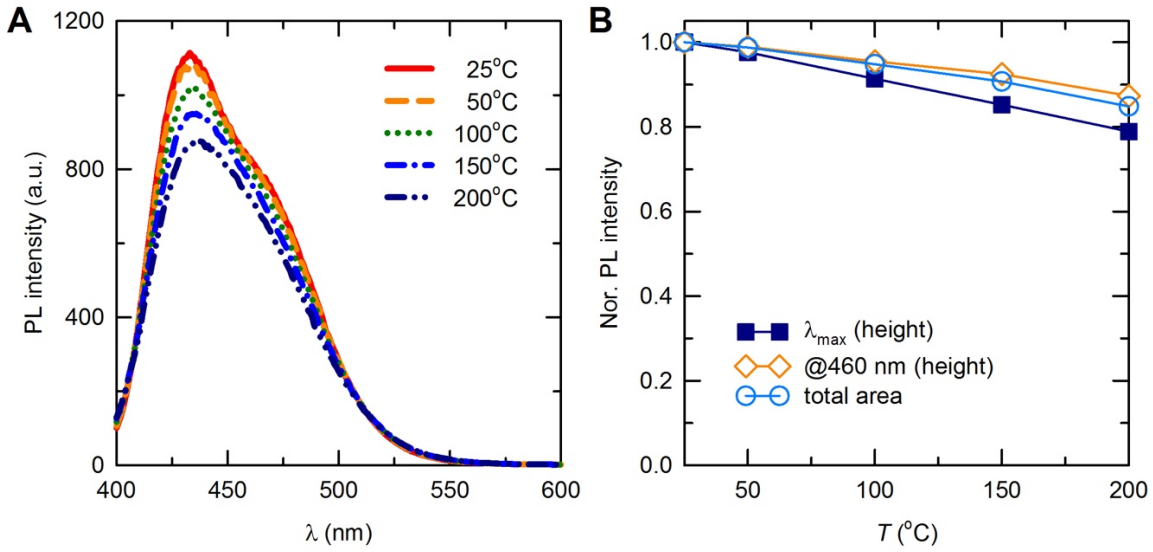

Figure 4.13 Thermal quenching of Sr_2LiAlO_4:0.005Ce^{3+}. (A) Temperature-dependent emission spectra under 382 nm excitation in the temperature range of 25-200ºC. (B) Temperature-dependent normalized emission spectra under the peak emission wavelength, 460 nm and integrated emission intensity with a temperature interval of 25ºC.

4.4.5 Performance of pc-WLEDs

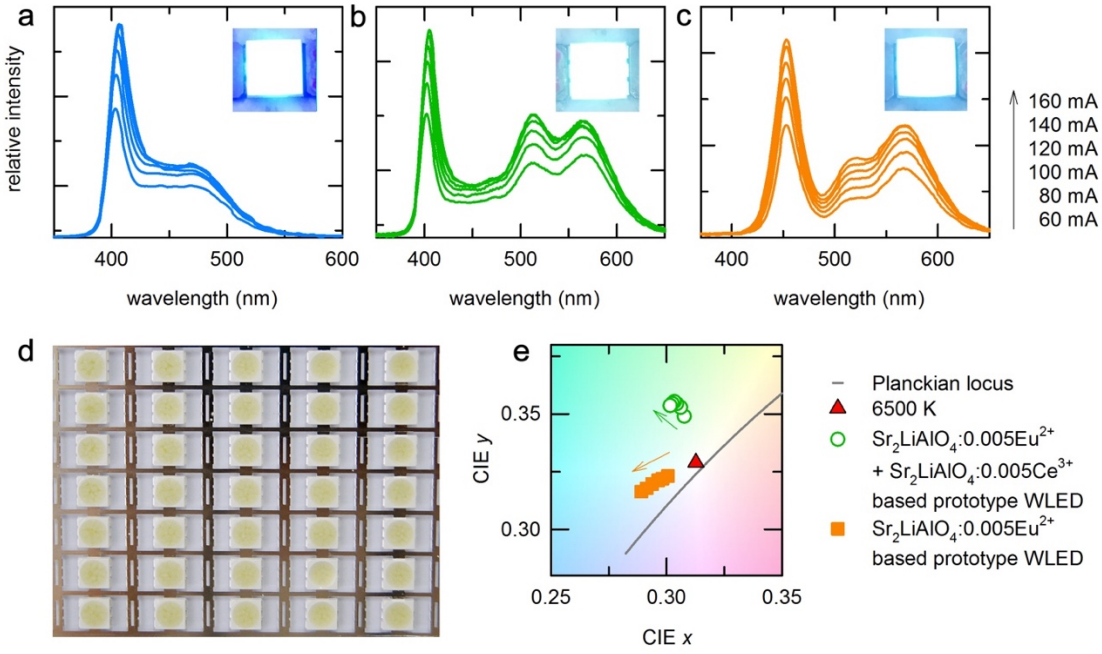

Figure 4.14 Performance of prototype pc-WLED using the single $Sr_2LiAlO_4:Ce^{3+}$ and $Sr_2LiAlO_4:Eu^{2+}$ phosphor. (a) Electroluminescence (EL) spectra and photograph of the InGaN LED (λ_{max} = 400 nm) + $Sr_2LiAlO_4:0.005Ce^{3+}$ phosphor. (b) EL spectra and photograph of the InGaN LED (λ_{max} = 400 nm) + $Sr_2LiAlO_4:0.005Ce^{3+}$ + $Sr_2LiAlO_4:0.005Eu^{2+}$ phosphor. (c) EL spectra and photograph of the InGaN LED (λ_{max} = 450 nm) + $Sr_2LiAlO_4:0.005Eu^{2+}$ phosphor. (d) photo of WLEDs packaged with $Sr_2LiAlO_4:0.005Eu^{2+}$ phosphor. (e) CIE chromatic coordinated of the fabricated Sr_2LiAlO_4-based phosphors WLED under various forward bias currents.

Finally, we constructed a prototype WLED device using $Sr_2LiAlO_4:Eu^{2+}$, $Sr_2LiAlO_4:Ce^{3+}$ as well as a mixture of $Sr_2LiAlO_4:Eu^{2+}/Ce^{3+}$. The electroluminescence (EL) spectra of these WLEDs are shown in Figure 6a-c. The prototype WLED using $Sr_2LiAlO_4:Eu^{2+}$ exhibits CIE color coordinates of 0.301 and 0.323, with high CRI of 93 and a CCT of 7527 K at a forward bias current of 60 mA (Table 4.3). The excellent CRI of the $Sr_2LiAlO_4:Eu^{2+}$ phosphor can be attributed to the feature of its broad band emission by two Sr sites. The CCT of the WLED can be further lowered by using a mixture of $Sr_2LiAlO_4:Eu^{2+}/Ce^{3+}$, as shown in Table S4, as well as via the addition of a

red component. For instance, the recently reported $SrLiAl_3N_4:Eu^{2+}$ narrow-band red phosphor[1] would be a particularly interesting option, which would allow for the construction of an oxide + nitride device using the same earth-abundant elements. To further improve the quantum efficiency of Sr_2LiAlO_4, crystal-site engineering techniques [162, 176], e.g., co-doping with Ba or Ca, may be used to shift the energetic preference and/or tune the CFS of the two Sr sites.

4.5 Conclusion

To conclude, we have identified a novel earth-abundant Sr_2LiAlO_4 phosphor host – the first known Sr-Li-Al-O quaternary compound – by composing a "solid-state lighting" periodic table based on statistical analysis of the ICSD to identify unexplored, yet promising chemical spaces with data-mined structure prediction and high-throughput DFT property computations. Sr_2LiAlO_4 comprises inexpensive, earth-abundant elements (other than the rare-earth activator, which is required in small quantities), and the DFT and PL results show $Sr_2LiAlO_4:Eu^{2+}/Ce^{3+}$ to have efficient near-UV excitation, good thermal quenching resistance and broad green-yellow/blue emission. High purity Sr_2LiAlO_4-based phosphors can be synthesized with scalable, industrially-relevant methods. We therefore believe the novel $Sr_2LiAlO_4:Eu^{2+}/Ce^{3+}$ phosphors to be highly promising candidates for low-cost, high-CRI WLED applications.

Chapter 4, in full, is a reprinted of the materials as it appears in "Mining Unexplored Chemistries for Phosphors for High-Color-Quality White-Light-Emitting Diodes", *Joule*, 2, 1-13, 2018. This work was coauthored by Z. Wang, Y. H. Kim, J. McKittrick, S. P. Ong, W. B. Im are the corresponding authors. The dissertation author is the first author of this work.

CHAPTER 5: COLOR TUNABLE SINGLE-PHASE Eu^{2+} AND Ce^{3+} CO-ACTIVATED Sr_2LiAlO_4 PHOSPHORS

5.1 Abstract

High purity Eu^{2+} and Ce^{3+} singly and co-activated Sr_2LiAlO_4 phosphors were successfully synthesized through a facile combustion reaction. Fabrication of color tunable, single-phase phosphors was achieved by varying the Eu^{2+}/Ce^{3+} ratio that utilized the energy transfer between Ce^{3+} to Eu^{2+}. For the singly activated compositions, the highest quantum efficiencies were 25% and 40% for $Sr_{1.998}Eu_{0.002}LiAlO_4$ and $Sr_{1.998}Ce_{0.002}LiAlO_4$, respectively. The emission of $Sr_2LiAlO_4:Ce^{3+}$ and the excitation of $Sr_2LiAlO_4:Eu^{2+}$ overlap in the range of 400 nm - 500 nm, so that energy transfer from $Ce^{3+} \rightarrow Eu^{2+}$ takes place. The emission color of Eu^{2+} and Ce^{3+} co-activated Sr_2LiAlO_4 changes from blue, to cool-white, to green depending on the activator concentrations. The maximum quantum efficiency of Eu^{2+} and Ce^{3+} co-activated Sr_2LiAlO_4 was 55%, a 40% increase over the singly activated phosphors, which demonstrates that the quantum efficiency improves by co-activation.

5.2 Introduction

Phosphor-converted white-light-emitting diodes (pc-WLEDs) are considered as the most promising next generation solid-state lighting technology due to their longer life time, superior efficiency, and low operating temperatures compared with traditional incandescent bulb and fluorescent lamp technologies [44, 79, 151]. Typical approaches to produce pc-WLEDs is a combination a blue-emitting (450 nm) InGaN LED with yellow-emitting phosphors ($Y_3Al_5O_{12}:Ce^{3+}$), but it suffers from a low color rendering index (CRI) value < 80 and high correlated color temperature CCT > 5000 K due to a lack of red emission [181-183]. To improve

the CRI and CCT, an alternative approach is to utilize near-UV (380-420 nm) LEDs with a mixture of red, green, and blue (RGB) phosphors [15]. However, in the RGB phosphors converted system, the efficiency of blue emission is poor due to the strong re-absorption of blue light by the red and green phosphors. Single phase phosphors are considered as a possible solution to avoid this re-absorption issue [184-186]. In the LED device, heat generation occurs during LED lighting operation (~200ºC), leading to emission loss from the phosphors (thermal quenching) is also an important property to be considered [75, 151].

There are several methods to produce white light or color tunable light in single-phase phosphors with (1) single rare earth ions such as Eu^{3+}, Eu^{2+}, or Dy^{3+} as an activator in proper hosts [187, 188]; (2) the combination of multiple rare earth ions such as $Tm^{3+}/Tb^{3+}/Sm^{3+}$ and $Tm^{3+}/Tb^{3+}/Eu^{3+}$ emitting blue, green and yellow, or blue and yellow light [189]; (3) rare earth ion pair co-activators to use energy transfer mechanisms such as $Ce^{3+} \rightarrow Eu^{2+}$, $Ce^{3+}/Eu^{2+} \rightarrow Tb^{3+}$, $Eu^{2+} \rightarrow Mn^{2+}$, or $Ce^{3+} \rightarrow Mn^{2+}$ [190-199]; and (4) emission of white light by controlling the point defect concentration [200, 201].

In the rare-earth ion pair co-activators, luminescent properties of single phase phosphors with Ce^{3+} and Tb^{3+} have been reported [190, 192, 202-205], showing that the color could be adjusted between blue- (Ce^{3+}) and green-, (Tb^{3+}) emissions, depending on the activator concentrations. For example, Jia et al. [190] reported a color tunable phosphor $NaBa_3La_3Si_6O_{12}:Ce^{3+},Tb^{3+}$. The emission of $NaBa_3La_3Si_6O_{12}:0.07Ce^{3+}$ was a broad band ranging from 340 nm to 500 nm in the blue emitting range for the excitation wavelength (λ_{ex}) of 331 nm. On the other hand, λ_{ex} of $NaBa_3La_3Si_6O_{12}:0.02Tb^{3+}$ were 268 nm and 378 nm. Energy transfer from $Ce^{3+} \rightarrow Tb^{3+}$ enhanced the green emission of Tb^{3+} due to the overlapping emission band of Ce^{3+} and excitation band of Tb^{3+} and color tunable emission from blue to green was achieved,

depending on the Ce^{3+} and Tb^{3+} concentrations. Quantum efficiency (Φ) was not reported for this phosphor.

Single-phase phosphors activated by Ce^{3+} and Eu^{2+} have been studied for application in solid state lighting devices [193, 195-199]. For the blue emitting phosphor, co-activated $Ca_8La_2(PO_4)_6O_2$:$0.04Ce^{3+}$,$0.02Eu^{2+}$ [195], Φ (43%) was enhanced compared to that of the single activator Eu^{2+} (13%). Furthermore, the color tunable (blue to yellow) phosphors Li_2SrSiO_4:xEu^{2+}:$0.01Ce^{3+}$ ($0.0025 \leq x \leq 0.01$) were studied to examine the energy transfer from $Ce^{3+} \rightarrow Eu^{2+}$ [196]. The emission intensity of Eu^{2+} was enhanced with Ce^{3+} co-activator although the Φ was not reported. Ce^{3+} and Eu^{2+} co-activated Ca_2BO_3Cl phosphors exhibited a color change from blue to yellow with $0.06Ce^{3+}$ and $0.015Eu^{2+}$ having CIE coordinates (0.326, 0.334) that are close to the white point (0.33, 0.33) [197]; however the Φ value was not reported. An emission wavelength shift from 461 to 494 nm was found for $Sr_{0.96-y}SiAl_2O_3N_2$:$0.04Ce^{3+}$,yEu^{2+} ($0 \leq y \leq 0.06$), because the emission from Eu^{2+} increased and the emission from Ce^{3+} decreased with an increase in y. The substitution of Ba in $Sr_{0.96-x}Ba_xSiAl_2O_3N_2$:$0.04Ce^{3+}$:$0.04Eu^{2+}$ ($0 \leq x \leq 0.92$) showed an emission shift from 491 nm to 505 nm, but Φ values were not reported. The series xEu^{2+} and yCe^{3+} in Li_2SrSiO_4 were prepared for white emission by a combinatorial approach [199]. A bright yellow luminescence was shown with $x = 0.005$ - 0.060 and $y = 0$. The yellow emission decreased with an increase in the concentration of Ce^{3+}, emitting bright blue light with $x = 0$ and $y = 0.005$ - 0.050. The CIE color coordinates, Φ and thermal quenching at 150˚C were (0.359, 0.341), 27%, and 69%, respectively [75, 151]. These previous studies using Eu^{2+} and Ce^{3+} as co-activators in a single-phase phosphor demonstrated that color tunable ability can be achieved and Φ can be enhanced.

This is the first report on the preparation and analysis of co-activated $Sr_{2-x-y}Eu_xCe_yLiAlO_4$. Building on our recently reported phosphors [71], $Sr_{2-x}Eu_xLiAlO_4$ (green-emitting) and $Sr_{2-y}Ce_yLiAlO_4$ (blue-emitting) were used to explore the possibility of fabricating color-tunable, single phase compositions. The purity of Sr_2LiAlO_4 synthesized by combustion reaction was reported previously [71], however, the present work provides new findings on the effect of (1) post-annealing temperature on the amount of impurity phases and (2) the addition of excess Li ions to compensate for Li loss during processing. The optimum concentrations of Ce^{3+} or Eu^{2+} were determined and the emission color changes were examined as a function of the concentration of Ce^{3+} and Eu^2. The improved Φs are investigated in Eu^{2+} and Ce^{3+} co-activated combustion reaction powders.

5.3 Experimental

5.3.1 Synthesis of host Sr_2LiAlO_4 and $Sr_2LiAlO_4:Eu^{2+}/Ce^{3+}$

All chemicals were used without further purification. Synthesis of host Sr_2LiAlO_4, $Sr_{2-x}Eu_xLiAlO_4$ ($0.001 \leq x \leq 0.040$), $Sr_{2-y}Ce_yLiAlO_4$ ($0.001 \leq x \leq 0.040$), and $Sr_{2-x-y}Eu_xCe_yLiAlO_4$ ($0.0005 \leq x, y \leq 0.05$) were performed through the combustion reaction using $Sr(NO_3)_2$ (99.99%, Sigma Aldrich), $LiNO_3$ (ReagentPlus, Sigma Aldrich), $Al(NO_3)_3 \bullet 9H_2O$ (ACS reagent, J. T. Baker), $Eu(NO_3)_3$ from Eu_2O_3 (99.99%, Alfa Aesar) with nitric acid (69.3%, Fisher Scientific), and $Ce(NO_3)_3$ (99.99%, Alfa Aesar) as precursors, assisted by the exothermic reaction between urea (Certified ACS, Fisher Scientific) and ammonium nitrate (Certified ACS, Fisher Scientific) at 600°C.

For Solution 1, $Sr(NO_3)$, $LiNO_3$, and $Al(NO_3)_3$ in the molar ratio of 2:1:1 was added to 50 mL of deionized water in a 100 mL beaker with a magnetic stirrer. Solution 2 consisted of the

desired amount of Eu_2O_3, which had been dissolved in 4 mL of nitric acid in a beaker to prepare $Eu(NO_3)_3$. For $Sr_{2-x}Eu_xLiAlO_4$ the desired amount of Solution 2 was introduced into Solution 1. For undoped Sr_2LiAlO_4, Solution 2 was not needed. For $Sr_{2-x}Ce_xLiAlO_4$, Solution 1 was used and the desired amount of $Ce(NO_3)_3$ was added. For $Sr_{2-x-y}Eu_xCe_yLiAlO_4$, Solution 2 and $Ce(NO_3)$ were introduced in Solution 1. Urea (1 g, CH_4N_2O) and ammonium hydroxide (1.3 g), with the molar ratio of urea/ammonium hydroxide = 1:1, were added into the solutions. After achieving transparency, it was poured into a large Pyrex beaker and placed into a muffle furnace at 600°C.

The solution boiled and after ~ 5 min. burst into flame due to the exothermic reaction of urea and the nitrates, producing a white-colored powder. The reaction during combustion is:

$$2Sr(NO_3)_2\,(s) + LiNO_3\,(s) + Al(NO_3)_3\,(s) + CH_4N_2O\,(s) + 3(NH_4)(NO_3)\,(s) \rightarrow Sr_2LiAlO_4\,(s) + 8N_2\,(g) + 10O_2\,(g) + 8H_2O\,(g) + CO_2\,(g)$$

Post-annealing was performed between 700 ºC and 850 ºC **for 1-5 h** in a 5%H_2 / 95%N_2 atmosphere to transform Eu^{3+} to Eu^{2+}. In some experiments, excess Li precursor was added in amounts up to 30 mol.% to compensate for Li sublimation during synthesis [206].

5.3.2 **Characterization**

The powders were analyzed by X-ray diffraction (XRD, Bruker D2 Phaser, Karlsruhe, Germany) using CuKα radiation and a step size of 0.014° over a 2θ range of 20 to 80°. Structural information of the synthesized samples was derived by refinement using the TOPAS 4.2 software (Bruker) suite from the XRD result. The calculated XRD data were taken from [71]. A field emission scanning electron microscope (FESEM, XL30, Philips, Amsterdam, Netherlands) at 10 keV was used to image the powders to determine size morphology. Samples were coated with iridium at 85 μA for 10 s before imaging. Quantum efficiency (Φ) measurements, photoluminescence (PL) emission and excitation spectra were performed using Hamamatsu

C9920-02 (Hamamatsu City, Shizuoka, Japan). Absolute Φ measurements were performed using an integrating sphere system, with sodium salicylate (Φ = 44%) as a reference standard. Φ is the ratio of the number of photons collated by the sample to the number of photons emitted from the sample: Φ = photons out/photons in. Color coordinates were obtained using ColorCalculator program (version 7.23, OSLAM SYLVANIA Inc., Beverly, MA, USA) by analyzing the emission spectra from the PL analysis. Thermal quenching analysis (25°C to 150 °C) was performed using a custom designed device that consists of a heater, thermocouple, and the spectrophotometer.

5.4 Results and Discussions

5.4.1 Synthesis of host Sr_2LiAlO_4, Eu^{2+} or Ce^{3+} activated Sr_2LiAlO_4

The optimal post-annealing condition was examined through XRD analysis (Figure 5.1a) resulting in the desired Sr_2LiAlO_4 phase with some impurities. Impurity peaks of $SrAl_4O_7$ and $Sr_2Al_6O_{11}$ are located at ~25º and ~27º, respectively. Post-annealing treatment at 700ºC for 1 hour produced 73 mol.% of Sr_2LiAlO_4 with 25 mol.% of $SrAl_4O_7$ and 2 mol.% of $Sr_2Al_6O_{11}$. Post-annealing at 800ºC for 1 hour reduced the amount of impurities (18 mol.% $SrAl_4O_7$, 3 mol.% $Sr_2Al_6O_{11}$) as illustrated in Figure 5.1a. After annealing at 850ºC for 5 h, the intensity of the (110) reflection at ~22º decreased, possibly arising from defects within the structure. The intensity in the XRD diffraction patterns is proportional to modulus squared of the structure factor, $I_{hkl} \propto |F_{hkl}|^2$ and the structure factor, F_{hkl}, is sum of the ionic locations value that are proportional to ionic scattering factor, f_j [207]. When one or more ions are absent on the plane, the f_j value of the absent ions is equal to zero, therefore the value of F decreases along with the corresponding diffraction intensity. The intensity of the (110) reflection at ~22º decreased with the post-annealing of 850ºC for 5 h, indicating that the one or more ions are absent on the plane. The decrease in the intensity

of diffraction peaks with vacancies on the diffraction plane has been shown in previous literature [208].

An impurity peak from $Sr_4Al_{14}O_{25}$ at ~26º was also found. The condition of 800ºC for 5 hours was selected as the optimal to obtain high crystallinity that typically occurs for high temperature annealing [209] and fewer impurities (7 wt.% $SrAl_4O_7$, 5 wt.% $Sr_2Al_6O_{11}$).

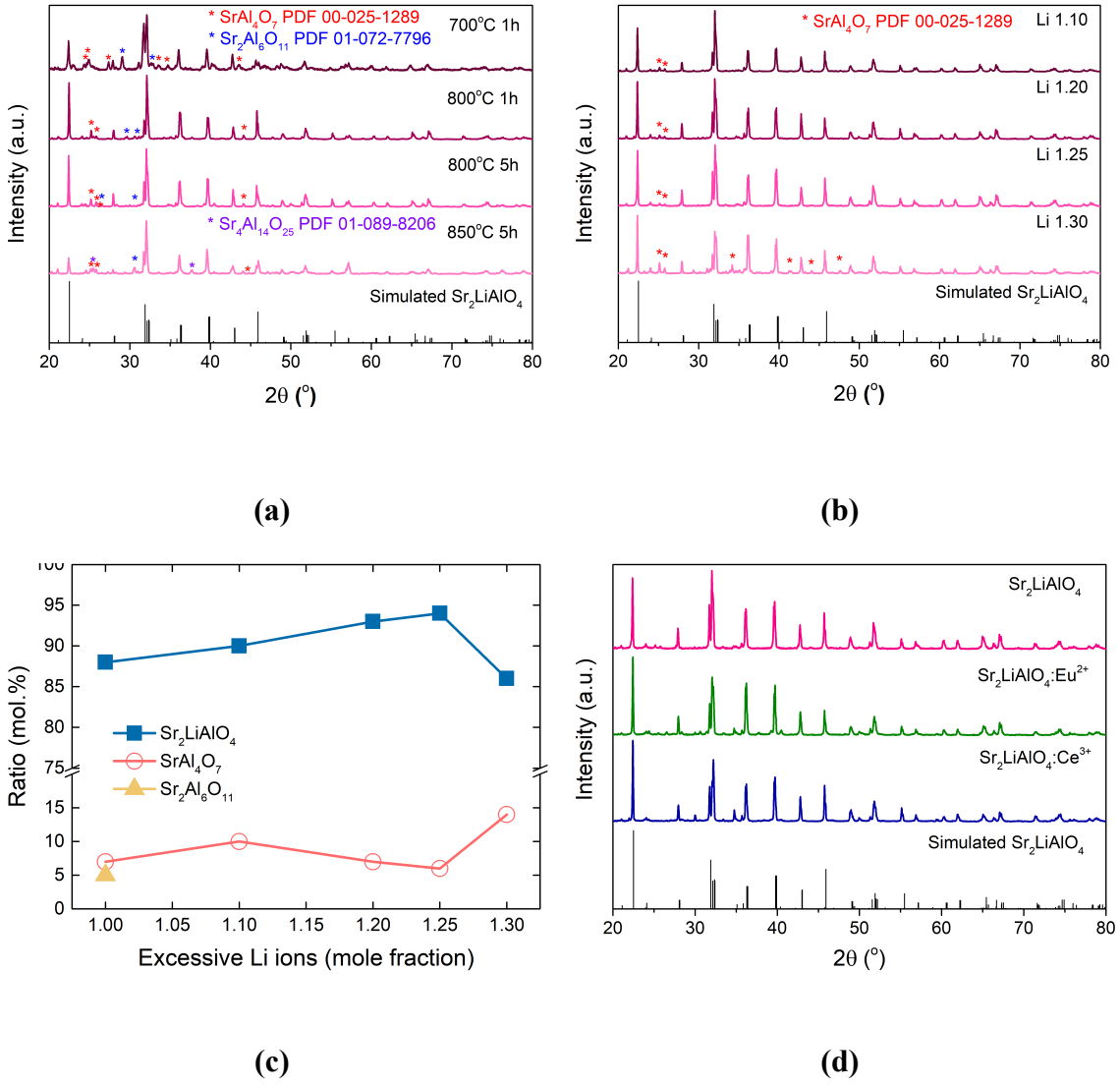

Figure 5.1 X-ray diffraction patterns of Sr_2LiAlO_4 with **(a)** different post annealing conditions and **(b)** different concentration of Li ions. **(c)** The ratio of Sr_2LiAlO_4 and impurities ($SrAl_4O_7$ and $Sr_2Al_6O_{11}$) with the excessive of Li ions. **(d)** X-ray diffraction patterns of Sr_2LiAlO_4, $Sr_2LiAlO_4:Eu^{2+}$, and $Sr_2LiAlO_4:Ce^{3+}$.

Table 5.1 The obtained R_{wp}, R_p, GOF values after Reitveld refinement for 1.00, 1.10, 1.20, 1.25, 1.30 mole fractions of Li ions in Sr_2LiAlO_4.

Excess Li ions (mole fraction)	R_{wp}	R_p	GOF
1.00	13.22	9.17	2.55
1.10	13.79	9.76	2.45
1.20	11.75	8.02	2.12
1.25	12.14	8.81	1.83
1.30	17.81	13.07	2.93

Due to the easy evaporation of Li ions during the synthesis or post-annealing process [206], the optimum concentration of excess Li ions to obtain high purity resultant material was analyzed by Reitveld refinement. The obtained R_{wp}, R_p, GOF values are presented in Table 5.1 with 1.10, 1.20, 1.25, and 1.30 mole fractions of Li, where R_{wp} is the weighted profiles residual factor, R_p is the profile residual factor, and GOF is the goodness of fit [210]. R_p and R_{wp} show how well the crystallographic model matches the experimental X-ray diffraction. Typically, the value of R_{wp} < 10% or GOF close to 1 is considered a close match. Figure 5.1b illustrates the XRD patterns for each concentration of Li. The impurities, $SrAl_4O_7$ and $Sr_2Al_5O_{11}$, were reduced from 7 mol.% to 6 mol.%, and from 5 mol.% to 0 mol.%, respectively, when the Li concentration was 1.25 mole fraction. This proves that Li evaporated during the synthesis or annealing process. When the concentration increased to 1.30 mole fraction, more impurity peaks of $SrAl_4O_7$ appeared (Figure 5.1c), but $Sr_2Al_6O_{11}$ was not present. In the calculated phase diagram of $SrO\text{-}Li_2O\text{-}Al_2O_3$ [71] in Figure 5.1d, $Sr_2Al_6O_{11}$ is located between $SrAl_2O_4$ and $SrAl_2O_7$, closer to the Sr_2LiAlO_4, and further away from Li_2O than $SrAl_4O_7$. Thus the Li concentration affects the $Sr_2Al_6O_{11}$ more than $SrAl_4O_7$ when synthesizing Sr_2LiAlO_4. Hence, the optimum processing conditions for Sr_2LiAlO_4 are a Li concentration of 1.25 mole fraction and an annealing treatment at 800ºC for 5 hours, which

results in a final purity of 94 mol.% with 6 mol.% of $SrAl_4O_7$ (Figure 5.1c). The XRD patterns of the Eu/Ce activated Sr_2LiAlO_4 are shown in Figure 5.1e. They were also well matched with the simulated Sr_2LiAlO_4 patterns previously reported [71].

Table 5.2 Calculated [71] and experimental parameters of Sr_2LiAlO_4 with 1.25 mole fraction of Li annealed at 800ºC for five hours. The experimental values were obtained from X-ray diffraction Rietveld refinement of the combustion reaction samples. Values in parentheses are the estimated standard deviations of the last significant figure.

Site	**Calculated**			**Experimental**			**Occupancy**	**Wyckoff Position**
	x	*y*	*z*	*x*	*y*	*z*		
Sr1	0.22801	0.25000	0.43191	0.25226 (78)	0.25000	0.43390 (91)	1	2e
Sr2	0.27038	0.25000	0.94227	0.23642 (82)	0.25000	0.93358 (87)	1	2e
Li3	0.30224	0.75000	0.69253	0.2599 (50)	0.75000	0.6796 (60)	1	2e
Al4	0.27851	0.75000	0.19918	0.3016 (33)	0.75000	0.2027 (40)	1	2e
O5	0.47754	0.50758	0.25164	0.4998 (29)	0.5063 (33)	0.1906 (24)	1	4f
O6	0.09917	0.75000	0.37670	0.1082 (31)	0.75000	0.4291 (29)	1	2e
O7	0.11359	0.75000	0.92812	0.1579 (58)	0.75000	0.9050 (58)	1	2e

Table 5.2 lists the calculated and experimental structure parameters of Sr_2LiAlO_4. The experimental *x*, *y*, *z* coordinates were found to be similar to the calculated *x*, *y*, *z* coordinates. The experimental and calculated lattice parameters are provided in Table 5.3, showing a good match. The obtained residual values were R_{wp} = 12.14%, R_p = 8.81%, and GOF = 1.83, therefore, the experimental values are in good agreement with those of the calculated values (Table 5.2 and 5.3).

Table 5.3 Calculated [71] and experimental Rietveld refinement parameters of Sr_2LiAlO_4 synthesized by the combustion reaction. R_{exp}: expected residual factor; R_{wp}: weighted profile residual factor; R_p: profile residual factor; GOF: goodness of fit. Values in parentheses are the estimated standard deviations of the last significant figure.

Rietveld refinement parameters		**Calculated**
Symmetry	Monoclinic	Monoclinic
Space group	$P2_1/m$	$P2_1/m$
a/nm	0.581565 (14)	0.58308
b/nm	0.563141 (16)	0.56386
c/nm	0.665946 (16)	0.66545
β/°	106.4558 (17)	106.70
Volume/nm^3	0.2091658 (95)	0.20956
R_{exp} (%)	6.65	-
R_{wp} (%)	12.14	-
R_p (%)	8.81	-
GOF	1.83	-

5.4.2 Photoluminescence spectra and quantum efficiency of Eu^{2+} or Ce^{3+} activated Sr_2LiAlO_4

The PL excitation (PLE) and PL emission spectra were measured for the Eu^{2+} or Ce^{3+} activated Sr_2LiAlO_4 (Figure 5.2). The PLE spectrum of Sr_2LiAlO_4:Eu^{2+} was monitored at 515 nm and showed two broad peaks centered at 390 nm and 315 nm. The PL emission spectra for this material (λ_{ex} = 390 nm) showed two broad peaks at 515 nm as a maximum and 565 nm as a shoulder (see Figure 5.2a). The two broad peaks in the PLE and PL are attributed to the two sites of Sr^{2+} where Eu^{2+} was substituted [71]. To determine the optimal x in $Sr_{2-x}Eu_xLiAlO_4$, the PL emission spectra were analyzed for concentrations of $0.001 < x < 0.04$, as shown in Figure 2c. The

corresponding intensities were normalized for x = 0.002, which had the maximum emission intensity with Φ = 25%.

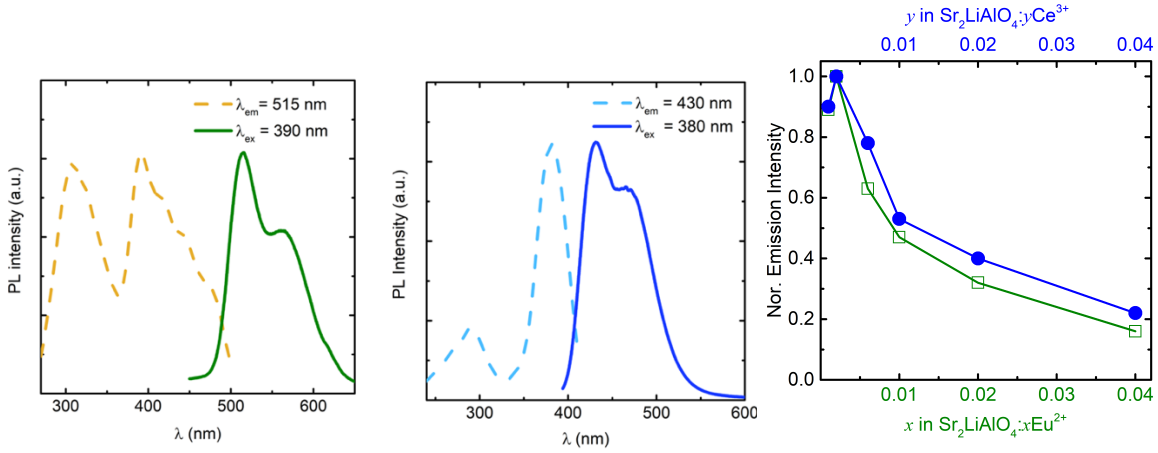

(a) **(b)** **(c)**

Figure 5.2 Photoluminescence excitation (dashed line) and emission (solid line) of **(a)** $Sr_2LiAlO_4:Eu^{2+}$ and **(b)** $Sr_2LiAlO_4:Ce^{3+}$. **(c)** The normalized (to x or y = 0.002) emission intensities of $Sr_2LiAlO_4:Eu^{2+}$ (green line) and $Sr_2LiAlO_4:Ce^{3+}$ (blue line) as a function of activator concentration.

The PLE of $Sr_2LiAlO_4:Ce^{3+}$ was measured under 430 nm and showed two peaks centered at 290 nm and 380 nm (dashed line in Figure 5.2b). The PL emission spectra (λ_{ex} = 380 nm) showed two broad peaks at 430 nm as a maximum and 470 as a shoulder (solid line in Figure 5.2b). These two broad peaks in the PLE and PL emission spectra are also from the two sites of Sr^{2+} where Ce^{3+} was substituted [71]. Several Ce^{3+} concentrations, $0.001 < y < 0.04$, were examined to obtain the optimum concentration shown in Figure 5.2c. The emission intensities were normalized for y = 0.002, which had the maximum emission intensity with Φ = 40%. When there are impurities phases in Sr_2LiAlO_4, the activators are located in both impurities phases as well as in Sr_2LiAlO_4. The impurity content in the solid-state reacted powders ($SrAl_4O_7$, 5 mol.%; $Sr_2Al_6O_{11}$, 6 mol.%; SrO, 3 mol.%) is greater than in the combustion reactied powders ($SrAl_4O_7$, 6 mol.%). Therefore,

the higher Φ of the combustion reacted powders (40%) than the solid-state reacted powders (32%) may be due to the reduced impurity content.

The Φ of $Sr_{1.998}Ce_{0.002}LiAlO_4$ was higher than the Φ of $Sr_{1.998}Eu_{0.002}LiAlO_4$ although the host lattice is the same. There are several examples that different activators (Eu^{2+} and Ce^{3+}) were in the same host lattice, but the Φs (or emission intensity) were also not similar between them. The Φs of $Ba_2SiO_4:Eu^{2+}$ and $Ba_2SiO_4:Ce^{3+}$ were 94% [211] and 69% [87], respectively. For $Ba_9Lu_2Si_6O_{24}$, the Φ for Eu^{2+} activation was 45% [212] and the Φ for Ce^{3+} activation was 82% [213]. Another example is $Ca_8La_2(PO_4)_6O_2$ where the Φs of the Eu^{2+} and Ce^{3+} activators were 14% and 67%, respectively [195]. Some phosphors showed higher Φ with Eu^{2+} than with Ce^{3+}, but other phosphors showed higher Φ with Ce^{3+} activator than with Eu^{2+} activator [87, 122, 195, 211, 212]. This indicates that Φ depends on the host lattice, not activators and it needs to be further investigation.

Both $Sr_{2-x}Eu_xLiAlO_4$ and $Sr_{2-y}Ce_yLiAlO_4$ have a low optimum concentration x, y = 0.002 while the optimum activator concentration is typically > 0.01 [75, 123, 211]. Since concentration quenching is related to the distance between activators [214], the critical distance (R_c) between activators was calculated using [215]:

$$R_c = 2\left(\frac{3V}{4\pi x_c N}\right)^{1/3} \quad (1)$$

where x_c is the critical activator concentration when the emission intensity is the maximum value, V is the volume of the unit cell, and N is the total number cations in the unit cell in the host lattice. The obtained R_c, was 2.9 nm from V (0.209 nm^3), N (8), and X_c (0.002). This value of R_c is attributed to the small Stokes shift, arising from the stiffness of the host lattice from the AlO_4 tetrahedral network [216, 217]. For example, $Li_2Sr_{1-x}Eu_xSiO_4$ [218] also has a small optimal

activator concentration (x = 0.005) with R_c = 3.4 nm, similar to the present work, which is also due to the small Stocks shift [218].

As shown on Figure 5.2, there are two emission peaks from both $Sr_2LiAlO_4:Eu^{2+}$ and $Sr_2LiAlO_4:Ce^{3+}$. According to Uitert [219], the emission wavelength of Eu^{2+} or Ce^{3+} ions strongly depends on its local environment. The possible positions of the emission peaks can be estimated by the following equation [219-221]:

$$E(cm^{-1}) = Q\left[1 - \left(\frac{V}{4}\right)^{1/V} \times 10^{(-nrE_a)/8}\right] \quad (2)$$

where E is the position of the emission peaks from Eu^{2+} or Ce^{3+}, Q is the energy from the lower d-band edge of Eu^{2+} or Ce^{3+} ions (34,000 cm^{-1} for Eu^{2+} or 50,000 cm^{-1} for Ce^{3+} [219-221]), V is the valence of Eu^{2+} and Ce^{3+} (2 for Eu^{2+}, 3 for Ce^{3+}), n is the coordination number for Eu^{2+} or Ce^{3+} (n = 8 for both of Eu^{2+} and Ce^{3+}), E_a is the electron affinity of the atoms that form anions (eV), and r is the radius (nm) of the cation replaced by Eu^{2+} or Ce^{3+}. The value of E_a for Sr_2LiAlO_4 was taken from that for aluminates [219], approximately, as 1.6 eV and r = 0.126 nm (Sr^{2+}). The calculated and experimental emission wavelengths for Eu^{2+} and Ce^{3+} are listed in the Table 5.4. The calculated emission wavelengths of Eu^{2+} and Ce^{3+} were 529 nm and 466 nm, respectively, which were in a good agreement with the experimental values (515 nm and 565 nm for Eu^{2+}; 430 nm and 470 nm for Ce^{3+}). Although the host has two symmetrically distinct Sr sites [71], the sites have the same coordination number so that the E value has only one estimation for each activator. To compare these two experimental values with the one calculated value, the average experimental values were 540 nm for Eu^{2+} and 450 nm for Ce^{3+}, which were similar to the calculated values.

Table 5.4 Calculated and experimental emission wavelength of Eu^{2+} and Ce^{3+} in Sr_2LiAlO_4. *E* is the position of the emission peaks from Eu^{2+} or Ce^{3+}, *Q* is the energy from the lower *d*-band edge of Eu^{2+} or Ce^{3+} ions, *V* is the valence of Eu^{2+} and Ce^{3+}, *n* is the coordination number for Eu^{2+} or Ce^{3+}, E_a is the electron affinity of the atoms that form anions, and *r* is the radius of the cation replaced by Eu^{2+} or Ce^{3+}.

activator	Q (cm^{-1})	V	n	r (nm)	E_a (eV)	E (nm)	E_{calc} (nm)	E_{exp} (nm)
Eu^{2+}	34,000	2	8	0.126	1.6	1888.7	529	515, 565
Ce^{3+}	50,000	3	8	0.126	1.6	2144.2	466	430, 470

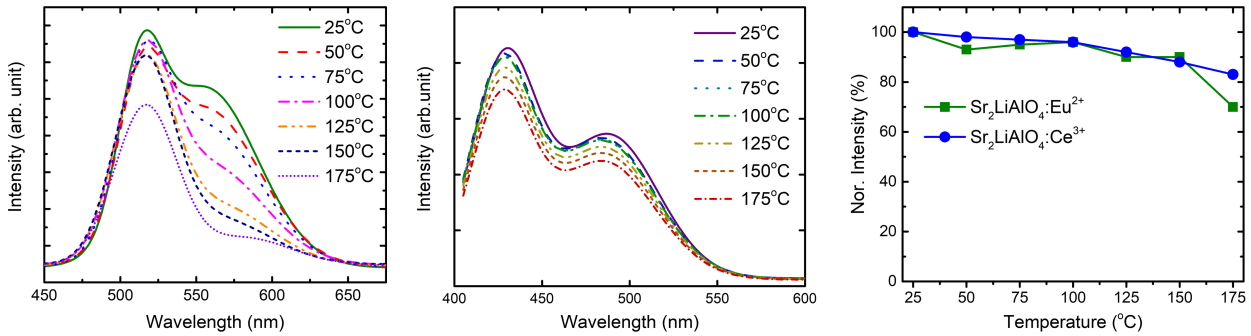

(a) **(b)** **(c)**

Figure 5.3 Emission intensities as a function of temperature: **(a)** $Sr_2LiAlO_4:Eu^{2+}$ (λ_{ex} = 390 nm) and **(b)** $Sr_2LiAlO_4:Ce^{3+}$ (λ_{ex} = 380 nm). **(c)** Normalized (to room temperature) emission intensities of $Sr_2LiAlO_4:Eu^{2+}$ (green line) and $Sr_2LiAlO_4:Ce^{3+}$ (blue line).

5.4.3 Thermal quenching properties and particles morphologies

The thermal quenching properties of $Sr_{1.998}Eu_{0.002}LiAlO_4$ and $Sr_{1.998}Ce_{0.002}LiAlO_4$ were measured and Figure 3a,b shows that as the temperature increases, the PL emission intensity for both materials decreases. For $Sr_{1.998}Eu_{0.002}LiAlO_4$, the emission intensity at 150ºC was 90% of the room temperature value, showing a very good thermal quenching property. Minimal thermal quenching means that in the host there are rigid bonding networks and high bond strength, enabling

minimization of the emission loss with increasing temperature [222]. The obtained good thermal quenching behavior implies that Sr_2LiAlO_4 has a rigid bonding network together with high bond strength. For $Sr_{1.998}Ce_{0.002}LiAlO_4$, a similar trend was observed, retaining 88% of emission intensity at 25ºC. This matches well with our previously reported value (91% of emission intensity at 25ºC for powders synthesized by the solid-state reaction) [71].

The SEM images of the $Sr_{1.998}Eu_{0.002}LiAlO_4$ and $Sr_{1.998}Ce_{0.002}LiAlO_4$ powders after annealing at 800ºC for 5 hours are shown in Figure 4a and Figure 4b, respectively. The particles were sub-micrometer sized, ~102 ±15 nm, non-aggregated and had a narrow size distribution. As shown, the morphology of powders was oval shaped with a smooth surface.

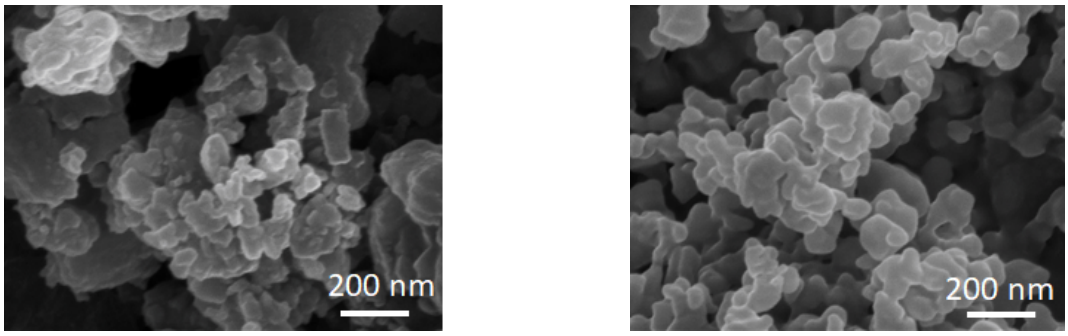

(a) **(b)**

Figure 5.4 Scanning electron microscope images of **(a)** $Sr_2LiAlO_4:Eu^{2+}$ and **(b)** $Sr_2LiAlO_4:Ce^{3+}$.

5.4.4 Luminescence properties of Eu^{2+} and Ce^{3+} co-activated Sr_2LiAlO_4

The excitation spectrum of $Sr_{2-x}Eu_xLiAlO_4$ partially overlaps with the emission spectrum of $Sr_{2-y}Ce_yLiAlO_4$ in the range of 400-500 nm (Figure 5a) and, therefore, the emission from $Sr_2LiAlO_4:Ce^{3+}$ can be partially re-absorbed by $Sr_2LiAlO_4:Eu^{2+}$, indicating that Ce^{3+} acts as a sensitizer for Eu^{2+} [223]. The Ce^{3+} is excited from $^7F_{5/2}$ to $5d$ energy level (λ_{ex} = 380 nm) and then returns to its ground state with visible light radiation. Photons in the Ce^{3+} $5d$ energy level transfer to the Eu^{2+} $4f^6 5d^1$ energy level, resulting in the Eu^{2+} $4f^6 5d \rightarrow 4f^7$, and then Eu^{2+} emits a green

emission (~515 nm), as illustrated in Figure 5b. This process enables the emission intensity of Eu^{2+} to improve with the presence of Ce^{3+}. Since $Sr_{1.998-x}Eu_xCe_{0.0020}LiAlO_4$ and $Sr_{1.998-y}Eu_{0.0020}Ce_yLiAlO_4$ showed maximum emission intensities (Figure 2c), at concentrations of $0.0005 \leq x \leq 0.0050$ and $0.0005 \leq y \leq 0.0040$, they were selected to examine for improvement of the optical properties. For $Sr_{1.998-x}Eu_xCe_{0.0020}LiAlO_4$, the emission intensity of Ce^{3+} decreased when x increased, as shown in Figure 6a, which is attributed to the energy transfer from Ce^{3+} to Eu^{2+} [193]. Meanwhile, the emission intensity of Eu^{2+} increased up to $x = 0.0020$ owing to the $Ce^{3+} \rightarrow Eu^{2+}$ energy transfer, remained constant and then decreased to $x = 0.0050$, which was attributed to concentration quenching. Figure 6b shows the change in the emission intensity of Eu^{2+} and Ce^{3+} depending on the Eu^{2+} concentration. For $Sr_{1.998-y}Eu_{0.0020}Ce_yLiAlO_4$, the emission intensity of Eu^{2+} increased from $y = 0.0005$ to 0.0010 and then decreased (Figure 6c), also attributed to the energy transfer from Ce^{3+} to Eu^{2+} [193]. Figure 6d shows the changes in the emission intensity for Eu^{2+} and Ce^{3+}. Although x is constant (0.002) and y increased, the emission intensity from Ce^{3+} leveled off for $y \geq 0.001$ after increasing from $y = 0.0005$ to 0.001. The emission intensity from Eu^{2+} increased until $y = 0.001$, and then decreased, attributed to the concentration quenching [75].

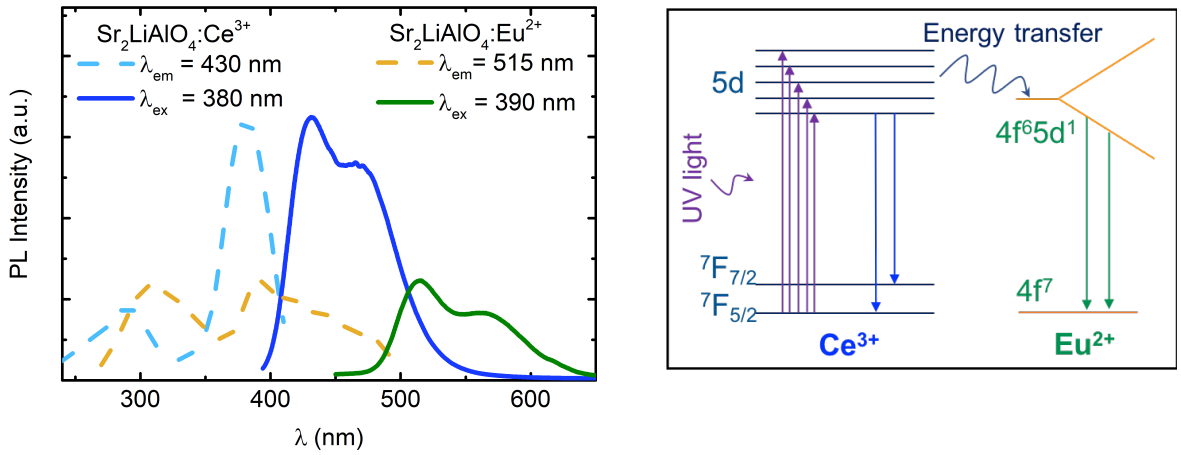

(a) **(b)**

Figure 5.5 **(a)** Overlapped photoluminescence emission (solid line) and excitation (dashed line) of $Sr_2LiAlO_4:Eu^{2+}$ and $Sr_2LiAlO_4:Ce^{3+}$, respectively. **(b)** Scheme of energy transfer between Ce^{3+} and Eu^{2+} in Sr_2LiAlO_4.

The energy transfer efficiency from Ce^{3+} to Eu^{2+} can be estimated by [224]:

$$\eta_T = 1 - {}^{I}/_{I_0} \quad (3)$$

where η_T is the energy transfer efficiency; I and I_0 are the emission intensities of the Ce^{3+} in the presence and absence of Eu^{2+}, respectively. Figure 6e shows the plot of η_T as a function of x ($0.0005 < x < 0.0050$) demonstrating that η_T increased with increase in x. For the concentrations of $x = y = 0.002$, $\eta_T =$ 55%, meaning that the 55% of the excited photons from the 5*d* level of Ce^{3+} transferred to the $4f^6 5d^1$ level of Eu^{2+} [184, 193, 225]. For x, y = 0.005, 0.002, η_T = 92%, which demonstrates that the energy transfer from Ce^{3+} to Eu^{2+} depends on the concentration of Eu^{2+}, corroborating results of previous studies [193, 195-197].

For evaluation of the energy transfer mechanism from Ce^{3+} to Eu^{2+}, the following equation can be applied, based on Dexter energy transfer expressions of multipolar interaction and Reisfeld approximation [226, 227]:

$$log\left(\frac{I_0}{I}\right) \propto \frac{n}{3} log(C_{Eu^{2+} + Ce^{3+}}) \quad (4)$$

where C is the total concentration of Ce^{3+} and Eu^{2+}, and n is a function of electric multipolar character. Values of n = 6, 8, 10 correspond to dipole-dipole (*d-d*), dipole-quadrupole (*d-q*), and quadrupole-quadrupole (*q-q*) interactions, respectively. Figure 6f shows the plot of $log(I_0/I)$ as a function of $log(C_{Eu^{2+} + Ce^{3+}})$. The slope was found to be 2.21, resulting in $n \approx 6$, which corresponds to the *d-d* interaction. The energy transfer rate of *d-d* interaction is typically higher than that of *d-q* or *q-q* interactions [228]. In this case, the photons of the 5*d* level of Ce^{3+} are rapidly absorbed to the $4f^6 5d^1$ level of Eu^{2+}, leading to a shortened luminescent lifetime of Ce^{3+}. Previous studies have also shown that the energy transfer mechanism from Ce^{3+} to Eu^{2+} as the *d-d* interaction [228, 229].

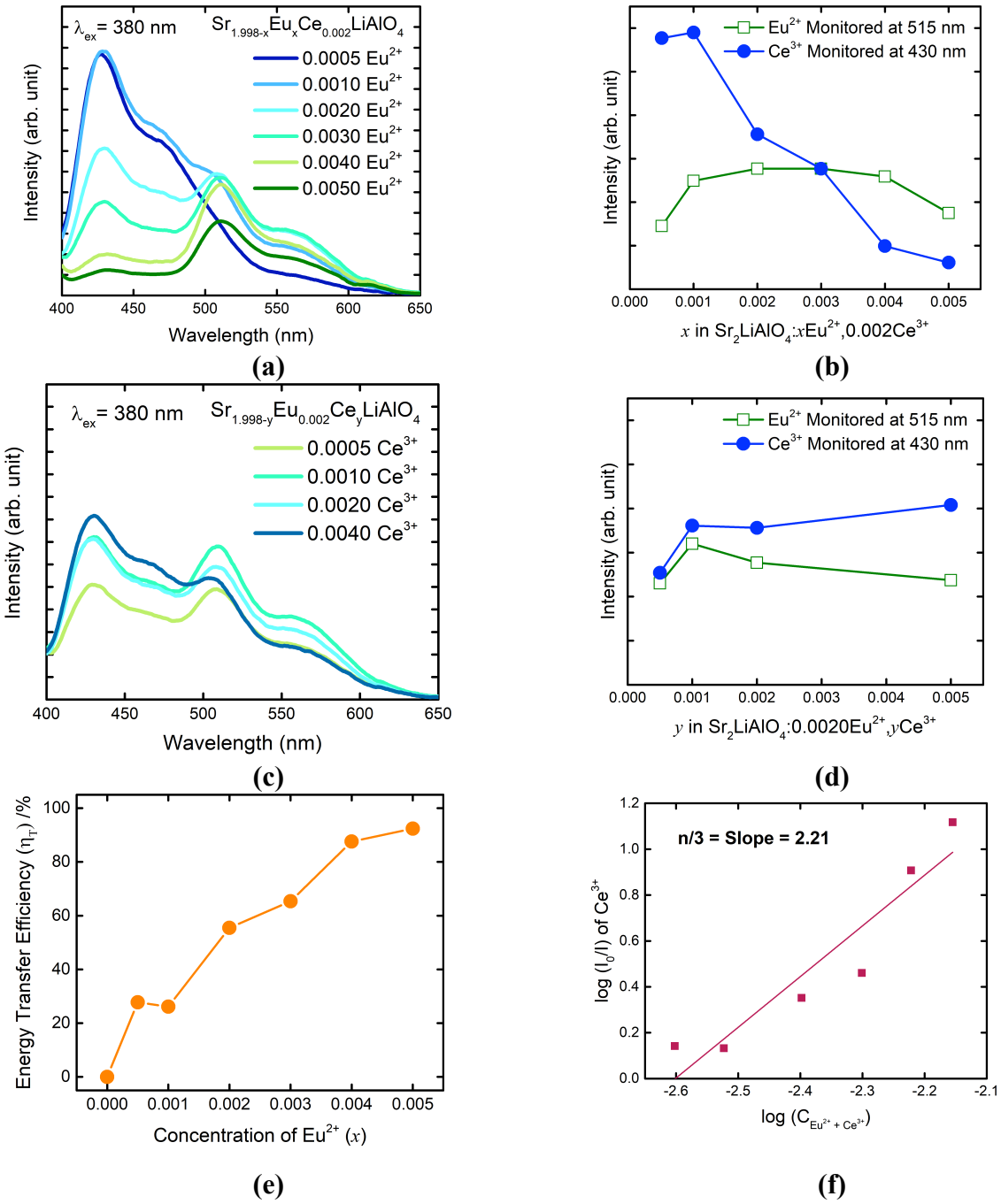

Figure 5.6 **(a)** Photoluminescence emission spectra of $Sr_{1.998-x}Eu_xCe_{0.002}LiAlO_4$ and **(b)** plot of emission intensities of Eu^{2+} and Ce^{3+}. **(c)** Photoluminescence spectra of $Sr_{1.998-y}Eu_{0.002}Ce_yLiAlO_4$ and **(d)** plot of emission intensities of Eu^{2+} and Ce^{3+}**. (e)** Plot of the energy transfer efficiency as a function of Eu^{2+} concentration (x) in $Sr_{1.998-x}Eu_xCe_{0.002}LiAlO_4$. **(f)** Plot of $\log(I_0/I)$ as a function of $\log(C_{Eu^{2+}+Ce^{3+}})$.

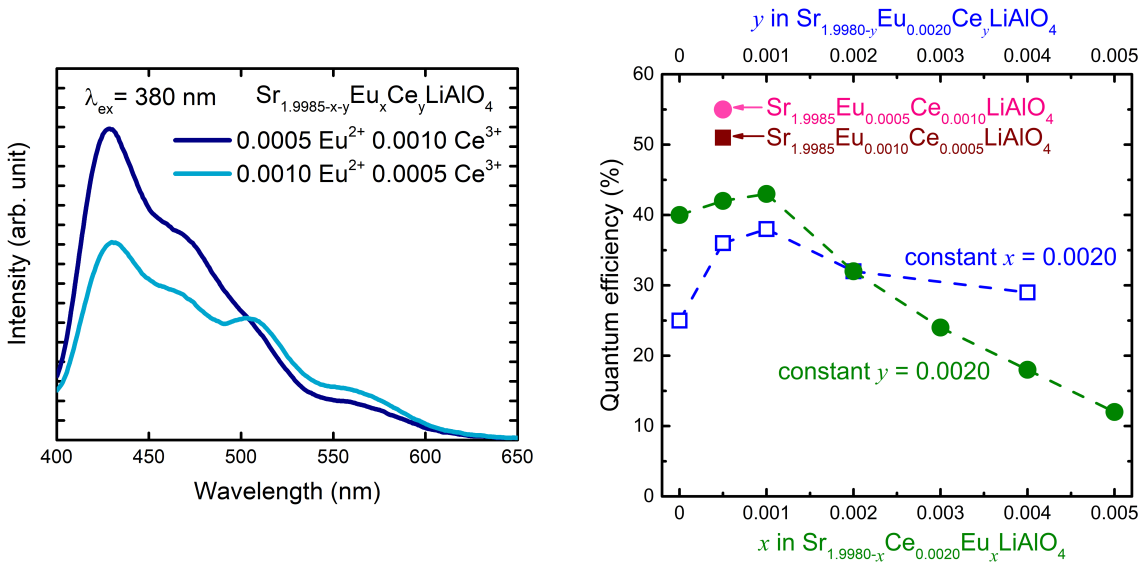

(a) **(b)**

Figure 5.7 **(a)** Photoluminescence spectra of $Sr_{1.9985-x-y}Eu_xCe_yLiAlO_4$ and **(b)** quantum efficiency as a function of activator concentration ($x + y \geq 0.0020$). Red circle and brown square are the efficiencies for a lower total activator concentration of $x + y = 0.0015$.

Furthermore, concentration quenching can potentially be present in these co-activated phosphors due to the higher total activator concentration. The maximum Φ values (Table 5) for $Sr_{2-x-y}Eu_xCe_yLiAlO_4$ were 43% for x, y = 0.0010, 0 and 38% for x, y = 0, 0.0010. The highest PL intensities of $Sr_{1.997}Eu_{0.0010}Ce_{0.0020}LiAlO_4$ and $Sr_{1.997}Eu_{0.0020}Ce_{0.0010}LiAlO_4$ corresponded to $x + y$ = 0.0030 are shown on Figure 6a and 6c. We selected a lower total activator concentration $x + y$ = 0.0015 to determine if further improvement in Φ is possible. Figure 7a shows the PL emission spectra for x, y = 0.0005, 0.0010 and x, y = 0.0010, 0.0005, exhibiting a maximum emission intensity for x, y = 0.0005, 0.0010.

Table 5 lists Φ for the compositions studied. Figure 7b shows Φ as a function of x and y. For x, y = 0, 0.002, Φ = 40%, which is higher than that for solid-state reacted powders (32% for x, y = 0, 0.005 optimal concentration for solid-state reacted powders) [71]. With an increase in x and at constant y = 0.002, Φ increased from 40% for x = 0 to 43% for x = 0.0010. For $x \geq 0.0010$, the

Φ value decreased due to the concentration quenching effect. For constant $x = 0.002$ and increasing y, Φ at $y = 0$ of the combustion reacted powders is 25%, same as the solid-state reacted powders [71]. The Φ increased from 25% at $y = 0$ to 38% for $y = 0.0010$ and then decreased. The maximum Φ = 55% was found for x, $y = 0.0005$, 0.0010 and a slightly lower value of Φ = 51% for x, $y = 0.0010$, 0.0005; both showing at least a 40% increase over those for $x + y \geq 0.0020$. This is due to a lower total activator concentration that suppressed concentration quenching and improved Φ [214].

To analyze the effect of the energy transfer from Ce^{3+} to Eu^{2+}, the normalized ($x = 0.002$) emission intensity of Ce^{3+} for $Sr_{1.998-x}Eu_xCe_{0.002}LiAlO_4$ ($0.0005 \leq x \leq 00050$) is shown in Figure 8a. With an increase in x and at constant $y = 0.002$, the emission peak of Ce^{3+} was red-shifted from 427 nm to 433 nm as shown in Figure 8a,b. Piquette *et al*. [230] investigated on the radiative reabsorption and the red shift of the Ce^{3+} emission in $(Lu_{1-x}Ce_x)_3Al_5O_{12}$. Radiative reabsorption is when the emission photons are reabsorbed, which occurs when the emission and absorption bands overlap [230-232]. $(Lu_{1-x}Ce_x)_3Al_5O_{12}$ exhibits the partially overlap between the excitation and the emission of Ce^{3+}. The photons emitted in the lower wavenegth range were reabsorbed by Ce^{3+} in the higher wavelength range, causing emission wavelength red-shift. Although the radiative reabsorption was demonstrated in a single activator, this can be also applied to the co-activators in the case where the emission and the absorption of the co-activators overlap [233]. For example, in Eu^{2+}/Ce^{3+} co-activated $SrSc_2O_4$ it was reported that the red-shift of the Ce^{3+} emission was observed with an increase in Eu^{2+} [233]. For $Sr_{1.998-x}Eu_xCe_{0.002}LiAlO_4$, the excitation spectrum of Eu^{2+} and emission spectrum of Ce^{3+} partially overlap (Figure 5) resulting in radiative reabsorption of the Ce^{3+} emission by Eu^{2+} thereby red-shifting the Ce^{3+} emission.

Table 5.5 The color coordinates (*x, y*) and quantum efficiency (Φ) of $Sr_{2-x-y}Eu_xCe_yLiAlO_4$. (a)-(m) are the points shown on the CIE diagram in Figure 5.8.

	$Sr_{2-x-y}Eu_xCe_yLiAlO_4$		**CIE coordinates (*x, y*)**	**Φ**
	x	**y**		
(a)	0	0.0020	(0.1472, 0.0972)	40%
(b)	0.0005	0.0020	(0.1636, 0.1849)	42%
(c)	0.0010	0.0020	(0.1804, 0.1849)	43%
(d)	0.0020	0.0040	(0.1907, 0.2221)	29%
(e)	0.0020	0.0020	(0.2072, 0.2716)	32%
(f)	0.0020	0.0010	(0.2149, 0.2900)	38%
(g)	0.0020	0.0005	(0.2094, 0.2845)	36%
(h)	0.0030	0.0020	(0.2302, 0.3382)	24%
(i)	0.0040	0.0020	(0.2426, 0.4208)	18%
(j)	0.0050	0.0020	(0.2503, 0.4344)	12%
(k)	0.0020	0	(0.3324, 0.5732)	25%
(l)	0.0005	0.0010	(0.1685, 0.1456)	55%
(m)	0.0010	0.0005	(0.1846, 0.2100)	51%

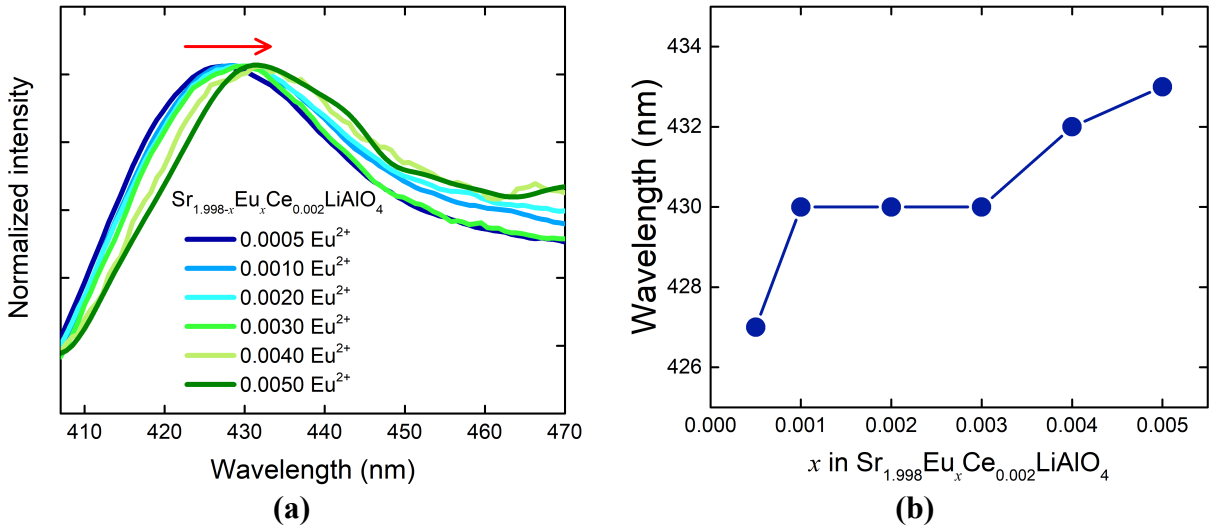

Figure 5.8 (a) Normalized (to x = 0.002) emission spectra from Ce3+ for Sr1.998-xEuxCe0.002LiAlO4 (0.0005 ≤ x ≤ 00050). (b) Plot of the emission wavelength as a function x.

5.4.5 Color coordinates and powders colors of Eu^{2+} and Ce^{3+} co-activated Sr_2LiAlO_4

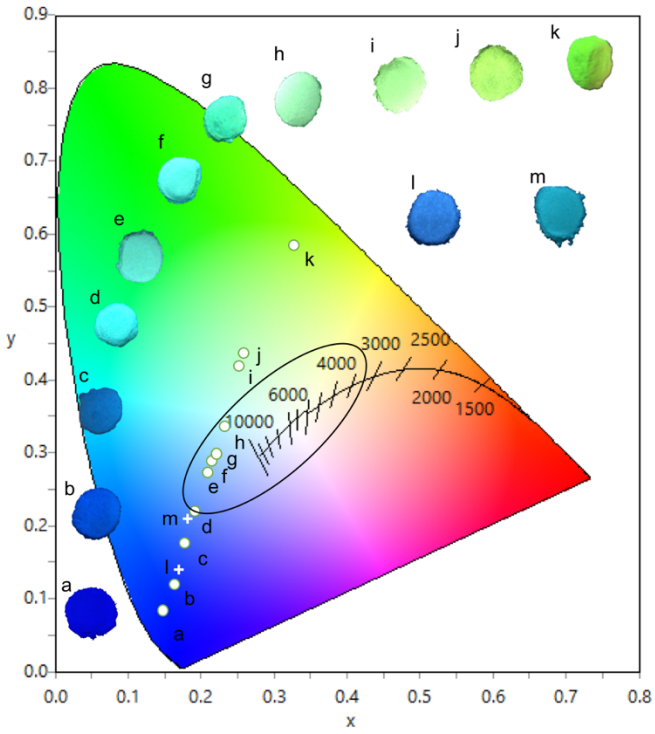

Figure 5.9 The CIE diagram showing coordinates of the phosphors and photographs of the powders $Sr_{2-x-y}Eu_xCe_yLiAlO_4$. The x and y values are shown in Table 5.4.

Since $Sr_{2-y}Ce_yLiAlO_4$ and $Sr_{2-x}Eu_xLiAlO_4$ emit blue and green, respectively, the combination of Eu^{2+} and Ce^{3+} in Sr_2LiAlO_4 showed color tunable ability from blue to cool-white and green emission. The color coordinates on the CIE diagram are listed in Table 5. The CIE chromaticity diagram and images of the powders under 365 nm UV light are shown in Figure 9. $Sr_{1.997}Eu_{0.002}Ce_{0.001}LiAlO_4$ (Φ = 38%) was in the cool-white region in the CIE diagram, having a CCT = 23450K, CRI = 60 and (0.2149, 0.2900) coordinates. The (*x, y*) coordinates changed linearly from (0.1472, 0.0972) for $Sr_{1.998}Ce_{0.002}LiAlO_4$ to (0.3324, 0.5732) for $Sr_{1.998}Eu_{0.002}LiAlO_4$, which is from blue to green emission. The phosphor powder photographs are also well matched with the color coordinate results, as presented in Figure 9. This indicates that the Eu^{2+} and Ce^{3+} co-activated Sr_2LiAlO_4 demonstrates good color tunable ability.

5.5 Conclusions

$Sr_{2-x}Eu_xLiAlO_4$ (green-emitting ~515 nm) and $Sr_{2-y}Ce_yLiAlO_4$ (blue-emitting ~430 nm) phosphors with 94% purity were prepared by the combustion synthesis method. The maximum quantum efficiencies were found for $Sr_{1.998}Eu_{0.002}LiAlO_4$ and $Sr_{1.998}Ce_{0.002}LiAlO_4$, (25% and 40%, respectively), which are higher than for solid state reacted powders. The emission intensities at 150°C of these compositions were 90% and 88% of the room temperature values, respectively, showing good thermal quenching resistance. For the first time, Eu^{2+} and Ce^{3+} co-activated Sr_2LiAlO_4 ($Sr_{2-x-y}Eu_xCe_yLiAlO_4$) were prepared to investigate the properties of color tunable single-phase phosphors. The emission color changed from blue, to cool-white, to green, depending on x and y. When y was constant and x increased, the emission intensity of Ce^{3+} decreased and that of Eu^{2+} increased, indicating that there was an energy transfer from Ce^{3+} to Eu^{2+}. With x, $y = 0.005$, 0.001, the maximum value of the quantum efficiency was 55%, an increase of 40% over those of the singlely activated powders. An increase in x at constant $y = 0.002$ exhibited a red shift of the emission spectra of Ce^{3+}, implying that radiative reabsorption occurred through the energy transfer from Ce^{3+} to Eu^{2+}. Eu^{2+} and Ce^{3+} co-activated Sr_2LiAlO_4 was found to be a promising color-tunable single-phase phosphor able to change color from blue, to cool-white and green for potential applications in phosphor converted white-emitting LEDs.

Chapter 5, in full, is a reprinted of the material as it appears in "Color tunable single-phase Eu^{2+} and Ce^{3+} co-activated Sr_2LiAlO_4 phosphors", Journal of Materials Chemistry C 2019. This work was coauthored by Y. H. Kim, E. Novitskaya, Z. Wang, M. Sanchez, O. A. Graeve, W. B. Im, S. P. Ong. J. McKittrick is the corresponding author. The dissertation author is the first author of this work.

CHAPTER 6: SYNTHESIS OF Mn^{4+} ACTIVATED Na_2SiF_6 RED-EMITTING PHOSPHORS USING AN IONIC LIQUID

6.1 Abstract

For the first time, the synthesis of Na_2SiF_6 powders was achieved through an ionothermal reaction using an ionic liquid, 1-butyl-3-methylimidazolium tetrafluoroborate without using toxic HF. These powders were then used as a host material to produce the red-emitting phosphor, $Na_2Si_{1-x}Mn_xF_6$ (x= 0.007-0.2) that was synthesized using a low concentration HF solution with dissolved $NaMnO_4$ as the Mn^{4+} source. The phosphors exhibited red-emission peaks at 610 nm, 618 nm, 629 nm, and 644 nm from the $^2E_{(g)} \rightarrow {}^4A_{2(g)}$ energy levels of Mn^{4+} under 460 nm excitation. The Na_2SiF_6 particles were rod-shaped (560 nm in length and 228 nm in diameter) and were non-agglomerated, while the $Na_2Si_{1-x}Mn_xF_6$ particles were spherically-shaped, ~ 500 nm in diameter, which is much smaller than typical fluoride powders (1 μm ~20 μm).

6.2 Introduction

A red-emitting phosphor is a crucial component for phosphor-converted white-light-emitting diodes (pc-WLEDs) [15, 51, 234]. A typical approach to produce pc-WLEDs is to combine a blue-emitting InGaN LED with a yellow-emitting phosphor ($Y_3Al_5O_{12}:Ce^{3+}$). This suffers from a low color rendering index (CRI) value < 80 and high correlated color temperature CCT > 5000 K due to a lack of red emission [181, 183, 235]. An alternative approach to overcome this is combining a near UV-LED (nUV-LED, 370 -410nm) with blue, green, and red phosphors to produce pc-WLEDs. The red phosphors are important to achieve pc-WLEDs with a high CRI value > 80 and low CCT < 5000 K [236, 237]. Also, the micrometer-sized particles of phosphors generate substantial light scattering in the remote phosphor configuration that is the placement and

the arrangement of particles of red, green, and blue phosphors on the LED chip to produce white emission in pc-WLEDs lighting [238], which reduces the efficiency of the lighting [239]. Therefore, the discovery of red-emitting phosphors with submicron particle sizes is essential to improve the CRI and CCT for pc-WLEDs.

Nitrides are attractive host materials for red-emitting phosphors activated by Eu^{2+} due to their narrow emission spectra, high quantum efficiency, and high thermal quenching resistance [44, 240]. The preparation of nitrides is usually performed via the solid-state reaction that requires harsh conditions such as high temperature and/or high pressure in a reducing atmosphere, which usually produce micron-sized, irregularly-shaped particles of ~ 20 μm [240-243].

Fluorides activated by Mn^{4+} can be an alternative red-emitting phosphor, showing excellent high-luminous efficient narrow-band red emission of ~650 nm under ambient conditions [235, 244, 245]. Their production does not require the use of these rigorous synthesis conditions required for nitrides [235, 244, 245]. They also resolve the issues of cost and supply connected to rare earth elements by replacing them with a transition metal. They have the potential for high quantum efficiency when activated by blue light/near UV LEDs for application in pc-WLEDs [15, 51, 234]. The compounds, A_2XF_6 (A = Na, K, $\frac{1}{2}$Ba and X = Ti, Ge, Si) activated with Mn^{4+} are representative red-emitting fluoride phosphors [246-253]. The narrow-band red emission of Mn^{4+} in A_2XF_6 is attributed to the $^2E_{(g)} \rightarrow {}^4A_{2(g)}$ transition that consists of emission peaks from the transitions $\nu 3(t_{1u})$, $\nu 4(t_{1u})$, $\nu 6(t_{2u})$ (anti-Stoke emissions), zero phonon line (ZPL), $\nu 6(t_{2u})$, $\nu 4(t_{1u})$, and $\nu 3(t_{1u})$ (Stokes emissions) vibronic modes of the octahedral group of $[MnF_6]^{2-}$ [54, 252-256]. The location of the ZPL depends on the constituent elements, composition, and the host lattice structure [252]. For example, the ZPL is located at ~622 nm for Mn^{4+} activated K_2TiF_6, K_2GeMnF_6, and K_2SiMnF_6, although the X element is not the same. Anti-Stokes and Stokes emissions are located on both

sides off the ZPL, at ~598 nm, ~607 nm, ~610 nm, ~632 nm, ~635 nm, and ~645 nm for K_2BF_6 (X = Ti, Ge, Si) [252]. However, the ZPL for Na_2SiF_6: Mn^{4+} located at ~ 617 nm, and three anti-Stokes and Stokes emissions are blue-shifted compared to those for K_2BF_6: Mn^{4+}. This implies that the substitution of the A element influences the $^2E_{(g)}$ energy level of Mn^{4+} more than the X element [252], which is corroborated in previous studies [257, 258]. It has been proposed that the decrease in the energy of the $^2E_{(g)}$ level is attributed to a decrease in the radii or electron affinity of the A element [252, 257-259]. However, this has not been proven theoretically and needs further studies. Among the A_2XF_6 compositions, $K_2Si_{1-x}Mn_xF_6$ is the most well-studied with a maximum 90% quantum efficiency (QE) reported for ~ x = 0.03 [260-262], although $K_2Ti_{1-x}Mn_xF_6$ showed the highest QE of ~98% for ~ x = 0.014 [250].

The typical methods to prepare $A_2X_{1-x}Mn_xF_6$ are (1) chemical etching [246, 247], (2) hydrothermal synthesis [248, 249], (3) cation exchange [250], and (4) co-precipitation [251-253]. Examples for each method and powder properties are listed in Table 6.1. Chemical etching is the simplest method which includes etching of a Si wafer with other starting materials. The main drawbacks for this method are a difficulty to control the amount of Mn^{4+} in the host and a low product yield. Next, hydrothermal synthesis can result in high emission intensity, but requires a long reaction time. The cation exchange method has a short reaction time, but requires the synthesis of the Mn^{4+} precursor. Lastly, the co-precipitation method is a simple process which takes a short time, and has a high product yield and low cost. Therefore, the co-precipitation is the best method for a rapid, high product yield reaction.

Generally, the preparation of Mn^{4+} activated fluorides has been carried out in high concentration HF solutions (> 20 M) with different Mn^{4+} precursors. The Mn^{4+} was obtained by dissolving powders of $KMnO_4$, $NaMnO_4$ or K_2MnF_6 that ultimately formed $[MnF_6]^{2-}$ by:

$$KMnO_4(s) \xrightarrow{HF/H_2O} K^+(aq) + M(VII)O_4^-(aq) \text{ [263, 264])} \quad (1)$$

$$NaMnO_4(s) \xrightarrow{HF/H_2O} Na^+(aq) + M(VII)O_4^-(aq) \text{ [263, 264])} \quad (2)$$

$$Mn(VII)O_4^-(aq) + 6\text{HF}(l) + H_2O_2(l) \xrightarrow{HF/H_2O} [MnF_6]^{2-}(aq) + 4H_2O(l) + O_2(g) \quad (3)$$

$$K_2MnF_6(s) \xrightarrow{HF/H_2O} 2K^+(aq) + [MnF_6]^{2-}(aq) \quad (4)$$

The crystalline structure of A_2BF_6 is not rigid, since the $[BF_6]^{2-}$ groups are isolated from each other by the large A^+. The dissolution-crystallization process of A_2BF_6 can be expressed by [265]:

$$A_2BF_6(s) \overset{H_2O}{\longleftrightarrow} 2A^+(aq) + [XF_6]^{2-}(aq) \quad (5)$$

The substitution of $[MnF_6]^{2-}$ with $[XF_6]^{2-}$ in a HF solution to synthesize fluorides is accomplished by:

$$2A^+(aq) + (1-x)[XF_6]^{2-}(aq) + x[MnF_6]^{2-}(aq) \xrightarrow{HF/H_2O} A_2X_{1-x}Mn_xF_6(s) \quad (6)$$

The actual value of *x* is likely smaller than the experimental one because it is difficult to transform all MnO_4^- to $[MnF_6]^{2-}$ (Eqn. 3) [248, 265]. There are two roles of HF in the synthesis of fluorides [265]: The first one is to reduce the pH of the solution in order to transform MnO_4^- into $[MnF_6]^{2-}$ and the second one is to provide enough F^- to form and maintain the $[MnF_6]^{2-}$ group before Mn^{4+} is reversibly reduced or oxidized.

To avoid the usage of HF, Huang et al. [265] developed a new method to utilize a low toxic $Mn(H_3PO_4)_2/KHF_2$ to hydrothermally synthesize $K_2Si_{1-x}Mn_xSiF_6$ (x = 0.01). The x value was evaluated with an assumption that all Mn^{4+} was incorporated in K_2SiF_6. The maximum luminescent intensity was measured when a relatively large concentration of KHF_2 (Si:F = 1:48) was used. However, the QE was only 28% [266], which is much smaller than the QE (74%) of the compound synthesized with HF solution [260, 261].

Another method to synthesize fluorides without HF is to use an ionic liquid that acts as both a solvent and a reactant [267-270]. An ionic liquid is defined as an organic salt that typically has a melting temperature <100°C [271, 272]. This organic component is assymmetric and large, providing the low melting temperature. An ionic liquid is used in an ionothermal reaction as the solvent, similar to the role of water in a hydrothermal reaction [273]. Olchowka *et al.* [267] synthesized A_2SiF_6 (A = Li, Na, K, Rb, Cs) in an ionic liquid, 1-butyl-3-methylimidazolium hexafluorophosphate ([Bmim]PF_6) as a solvent and F^- precursor under microwave radiation. PF_6^- decomposes to release F^- ($PF_6^- \rightarrow PF_5 + F^-$) at a temperature of 140°C. Furthermore, Lorbeer *et al.* [268] prepared LaF_3 activated by Dy^{3+}, Tm^{3+} using an ionic liquid, namely 1-butyl-3-methylimidazolium tetrafluoroborate ([Bmim]BF_4), where BF_4^- also decomposes to release F- ($BF_4^- \rightarrow BF_3 + F^-$) at ~120°C. The particle size of A_2SiF_6 was ~ 10 nm and no QE was reported. From the literature, the difference between using [Bmim]BF_4 and [Bmim]PF_6 is not clear since they both have the same organic cation, $[Bmim]^+$ and F^- precursor. Both of the byproducts, PF_5 and BF_3, were outgassed and removed during the synthesis, but [Bmim]BF_4 is less expensive than [Bmim]PF_6. In addition, Olchowka *et al.* [269] and Terraschke *et al.* [270] recently reported the synthesis of BaFBr:Eu^{2+} using [Bmim]BF_4. The particle size was ~100 nm although the QE was not reported. These studies demonstrated that the fluoride powders synthesized using an ionic

liquid were much smaller than those produced by other methods. Although the fluorides were successfully synthesized with ionic liquids, Mn^{4+} activated fluorides have yet to be reported due to problems finding a suitable Mn^{4+} precursor.

In this work, Na_2SiF_6 was first synthesized via an ionothermal reaction using an ionic liquid, 1-butyl-3-methylimidazolium tetrafluoroborate without HF. Considering that the typical crystallization process of fluoride hosts needs a high concentration HF solution [265], this method is a safe way to synthesize fluorides. Subsequently, $Na_2Si_{1-x}Mn_xF_6$ was prepared by adding the Na_2SiF_6 powders to a low HF concentration (6 M) aqueous solution with dissolved $NaMnO_4$ as the Mn^{4+} source [54]. $NaMnO_4$ is soluble in aqueous solutions and has no other impurity alkali ions that could replace Na^+; thus it is a suitable Mn^{4+} precursor. The crystal structure and particle morphologies of both Na_2SiF_6 and $Na_2Si_{1-x}Mn_xF_6$ were analyzed and the luminescence properties were evaluated.

Table 6.1 Typical methods to prepare $A_2X_{1-x}Mn_xF_6$ (A = Na, K, $\frac{1}{2}$Ba; X = Ti, Ge, Si)

Method	Composition	Starting materials	Results	Pros	Cons	Ref.
Chemical etching	$K_2Si_{1-x}M_xF_6$	Si wafer, $KMnO_4$, HF solution	Produced an unknown amount; no information of the targeted *x*, particles size, and QE; strong red emission with sharp peaks with λ_{ex} = 325 nm	Easy process; expensive cost for raw materials; low product yield	Unable to control the amount of final product and Mn^{4+} incorporation; HF required	[246]
Hydrothermal synthesis	$K_2Si_{1-x}M_xF_6$	SiO_2 powders (unknown particles size), KF powders, $KMnO_4$, H_2O_2, HF solution with at 120°C for 12 h in an autoclave	The measured $x < 0.01$; ~ 20 μm particles size; QE not reported	High emission intensity	Long reaction time; heating with HF required.	[248]
	$BaSi_{1-x}Mn_xF_6$	$Ba(NO_3)_2$, NH_4SiF_6, $KMnO_4$, HF solution at 120°C for 12 h in an autoclave	The highest emission intensity at x = 0.0023; QE not reported; particles were rod shaped~ 1 μm diameter, ~ 10 μm length.			[249]
Cation exchange	$K_2Ti_{1-x}Mn_xF_6$	K_2TiF_6, the synthesized K_2MnF_6 powders, HF solution (27 M). The synthesis of K_2MnF_6 as a Mn^{4+} precursor: $2KMnO_4(s) + 8HF(l) + 3H_2O_2(l) + 2KHF_2(s) \xrightarrow{HF/H_2O} 2K_2MnF_6(s) + 8H_2O(l) + 3O_2(g)$	The measured x = 0.014; the QE = 98%; ~ 20 μm particles size.	Short synthetic time; easy process	Need to use synthesized K_2MnF_6 for Mn^{4+} precursor; HF required; Host materials are purchased, not synthesized.	[250]

Table 6.2 Typical methods to prepare $A_2X_{1-x}Mn_xF_6$ (A = Na, K, $\frac{1}{2}$Ba; X = Ti, Ge, Si)

Co-precipitation	$K_2Ge_{1-x}Mn_xF_6$	GeO_2 powders (unknown particle size), the synthesized K_2MnF_6 powders, solution in 60°C. A KF/HF solution to precipitate $K_2Ge_{0.95}Mn_{0.05}F_6$.	The targeted x = 0.05; QE = 54%; an average particles size of~ 25 μm; assumption with Mn^{4+} (x = 0.05) from K_2MnF_6 incorporating into $K_2Ge_{1-x}Mn_xF_6$.	Short reaction time; simple process; high product yield; low cost;	HF required	[251]
	$Na_2Si_{1-x}Mn_xF_6$	K_2MnF_6, SiO_2, Na_2SO_3, HF solution (24 M)	The optimum x value = 0.07 ($0.012 \leq x \leq 0.07$), with an assumption of all Mn^{4+} incorporated in the Na_2SiF_6, at the highest emission intensity; QE not reported; ~ 2.7 μm particles size.			[256]
	$Na_2Si_{1-x}Mn_xF_6$	SiO_2, $NaMnO_4$, NaF, HF solution (20 M)	The targeted x = 0.019; ~20 μm particles sizes; QE not reported			[253]

6.3 Experimental Procedure

6.3.1 Synthesis of Na_2SiF_6

An ionothermal reaction was used with an ionic liquid, 1-butyl-3-methylimidazolium tetrafluoroborate ([Bmim]BF_4,) to synthesize Na_2SiF_6. NaBr (0.2073 g, A.C.S. Reagent, J. T. Baker) was added into a 50 mL beaker and 1 mL of ethanol was poured into the beaker. The solution was thoroughly mixed with a magnetic stirrer, followed by adding drop-wise 0.201 mL of tetraethyl orthosilicate (TEOS, Sigma Aldrich). The ionic liquid, (3 mL, Sigma Aldrich) was poured into the solution and stirred for 10 min. It was then transferred into a Teflon vessel and placed inside an autoclave. The autoclave was put into the furnace at 150°C for 2 h, removed and rinsed with DI water until it cooled down to room temperature. The vessel was then removed from the autoclave. The white precipitates, ~0.15 g, in the vessel were washed by transferring them to a centrifuge tube with 25 mL of ethanol and then centrifuged for 10 min at 4000 rpm. The precipitates were washed twice with ethanol and the obtained product was dried in air at 100°C for ~ 12 h to obtain the white colored final product.

Figure 6.1a shows a schematic diagram of the ionic liquid synthesis method to synthesize Na_2SiF_6 through the ionothermal reaction using [Bmim]BF_4. [Bmim]BF_4 is composed of an organic cation ($Bmim^+$) and an anion (BF_4^-). BF_4^- decomposed to release F^- ($BF_4^- \rightarrow BF_3 + F^-$) during the ionothermal reaction at 150°C, releasing F^- to form Na_2SiF_6 [268-270]. The formation of Na_2SiF_6 is expressed by:

$$2NaBr\ (s) + Si(OCH_3)_4(l) + 6[Bmim]BF_4(l)$$
$$\rightarrow Na_2SiF_6 + 2Br^-(aq) + 4(OCH_3)^-(aq) + 6BF_3(g) + 6[Bmim]^+(aq)$$

All byproducts were washed off/outgassed after the reaction.

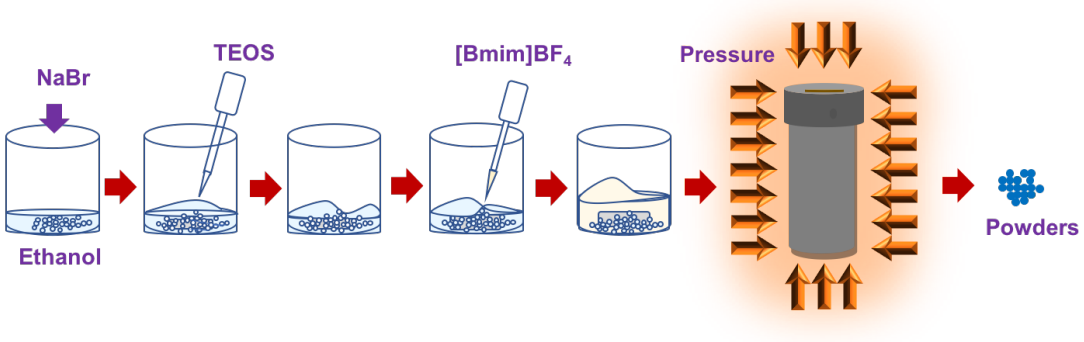

(a)

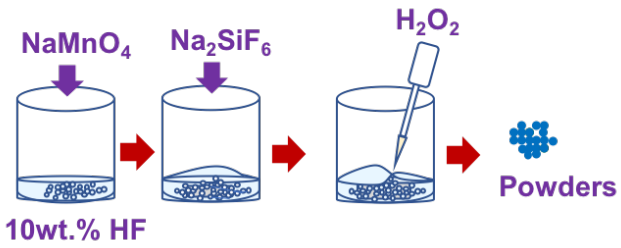

(b)

Figure 6.1 Schematic diagram of the processes to synthesize Na_2SiF_6 using the ionic liquid, $[Bmim]BF_4$. **(a)** TEOS was added to NaBr mixed with ethanol and then $[Bmim]BF_4$ was stirred into the solution. The ionothermal reaction took place; the final product was obtained after centrifugation and drying. **(b)** The process to synthesize $Na_2Si_{1-x}Mn_xF_6$ in a 6M HF solution. The synthesized Na_2SiF_6 powders from (a) were mixed in an HF solution with dissolved $NaMnO_4$ and then H_2O_2 was dropped into the solution. The final powders were obtained after filtering and drying.

6.3.2 Synthesis of $Na_2Si_{1-x}Mn_xF_6$

$NaMnO_4 \cdot H_2O$ (Sigma Aldrich, 0.003 g, 0.05 g, or 0.1 g) was added to 10 ml of a 6 M HF aqueous solution; the color of the solution turned to purple due to the presence of Mn^{7+} [263]. The concentration range of $[MnF_6]^{2-}$ in solution was selected (x = 0.007, 0.1, 0.2) to identify the highest emission intensity of resultant materials. This range was selected because concentration quenching in phosphors typically occurs around x > 0.03 [262]. Next, 0.5 g of the previously synthesized Na_2SiF_6 powder were mixed into the solution and stirred for 30 min. This was followed by adding 2 ml of H_2O_2 (31.1%, Fisher Scientific) to change Mn^{7+} to Mn^{4+} to form $[MnF_6]^{2-}$; the solution changed color from purple (Mn^{7+} ions) to yellowish white [54]. Next, the solution was filtered and washed with ethanol twice. The white powders were dried in the air at 100°C for ~ 12 h. Figure 6.1b shows a schematic diagram of the synthesis of $Na_2Si_{1-x}Mn_xF$.

6.3.3 Characterizations

The powders were analyzed by X-ray diffraction (XRD) with a D2 Phaser (Bruker, Karlsruhe, Germany) using CuKα radiation and a step size of 0.014° over a 2θ range of 10 to 90°. Structural information was derived by refinement using the TOPAS 4.2 software (Bruker) suite [274]. A field emission scanning electron microscope (FESEM, FEI, Hillsboro, OR, USA) at 10 keV was used to image the powders to determine sizes and morphologies. Samples were coated with iridium at 85 μA for 10 s before imaging. Photoluminescence (PL) emission and excitation spectra (PLE) was performed using a fluorescence spectrophotometer (Hitachi F-7000, Hitachi High-Technologies Corporation, Tokyo, Japan). The PL emission spectra were measured under an excitation wavelength of 460 nm.

Table 6.3 Structural parameters of Na_2SiF_6 (PDF 00-033-1280) [18], the synthesized host Na_2SiF_6 and $Na_2Si_{1-x}Mn_xF_6$ (x = 0.007, 0.1, 0.2) after Rietveld refinement. Values in parentheses are the estimated standard deviations of the last significant figure.

Structural parameters					
crystal system			triclinic		
space group			*P321* (150)		
Sample	Na_2SiF_6 [18]	Host Na_2SiF_6	$x = 0.007$	$x = 0.1$	$x = 0.2$
a/nm	0.88659	0.889010 (76)	0.886106 (55)	0.886183 (66)	0.886593 (50)
b/nm	0.88659	0.886522 (58)	0.888278 (68)	0.892060 (88)	0.886728 (49)
c/nm	0.50438	0.507182 (38)	0.505124 (33)	0.505066 (41)	0.505549 (37)
α/°	90	90.0574 (33)	90.2246 (50)	90.5250 (68)	89.8593 (39)
β/°	90	89.8095 (58)	89.6462 (53)	89.5307 (70)	89.8087 (37)
γ/°	120	120.0390 (34)	120.1695 (51)	120.2166 (62)	120.0044 (29)
R_{exp} (%)	-	6.78	7.19	7.48	7.04
R_{wp} (%)	-	11.31	12.70	12.29	12.16
R_p (%)	-	8.67	9.76	9.38	9.26
GOF	-	1.67	1.77	1.64	1.73

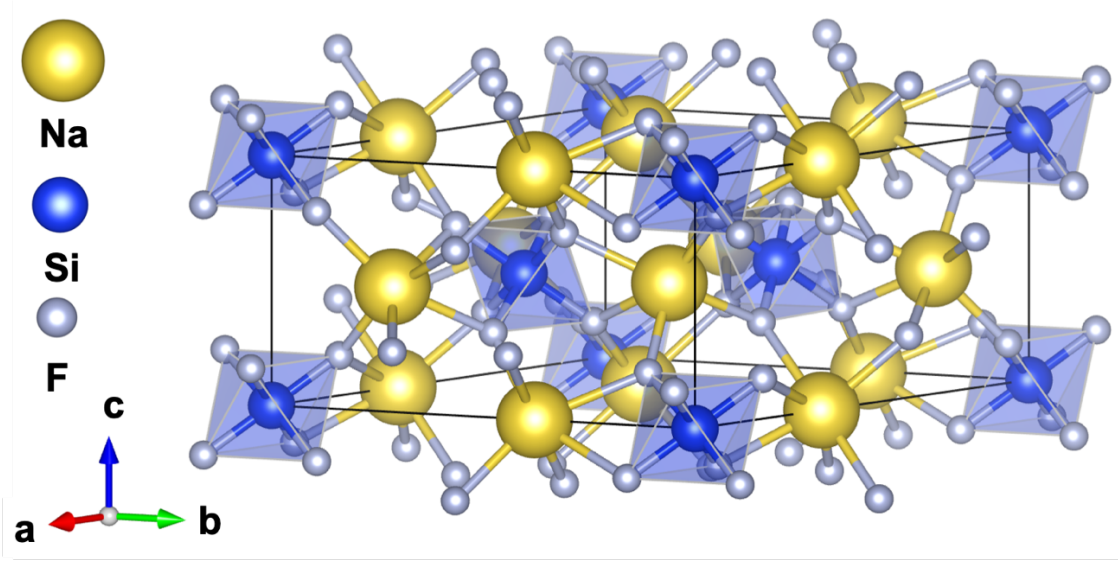

(a)

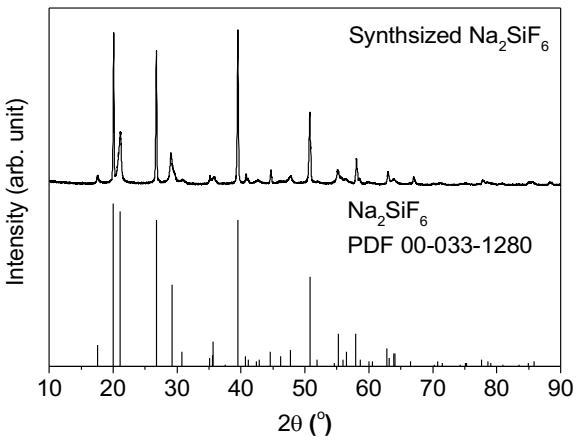

(b)

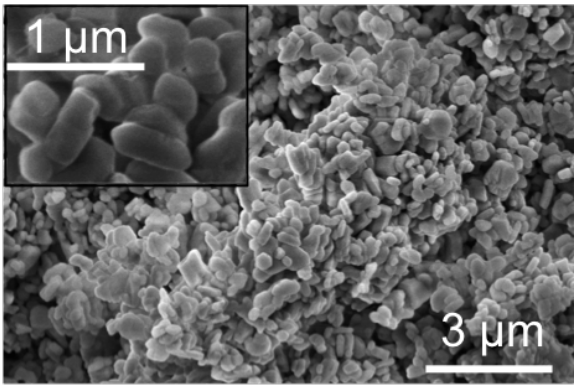

(c)

Figure 6.2 **(a)** Crystal structure of Na_2SiF_6 of a space group *P321* (150) where $a = b = 0.88659$ nm, $c = 0.50438$ nm, and $\gamma = 120°$, drawn by VESTA [104]. **(b)** X-ray diffraction patterns and **(c)** scanning electron micrograph of the synthesized Na_2SiF_6.

6.4 Results And Discussions

6.4.1 Na_2SiF_6

Figure 6.2a shows the crystal structure of Na_2SiF_6 drawn by VESTA [104]. It has a triclinic structure with a space group *P321* (150) where $a = b = 0.88659$ nm, $c = 0.50438$ nm, and $\gamma = 120°$ [18] (Table 6.2). The XRD pattern of the synthesized Na_2SiF_6 are shown in Figure 6.2b. The XRD pattern well-matched with the powder diffraction file for Na_2SiF_6 (PDF 00-033-1280) and there were no impurity peaks, indicating that the high purity material was achieved. To further analyze the lattice parameters, Rietveld refinement was performed using the TOPAS 4.2 software [274]. Table 6.2 shows the structure parameters after Rietveld refinement with the obtained R_{wp}, R_p, GOF values, where R_{wp} is the weighted profiles residual factor, R_p is the profile residual factor and GOF is the goodness of fit. R_p and R_{wp} show how well the crystallographic model matches the experimental X-ray diffraction. The obtained lattice parameters were a = 0.885890 (44), b = 0.883394 (40) nm, c = 0.506867 (40) nm, $\alpha = 89.6793$ (41)°, $\beta = 90.9210$ (49)°, and $\gamma = 119.2287$ (46)°, where values in parentheses are the estimated standard deviations of the last significant figure. The obtained residual values were R_{wp} =11.31%, R_p = 8.67%, GOF = 1.67. Typically, a value of $R_{wp} < 10\%$ or GOF close to 1 is considered to be a close match [210], meaning that the experimental values are in good agreement with the reference values. These results proved that Na_2SiF_6 was successfully synthesized using the ionic liquid, $[Bmim]BF_4$, as a fluoride source to avoid the use of HF. The SEM images (Figure 6.2c) show that particles are rod-shaped (~560 nm in length and ~228 nm in diameter). Given that typical synthesis of Na_2SiF_6 required a high concentration of HF (> 20 M, see Table 6.1) [253, 256], this study demonstrated that an ionothermal reaction using an ionic liquid produces Na_2SiF_6 without HF with resultant small particles , compared to those from other methods.

6.4.2 $Na_2Si_{1-x}Mn_xF_6$

During the synthesis of $Na_2Si_{1-x}Mn_xF$ (Figure 6.1b), the incorporation reaction of $[MnF_6]^{2-}$ in $Na_2Si_{1-x}Mn_xF_6$ occurred as described in Eqns. (5) and (6) with A = Na and X = Si. The *x* values were calculated from the amount of $NaMnO_4$ (0.003, 0.05, 0.1 g) and Na_2SiF_6 (0.5g), with an assumption that all Mn^{4+} was incorporated into Na_2SiF_6, which resulted in targeted values of *x* = 0.007, 0.1, and 0.2. There are only a few studies that report the targeted and measured *x* values [250, 253]. In one, using the cation exchange method, the measured value (0.037) was slightly smaller than the targeted value (0.055) [250]. In another, using a co-precipitation method, the measured value (0.019) was much smaller than the targeted value (0.17) [253] . This implies that different synthetic methods influenced the targeted/actual *x* value. Therefore, the actual *x* values in the present work are expected to be less than the targeted values, based on the measurements from the previous reports.

The XRD patterns of the synthesized $Na_2Si_{1-x}Mn_xF_6$ (*x* = 0.007, 0.1, 0.2) are shown in Figure 6.3a. Octahedrally coordinated Si^{4+} can be substituted by Mn^{4+} due to similar ionic radii (0.0400 nm for 6-coordinated Si^{4+} and 0.053 nm for 6-coordinated Mn^{4+}) [103]. All spectra demonstrated a close match to a PDF for Na_2SiF_6 (PDF 00-033-1280) and no impurity peaks were present. Rietveld refinement of the synthesized powders was also performed to confirm how well they were matched with the crystallographic model. The obtained structure parameters are summarized in Table 6.2. The lattice parameters of $Na_2Si_{1-x}Mn_xF_6$ (*x* = 0, 0.007, 0.1, 0.2) were plotted in Figure 6.3b to analyze the effect the Mn^{4+} concentration. As the *x* value increased from 0 to 0.2, the *a*, *b*, and *c* parameters did not show significant change. This demonstrates that the Na_2SiF_6 structure was not affected by Mn^{4+} activation. The SEM images of $Na_2Si_{0.9}Mn_{0.1}F_6$ are shown in Figure 6.3c. The particle sizes were ~ 500 nm, similar to the host, but less elongated.

This suggests that the HF solution etched the rod-shaped Na_2SiF_6 particles to form more spherically-shaped powders. The particle sizes are smaller than those from the previous reports of $Na_2Si_{1-x}Mn_xF_6$ (1 μm ~20 μm) [253, 256]), indicating that using of the ionic liquid precursors produced significantly smaller particles compared to other methods. These results corroborate other finding using the more expensive ([Bmim]PF_6 precursor to produce fluorides [267].

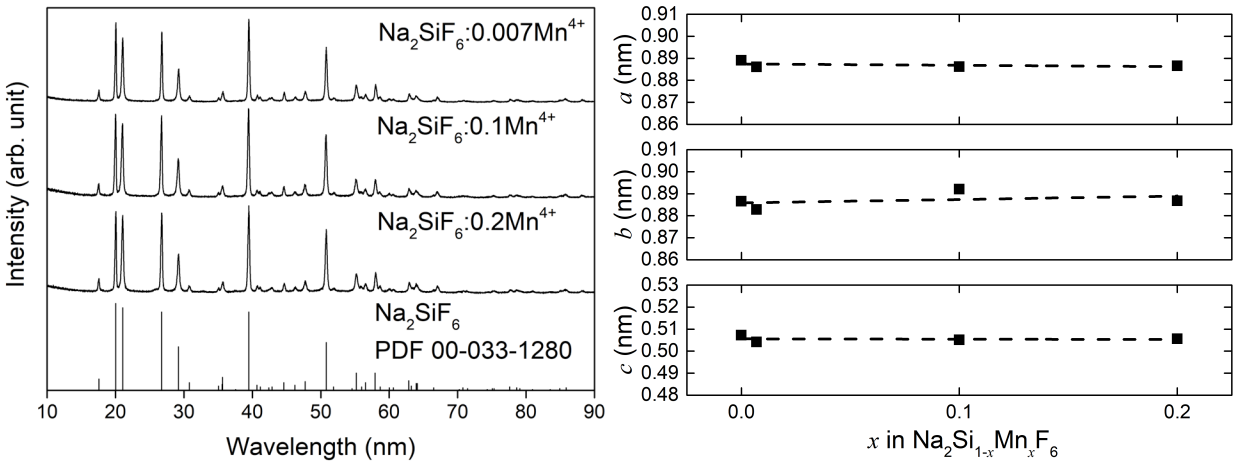

(a) **(b)**

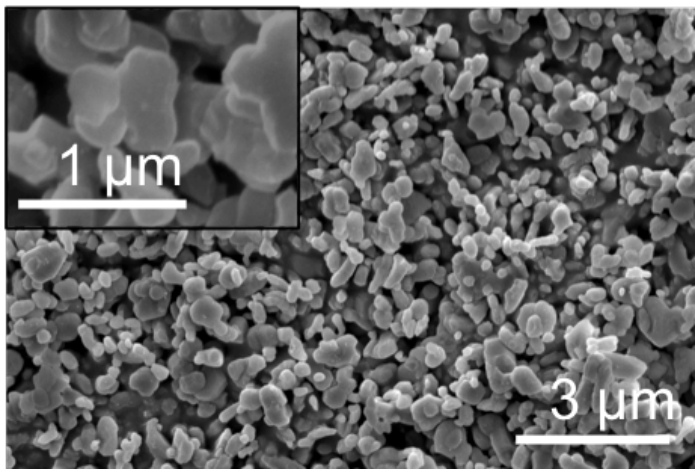

(c)

Figure 6.3 **(a)** X-ray diffraction patterns of $Na_2Si_{1-x}Mn_xF_6$ (x = 0.007, 0.1 and 0.2). **(b)** Calculated lattice parameters of $Na_2Si_{1-x}Mn_xF_6$ (x = 0, 0.007, 0.1, 0.2) from (a). **(c)** Scanning electron micrograph of $Na_2Si_{0.9}Mn_{0.1}F_6$.

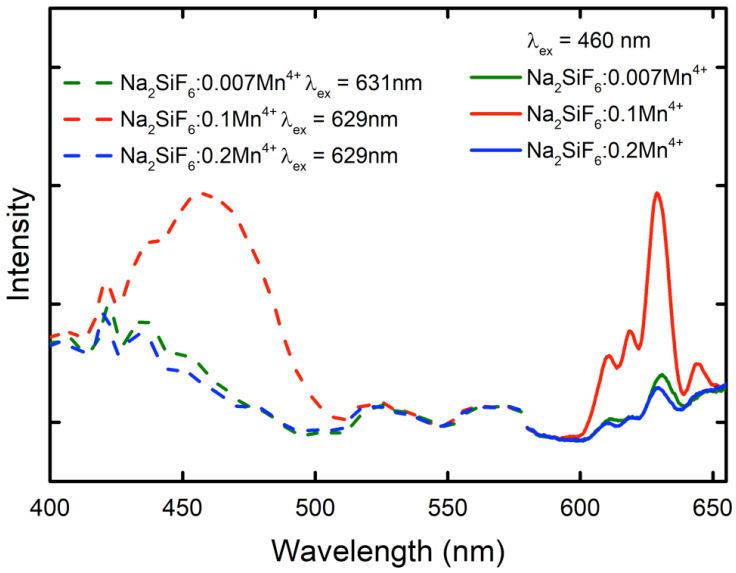

(a)

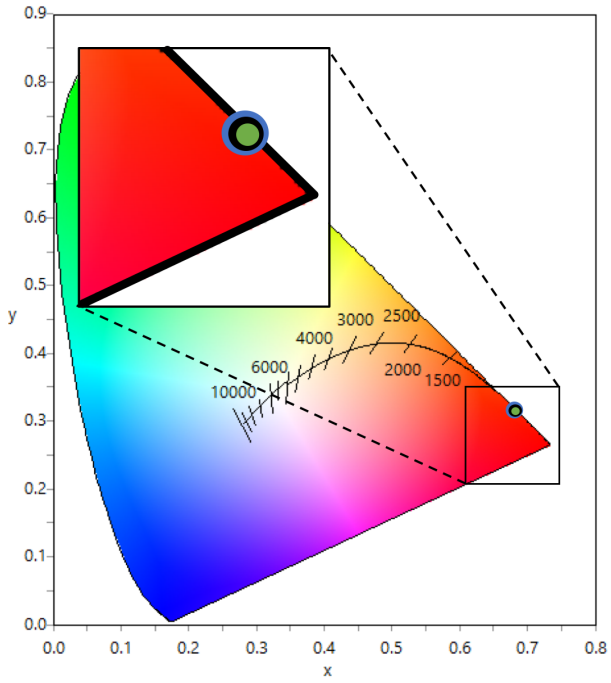

(b)

Figure 6.4 **(a)** Photoluminescence (PL) excitation (dashed line) and emission (solid line) for $Na_2Si_{1-x}Mn_xF_6$: x = 0.007 (green), x = 0.1 (black) and x = 0.2 (blue). The PL emission peaks are marked at 596 nm, 610 nm, 618 nm, 629 nm, and 644 nm, which are related to $\nu3(t_{1u})$, $\nu6(t_{2u})$, ZPL, $\nu6(t_{2u})$ and $\nu3(t_{1u})$ of Mn^{4+} , respectively [54, 250, 253, 256]. **(b)** The CIE chromaticity diagram showing coordinates for x = 0.007 (blue dot), x = 0.1 (black dot) and x = 0.2 (green dot). The chromaticity coordinate values are shown in Table 6.2.

Figure 6.4a shows the PLE and PL emission spectra (λ_{ex} = 460 nm) for $Na_2Si_{1-x}Mn_xF_6$ (x = 0.007, 0.1, and 0.2). The intensities increased from x = 0.007 to x = 0.1 and then decreased at x = 0.2, which is a common concentration quenching characteristic in transition metal ion-activated phosphors [214]. The targeted value of x = 0.1 can be compared to a previous study where the optimum x value was found to be 0.07 [256]. The difference may be attributed to the assumption in the present study that not all Mn^{4+} was incorporated into the structure.

The PLE spectra for x = 0.1 shows a broadband emission centered at 460 nm in the range from 400 nm to 500 nm, which is attributed to the spin-allowed transitions of $^4A_{2g} \rightarrow {}^4T_{1g}$ of Mn^{4+} [250, 256]. The PL emission spectra for x = 0.1 is between 600 and 650 nm due to the spin-forbidden $^2E_g \rightarrow {}^4A_{2g}$ transition of Mn^{4+}. The emission peaks are located at 596 nm, 610 nm, 618 nm, 629 nm, and 644 nm (identified in Figure 6.4a), which are related to $\nu3(t_{1u})$, $\nu6(t_{2u})$, ZPL, $\nu6(t_{2u})$ and $\nu3(t_{1u})$ of Mn^{4+} [54, 250, 253, 256]. $Na_2Si_{1-x}Mn_xF_6$ typically has seven peaks in the range between 590 nm and 650 nm, related to the transitions $\nu3(t_{1u})$, $\nu4(t_{1u})$, $\nu6(t_{2u})$, ZPL, $\nu6(t_{2u})$, $\nu4(t_{1u})$, and $\nu3(t_{1u})$ vibronic modes, as previously reported [250, 253, 256, 275]. However, in the current work, the peaks related to anti-Stokes (~ 605 nm) and Stokes (~ 631 nm) $\nu4(t_{1u})$ vibronic modes are missing, which present as weak shoulder peaks of the anti-Stokes and Stokes $\nu6(t_{2u})$ [250, 253, 256, 275]. The concentration of HF (6 M) used in the present study was much lower than other literature values (>20M), which may not have provided enough F^- to avoid Mn^{4+} reduction or oxidation during the reaction process (Eqn. (3) and (6)). This weakened the shoulder peaks resulted in indistinguishable anti-Stokes and Stokes peaks of $\nu4(t_{1u})$. Corroborating this, a previous report did not show anti-Stokes and Stokes peaks of $\nu4(t_{1u})$ from a fluoride synthesized in a low HF solution (<5 M) [53].

Table 6.4 Colorimetric coordinates (x, y) with x in $Na_2Si_{1-x}Mn_xF_6$.

	CIE coordinates (x, y)	
x in $Na_2Si_{1-x}Mn_xF_6$	***x***	***y***
0.007	0.6877	0.3122
0.1	0.6858	0.3140
0.2	0.6855	0.3143

Table 6.3 shows the Commission International de I'Eclairage (CIE) colorimetric coordinates (x, y) for $Na_2Si_{1-x}Mn_xF_6$, depending on the Mn^{4+} concentration. The coordinates for x = 0.007, x = 0.1 and x = 0.2 are (0.6877, 0.3122), (0.6858, 0.3140), and (0.6855, 0.3143), respectively. Figure 6.4b shows the coordinates for x = 0.007 (blue dot), x = 0.1 (black dot) and x = 0.2 (green dot) on the CIE diagram, which are all in the red region. The CIE colorimetric coordinates for these values of x overlap, showing they are in similar location (Figure 6.4b), close to those of $Na_2Si_{1-x}Mn_xF_6$ reported previously (0.6364, 0.3566) [54]. The difference may be attributed to the lack of the shoulder peaks on $\nu 6(t_{2u})$ in the present work. The obtained CIE values are close to those of a commercial red-emitting nitride (0.642, 0.358) [276] and to the standard values of a red-emitting phosphor according to the National Television System Committee (0.670, 0.330) [277], which are used in the literature to identify a good red-emitting phosphor [249, 278]. This demonstrates that $Na_2Si_{1-x}Mn_xF_6$ is has a desirable red-emission.

6.5 Conclusions

In this study, Na_2SiF_6 powders were synthesized by using an ionic liquid, 1-butyl-3-methylimidazolium tetrafluoroborate ([Bmim]BF_4) as a F^- precursor by an ionothermal reaction without using HF. Also, red-emitting $Na_2Si_{1-x}Mn_xF_6$ phosphors were prepared by dissolved $NaMnO_4$ in a low concentration of HF (6 M) using the Na_2SiF_6 powders as the host lattice. The lattice parameters of $Na_2Si_{1-x}Mn_xF_6$ were not modified from the host. $Na_2Si_{1-x}Mn_xF_6$ showed red-emission under 460 nm excitation with four emission peaks at 610 nm, 618 nm, 629 nm, and 644 nm, arising from $^2E_{(g)} \rightarrow {}^4A_{2(g)}$ emissions of Mn^{4+}. The weak anti-Stokes and Stokes $\nu4(t_{1u})$ vibronic modes were not present, which was attributed to the low concentration of HF that provided insufficient F^- to prevent the oxidation or reduction of Mn^{4+}. The emission intensity increased from $x = 0.007$ to $x = 0.1$ and then decreased at $x = 0.2$ due to concentration quenching. Na_2SiF_6 particles were rod-shaped with 560 nm in length and 228 nm in diameter, while the $Na_2Si_{1-x}Mn_xF_6$ particles were spherically-shaped with ~ 500 nm. The particles sizes for $Na_2Si_{1-x}Mn_xF_6$ were significantly smaller than those reported from other synthesis methods (1 μm ~20 μm). The CIE chromaticity coordinates are in the red emission region and are similar to previously reported values. This work successfully demonstrates as the use of the ionothermal method, using an ionic liquid to synthesize Na_2SiF_6 without HF, and the synthesis of red-emitting phosphor, $Na_2Si_{1-x}Mn_xF_6$, in a low concentration of HF.

Chapter 6, in full, has been submitted for publication of the material as it may appear in "Synthesis of Mn^{4+} activated Na_2SiF_6 red-emitting phosphors using an ionic liquid", Journal of Luminescence 2019. This work was coauthored by E. Novitskaya, Natalie Lam, M. Sanchez, Y. H. Kim, Z. Li, W. B. Im, O. A. Graeve. J. McKittrick is the corresponding author. The dissertation author is the first author of this work.

CHAPTER 7: CONCLUSIONS AND RECOMMENDATION FOR FURUTRE WORK

This work mainly focused on the design and synthetic methods to produce phosphors for near-UV white-LEDs applications. Five projects were performed to develop phosphors: An integrated first principle and experimental investigation to predict Φ; an approach to improve of Φ using a flux; a discovery of a new phosphor composition; a design of color-tunable single-phase phosphors to improve Φ; and a synthesis of red-emitting Mn^{4+} activated Na_2SiF_7 phosphor.

The approach to predict Φ with an integrated first principle and empirical study applied Debye temperature (Θ) of crystal structures as a descriptor to predict Φ of phosphors for white-emitting LEDs. It had been proposed that host lattices with Θ >500 K could be good phosphor candidates having Φ > 80%. For validation of the descriptor Θ for Φ > 80%, the Θ values of the candidates, $CaMgSi_2O_6$ and $Ca_7Mg(SiO_4)_4$ were calculated as 665 K and 601 K, respectively. $Ca_{0.94}Eu_{0.06}MgSi_2O_6$ was synthesized by a co-precipitation method and $(Ca_{0.96}Eu_{0.04})_7Mg(SiO_4)_4$ was synthesized by a sol-gel method. The emission spectra were centered at 458 nm for $Ca_{0.94}Eu_{0.06}Mg(SiO_3)_2$ and at 511 nm for $(Ca_{0.96}Eu_{0.04})_7Mg(SiO_4)_4$ under excitation of 350 nm. However, the Φ values of $Ca_{0.94}Eu_{0.06}MgSi_2O_6$ and $(Ca_{0.96}Eu_{0.04})_7Mg(SiO_4)_4$ were lower than 80% at room temperature. Additionally, the emission intensities of $Ca_{0.94}Eu_{0.06}MgSi_2O_6$ and $(Ca_{0.96}Eu_{0.04})_7Mg(SiO_4)_4$ decreased with the increase of temperature. This implies that the use of high Θ as a descriptor for high Φ is not valid.

Secondly, the improvement of Φ by using a flux was performed for blue-emitting $Ca_{0.94}Eu_{0.06}MgSi_2O_6$ phosphor with nano-sized particles. The $Ca_{0.94}Eu_{0.06}MgSi_2O_6$ phosphor synthesized by the co-precipitation reaction had only 5% of Φ. Fluxes, NH_4F, NH_4Cl, and H_3BO_3, were used during the post-annealing process of $Ca_{0.94}Eu_{0.06}MgSi_2O_6$ to enhance the diffusion in the material. The Φ of $Ca_{0.94}Eu_{0.06}MgSi_2O_6$ was improved up to 17% with 10 wt.% of NH_4F flux

without change of the particles size; the crystallize size increased from 13 nm to 31 nm. The Φ of $Ca_{0.94}Eu_{0.06}MgSi_2O_6$ with NH_4Cl flux was improved up to 11% with the increase in the crystallite size from 13 nm to 18 nm. However, the Φ of $Ca_{0.94}Eu_{0.06}MgSi_2O_6$ with H_3BO_3 flux was decreased due to the SiO_2 impurity associated with the B ions replacement in Si ions of $Ca_{0.94}Eu_{0.06}MgSi_2O_6$. This work proves that the poor Φ of phosphors can be improved by the addition of a flux, but flux composition and amount must be carefully investigated to expect the improvement of Φ without the presence of secondary phases.

A new phosphor composition for near-UV white LED was explored through mining unexplored chemistries and experimental approaches. A new candidate host, Sr_2LiAlO_4, was discovered and this is the first known Sr-Li-Al-O quaternary crystal. $Sr_2LiAlO_4:Ce^{3+}$ and $Sr_2LiAlO_4:Eu^{2+}$ were synthesized by solid-state reaction with 86% purity and by combustion reaction with 94% purity. The emission of $Sr_2LiAlO_4:Ce^{3+}$ and $Sr_2LiAlO_4:Eu^{2+}$ were ~ 434 nm (green-yellow) and 512 nm (blue) under the 394 nm and 384 nm excitation, respectively. The Φs of $Sr_2LiAlO_4:Ce^{3+}$ and $Sr_2LiAlO_4:Eu^{2+}$ were 32% and 25%, respectively. $Sr_2LiAlO_4:Ce^{3+}$ and $Sr_2LiAlO_4:Eu^{2+}$ demonstrated good thermal stabilities. The emission intensities of $Sr_2LiAlO_4:Ce^{3+}$ and $Sr_2LiAlO_4:Eu^{2+}$ were 91% and 88%, respectively, comparing to the intensities at room temperature. This work shows the possibility to explore a novel phosphor composition through the integrated calculations and empirical studies of initial phosphors.

Another approach to improve Φ was the design of a color tunable phosphors using co-activating of Eu^{2+} and Ce^{3+} in a single-phase host lattice. $Sr_{2-x-y}Eu_xCe_yLiAlO_4$ was synthesized using a combustion reaction; the concentrations of Eu^{2+} and Ce^{3+} were varied to change the emission from blue to green. The highest Φ of 55% with $Sr_{1.9985}Eu_{0.001}Ce_{0.0005}LiAlO_4$ was obtained.

Eu^{2+} and Ce^{3+} co-activated Sr_2LiAlO_4 was found to be a promising color-tunable phosphor to improve Φ.

Furthermore, Na_2SiF_6, was synthesized as a host material with a green method using an ionic liquid via an ionothermal reaction. The synthesized Na_2SiF_6 was used for a red-emitting phosphor, $Na_2SiF_6:Mn^{4+}$ that was synthesized in low concentration HF; the particles sizes (200-500 nm) were much smaller than those prepared by other methods (tens of microns). $Na_2SiF_6:Mn^{4+}$ showed red-emission with four narrow emission peaks at 610nm, 618 nm, 629 nm, and 644 nm, arising from $^2E_{(g)} \rightarrow {}^4A_{2(g)}$ emissions of Mn^{4+} under 460 nm excitation. This work successfully demonstrates the use of an ionothermal method, with an ionic liquid to synthesize Na_2SiF_6 without HF, and the synthesis of red-emitting phosphor, $Na_2Si_{1-x}Mn_xF_6$, in a low concentration of HF.

In summary, this dissertation validates approaches to improve Φ of phosphors through the collaborative study of calculations and experiments together with the synthetic process modifications, and the incorporation of co-activated phosphors.

Future work for this research is following: First, exploring methods to predict high Φ phosphors is an urgent task to avoid time and effort to explore phosphors with high Φ using an empirical approach. Several approaches have already been reported to predict high Φ through first-principle calculations and crystal structures properties, but it is not simple to predict high Φ using only one value of crystal structure properties such as Debye temperature (Θ) due to the complexity of factors influenced the Φ. For example, synthetic methods and the thermal quenching property change the Φ, although the phosphor materials are identical. Thus the exploration of predicted factors for Φ requires further investigation.

Secondly, developing methods to improve Φ of nano-/submicron sized phosphors during synthetic processes is necessary. Final phosphor converted LED efficiency depends on the LED

efficiency, package efficiency (extraction efficiency), Stokes conversion efficiency, and phosphor Φ. All of these must be optimized to produce the high efficient LED lighting. The improvement of Φ for phosphors is an efficient approach. Although this work suggested to utilize a flux material to facilitate the ionic diffusion in the particles to have phosphor particles with an improved Φ, it is still a challenge to obtain nano-sized phosphors with high Φ.

Thirdly, developing more safe methods to synthesize Mn^{4+} activated fluorides for the red-emitting phosphors is required. High toxic HF solution is a crucial to obtain Mn^{4+} activated fluorides with high Φ up to now. However, handling HF solution must be careful due to the toxity. The effort to develop new synthetic methods for red-emitting fluoride phosphors has been investigated to avoid the use of HF solution. However, Mn^{4+} activated fluorides synthesized without HF or with low concentration of HF suffers from the low Φ comparing to the method performed with high concentration HF solution. Therefore, it needs further investigation on a novel synthetic method without using high concentration toxic HF solution, yet to produce phosphors with high Φ.

REFERENCES

[1] J. Phillips, P. Burrows, R. Davis, J. Simmons, G. Malliaras, F. So, J. Misewich, A. Nurmikko, D. Smith, and J. Tsao, *Basic Research Needs for Solid-State Lighting. Report of the Basic Energy Sciences Workshop on Solid-State Lighting, May 22-24, 2006*, DOESC (USDOE Office of Science (SC)), 2006.

[2] J. Penning, K. Stober, V. Taylor, and M. Yamada, *Energy savings forecast of solid-state lighting in general illumination applications*, Navigant Consulting Inc., Washington, DC (United States), 2016.

[3] H. M. Bardsley N, Pattison L, Pattison M, Stober K, Taylor V, Tsao J, Yamada M, *Solid-State Lighting R&D Plan, DOE/EE-1418*, EERE Publication and Product Library, 2016.

[4] J. McKittrick, L. E. Shea-Rohwer, and D. J. Green, "Review: Down Conversion Materials for Solid-State Lighting," *Journal of the American Ceramic Society,* vol. 97, no. 5, pp. 1327-1352, 2014.

[5] T. Smith, and J. Guild, "The CIE colorimetric standards and their use," *Transactions of the optical society,* vol. 33, no. 3, pp. 73, 1931.

[6] J. Brodrick, *Solid-state lighting research and development: Multi-year program plan, Lighting Research and Development, Building Technologies Program, Washington D.C., 2012.*

[7] F. Rubinstein, S. Johnson, *Advanced lighting program development*, Final report to California Institute for energy efficiency, Feb. 1998.

[8] T. Bosschaert, "How to choose the best lamp for your purpose " *LED & Artificial Light Guide*, 2011, (http://www.except.nl/en/articles/92-led-artificial-light-guide).

[9] H. S. Jang, W. B. Im, D. C. Lee, D. Y. Jeon, and S. S. Kim, "Enhancement of red spectral emission intensity of $Y_3Al_5O_{12}:Ce^{3+}$ phosphor via Pr co-doping and Tb substitution for the application to white LEDs," *Journal of Luminescence,* vol. 126, pp. 371-377, 2007.

[10] G. Li, M. Li, L. Li, H. Yu, H. Zou, L. Zou, S. Gan, and X. Xu, "Luminescent properties of Sr2Al2SiO7:Ce3+,Eu2+ phosphors for near UV-excited white light-emitting diodes," *Materials Letters,* vol. 65, no. 23-24, pp. 3418-3420, 2011.

[11] J. McKittrick, M. E. Hannah, A. Piquette, J. K. Han, J. I. Choi, M. Anc, M. Galvez, H. Lugauer, J. B. Talbot, and K. C. Mishra, "Phosphor Selection Considerations for Near-UV LED Solid State Lighting," *ECS Journal of Solid State Science and Technology,* vol. 2, no. 2, pp. R3119-R3131, 2012.

[12] J. K. Sheu, S. J. Chang, C. H. Kuo, Y. K. Su, L. W. Wu, Y. C. Lin, W. C. Lai, J. M. Tsai, G. C. Chi, and R. K. Wu, "White-light emission from near UV InGaN-GaN LED chip precoated with blue/green/red phosphors," *IEEE Photonics Technology Letters,* vol. 15, pp. 18-20, 2003.

[13] S. Neeraj, N. Kijima, and A. K. Cheetham, "Novel red phosphors for solid-state lighting: the system $NaM(WO_4)_{2-x}(MoO_4)_x:Eu^{3+}$ (M=Gd, Y, Bi)," *Chemical Physics Letters,* vol. 387, pp. 2-6, 2004.

[14] S. H. M. Poort, W. Janssen, and G. Blasse, "Optical properties of Eu^{2+}-activated orthosilicates and orthophosphates," *Journal of Alloys and Compounds,* vol. 260, pp. 93-97, 1997.

[15] S. Pimputkar, J. S. Speck, S. P. DenBaars, and S. Nakamura, "Prospects for LED lighting," *Nature Photonics,* vol. 3, no. 4, pp. 180, 2009.

[16] J. Choi, M. Anc, A. Piquette, M. Hannah, K. Mishra, J. McKittrick, and J. Talbot, "Electrophoretic deposition of phosphors for white solid state lighting using near UV-emitting LEDs," *ECS Journal of Solid State Science and Technology,* vol. 2, no. 7, pp. R153-R159, 2013.

[17] X. Qiao, S. Qi, Y. Lu, Y. Pu, Y. Huang, and X. Wang, "Synthesis, structure and red-emitting luminescence properties of Eu^{3+} -activated perovskite-related tungstate $Ba_4Na_2W_2O_{11}$," *Journal of Alloys and Compounds,* vol. 656, pp. 189-195, 2016.

[18] A. Zalkin, J. Forrester, and D. H. Templeton, "The crystal structure of sodium fluorosilicate," *Acta Crystallographica,* vol. 17, no. 11, pp. 1408-1412, 1964.

[19] http://www.lightage-tech.com/milky-white-cover-60mm-5w-high-power-led-bulb-light-la5-bb05/.

[20] G. Blasse, and B. C. Grabmaier, *Luminescent Materials*, Berlin Heidlberg: Springer-Verlag, 1994.

[21] H. Yamamoto, *Fundamentals of Luminescence*, p.^pp. 25-26: CRC Press, Boca Raton, FL, 2007.

[22] D. C. Harris, and M. D. Bertolucci, *Symmetry and Spectroscopy*, Oxford, United Kingdom: Oxford University Press, 1978.

[23] S. S. M. Y. Willian, H. Yamamoto, *Phosphor handbook*, 2nd edition ed.: CRC press, Boca Raton, FL, US, 2007.

[24] G. H. Dieke, *Spectra and Energy Levels of Rare Earth Ions in Crystals*: Wiley Interscience, New York, US, 1968.

[25] E. J. Bosze, J. Carver, S. Singson, J. McKittrick, and G. A. Hirata, "Long-ultraviolet-excited white-light emission in rare-earth-activated yttrium-oxyorthosilicate," *Journal of the American Ceramic Society,* vol. 90, no. 8, pp. 2484-2488, 2007.

[26] L. Muresan, Y. Karabulut, A. Cadis, I. Perhaita, A. Canimoglu, J. G. Guinea, L. B. Tudoran, D. Silipas, M. Ayvacikli, and N. Can, "Tunable luminescence of broadband-excited and

narrow line green emitting $Y_2SiO_5:Ce^{3+},Tb^{3+}$ phosphor," *Journal of Alloys and Compounds,* vol. 658, pp. 356-366, 2016.

[27] D. F. Shriver, P. W. Akins, and C. H. Langford, *Inorganic chemisty*: WH. Freeman and company, New York, N.Y. 1990.

[28] E. Van der Kolk, P. Dorenbos, A. Vink, R. Perego, C. Van Eijk, and A. Lakshmanan, "Vacuum ultraviolet excitation and emission properties of Pr^{3+} and Ce^{3+} in MSO_4 (M= Ba,Sr, and Ca) and predicting quantum splitting by P^{3+} in oxides and fluorides," *Physical Review B,* vol. 64, no. 19, pp. 195129, 2001.

[29] J. Han, M. Hannah, A. Piquette, J. Talbot, K. Mishra, and J. McKittrick, "Sol-gel synthesis of single phase, high quantum efficiency $LiCaPO_4:Eu^{2+}$ phosphors," *ECS Journal of Solid State Science and Technology,* vol. 1, no. 1, pp. R37-R40, 2012.

[30] Z. Wu, J. Shi, J. Wang, M. Gong, and Q. Su, "A novel blue-emitting phosphor $LiSrPO_4$: Eu^{2+} for white LEDs," *Journal of Solid State Chemistry,* vol. 179, no. 8, pp. 2356-2360, 2006.

[31] Z. Wu, J. Liu, and M. Gong, "Thermally stable luminescence of $SrMg_2(PO_4)_2:Eu^{2+}$ phosphor for white light NUV light-emitting diodes," *Chemical Physics Letters,* vol. 466, no. 1-3, pp. 88-90, 2008.

[32] K. H. Kwon, W. B. Im, H. S. Jang, H. S. Yoo, and D. Y. Jeon, "Luminescence properties and energy transfer of site-sensitive $Ca_{6-x-y}Mg_{x-z}(PO_4)_4:Eu_y^{2+},Mn_z^{2+}$ phosphors and their application to near-UV LED-based white LEDs," *Inorganic chemistry,* vol. 48, no. 24, pp. 11525-11532, 2009.

[33] W. B. Im, S. Brinkley, J. Hu, A. Mikhailovsky, S. P. DenBaars, and R. Seshadri, "$Sr_{2.975-x}Ba_xCe_{0.025}AlO_4F$: a highly efficient green-emitting oxyfluoride phosphor for solid state white lighting," *Chemistry of Materials,* vol. 22, no. 9, pp. 2842-2849, 2010.

[34] C. Guo, M. Li, Y. Xu, T. Li, Z. Ren, and J. Bai, "A potential green-emitting phosphor $Ca_8Mg(SiO_4)_4Cl_2:Eu^{2+}$ for white light emitting diodes prepared by sol–gel method," *Applied Surface Science,* vol. 257, no. 21, pp. 8836-8839, 2011.

[35] W. Ding, J. Wang, M. Zhang, Q. Zhang, and Q. Su, "A novel orange phosphor of Eu^{2+}-activated calcium chlorosilicate for white light-emitting diodes," *Journal of Solid State Chemistry,* vol. 179, no. 11, pp. 3582-3585, 2006.

[36] J. K. Han, M. E. Hannah, A. Piquette, J. B. Talbot, K. C. Mishra, and J. McKittrick, "Particle morphology and luminescence properties of green emitting $Ba_2SiO_4:Eu^{2+}$ through a hydrothermal reaction route," *Journal of Luminescence,* vol. 161, pp. 20-24, 2015.

[37] X. Zhang, J. Zhang, R. Wang, and M. Gong, "Photo-physical behaviors of efficient green phosphor $Ba_2MgSi_2O_7:Eu^{2+}$ and its application in light-emitting diodes," *Journal of the American Ceramic Society,* vol. 93, no. 5, pp. 1368-1371, 2010.

[38] L. Jiang, C. Chang, D. Mao, and C. Feng, "Concentration quenching of Eu^{2+} in $Ca_2MgSi_2O_7:Eu^{2+}$ phosphor," *Materials Science and Engineering: B,* vol. 103, no. 3, pp. 271-275, 2003.

[39] T. L. Barry, "Equilibria and Eu^{2+} luminescence of subsolidus phases bounded by $Ba_3MgSi_2O_8$, $Sr_3MgSi_2O_8$, and $Ca_3MgSi_2O_8$," *Journal of The Electrochemical Society,* vol. 115, no. 7, pp. 733-738, 1968.

[40] S.-D. Jee, J. K. Park, and S.-H. Lee, "Photoluminescence properties of Eu^{2+}-activated Sr_3SiO_5 phosphors," *Journal of materials science,* vol. 41, no. 10, pp. 3139-3141, 2006.

[41] J.-Y. Tang, W.-J. Xie, K. Huang, L.-Y. Hao, X. Xu, and R.-J. Xie, "A high stable blue $BaSi_3Al_3O_4N_5:Eu^{2+}$ phosphor for white leds and display applications," *Electrochemical and Solid-State Letters,* vol. 14, no. 8, pp. J45-J47, 2011.

[42] T. Suehiro, N. Hirosaki, R.-J. Xie, and T. Sato, "Blue-emitting $LaSi_3N_5:Ce^{3+}$ fine powder phosphor for UV-converting white light-emitting diodes," *Applied Physics Letters,* vol. 95, no. 5, pp. 051903, 2009.

[43] K. Takahashi, N. Hirosaki, R.-J. Xie, M. Harada, K.-i. Yoshimura, and Y. Tomomura, "Luminescence properties of blue $La_{1-x}Ce_xAl(Si_{6-z}Al_z)(N_{10-z}O_z)(z\sim1)$ oxynitride phosphors and their application in white light-emitting diode," *Applied Physics Letters,* vol. 91, no. 9, pp. 091923, 2007.

[44] P. Pust, V. Weiler, C. Hecht, A. Tücks, A. S. Wochnik, A.-K. Henß, D. Wiechert, C. Scheu, P. J. Schmidt, and W. Schnick, "Narrow-band red-emitting $Sr[LiAl_3N_4]:Eu^{2+}$ as a next-generation LED-phosphor material," *Nature Materials,* vol. 13, no. 9, pp. 891, 2014.

[45] D. Palumbo, and J. Brown, "Electronic states of Mn^{2+}-activated phosphors. I. green-emitting phosphors," *Journal of The Electrochemical Society,* vol. 117, no. 9, pp. 1184-1188, 1970.

[46] G. Burns, E. Geiss, B. Jenkins, and M. I. Nathan, "Cr^{3+} fluorescence in garnets and other crystals," *Physical Review,* vol. 139, no. 5A, pp. A1687, 1965.

[47] Q. Zhou, L. Dolgov, A. M. Srivastava, L. Zhou, Z. Wang, J. Shi, M. D. Dramićanin, M. G. Brik, and M. Wu, "Mn^{2+} and Mn^{4+} red phosphors: synthesis, luminescence and applications in WLEDs. A review," *Journal of Materials Chemistry C,* vol. 6, no. 11, pp. 2652-2671, 2018.

[48] http://chemistrysaanguyen.weebly.com/117-the-hydrogen-orbitals.html.

[49] https://www.dlt.ncssm.edu/tiger/chem8.htm.

[50] S. Sugano, Y. Tanabe, and H. Kamimura, *Multiples of Transition Metal Ions in Crystals*: New brk: Academic Press, 1970.

[51] Y. Li, S. Qi, P. Li, and Z. Wang, "Research progress of Mn doped phosphors," *RSC Advances,* vol. 7, no. 61, pp. 38318-38334, 2017.

[52] R. Cao, F. Zhang, C. Cao, X. Yu, A. Liang, S. Guo, and H. Xue, "Synthesis and luminescence properties of $CaAl_2O_4:Mn^{4+}$ phosphor," *Optical Materials,* vol. 38, pp. 53-56, 2014.

[53] X. Gao, Y. Song, G. Liu, X. Dong, J. Wang, and W. Yu, "Narrow-band red emitting phosphor $BaTiF_6:Mn^{4+}$: preparation, characterization and application for warm white LED devices," *Dalton Transactions,* vol. 45, no. 44, pp. 17886-17895, 2016.

[54] T.-C. Lang, T. Han, L.-L. Peng, and M.-J. Tu, "Luminescence properties of Na_2SiF_6: Mn^{4+} red phosphors for high colour-rendering white LED applications synthesized via a simple exothermic reduction reaction," *Materials Chemistry Frontiers,* vol. 1, no. 5, pp. 928-932, 2017.

[55] T. Deng, E. Song, J. Sun, L. Wang, Y. Deng, S. Ye, J. Wang, and Q. Zhang, "The design and preparation of the thermally stable, Mn^{4+} ion activated, narrow band, red emitting fluoride Na_3GaF_6: Mn^{4+} for warm WLED applications," *Journal of Materials Chemistry C,* vol. 5, no. 11, pp. 2910-2918, 2017.

[56] R. Cao, M. Peng, E. Song, and J. Qiu, "High efficiency Mn^{4+} doped $Sr_2MgAl_{22}O_{36}$ red emitting phosphor for white LED," *ECS Journal of Solid State Science and Technology,* vol. 1, no. 4, pp. R123-R126, 2012.

[57] Z. Liu, M. Yuwen, J. Liu, C. Yu, T. Xuan, and H. Li, "Electrospinning, optical properties and white LED applications of one-dimensional $CaAl_{12}O_{19}:Mn^{4+}$ nanofiber phosphors," *Ceramics International,* vol. 43, no. 7, pp. 5674-5679, 2017.

[58] R. Cao, D. Ceng, X. Yu, S. Guo, Y. Wen, and G. Zheng, "Synthesis and luminescence properties of novel deep red emitting phosphors $Li_2MgGeO_4:Mn^{4+}$," *Functional Materials Letters,* vol. 8, no. 04, pp. 1550046, 2015.

[59] C. Shivakumara, R. Saraf, S. Behera, N. Dhananjaya, and H. Nagabhushana, "Scheelite-type MWO_4 (M=Ca, Sr, and Ba) nanophosphors: Facile synthesis, structural characterization, photoluminescence, and photocatalytic properties," *Materials Research Bulletin,* vol. 61, pp. 422-432, 2015.

[60] P. Dorenbos, "The 5d level positions of the trivalent lanthanides in inorganic compounds," *Journal of Luminescence,* vol. 91, pp. 155–176, 2000.

[61] P. Dorenbos, "Energy of the first $4f^7 \rightarrow 4f^6 5d$ transition of Eu^{2+} in inorganic compounds," *Journal of Luminescence,* vol. 104, no. 4, pp. 239-260, 2003.

[62] P. Dorenbos, "Predictability of 5d level positions of the triply ionized lanthanides in halogenides and chalcogenides," *Journal of Luminescence,* vol. 87, pp. 970-972, 2000.

[63] P. Dorenbos, "Anomalous luminescence of Eu^{2+} and Yb^{2+} in inorganic compounds," *Journal of Physics: Condensed Matter,* vol. 15, no. 17, pp. 2645, 2003.

[64] P. Dorenbos, "5 d-level energies of Ce^{3+} and the crystalline environment. III. Oxides containing ionic complexes," *Physical Review B,* vol. 64, no. 12, pp. 125117, 2001.

[65] P. Dorenbos, ″Energy of the first $4f^7 \rightarrow 4f^6 5d$ transition of Eu^{2+} in inorganic compounds,″ *Journal of luminescence,* vol. 104, no. 4, pp. 239-260, 2003.

[66] P. Dorenbos, "5*d*-level energies of Ce^{3+} and the crystalline environment. I. Fluoride compounds," *Physical Review B,* vol. 62, no. 23, pp. 15640, 2000.

[67] H. C. V. D. Hulst, *Light Scattering by Small Particles*, New York: John Wiley & Sons, 1957.

[68] D. Van der Heggen, J. J. Joos, and P. F. Smet, "Importance of evaluating the intensity dependency of the quantum efficiency: impact on LEDs and persistent phosphors," *ACS Photonics,* vol. 5, no. 11, pp. 4529-4537, 2018.

[69] H. Luo, J. Liu, X. Zheng, L. Han, K. Ren, and X. Yu, "Enhanced photoluminescence of $Sr_3SiO_5:Ce^{3+}$ and tuneable yellow emission of $Sr_3SiO_5:Ce^{3+},Eu^{2+}$ by Al^{3+} charge compensation for W-LEDs," *Journal of Materials Chemistry,* vol. 22, no. 31, pp. 15887-15893, 2012.

[70] S. H. Lee, J. I. Choi, Y. J. Kim, J. K. Han, J. Ha, E. Novitskaya, J. B. Talbot, and J. McKittrick, "Comparison of luminescent properties of $Y_2O_3:Eu^{3+}$ and $LaPO_4:Ce^{3+}$, Tb^{3+} phosphors prepared by various synthetic methods," *Materials Characterization,* vol. 103, pp. 162-169, 2015.

[71] Z. Wang, J. Ha, Y. H. Kim, W. B. Im, J. McKittrick, and S. P. Ong, "Mining unexplored chemistries for phosphors for high-color-quality white-light-emitting diodes," *Joule,* vol. 2, no. 5, pp. 914-926, 2018/05/16/, 2018.

[72] J. Han, J. Choi, A. Piquette, M. Hannah, M. Anc, M. Galvez, J. Talbot, and J. McKittrick, "Phosphor development and integration for near-UV LED solid state lighting," *ECS Journal of Solid State Science and Technology,* vol. 2, no. 2, pp. R3138-R3147, 2013.

[73] J. Han, M. Hannah, A. Piquette, J. Talbot, K. Mishra, and J. McKittrick, "Nano-and submicron sized europium activated silicate phosphors prepared by a modified co-precipitation method," *ECS Journal of Solid State Science and Technology,* vol. 1, no. 3, pp. R98-R102, 2012.

[74] J. Ha, E. Novitskaya, G. Hirata, C. Zhou, R. Ridley, O. Graeve, and J. McKittrick, "A Facile Method Using a Flux to Improve Quantum Efficiency of Submicron Particle Sized Phosphors for Solid-State Lighting Applications," *Ceramics,* vol. 1, no. 1, pp. 38-53, 2018.

[75] J. Ha, Z. Wang, E. Novitskaya, G. A. Hirata, O. A. Graeve, S. P. Ong, and J. McKittrick, "An integrated first principles and experimental investigation of the relationship between

structural rigidity and quantum efficiency in phosphors for solid state lighting," *Journal of Luminescence,* vol. 179, pp. 297-305, 2016.

[76] H. Terraschke, and C. Wickleder, "UV, blue, green, yellow, red, and small: newest developments on Eu-doped nanophosphors," *Chemcal Reveiws,* vol. 115, pp. 11352-11378, 2015.

[77] J. K. Han, M. E. Hannah, A. Piquette, G. A. Hirata, J. B. Talbot, K. C. Mishra, and J. McKittrick, "Structure dependent luminescence characterization of green–yellow emitting Sr_2SiO_4:Eu^{2+} phosphors for near UV LEDs," *Journal of Luminescence,* vol. 132, no. 1, pp. 106-109, 2012.

[78] J. Han, M. Hannah, A. Piquette, J. Talbot, K. Mishra, and J. McKittrick, "Particle morphology and luminescence properties of green emitting Ba 2 SiO 4: Eu 2+ through a hydrothermal reaction route," *Journal of Luminescence,* vol. 161, pp. 20-24, 2015.

[79] S. Nakamura, and G. Fasol, *The Blue Laser Diode*, Berlin: Springer, 1996.

[80] N. Narendran, N. Maliyagoda, A. Bierman, R. M. Pysar, and M. Overington, "Characterizing white LEDs for general illumination applications," *Proc. SPIE Int. Soc. Opt. Eng. ,* vol. 3938, pp. 240-248, 2000.

[81] M. G. Craford, *Light Emitting Diode Technology*, Dordrecht: Kluwer Academic Publishers, 1996.

[82] Y. Q. Li, A. C. A. Delsing, G. de With, and H. T. Hintzen, "Luminescence properties of Eu^{2+}-activated alkaline-earth silicon-oxynitride $MSi_2O_{2-\delta}N_{2+2/3\delta}$ (M = Ca, Sr, Ba): a promising class of novel LED conversion phosphors," *Chemistry of Materials,* vol. 17, pp. 3242-3248, 2005.

[83] Y. Chen, Y. Li, J. Wang, M. Wu, and C. Wang, "Color-Tunable Phosphor of $Eu^{2+}$and Mn^{2+}Codoped $Ca_2Sr(PO_4)_2$for UV Light-Emitting Diodes," *The Journal of Physical Chemistry C,* vol. 118, no. 23, pp. 12494-12499, 2014.

[84] Z. Xia, Z. Xu, M. Chen, and Q. Liu, "Recent developments in the new inorganic solid-state LED phosphors," *Dalton Trans.,* vol. 45, pp. 11214-11232, 2016.

[85] T. Takeda, N. Hirosaki, S. Funahshi, and R.-J. Xie, "Narrow-band green-emitting phosphor $Ba_2LiSi_7AlN_{12}$:Eu^{2+} with high thermal stability discovered by a single particle diagnosis approach," *Chemistry of Materials,* vol. 27, no. 17, pp. 5892-5898, 2015.

[86] Z. Wang, I.-H. Chu, F. Zhou, and S. P. Ong, "Electronic structure descriptor for the discovery of narrow-band red-emitting phosphors," *Chemistry of Materials,* vol. 28, no. 11, pp. 4024-4031, 2016.

[87] J. Brgoch, S. P. DenBaars, and R. Seshadri, "Proxies from Ab initio calculations for screening efficient Ce^{3+} phosphor hosts," *The Journal of Physical Chemistry C,* vol. 117, no. 35, pp. 17955-17959, 2013.

[88] Y. Jia, H. Qiao, Y. Zheng, N. Guo, and H. You, "Synthesis and photoluminescence properties of Ce^{3+} and Eu^{2+}-activated $Ca_7Mg(SiO_4)_4$ phosphors for solid state lighting," *Phys Chem Chem Phys,* vol. 14, no. 10, pp. 3537-3542, Mar 14, 2012.

[89] K. H. Lee, S. H. Park, H. S. Yoon, Y.-I. Kim, H. G. Jang, and W. B. Im, "Bredigite-structure orthosilicate phosphor as a green component for white LED: the structural and optical properties," *Optical Express,* vol. 20, no. 6, pp. 6248-6259, 2012.

[90] P. E. Blöchl, "Projector augmented-wave method," *Physical Review B,* vol. 50, no. 24, pp. 17953-17979, 1994.

[91] G. Kresse, "Efficient iterative schemes for ab initio total-energy calculations using a plane-wave basis set," *Physical Review B,* vol. 54, pp. 11169-11186, 1996.

[92] J. P. Perdew, K. Burke, and M. Ernzerhof, "Generalized gradient approximation made simple," *Physical Review Letters,* vol. 77, pp. 3865-3868, 1996.

[93] S. P. Ong, S. Cholia, A. Jain, M. Brafman, D. Gunter, G. Ceder, and K. A. Persson, "The materials application programming interface (API): a simple, flexible and efficient API for materials data based on representational state transfer (REST) principles," *Computational Materials Science,* vol. 97, pp. 209-215, 2015.

[94] A. Jain, S. P. Ong, G. Hautier, W. Chen, W. D. Richards, S. Dacek, S. Cholia, D. Gunter, D. Skinner, G. Ceder, and K. A. Persson, "Commentary: The materials project: a materials genome approach to accelerating materials innovation," *APL Materials,* vol. 1, no. 1, pp. 011002, 2013.

[95] Z. Deng, Z. Wang, I.-H. Chu, J. Luo, and S. P. Ong, "Elastic properties of alkali superionic conductor electrolytes from first principles calculations," *Journal of The Electrochemical Society,* vol. 163, no. 2, pp. A67-A74, 2015.

[96] A. Chaudhry, R. Boutchko, G. Zhang, N. Grønbech-Jensen, and A. Canning, "First-principles study of luminescence in Ce-doped inorganic scintillators," *Physical Review B,* vol. 89, pp. 155105, 2014.

[97] F. Tran, and P. Blaha, "Accurate band gaps of semiconductors and insulators with a semilocal exchange-correlation potential," *Physical Review Letters,* vol. 102, pp. 5-8, 2009.

[98] P. Dorenbos, "Absolute location of lanthanide energy levels and the performance of phosphors," *Journal of Luminescence,* vol. 122-123, pp. 315-317, 2007.

[99] Z. Zhang, O. M. ten Kate, A. Delsing, E. van der Kolk, P. H. L. Notten, P. Dorenbos, J. Zhao, and H. T. Hintzen, "Photoluminescence properties and energy level locations of RE^{3+} (RE = Pr, Sm, Tb, Tb/Ce) in $CaAlSiN_3$ phosphors," *Journal of Materials Chemistry,* vol. 22, pp. 9813-9820, 2012.

[100] P. Dorenbos, "Thermal quenching of Eu^{2+} 5d–4f luminescence in inorganic compounds," *Journal of Physics: Condensed Matter,* vol. 17, pp. 8103-8111, 2005.

[101] A. U. Pawar, A. P. Jadhav, U. Pal, B. K. Kim, and Y. S. Kang, "Blue and red dual emission nanophosphor $CaMgSi_2O_6:Eu^{n+}$; crystal structure and electronic configuration," *Journal of Luminescence,* vol. 132, no. 3, pp. 659-664, 2012.

[102] J. Wang, Y. Huang, X. Wang, L. Qin, and H. J. Seo, "Luminescence properties of Eu-activated alkaline and alkaline-earth silicate $Na_2Ca_3Si_6O_{16}$," *Materials Research Bulletin,* vol. 55, pp. 126-130, 2014.

[103] R. D. Shannon, "Revised effective ionic radii and systematic studies of interatomie distances in halides and chaleogenides," *Acta Crystallographica Section A: Crystal Physics, Diffraction, Theoretical and General Crystallography,* vol. 32, pp. 751-767, 1976.

[104] K. Momma, and F. Izumi, "VESTA 3 for three-dimensional visualization of crystal, volumetric and morphology data," *Journal of Applied Crystallography,* vol. 44, no. 6, pp. 1272-1276, 2011.

[105] P. B. Moore, and T. Araki, "The crystal structure of bredigite and genealogy of some alkaline earth orthosilicates," *American Mineralogist,* vol. 61, pp. 74-87, 1976.

[106] L. Levien, and C. T. Prewitt, "High-pressure structural study of diopside," *American Mineralogist,* vol. 66, pp. 315-323, 1981.

[107] W.-N. Wang, W. Widiyastuti, T. Ogi, I. W. Lenggoro, and K. Okuyama, "Correlations between crystallite/particle size and photoluminescence properties of submicrometer phosphors," *Chem. Mater.,* vol. 19, pp. 1723-1730, 2007.

[108] J. K. Han, M. E. Hannah, A. Piquette, J. B. Talbot, K. C. Mishra, and J. McKittrick, "Nano- and submicron sized europium activated silicate phosphors prepared by a modified co-precipitation method," *ECS Journal of Solid State Science and Technology,* vol. 1, no. 3, pp. R98-R102, 2012.

[109] G. Y. Hong, B. S. Jeon, Y. K. Yoo, and J. S. Yoo, "Photoluminescence Characteristics of Spherical Y_2O_3:Eu Phosphors by Aerosol Pyrolysis," *Journal of The Electrochemical Society,* vol. 148, no. 11, pp. H161, 2001.

[110] I. W. Lenggoro, Y. Itoh, K. Okuyama, and T. O. Kim, "Nanoparticles of a doped oxide phosphor prepared by direct-spray pyrolysis," *Journal of Materials Research,* vol. 19, no. 12, pp. 3534-3539, 2011.

[111] S. Jun, J. Lee, and E. Jang, "Highly luminescent and photostable quantum dot silica monolith and its application to light-emitting diodes," *ACS Nano,* vol. 7, pp. 1472–1477, 2013.

[112] J. Zhang, and C. Jiang, "Luminescence properties of $Ca_{14}Mg_2(SiO_4)_8:Eu^{2+}$ from various Eu^{2+} sites for white-light-emitting diodes," *Materials Research Bulletin,* vol. 60, pp. 467-473, 2014.

[113] A. Pawar, A. Jadhav, C. W. Kim, H. G. Cha, U. Pal, and Y. S. Kang, "Emission controlled dual emitting Eu-doped $CaMgSi_2O_6$ nanophosphors," *Journal of Luminescence,* vol. 157, pp. 131-136, Jan, 2015.

[114] D. Cervantes-Vasquez, O. E. Contreras, and G. A. Hirata, "Quantum efficiency of silica-coated rare-earth doped yttrium silicate," *Journal of Luminescence,* vol. 143, pp. 226-232, Nov, 2013.

[115] J. H. Oh, S. J. Yang, Y.-G. Sung, and Y. R. Do, "Improved color coordinates of green monochromatic pc-LED capped with a band-pass filter," *Optical Express,* vol. 21, no. 4, pp. 4539-4550, 2013.

[116] G. Blasse, "Energy transfer betwen inequivalent Eu^{2+} ions," *Journal of Solid State Chemistry,* vol. 62, pp. 207-211, 1986.

[117] D. L. Dexter, "A Theory of Sensitized Luminescence in Solids," *The Journal of Chemical Physics,* vol. 21, no. 5, pp. 836, 1953.

[118] L. G. V. Uitert, "Characterization of energy transfer interactions between rare earth ions," *Journal of Electochem. Soc.,* vol. 114, pp. 1048-1053, 1967.

[119] L. Ozawa, and P. M. Jaffe, "The mechanism of the emission color shift with activator concentration in Eu^{3+} activated phosphors," *J. Electrochem. Soc.,* vol. 118, pp. 1678-1679, 1971.

[120] W. B. Im, Y.-I. Kim, J. H. Kang, D. Y. Jeon, H. K. Jung, and K. Y. Jung, "Neutron rietveld analysis for optimized $CaMgSi_2O_6:Eu^{2+}$ and its luminescent properties," *Journal of Materials Research,* vol. 20, no. 08, pp. 2061-2066, 2005.

[121] S. Poncé, Y. Jia, M. Giantomassi, M. Mikami, and X. Gonze, "Understanding thermal quenching of photoluminescence in oxynitride phosphors from first principles," *The Journal of Physical Chemistry C,* vol. 120, pp. 4040−4047, 2016.

[122] L. Chen, X. Chen, F. Liu, H. Chen, H. Wang, E. Zhao, Y. Jiang, T. S. Chan, C. H. Wang, W. Zhang, Y. Wang, and S. Chen, "Charge deformation and orbital hybridization: intrinsic mechanisms on tunable chromaticity of $Y_3Al_5O_{12}:Ce^{3+}$ luminescence by doping Gd^{3+} for warm white LEDs," *Sci Rep,* vol. 5, pp. 11514, 2015.

[123] J. K. Han, J. I. Choi, A. Piquette, M. Hannah, M. Anc, M. Galvez, J. B. Talbot, and J. McKittrick, "Phosphor development and integration for near-UV LED solid state lighting," *ECS Journal of Solid State Science and Technology,* vol. 2, no. 2, pp. R3138-R3147, 2012.

[124] K. Y. Jung, C. H. Lee, and Y. C. Kang, "Effect of surface area and crystallite size on luminescent intensity of Y_2O_3:Eu phosphor prepared by spray pyrolysis," *Materials Letters,* vol. 59, no. 19-20, pp. 2451-2456, 2005.

[125] C. H. Chiang, T. H. Liu, H. Y. Lin, H. Y. Kuo, and S. Y. Chu, "Effects of flux additives on the characteristics of $Y_{2.95}Al_5O_{12}:0.05Ce^{3+}$ phosphor: particle growth mechanism and luminescence," *Journal of Applied Physics,* vol. 114, no. 24, pp. 243517, 2013.

[126] Q. Zhang, H. Ni, L. Wang, and F. Xiao, "Effects of BaF_2 flux on the synthesis of green emitting phosphor $CaSc_2O_4:Ce^{3+}$," *ECS Journal of Solid State Science and Technology,* vol. 4, no. 2, pp. R23-R26, 2014.

[127] P. Dai, X. Zhang, P. Sun, J. Yang, L. Wang, S. Yan, Y. Liu, and J. Ballato, "Influence of flux on morphology and luminescence properties of phosphors: a Case Study on $Y_{1.55}Ti_2O_7:0.45Eu^{3+}$," *Journal of the American Ceramic Society,* vol. 95, no. 4, pp. 1447-1453, 2012.

[128] G.-H. Lee, C. Yoon, and S. Kang, "Role of flux in the production process of red phosphors for white LEDs," *Journal of Materials Science,* vol. 43, no. 18, pp. 6109-6115, 2008.

[129] B. R. Pamplin, *Crystal Growth, 2nd edition*, Beccles and London, UK: Pergamon Press, 1980.

[130] S. L. Stoll, and A. M. Stacy, "Single-crystal growth, alkali metal ordering, and superconductivity in $La_{2-x}M_xCuO_4$ (M = Na, K)," *Inorganic Chemistry,* vol. 33, pp. 2761-2765, 1994.

[131] Y. B. Chen, M. L. Gong, and K. W. Cheah, "Effects of fluxes on the synthesis of $Ca_3Sc_2Si_3O_{12}:Ce^{3+}$ green phosphors for white light-emitting diodes," *Materials Science and Engineering B-Advanced Functional Solid-State Materials,* vol. 166, no. 1, pp. 24-27, Jan, 2010.

[132] J. Y. Tang, Y. M. He, L. Y. Hao, X. Xu, and S. Agathopoulos, "Fine-sized $BaSi_3Al_3O_4N_5:Eu^{2+}$ phosphors prepared by solid-state reaction using BaF_2 flux," *Journal of Materials Research,* vol. 28, no. 18, pp. 2598-2604, Sep, 2013.

[133] X. Wang, J. H. Li, P. L. Shi, W. M. Guan, and H. Y. Zhang, "High dispersibility and enhanced luminescence properties of $BaMgAl_{10}O_{17}:Eu^{2+}$ phosphors derived from molten salt synthesis," *Optical Materials,* vol. 46, pp. 432-437, Aug, 2015.

[134] J. Q. Liu, X. J. Wang, T. T. Xuan, C. B. Wang, H. L. Li, and Z. Sun, "$Lu_3(Al,Si)_5(O,N)_{12}:Ce^{3+}$ phosphors with broad emission band and high thermal stability for white LEDs," *Journal of Luminescence,* vol. 158, pp. 322-327, Feb, 2015.

[135] K. Dong, Z. L. Li, S. G. Xiao, Z. F. Xiang, X. A. Zhang, X. L. Yang, and X. L. Jin, "Yellowish-orange luminescence in $Sr_8Al_{12}O_{24}S_2:Eu^{2+}$ phosphor," *Journal of Alloys and Compounds,* vol. 543, pp. 105-108, Dec, 2012.

[136] S. H. Lee, D. S. Jung, J. M. Han, H. Y. Koo, and Y. C. Kang, "Fine-sized $Y_3Al_5O_{12}$:Ce phosphor powders prepared by spray pyrolysis from the spray solution with barium fluoride flux," *Journal of Alloys and Compounds,* vol. 477, no. 1-2, pp. 776-779, May, 2009.

[137] H. S. Kang, Y. C. Kang, K. Y. Jung, and S. B. Park, "Eu-doped barium strontium silicate phosphor particles prepared from spray solution containing NH_4Cl flux by spray pyrolysis," *Materials Science and Engineering B-Solid State Materials for Advanced Technology,* vol. 121, no. 1-2, pp. 81-85, Jul, 2005.

[138] J. S. Wang, D.-C. Zhu, Q. Zheng, and T. Han, "Effect of flux on the composition and luminescent properties of $Ca_{0.68}Mg_{0.2}SiO_3$:0.12Eu^{3+} red phosphor," *Journal of Luminescence,* vol. 179, pp. 183-188, 2016.

[139] B. Zhang, L. Feng, and Y. Qiang, "Preparation and photoluminescence properties of the $Sr_{1.56}Ba_{0.4}SiO_4$:0.04Eu^{2+} phosphor," *Journal of Luminescence,* vol. 132, no. 5, pp. 1274-1277, 2012.

[140] A. M. Pires, and M. R. Davolos, "Luminescence of europium (III) and manganese (II) in barium and zinc orthosilicate," *Chemisty of Materials,* vol. 13, pp. 21-27, 2001.

[141] James T. Cahill, Jesse N. Ruppert, Bryce Wallis, Yanming Liu, and O. A. Graeve, "Development of mesoporosity in scandia-stabilized zirconia: particle size, solvent, and calcination effects," *Langmuir,* vol. 30, no. 19, pp. 5585−5591, 2014.

[142] Olivia A. Graeve, Hoorshad Fathi, James P. Kelly, Michael S. Saterlie, Kaustav Sinha, Gabriel Rojas-George, Raghunath Kanakala, David R. Brown, and E. A. Lopez, "Reverse micelle synthesis of oxide nanopowders: mechanisms of precipitate formation and agglomeration effects," *Journal of Colloid and Interface Science,* vol. 407, pp. 302–309, 2013.

[143] H. S. Michael S. Saterlie, Barkan Kavlicoglu, Yanming Liu, Olivia A. Graeve, "Surfactant effects on dispersion characteristics of copper-based nanofluids: a dynamic light scattering study," *Chemistry of Materials,* vol. 24, no. 17, pp. 3299−3306, 2012.

[144] K. Momma, and F. Izumi, "VESTA: a three-dimensional visualization system for electronic and structural analysis," *Journal of Applied Crystallography,* vol. 41, no. 3, pp. 653-658, 2008.

[145] A. V. Knyazev, E. N. Bulanov, A. O. Korshunov, and O. V. Krasheninnikova, "Synthesis and thermal expansion of some lanthanide-containing apatites," *Inorganic Materials,* vol. 49, no. 11, pp. 1133-1137, 2013.

[146] B. Marler, M. Borowski, U. Wodara, and W. Schreyer, "Synthetic tourmaline (olenite) with excess boron replacing silicon in the tetrahedral site: II. Structure analysis," *European Journal of Mineralogy,* vol. 14, pp. 763 - 771, 2002.

[147] Z. Xia, M. S. Molokeev, W. B. Im, S. Unithrattil, and Q. Liu, "Crystal structure and photoluminescence evolution of $La_5(Si_{2+x}B_{1-x})(O_{13-x}N_x)$:$Ce^{3+}$ solid solution phosphors," *The Journal of Physical Chemistry C,* vol. 119, no. 17, pp. 9488-9495, 2015.

[148] A. R. Denton, and N. W. Ashcroft, "Vegard's law," *Physical Review A,* vol. 43, pp. 3161-3164, 1991.

[149] D. D. Irene Prencipe, Alessandro Zani, Daniele Rizzo, Matteo Passoni, "Energy dispersive x-ray spectroscopy for nanostructured thin film density evaluation," *Science and Technology of Advanced Materials,* vol. 16, pp. 025007, 2015.

[150] G. Dantelle, M. Salaün, R. Bruyère, S. Kodjikian, and A. Ibanez, "Luminescent coatings prepared from optimized YAG:Ce nanoparticles," *Thin Solid Films*, 2017.

[151] Y. H. Kim, P. Arunkumar, B. Y. Kim, S. Unithrattil, E. Kim, S.-H. Moon, J. Y. Hyun, K. H. Kim, D. Lee, J.-S. Lee, and W. B. Im, "A zero-thermal-quenching phosphor," *Nature Materials,* vol. 16, no. 5, pp. 543, 2017.

[152] N. Bardsley, S. Bland, L. Pattison, M. Pattison, K. Stober, F. Welsh, and M. Yamada, "Solid-state lighting research and development multi-year program plan," *US Department of Energy*, 2014.

[153] H. Jang, Y.-H. Won, and D. Jeon, "Improvement of electroluminescent property of blue LED coated with highly luminescent yellow-emitting phosphors," *Applied Physics B,* vol. 95, no. 4, pp. 715-720, 2009.

[154] L. Chen, C.-C. Lin, C.-W. Yeh, and R.-S. Liu, "Light converting inorganic phosphors for white light-emitting diodes," *Materials,* vol. 3, no. 3, pp. 2172-2195, 2010.

[155] X. Piao, K.-i. Machida, T. Horikawa, H. Hanzawa, Y. Shimomura, and N. Kijima, "Preparation of $CaAlSiN_3$: Eu^{2+} phosphors by the self-propagating high-temperature synthesis and their luminescent properties," *Chemistry of Materials,* vol. 19, no. 18, pp. 4592-4599, 2007.

[156] X. Piao, K.-i. Machida, T. Horikawa, and B. Yun, "Acetate reduction synthesis of $Sr_2Si_5N_8$: Eu^{2+} phosphor and its luminescence properties," *Journal of Luminescence,* vol. 130, no. 1, pp. 8-12, 2010.

[157] X. Li, J. D. Budai, F. Liu, J. Y. Howe, J. Zhang, X.-J. Wang, Z. Gu, C. Sun, R. S. Meltzer, and Z. Pan, "New yellow $Ba_{0.93}Eu_{0.07}Al_2O_4$ phosphor for warm-white light-emitting diodes through single-emitting-center conversion," *Light: Science & Applications,* vol. 2, no. 1, pp. e50, 2013.

[158] W. B. Park, S. P. Singh, and K.-S. Sohn, "Discovery of a phosphor for light emitting diode applications and its structural determination, $Ba(Si,Al)_5(O,N)_8:Eu^{2+}$," *Journal of the American Chemical Society,* vol. 136, no. 6, pp. 2363-2373, 2014.

[159] N. Hirosaki, T. Takeda, S. Funahashi, and R.-J. Xie, "Discovery of new nitridosilicate phosphors for solid state lighting by the single-particle-diagnosis approach," *Chemistry of Materials,* vol. 26, no. 14, pp. 4280-4288, 2014.

[160] J. Greeley, T. F. Jaramillo, J. Bonde, I. Chorkendorff, and J. K. Nørskov, "Computational high-throughput screening of electrocatalytic materials for hydrogen evolution," *Materials For Sustainable Energy: A Collection of Peer-Reviewed Research and Review Articles from Nature Publishing Group*, pp. 280-284: World Scientific, 2011.

[161] G. Hautier, A. Jain, S. P. Ong, B. Kang, C. Moore, R. Doe, and G. Ceder, "Phosphates as lithium-ion battery cathodes: an evaluation based on high-throughput ab initio calculations," *Chemistry of Materials,* vol. 23, no. 15, pp. 3495-3508, 2011.

[162] R. Gautier, X. Zhang, L. Hu, L. Yu, Y. Lin, T. O. Sunde, D. Chon, K. R. Poeppelmeier, and A. Zunger, "Prediction and accelerated laboratory discovery of previously unknown 18-electron ABX compounds," *Nature chemistry,* vol. 7, no. 4, pp. 308, 2015.

[163] G. Bergerhoff, R. Hundt, R. Sievers, and I. Brown, "The inorganic crystal structure data base," *Journal of chemical information and computer sciences,* vol. 23, no. 2, pp. 66-69, 1983.

[164] G. Kresse, and J. Furthmüller, "Efficient iterative schemes for ab initio total-energy calculations using a plane-wave basis set," *Physical Review B,* vol. 54, pp. 11169-11186, 1996.

[165] S. P. Ong, W. D. Richards, A. Jain, G. Hautier, M. Kocher, S. Cholia, D. Gunter, V. L. Chevrier, K. A. Persson, and G. Ceder, "Python Materials Genomics (pymatgen): A robust, open-source python library for materials analysis," *Computational Materials Science,* vol. 68, pp. 314-319, 2013.

[166] S. P. Ong, L. Wang, B. Kang, and G. Ceder, "Li− Fe− P− O_2 phase diagram from first principles calculations," *Chemistry of Materials,* vol. 20, no. 5, pp. 1798-1807, 2008.

[167] W. Sun, S. T. Dacek, S. P. Ong, G. Hautier, A. Jain, W. D. Richards, A. C. Gamst, K. A. Persson, and G. Ceder, "The thermodynamic scale of inorganic crystalline metastability," *Science Advances,* vol. 2, no. 11, pp. e1600225, 2016.

[168] A. Togo, and I. Tanaka, "First principles phonon calculations in materials science," *Scripta Materialia,* vol. 108, pp. 1-5, 2015.

[169] S.-H. Wei, and S. Zhang, "Chemical trends of defect formation and doping limit in II-VI semiconductors: The case of CdTe," *Physical Review B,* vol. 66, no. 15, pp. 155211, 2002.

[170] J. Heyd, G. E. Scuseria, and M. Ernzerhof, "Hybrid functionals based on a screened Coulomb potential," *The Journal of chemical physics,* vol. 118, no. 18, pp. 8207-8215, 2003.

[171] J. Heyd, and G. E. Scuseria, "Erratum: "Hybrid functionals based on a screened Coulomb potential" [J. Chem. Phys. 118, 8207 (2003)]," *The Journal of Chemical Physics,* vol. 124, no. 21, pp. 219906, 2006.

[172] M. Shishkin, M. Marsman, and G. Kresse, "Accurate quasiparticle spectra from self-consistent GW calculations with vertex corrections," *Physical review letters,* vol. 99, no. 24, pp. 246403, 2007.

[173] S. Albrecht, L. Reining, R. Del Sole, and G. Onida, "Ab initio calculation of excitonic effects in the optical spectra of semiconductors," *Physical review letters,* vol. 80, no. 20, pp. 4510, 1998.

[174] K. A. Denault, J. Brgoch, M. W. Gaultois, A. Mikhailovsky, R. Petry, H. Winkler, S. P. DenBaars, and R. Seshadri, "Consequences of optimal bond valence on structural rigidity and improved luminescence properties in $Sr_xBa_{2-x}SiO_4:Eu^{2+}$ orthosilicate phosphors," *Chemistry of Materials,* vol. 26, no. 7, pp. 2275-2282, 2014.

[175] N. C. George, K. A. Denault, and R. Seshadri, "Phosphors for solid-state white lighting," *Annual Review of Materials Research,* vol. 43, pp. 481-501, 2013.

[176] Z. Xia, and Q. Liu, "Progress in discovery and structural design of color conversion phosphors for LEDs," *Progress in Materials Science,* vol. 84, pp. 59-117, 2016.

[177] P. Villars, M. Berndt, K. Brandenburg, K. Cenzual, J. Daams, F. Hulliger, T. Massalski, H. Okamoto, K. Osaki, and A. Prince, "The pauling file," *Journal of Alloys and Compounds,* vol. 367, no. 1-2, pp. 293-297, 2004.

[178] G. Hautier, C. Fischer, V. Ehrlacher, A. Jain, and G. Ceder, "Data mined ionic substitutions for the discovery of new compounds," *Inorganic chemistry,* vol. 50, no. 2, pp. 656-663, 2011.

[179] S. Poncé, Y. Jia, M. Giantomassi, M. Mikami, and X. Gonze, "Understanding thermal quenching of photoluminescence in oxynitride phosphors from first principles," *The Journal of Physical Chemistry C,* vol. 120, no. 7, pp. 4040-4047, 2016.

[180] Z. Wang, W. Ye, I.-H. Chu, and S. P. Ong, "Elucidating structure–composition–property relationships of the β-SiAlON:Eu^{2+} Phosphor," *Chemistry of Materials,* vol. 28, no. 23, pp. 8622-8630, 2016.

[181] V. V. Atuchin, N. F. Beisel, E. N. Galashov, E. M. Mandrik, M. S. Molokeev, A. P. Yelisseyev, A. A. Yusuf, and Z. Xia, "Pressure-stimulated synthesis and luminescence properties of microcrystalline $(Lu,Y)_3Al_5O_{12}$: Ce^{3+} garnet phosphors," *ACS applied materials & interfaces,* vol. 7, no. 47, pp. 26235-26243, 2015.

[182] H. Ji, L. Wang, M. S. Molokeev, N. Hirosaki, R. Xie, Z. Huang, Z. Xia, M. Otmar, L. Liu, and V. V. Atuchin, "Structure evolution and photoluminescence of $Lu_3(Al,Mg)_2(Al,Si)_3O_{12}:Ce^{3+}$ phosphors: new yellow-color converters for blue LED-driven solid state lighting," *Journal of Materials Chemistry C,* vol. 4, no. 28, pp. 6855-6863, 2016.

[183] E. Galashov, V. Atuchin, T. Gavrilova, I. Korolkov, Y. Mandrik, A. Yelisseyev, and Z. Xia, "Synthesis of $Y_3Al_5O_{12}:Ce^{3+}$ phosphor in the Y_2O_3–Al metal–CeO_2 ternary system," *Journal of Materials Science,* vol. 52, no. 22, pp. 13033-13039, 2017.

[184] J. Hou, W. Jiang, Y. Fang, and F. Huang, "Red, green and blue emissions coexistence in white-light-emitting $Ca_{11}(SiO_4)_4(BO_3)_2:Ce^{3+},Eu^{2+},Eu^{3+}$ phosphor," *Journal of Materials Chemistry C,* vol. 1, no. 37, pp. 5892-5898, 2013.

[185] X. Piao, T. Horikawa, H. Hanzawa, and K.-i. Machida, "Characterization and luminescence properties of $Sr_2Si_5N_8:Eu^{2+}$ phosphor for white light-emitting-diode illumination," *Applied Physics Letters,* vol. 88, no. 16, pp. 161908, 2006.

[186] M. Shang, C. Li, and J. Lin, "How to produce white light in a single-phase host?," *Chemical Society Reviews,* vol. 43, no. 5, pp. 1372-1386, 2014.

[187] C.-H. Huang, P.-J. Wu, J.-F. Lee, and T.-M. Chen, "$(Ca,Mg,Sr)_9Y(PO_4)_7:Eu^{2+},Mn^{2+}$:phosphors for white-light near-UV LEDs through crystal field tuning and energy transfer," *Journal of Materials Chemistry,* vol. 21, no. 28, pp. 10489-10495, 2011.

[188] Z.-C. Wu, J. Liu, W.-G. Hou, J. Xu, and M.-L. Gong, "A new single-host white-light-emitting $BaSrMg(PO_4)_2:Eu^{2+}$ phosphor for white-light-emitting diodes," *Journal of Alloys and Compounds,* vol. 498, no. 2, pp. 139-142, 2010.

[189] G. Li, Z. Hou, C. Peng, W. Wang, Z. Cheng, C. Li, H. Lian, and J. Lin, "Electrospinning Derived One-Dimensional LaOCl: Ln^{3+} (Ln= Eu/Sm, Tb, Tm) Nanofibers, Nanotubes and Microbelts with Multicolor-Tunable Emission Properties," *Advanced Functional Materials,* vol. 20, no. 20, pp. 3446-3456, 2010.

[190] Z. Jia, and M. Xia, "Blue-green tunable color of Ce^{3+}/Tb^{3+} coactivated $NaBa_3La_3Si_6O_{20}$ phosphor via energy transfer," *Scientific Reports,* vol. 6, pp. 33283, 2016.

[191] F. Ruan, D. Deng, M. Wu, C. Wu, and S. Xu, "Tunable single-host full-color-emitting $Ca_9Zn_{1.5}(PO_4)_7$:Eu,Tb phosphor via Eu^{2+}/Eu^{3+} dual-emitting," *Journal of Luminescence,* vol. 198, pp. 1-9, 2018.

[192] D. Geng, M. Shang, D. Yang, Y. Zhang, Z. Cheng, and J. Lin, "Green/green-yellow-emitting $KSrGd(PO_4)_2:Ce^{3+},Tb^{3+}/Mn^{2+}$ phosphors with high quantum efficiency for LEDs and FEDs," *Dalton Transactions,* vol. 41, no. 46, pp. 14042-14045, 2012.

[193] C. Xu, H. Guan, Y. Song, Z. An, X. Zhang, X. Zhou, Z. Shi, Y. Sheng, and H. Zou, "Novel highly efficient single-component multi-peak emitting aluminosilicate phosphors co-activated with Ce^{3+},Tb^{3+} and Eu^{2+}: luminescence properties, tunable color, and thermal properties," *Physical Chemistry Chemical Physics*, 2018.

[194] Z. Wang, S. Lou, P. Li, and Z. Lian, "Single-phase tunable white-light-emitting $Sr_3La(PO_4)_3:Eu^{2+},Mn^{2+}$ phosphor for white LEDs," *Applied Optics,* vol. 56, no. 4, pp. 1167-1172, 2017.

[195] M. Shang, G. Li, D. Geng, D. Yang, X. Kang, Y. Zhang, H. Lian, and J. Lin, "Blue emitting $Ca_8La_2(PO_4)_6O_2$: Ce^{3+}/Eu^{2+} phosphors with high color purity and brightness for white LED: soft-chemical synthesis, luminescence, and energy transfer properties," *The Journal of Physical Chemistry C,* vol. 116, no. 18, pp. 10222-10231, 2012.

[196] H. He, R. Fu, Y. Cao, X. Song, Z. Pan, X. Zhao, Q. Xiao, and R. Li, "$Ce^{3+}\rightarrow Eu^{2+}$ energy transfer mechanism in the $Li_2SrSiO_4:Eu^{2+},Ce^{3+}$ phosphor," *Optical Materials,* vol. 32, no. 5, pp. 632-636, 2010.

[197] C. Guo, L. Luan, F. G. Shi, and X. Ding, "White-emitting phosphor Ca_2BO_3Cl: Ce^{3+},Eu^{2+} for UV light-emitting diodes," *Journal of the Electrochemical Society,* vol. 156, no. 6, pp. J125-J128, 2009.

[198] W.-Y. Huang, F. Yoshimura, K. Ueda, Y. Shimomura, H.-S. Sheu, T.-S. Chan, C.-Y. Chiang, W. Zhou, and R.-S. Liu, "Chemical pressure control for photoluminescence of $MSiAl_2O_3N_2$: Ce^{3+}/Eu^{2+} (M= Sr, Ba) oxynitride phosphors," *Chemistry of Materials,* vol. 26, no. 6, pp. 2075-2085, 2014.

[199] L. Chen, A. Luo, Y. Zhang, F. Liu, Y. Jiang, Q. Xu, X. Chen, Q. Hu, S.-F. Chen, and K.-J. Chen, "Optimization of the single-phased white phosphor of $Li_2SrSiO_4:Eu^{2+},Ce^{3+}$ for light-emitting diodes by using the combinatorial approach assisted with the Taguchi method," *ACS Combinatorial Science,* vol. 14, no. 12, pp. 636-644, 2012.

[200] A. M. Jakob, and T. A. Schmedake, "A novel approach to monodisperse, luminescent silica spheres," *Chemistry of Materials,* vol. 18, no. 14, pp. 3173-3175, 2006.

[201] L. Ma, Z. Xia, V. Atuchin, M. Molokeev, S. Auluck, A. Reshak, and Q. Liu, "Engineering oxygen vacancies towards self-activated $BaLuAl_xZn_{4-x}O_{7-(1-x)/2}$ photoluminescent materials: an experimental and theoretical analysis," *Physical Chemistry Chemical Physics,* vol. 17, no. 46, pp. 31188-31194, 2015.

[202] S. A. Khan, Z. Hao, H. Wei-Wei, L.-Y. Hao, X. Xu, N. Z. Khan, and S. Agathopoulos, "Novel single-phase full-color emitting $Ba_9Lu_2Si_6O_{24}:Ce^{3+}/Mn^{2+}/Tb^{3+}$ phosphors for white LED applications," *Journal of Materials Science,* vol. 52, no. 18, pp. 10927-10937, 2017.

[203] Z. Xia, and R.-S. Liu, "Tunable blue-green color emission and energy transfer of $Ca_2Al_3O_6F$: Ce^{3+},Tb^{3+} phosphors for near-UV white LEDs," *The Journal of Physical Chemistry C,* vol. 116, no. 29, pp. 15604-15609, 2012.

[204] N. Guo, Y. Song, H. You, G. Jia, M. Yang, K. Liu, Y. Zheng, Y. Huang, and H. Zhang, "Optical properties and energy transfer of $NaCaPO_4:Ce^{3+},Tb^{3+}$ phosphors for potential application in light-emitting diodes," *European Journal of Inorganic Chemistry,* vol. 2010, no. 29, pp. 4636-4642, 2010.

[205] H. Y. Chung, C. H. Lu, and C. H. Hsu, "Preparation and photoluminescence properties of novel color-tunable $MgY_4Si_3O_{13}:Ce^{3+},Tb^{3+}$ phosphors for ultraviolet light-emitting diodes," *Journal of the American Ceramic Society,* vol. 93, no. 7, pp. 1838-1841, 2010.

[206] V. Dotsenko, S. Levshov, I. Berezovskaya, G. Stryganyuk, A. Voloshinovskii, and N. Efryushina, "Luminescent properties of Eu^{2+} and Ce^{3+} ions in strontium litho-silicate Li_2SrSiO_4," *Journal of Luminescence,* vol. 131, no. 2, pp. 310-315, 2011.

[207] M. De Graef, and M. E. McHenry, *Structure of Materials: An Introduction to Crystallography, Diffraction and Symmetry*: Cambridge University Press, 2012.

[208] J. Makinson, J. Lee, S. Magner, R. De Angelis, W. Weins, and A. Hieronymus, "X-ray diffraction signatures of defects in nanocrystalline materials," *Adv. X-Ray Anal,* vol. 42, pp. 407-411, 2000.

[209] J. Ha, E. Novitskaya, G. Hirata, C. Zhou, R. Ridley, O. Graeve, and J. McKittrick, "A facile method using a flux to improve quantum efficiency of submicron particle sized phosphors for solid-state lighting applications," *Ceramics,* vol. 1, pp. 5, 2018.

[210] B. H. Toby, "*R* factors in Rietveld analysis: How good is good enough?," *Powder Diffraction,* vol. 21, no. 1, pp. 67-70, 2006.

[211] J. K. Han, M. E. Hannah, A. Piquette, J. Micone, G. A. Hirata, J. B. Talbot, K. C. Mishra, and J. McKittrick, "Europium-activated barium/strontium silicates for near-UV light emitting diode applications," *Journal of Luminescence,* vol. 133, pp. 184-187, 2013.

[212] Y. Liu, C. Zhang, Z. Cheng, Z. Zhou, J. Jiang, and H. Jiang, "Origin and luminescence of anomalous red-emitting center in rhombohedral $Ba_9Lu_2Si_6O_{24}$: Eu^{2+} blue phosphor," *Inorganic chemistry,* vol. 55, no. 17, pp. 8628-8635, 2016.

[213] Y. Liu, J. Zhang, C. Zhang, J. Xu, G. Liu, J. Jiang, and H. Jiang, "$Ba_9Lu_2Si_6O_{24}$:Ce^{3+}: an efficient green phosphor with high thermal and radiation stability for solid-state lighting," *Advanced Optical Materials,* vol. 3, no. 8, pp. 1096-1101, 2015.

[214] D. Dexter, and J. H. Schulman, "Theory of concentration quenching in inorganic phosphors," *The Journal of Chemical Physics,* vol. 22, no. 6, pp. 1063-1070, 1954.

[215] G. Blasse, "Energy transfer between inequivalent Eu^{2+} ions," *Journal of Solid State Chemistry,* vol. 62, no. 2, pp. 207-211, 1986.

[216] F. Lucas, S. Jaulmes, M. Quarton, T. Le Mercier, F. Guillen, and C. Fouassier, "Crystal structure of $SrAl_2B_2O_7$ and Eu^{2+} luminescence," *Journal of Solid State Chemistry,* vol. 150, no. 2, pp. 404-409, 2000.

[217] A. Meijerink, and G. Blasse, "Luminescence properties of Eu^{2+}-activated alkaline earth haloborates," *Journal of Luminescence,* vol. 43, no. 5, pp. 283-289, 1989.

[218] M. P. Saradhi, and U. Varadaraju, "Photoluminescence studies on Eu^{2+}-activated Li_2SrSiO_4 a potential orange-yellow phosphor for solid-state lighting," *Chemistry of materials,* vol. 18, no. 22, pp. 5267-5272, 2006.

[219] L. Van Uitert, "An empirical relation fitting the position in energy of the lower d-band edge for Eu^{2+} or Ce^{3+} in various compounds," *Journal of Luminescence,* vol. 29, no. 5-6, pp. 1-9, 1984.

[220] J. Fan, J. Gou, Y. Chen, B. Yu, and S. F. Liu, "Enhanced luminescence and tunable color of $Sr_8CaSc(PO_4)_7:Eu^{2+},Ce^{3+},Mn^{2+}$ phosphor by energy transfer between Ce^{3+}-Eu^{2+}-Mn^{2+}," *Journal of Alloys and Compounds,* vol. 731, pp. 796-804, 2018.

[221] W. Geng, X. Zhou, and Y. Wang, "Potential single-phased white-emitting phosphor $(Ca_{0.33}Sr_{0.67})_7(SiO_3)_6Cl_2:Ce^{3+},Eu^{2+}$ for ultraviolet light-emitting diode," *RSC Advances,* vol. 6, no. 110, pp. 108964-108968, 2016.

[222] G. Blasse, "Thermal quenching of characteristic fluorescence," *The Journal of Chemical Physics,* vol. 51, no. 8, pp. 3529-3530, 1969.

[223] C. R. Ronda, "Emission and excitation mechanisms of phosphors," *Luminescence: From theory to applications*, pp. 1-34, 2008.

[224] J. Zhou, and Z. Xia, "Luminescence color tuning of Ce^{3+},Tb^{3+} and Eu^{3+} codoped and tri-doped $BaY_2Si_3O_{10}$ phosphors via energy transfer," *Journal of Materials Chemistry C,* vol. 3, no. 29, pp. 7552-7560, 2015.

[225] K. Li, M. Shang, H. Lian, and J. Lin, "Recent development in phosphors with different emitting colors via energy transfer," *Journal of Materials Chemistry C,* vol. 4, no. 24, pp. 5507-5530, 2016.

[226] G. Blasse, "Energy transfer in oxidic phosphors," *Physics Letters A,* vol. 28, no. 6, pp. 444-445, 1968.

[227] H. Guan, Y. Song, K. Zheng, Y. Sheng, and H. Zou, "$BaGdF_5:Dy^{3+},Tb^{3+},Eu^{3+}$ multifunctional nanospheres: paramagnetic, luminescence, energy transfer, and tunable color," *Physical Chemistry Chemical Physics,* vol. 18, no. 20, pp. 13861-13873, 2016.

[228] G. Caldino, "Energy transfer in CaF_2 doped with Ce^{3+}, Eu^{2+} and Mn^{2+} ions," *Journal of Physics-Condensed Matter,* vol. 15, no. 41, pp. 7127-7138, 2003.

[229] L. Zhou, H. Liang, P. A. Tanner, S. Zhang, D. Hou, C. Liu, Y. Tao, Y. Huang, and L. Li, "Luminescence, cathodoluminescence and $Ce^{3+} \rightarrow Eu^{2+}$ energy transfer and emission enhancement in the $Sr_5(PO_4)_3Cl:Ce^{3+},Eu^{2+}$ phosphor," *Journal of Materials Chemistry C,* vol. 1, no. 43, pp. 7155-7165, 2013.

[230] A. P. Piquette, M. E. Hannah, and K. C. Mishra, "An investigation of self-absorption and corresponding spectral shift in phosphors," *ECS Transactions,* vol. 41, no. 37, pp. 1-9, 2012.

[231] H. A. Höppe, H. Lutz, P. Morys, W. Schnick, and A. Seilmeier, "Luminescence in Eu^{2+}-doped $Ba_2Si_5N_8$: fluorescence, thermoluminescence, and upconversion," *Journal of Physics and Chemistry of Solids,* vol. 61, pp. 2001-2006, 2000.

[232] K. Sakuma, N. Hirosaki, and R.-J. Xie, "Red-shift of emission wavelength caused by reabsorption mechanism of europium activated Ca-α-SiAlON ceramic phosphors," *Journal of Luminescence,* vol. 126, no. 2, pp. 843-852, 2007.

[233] J. Zhao, X. Sun, and Z. Wang, "Ce^{3+}/Eu^{2+} doped $SrSc2O_4$ phosphors: Synthesis, luminescence and energy transfer from Ce^{3+} to Eu^{2+}," *Chemical Physics Letters,* vol. 691, pp. 68-72, 2018.

[234] C. C. Lin, A. Meijerink, and R.-S. Liu, "Critical red components for next-generation white LEDs," *The Journal of Physical Chemistry Letters,* vol. 7, no. 3, pp. 495-503, 2016.

[235] Y. Jin, M.-H. Fang, M. Grinberg, S. Mahlik, T. Lesniewski, M. Brik, G.-Y. Luo, J. G. Lin, and R.-S. Liu, "Narrow red emission band fluoride phosphor $KNaSiF_6:Mn^{4+}$ for warm white light-emitting diodes," *ACS Applied Materials & Interfaces,* vol. 8, no. 18, pp. 11194-11203, 2016.

[236] J.-K. Sheu, S.-J. Chang, C. Kuo, Y.-K. Su, L. Wu, Y. Lin, W. Lai, J. Tsai, G.-C. Chi, and R. Wu, "White-light emission from near UV InGaN-GaN LED chip precoated with blue/green/red phosphors," *IEEE Photonics Technology Letters,* vol. 15, no. 1, pp. 18-20, 2003.

[237] S. Neeraj, N. Kijima, and A. Cheetham, "Novel red phosphors for solid-state lighting: the system $NaM(WO_4)_{2-x}(MoO_4)_x:Eu^{3+}$ (M=Gd, Y, Bi)," *Chemical Physics Letters,* vol. 387, no. 1-3, pp. 2-6, 2004.

[238] J. K. Kim, H. Luo, E. F. Schubert, J. Cho, C. Sone, and Y. Park, "Strongly enhanced phosphor efficiency in GaInN white light-emitting diodes using remote phosphor configuration and diffuse reflector cup," *Japanese Journal of Applied Physics,* vol. 44, no. 5L, pp. L649, 2005.

[239] H. Terraschke, and C. Wickleder, "UV, blue, green, yellow, red, and small: newest developments on Eu^{2+}-doped nanophosphors," *Chemical Reviews,* vol. 115, no. 20, pp. 11352-11378, 2015.

[240] R.-J. Xie, N. Hirosaki, Y. Li, and T. Takeda, "Rare-earth activated nitride phosphors: synthesis, luminescence and applications," *Materials,* vol. 3, no. 6, pp. 3777-3793, 2010.

[241] L. Chen, R. Liu, W. Zhuang, Y. Liu, Y. Hu, X. Zhou, and X. Ma, "A study on photoluminescence and energy transfer of $SrAlSi_4N_7$: Eu^{2+}, Ce^{3+} phosphors for application in white-light LED," *Journal of Alloys and Compounds,* vol. 627, pp. 218-221, 2015.

[242] J. Van Krevel, J. Van Rutten, H. Mandal, H. Hintzen, and R. Metselaar, "Luminescence properties of terbium-, cerium-, or europium-doped α-sialon materials," *Journal of Solid State Chemistry,* vol. 165, no. 1, pp. 19-24, 2002.

[243] T. Suehiro, R.-J. Xie, and N. Hirosaki, "Facile synthesis of $(Sr,Ca)_2Si_5N_8$: Eu^{2+}-based red-emitting phosphor for solid-state lighting," *Industrial & Engineering Chemistry Research,* vol. 52, no. 22, pp. 7453-7456, 2013.

[244] T. Takahashi, and S. Adachi, "Mn^{4+}-activated red photoluminescence in K_2SiF_6 phosphor," *Journal of The Electrochemical Society,* vol. 155, no. 12, pp. E183-E188, 2008.

[245] P. Arunkumar, Y. H. Kim, H. J. Kim, S. Unithrattil, and W. B. Im, "Hydrophobic organic skin as a protective shield for moisture-sensitive phosphor-based optoelectronic devices," *ACS applied materials & interfaces,* vol. 9, no. 8, pp. 7232-7240, 2017.

[246] S. Adachi, and T. Takahashi, "Direct synthesis and properties of $K_2SiF_6:Mn^{4+}$ phosphor by wet chemical etching of Si wafer," *Journal of Applied Physics,* vol. 104, no. 2, pp. 023512, 2008.

[247] Y. K. Xu, and S. Adachi, "Properties of $Na_2\ SiF_6:Mn^{4+}$ and $Na_2GeF_6:Mn^{4+}$ red phosphors synthesized by wet chemical etching," *Journal of Applied Physics,* vol. 105, no. 1, pp. 013525, 2009.

[248] L. Lv, X. Jiang, S. Huang, X. Chen, and Y. Pan, "The formation mechanism, improved photoluminescence and LED applications of red phosphor $K_2SiF_6:Mn^{4+}$," *Journal of Materials Chemistry C,* vol. 2, no. 20, pp. 3879-3884, 2014.

[249] X. Jiang, Y. Pan, S. Huang, X. a. Chen, J. Wang, and G. Liu, "Hydrothermal synthesis and photoluminescence properties of red phosphor $BaSiF_6:Mn^{4+}$ for LED applications," *Journal of Materials Chemistry C,* vol. 2, no. 13, pp. 2301-2306, 2014.

[250] H. Zhu, C. C. Lin, W. Luo, S. Shu, Z. Liu, Y. Liu, J. Kong, E. Ma, Y. Cao, and R.-S. Liu, "Highly efficient non-rare-earth red emitting phosphor for warm white light-emitting diodes," *Nature Communications,* vol. 5, pp. 4312, 2014.

[251] L.-L. Wei, C. C. Lin, M.-H. Fang, M. G. Brik, S.-F. Hu, H. Jiao, and R.-S. Liu, "A low-temperature co-precipitation approach to synthesize fluoride phosphors $K_2MF_6:Mn^{4+}$ (M= Ge, Si) for white LED applications," *Journal of Materials Chemistry C,* vol. 3, no. 8, pp. 1655-1660, 2015.

[252] F. Tang, Z. Su, H. Ye, M. Wang, X. Lan, D. L. Phillips, Y. Cao, and S. Xu, "A set of manganese ion activated fluoride phosphors ($A_2BF_6:Mn^{4+}$, A = K, Na, B= Si, Ge, Ti): synthesis below 0° C and efficient room-temperature photoluminescence," *Journal of Materials Chemistry C,* vol. 4, no. 40, pp. 9561-9568, 2016.

[253] Z. Wang, Y. Liu, Y. Zhou, Q. Zhou, H. Tan, Q. Zhang, and J. Peng, "Red-emitting phosphors Na_2XF_6: Mn^{4+} (X= Si, Ge, Ti) with high colour-purity for warm white-light-emitting diodes," *RSC Advances,* vol. 5, no. 72, pp. 58136-58140, 2015.

[254] Y. K. Xu, and S. Adachi, "Properties of $Na_2SiF_6:Mn^{4+}$ and $Na_2GeF_6:Mn^{4+}$ red phosphors synthesized by wet chemical etching," *Journal of Applied Physics,* vol. 105, pp. 013525, 2009.

[255] R. Kasa, and S. Adachi, "Red and deep red emissions from cubic $K_2SiF_6:Mn^{4+}$ and hexagonal K_2MnF_6 synthesized in $HF/KMnO_4/KHF_2$/Si solutions," *Journal of The Electrochemical Society,* vol. 159, no. 4, pp. J89-J95, 2012.

[256] H.-D. Nguyen, C. C. Lin, M.-H. Fang, and R.-S. Liu, "Synthesis of $Na_2SiF_6:Mn^{4+}$ red phosphors for white LED applications by co-precipitation," *Journal of Materials Chemistry C,* vol. 2, no. 48, pp. 10268-10272, 2014.

[257] Y. K. Xu, and S. Adachi, "Properties of $Na_2SiF_6:Mn^{4+}$ and $Na_2GeF_6:Mn^{4+}$ red phosphors synthesized by wet chemical etching," *Journal of Applied Physics,* vol. 105, no. 1, pp. 013525, 2009.

[258] X. Yi, R. Li, H. Zhu, J. Gao, W. You, Z. Gong, W. Guo, and X. Chen, "$K_2NaAlF_6:Mn^{4+}$ red phosphor: room-temperature synthesis and electronic/vibronic structures," *Journal of Materials Chemistry C,* vol. 6, no. 8, pp. 2069-2076, 2018.

[259] T. Senden, R. Geitenbeek, and A. Meijerink, "Co-precipitation synthesis and optical properties of Mn^{4+}-doped hexafluoroaluminate w-LED phosphors," *Materials,* vol. 10, no. 11, pp. 1322, 2017.

[260] H. F. Sijbom, R. Verstraete, J. J. Joos, D. Poelman, and P. F. Smet, "$K_2SiF_6:Mn^{4+}$ as a red phosphor for displays and warm-white LEDs: a review of properties and perspectives," *Optical Materials Express,* vol. 7, no. 9, pp. 3332-3365, 2017.

[261] C. Liao, R. Cao, Z. Ma, Y. Li, G. Dong, K. N. Sharafudeen, and J. Qiu, "Synthesis of $K_2SiF_6:Mn^{4+}$ phosphor from SiO_2 powders via redox reaction in $HF/KMnO_4$ solution and their application in warm-white LED," *Journal of the American Ceramic Society,* vol. 96, no. 11, pp. 3552-3556, 2013.

[262] F. Garcia-Santamaria, J. Murphy, A. Setlur, and S. Sista, "Concentration quenching in $K_2SiF_6:Mn^{4+}$ phosphors," *ECS Journal of Solid State Science and Technology,* vol. 7, no. 1, pp. R3030-R3033, 2018.

[263] S. Das, S. Patel, and B. K. Mishra, "Oxidation by permanganate: synthetic and mechanistic aspects," *Tetrahedron,* vol. 65, pp. 707-739, 2009.

[264] A. H. Reidies, "Manganese compounds," *Ullmann's Encyclopedia of Industrial Chemistry*, Weinheim, Germany: Wiley-VCH Verlag GmbH & Co. KGaA, 2012.

[265] L. Huang, Y. Zhu, X. Zhang, R. Zou, F. Pan, J. Wang, and M. Wu, "HF-free hydrothermal route for synthesis of highly efficient narrow-band red emitting phosphor $K_2Si_{1-x}F_6:xMn^{4+}$ for warm white light-emitting diodes," *Chemistry of Materials,* vol. 28, no. 5, pp. 1495-1502, 2016.

[266] Z. Hou, X. Tang, X. Luo, T. Zhou, L. Zhang, and R.-J. Xie, "A green synthetic route to the highly efficient $K_2SiF_6:Mn_{4+}$ narrow-band red phosphor for warm white light-emitting diodes," *Journal of Materials Chemistry C,* vol. 6, no. 11, pp. 2741-2746, 2018.

[267] J. Olchowka, M. Suta, and C. Wickleder, "Green synthesis of A_2SiF_6 (A= Li–Cs) nanoparticles using ionic liquids as solvents and as fluorine sources: a simple approach without HF," *Chemistry–A European Journal,* vol. 23, no. 50, pp. 12092-12095, 2017.

[268] C. Lorbeer, and A. V. Mudring, "Ionic liquid-assisted route to nanocrystalline single-phase phosphors for white light-emitting diodes," *ChemSusChem,* vol. 6, no. 12, pp. 2382-2387, 2013.

[269] J. Olchowka, H. Hagemann, T. Delgado, and C. Wickleder, "The influence of ionothermal synthesis using $BmimBF_4$ as a solvent on nanophosphor $BaFBr:Eu^{2+}$ photoluminescence," *Nanoscale,* vol. 10, no. 42, pp. 19706-19710, 2018.

[270] H. Terraschke, J. Olchowka, E. Geringer, A. V. Rodrigues, and C. Wickleder, "Facile ionic liquid-assisted strategy for direct precipitation of Eu^{2+}-activated nanophosphors under ambient conditions," *Small,* vol. 14, no. 17, pp. 1703707, 2018.

[271] H. Xue, R. Verma, and M. S. Jean'ne, "Review of ionic liquids with fluorine-containing anions," *Journal of Fluorine Chemistry,* vol. 127, no. 2, pp. 159-176, 2006.

[272] D. Freudenmann, S. Wolf, M. Wolff, and C. Feldmann, "Ionic liquids: new perspectives for inorganic synthesis?," *Angewandte Chemie International Edition,* vol. 50, no. 47, pp. 11050-11060, 2011.

[273] R. E. Morris, "Ionothermal synthesis—ionic liquids as functional solvents in the preparation of crystalline materials," *Chemical Communications*, no. 21, pp. 2990-2998, 2009.

[274] A. Bruker, "TOPAS, Version 4.2," *Bruker AXS, Karlsruhe, Germany*, 2009.

[275] T.-C. Lang, T. Han, L.-L. Peng, and M.-J. Tu, "Luminescence properties of $Na_2SiF_6:Mn^{4+}$ red phosphors for high colour-rendering white LED applications synthesized via a simple exothermic reduction reaction," *Materials Chemistry Frontiers,* vol. 1, no. 5, pp. 928-932, 2017.

[276] D. Tao, and Y.-Q. Li, *Red-emitting nitride-based phosphors, US 9,422,472 B2*, United State, U. S. Patent, 2014.

[277] L. DeMarsh, "SMPTE Tutorial: TV Display Phosphors/Primaries—Some History," *SMPTE journal,* vol. 102, no. 12, pp. 1095-1098, 1993.

[278] E. V. Radkov, A. A. Setlur, A. M. Srivastava, and L. S. Grigorov, *Red line emitting phosphors for use in LED applications, US 7,648,649 B2*, United State, U. S. Patent, 2010.